Pushing and Shaking of Skyrmion Lattices

Alla Bezvershenko

PUSHING AND SHAKING OF SKYRMION LATTICES

Inaugural-Dissertation

zur
Erlangung des Doktorgrades
der Mathematisch-Naturwissenschaftlichen Fakultät
der Universität zu Köln

vorgelegt von

Alla Bezvershenko

aus Tscherkasy, Ukraine

Köln, 2024

Berichterstatter: PROF. DR. ACHIM ROSCH
PROF. DR. SIMON TREBST

Vorsitzender der Prüfungskommission: PROF. DR. JOACHIM HEMBERGER

Tag der mündlichen Prüfung: 11. DECEMBER 2024

Die vorliegende Dissertation wurde von der Mathematisch-Naturwissenschaftlichen Fakultät der Universität zu Köln angenommen.

Abstract

Magnetic skyrmions are topologically non-trivial spin textures that attract great interest, offering a possible avenue towards novel spintronics applications. One of the reasons for it is the small critical current density of about 10^6 A/m^2 needed to depin the skyrmion lattice. Pinning by disorder remains arguably one of the most important obstacles for all skyrmion-based non-equilibrium experiments and the creation of useful skyrmion devices.

In the presence of a current but in the absence of an oscillating magnetic field, only two phases describe the skyrmion lattice: a pinned phase, where the skyrmions are not moving and an unpinned phase, where skyrmions are moving. We study the unpinning process with the help of slowly oscillating tilted magnetic fields, so-called shaking fields. Strikingly, the depinning happens already at tiny transverse magnetic fields of only a few mT, which corresponds to a small tilting angle of the magnetic field of around 1°.

In the first Part of this Thesis, we introduce an elastic model for skyrmion strings in the bulk of a skyrmion-hosting material in the presence of pinning forces under oscillating magnetic fields. We study the dynamics of this system using the Thiele-like approach and provide an analytic solution in the adiabatic limit. Using this model, we predict three phases and find the signatures of phase transitions in the Time-Involved Small Angle Neutron scattering Experiment (TISANE). We examine the unpinning process for different materials, including the metallic systems $\mathrm{Mn}_{1-x}\mathrm{Fe}_x\mathrm{Si}$, with $x = 0, 0.02, 0.04$, 0.06 and the insulator $\mathrm{Cu}_2\mathrm{OSeO}_3$. We find a high degree of universality in the unpinning processes across all these materials.

In the second Part, we study the dynamics within our model under the simultaneous application of a shaking field and an external current. A remarkably rich non-equilibrium phase diagram appears, which includes the so-called "walking" and "running" phases. Strikingly, the critical current density to depin the lattice drops to zero upon shaking the MnSi skyrmion lattice, starting from the critical magnetic field amplitude. Results obtained from this effective model qualitatively reproduce the experimental findings from the transverse susceptibility measurements on MnSi.

In the third Part, we find, from the symmetry analysis of the skyrmion lattice, the periodic magnetic driving schemes under which a directed motion of skyrmion strings becomes possible. We are arguing that counterintuitively, pinning might facilitate a more efficient motion of skyrmion lines.

This Thesis was conducted in close collaboration with Prof. Christian Pfleiderer's group, where most of the relevant experiments were performed. In this Thesis we aim to show that we have acquired important new insights into the nature of pinning in the bulk of skyrmion lattices.

Kurzzusammenfassung

Magnetische Skyrmionen sind topologische, nicht-triviale, Spintexturen, welche großes Interesse erregen und die Möglichkeit bieten, einen Weg zu neuen Spintronikanwendungen zu ebnen. Einer der Gründe hierfür ist, dass die Stromdichte, welche notwendig ist um das Skyrmiongitter zu lösen, mit 10 A/m^2 sehr klein ist. Das „pinning“ durch Unordnung bleibt einer der wichtigsten zu lösenden Hindernisse für alle auf skyrmion basierenden Nicht-Gleichgewichtsexperimenten und der Konstruktion brauchbarer Skyrmiongeräte.

In der Anwesenheit eines Stroms und gleichzeitigen Abwesenheit eines oszillierenden magnetischen Felds, beschreiben nur zwei Phasen das Skyrmiongitter: eine „pinned“ Phase, in welcher sich skyrmionen nicht bewegen und eine „unpinned“ Phase in welcher Sie es tun. In dieser Arbeit betrachten wir den unpinning-Prozess mit der Hilfe eines langsam oszillierenden, gewinkelten, magnetischen Felds, einem sogenannten wackelnden Felds. Erstaunlicherweise geschieht der unpinning-Prozess bereits bei sehr kleinen Stärken des magnetischen Querfelds von nur einigen mT, was einem kleinen Neigungswinkel des magnetischen Felds von ca 1° entspricht.

Innerhalb dieser Arbeit führen wir im ersten Abschnitt ein elstisches Model für skyrmion Bänder im Inneren eines skyrmionenthaltenden Materials in der Gegenwart von pinning Kräften unter oszillierenden magnetischen Feldern ein. Wir untersuchen die Dynamik dieses Sytems in dem wir einen Thiele ähnlichen Ansatz anwenden und leiten eine analytische Lösung im adiabatischen Grenzfall her. Unter der Verwendung dieses Models sagen wir drei Phasen vorher und finden Signaturen von Phasenübergängen in einem zeitaufgelösten Kleinwinkel-Neutrino-Streuexperiment (engl. TISANE). Wir untersuchen den unpinning-Prozess für verschiedene Materialien, einschließlich dem metallischen System $\mathrm{Mn}_{1-x}\mathrm{Fe}_x\mathrm{Si}$, mit $x = 0, 0.02, 0.04$, 0.06 und dem Insulator $\mathrm{Cu_2OSeO_3}$. Wir finden ein hohen Grad an Universalität in den unpinning-Prozessen für alle untersuchten Materialien.

In dem zweiten Abschnitt untersuchen wir die Dynamik innerhalb unseres Models unter der gleichzeitigen Anwendung eines Wackelfelds und eines externen Stroms. Es ergibt sich ein bemerkenswert reichhaltiges, nicht-gleichgewichts, Phasendiagramm, welches die sogenannten „gehenden“ und „laufenden “ Phasen enthält. Erstaunlicherweise fällt die kritische Strohmdichte, welche notwendig ist, um das Gitter zu depinnen beim Schütteln des MnSi Skyrmionengitters auf Null, beginnend ab einer kritischen Amplitude des magnetischen Felds. Die Resultate, welche wir mit unserem effektiven Model berechnet haben, reproduzieren qualitativ die experimentellen Ergebnisse von querlaufenden Suszeptibilitätsmessungen auf MnSi.

Im dritten Abschnitt finden wir durch eine Symmetrieanalyse des Skrymiongitters die periodischen, magnetischen Antreibungschemas, durch welche eine gerichtete Bewegung eines Skyrmionbands möglich wird. Wir argumentieren dafür, dass, unintuitiver Weise, pinning eine effizientere Bewegung der Skyrmionline verursachen kann.

Diese Dissertation wurde in enger Zusammenarbeit mit Prof. Christian Pfleiderer's Gruppe durchgeführt, welche den Großteil der relevanten Experimente ausgeführt hat. Mit dieser Arbeit möchten wir demonstrieren, dass wir wichtige neue Erkenntnisse über die Natur des pinnings im inneren eines Skyrmionengitter erlangt haben.

Героям Слава

Glory to the Heroes

Contents

Introduction **1**

I Magnetism, Topology and Disorder **5**

1 Topology in Magnetism **7**
1.1 Topological Protection 7
1.2 Topological Invariants: Skyrmions 9
1.3 Energetic Stability 12

2 The Energetics of Twists **15**
2.1 Spin Interactions 15
2.2 On the Free Energy of Chiral Magnets 17
2.3 Helical, Conical, and Skyrmion Phases 20

3 Pinning and Creep **27**
3.1 Pinning - Depinning Transitions 27
3.2 Emergent Electrodynamics. Skyrmion Hall effect 28
3.3 Skyrmion Dynamics 30
3.4 Skyrmion Lines in Disorder Potentials 32
3.5 Bending and Breaking of Skyrmion Lines 35
3.6 Creep 38

II Skyrmion Lattice Under External Drives **41**

4 Skyrmion Lattices under Slow AC-Drives **43**
4.1 Transverse AC Magnetic Susceptibility 43
4.2 Time-Resolved SANS and TISANE 47

5 Unpinning Skyrmion Lattices with Shaking Fields **53**
5.1 Skyrmion Lines Under Tilted Magnetic Fields 53
5.2 Free Energy of Skyrmion Lines in External Oscillating Field 56
5.3 Equation of Motion and Elastic Forces 59
5.4 Pinning Force 61
5.5 Rescaled Thiele Equation 63
5.6 Dynamic Phases in the Adiabatic Limit 64
5.7 Experimental Signatures of Critical Fields 69
5.8 Tracking Dynamic Phase Transitions with TISANE 72
5.9 Effects of Time Binning and Domain Length Distribution 75

5.10 Universality of Depinning Transitions in Different Materials 78

6 Slow and Fast Shaking **83**
6.1 On a Search for Solution of Thiele's Equation 83
6.2 Exact Solution for Large Frequencies 85
6.3 Transverse Susceptibility 87
6.4 Transverse Susceptibility in the Case of Isotropic Pinning 89
6.5 Anisotropic Surface Pinning 94
6.6 Non-Linear Susceptibilities 98

7 Pushing and Shaking **101**
7.1 Skyrmion Lattice Under External Current 101
7.2 Phases Under Pushing and Shaking: Isotropic Surface Pinning 103
7.3 Phases Under Pushing and Shaking: Anisotropic Surface Pinning 108

III Net Motion Under Oscillating Fields **111**

8 Onset of a Net Motion Under Oscillating Fields **113**
8.1 Symmetries of the Skyrmion Lattice 113
8.2 Directed Motion of Skyrmion Lines 114
8.3 Higher Order Terms in the Free Energy 117
8.4 Net motion Without Pinning 120
8.5 Numerical Results for the Net Motion 122

Conclusions **127**

A Derivation of the free energy **139**

B Numerics **141**

C Solution with damping **143**

D Nonlinear terms **144**

E Derivation of forces **146**

Acknowledgements **149**

Introduction

"Where shall I begin, please your Majesty?" he asked. "Begin at the beginning,"
the King said gravely, "and go on till you come to the end; then stop."
Lewis Carroll, *Alice in Wonderland*

The building blocks of the Standard Model are fundamental particles like electrons, neutrons, etc. In modern physics, they appear as stable and localised vacuum excitations. Each of them has a set of fundamental properties, such as mass, electric charge, and spin, which determine how they interact and propagate through a medium. Fundamental particles in nature are rarely seen alone: they interact and form the beautiful world around us, constituted of solids, liquids, gases, etc. The study of emergent phenomena, summarised in the legendary phrase 'More is Different' by Anderson [1], remains to this day a central theme in condensed matter physics:

> "One cannot use the laws learned at a certain scale as building blocks to directly explain the emergent properties at higher scales. Reality is a collection of layers of emergence, and all the laws and frameworks needed to understand them share the same universal and fundamental quality." [2]

In fact, solids are built out of many electrons, protons and neutrons, the latter two being themselves formed out of other fundamental particles, whose interactions are described by the Standard Model. Naively, we would be led to believe that any description of a solid is doomed to fail due to an ever-increasing amount of complexity. In practice, however, we find that for the description of low-energy phenomena in solids, an understanding of the collective behaviour of many particles is already sufficient. Furthermore, out of this collective behavior, a new layer of emergent phenomena may arise, which often turned out to fundamentally enhance our understanding of solids. One of the primary examples of such emergent phenomena is the concept of quasiparticles, defined as long-lived and spatially localised excitations of the host medium. They have particle-like properties and can be assigned an effective mass, charge, and spin similar to their fundamental counterparts. Well-known examples include quasielectrons and quasiholes in metals, phonon excitations travelling through a solid and magnons in a magnet.

Although particle-like objects appear in many different contexts, it turns out to be a highly non-trivial question of how one can construct an object with emergent particle-like properties from a field-theory perspective. Many theories in physics are linear and the superposition principle applies (e.g. Maxwell equations and Schrödinger equation). Full non-linear theories are often too complicated to be treated exactly and methods of perturbation theory are applied in order to obtain any kind of approximation to exact solutions. There do exist however a few cases where non-linearities can be treated exactly, a primary example of which are exactly integrable models. So-called solitons appear as exact solutions to certain non-linear partial differential equations. They are localised wave packets, which are robust against perturbations and recover their shape even after collisions with other such wave packets. As such, they are considered to be quasiparticle excitations [1].

Solitons can be realised as excitations of a medium such as localised waves in water, vortices in superconductors, optical solitons, and many others. While one-dimensional soliton solutions do exist and are well studied for many different non-linear equations, two- or three-dimensional solitons turn out to be radially unstable for most field theories [3]. Thus, one requires a mechanism that protects these quasiparticle excitations from collapse onto a singularity. It was Tony Skyrme, who in the 1960s while working on his aim to construct an effective theory of the nuclei, found such a stable solution. In his endeavour, he introduced a stabilisation term (higher-order in spatial derivatives), with which certain peculiar solutions, nowadays known as skyrmions, become radially stable [4, 5]. In addition to this, T. Skyrme discovered that these solutions, which described the nucleons in his model, enjoy non-trivial topological properties, which are stable against the decay to a topologically trivial state (such as pions, quantised excitations of the pion field [6]). Skyrmions, in fact, are part of a larger family of so-called topological solitons. The latter are localised, smooth solutions of field equations with finite energy which satisfy the following fixed boundary conditions: the field experiences a topological twist around the centre, and the field value becomes uniform at infinity. These objects are stable against decay to the trivial solution under continuous deformations of the field, a mechanism known as topological protection. We will explore the idea of topological protection, as well as the associated concept of a topological invariant, in Chapter 1.

What T. Skyrme achieved is quite remarkable: due to the topological protection, skyrmions show particle-like properties, therefore achieving an emergent particle-like solution from field equations. Although the skyrmion solutions discovered by T. Skyrme are particles in the empty space, later topological solitons have been predicted to as well emerge in the context of condensed matter systems. In the end of the 1980s, finite-size solutions for two-dimensional topological solitons, stabilised by a different mechanism (adding linear terms with respect to the first spatial derivatives, known as Lifshitz invariants [7, 8]), were reported by A. N. Bogdanov and D. A. Yablonskii [9, 10]. They moreover predicted that these solutions can be realised in systems with broken inversion symmetry such as chiral magnets, chiral liquid crystals, multiferroics, etc., in the form of a skyrmion crystal. For chiral magnets, such Lifshitz invariants are realised by so-called Dzyaloshinskii-Moriya interactions. However, A. N. Bogdanov and D. A. Yablonskii have shown that within the mean-field analysis, this phase is always higher in free energy than the conical phase for cubic systems. Later, several different mechanisms of stabilisation have been proposed, including long-ranged interactions [11, 12] or extra phenomenological parameters [13].

It came as a surprise when almost 20 years later the first skyrmion lattice was observed in experiments, with the help of neutron scattering in a bulk chiral magnet MnSi [14]

---

[1] The suffix (-on) was introduced already by Ancient Greek and appears in names of many particle-like objects, like electrons, photons, magnons etc. Thus, the particle-like properties of 'solitons' and 'skyrmions' are also reflected in their names.

in a small pocket of temperature and the external magnetic field strength, known previously as an "A-phase". Remarkably, thermal fluctuations stabilise the skyrmion phase in these systems [14, 15]. In bulk systems, skyrmions appear in the form of a hexagonal lattice of skyrmion strings. Already the first studies reported ultralow current densities of about 10^6 A/m^2, needed to depin skyrmions in these systems, five orders smaller than the current densities needed to depin, e.g. ferromagnetic domain walls in spin-torque experiments [16]. Single skyrmions are considered to be promising candidates for spintronics, a field where information can be carried by the electron spin, instead of the usually employed electron charge. Pinning due to disorder remains one of the outstanding problems both for fundamental science and for applications. Although it was already clear from the first experimental studies that the strength of the disorder is relatively weak, the critical exponents of the transition are still unknown. Moreover, the regimes of plastic depinning and creep largely complicate the theoretical description.

In this Thesis, we go through a number of complexity layers in magnetism, starting from single spins to large (as compared to the atomic distance) objects - magnetic skyrmions. From the single skyrmions, in 3D systems, another emergent objects - skyrmion lines - appear, which can bend elastically when subject to disorder. We report a study on elastic bending of skyrmion lines subject to external slowly oscillating "shaking" fields and external currents.

Here is a short outline of this Thesis. In Chapter 1, we introduce skyrmions and the concept of topological protection, which is manifested through an energy barrier in real systems. In Chapter 2, we discuss in more detail how the chirality of the underlying crystallographic structure gives rise to a special Dzyaloshinskii-Moriya interaction, which favours twisted magnetic phases. This interaction is a crucial ingredient to stabilise skyrmion textures in chiral magnets. Furthermore, we discuss in more detail the resulting phase diagram and the skyrmion phase in MnSi. In Chapter 3, we sketch some basics of the pinnining-depinning transitions, a phenomenon studied in many parts of physics as for example in the context of the Abrikosov vortex lattice in superconductors. In Chapters 5 and 6, we present our study on the dynamics of elastic skyrmion lines under applied shaking fields using a phenomenological theory of pinning. We compare our results with the experimental results on measurements with TISANE and susceptibility measurements. We proceed in Chapter 7 to study the dynamics of skyrmion lines under simultaneous application of shaking field and external current. In the final Chapter 8, we move beyond the model presented in the previous Chapters and study conditions under which a net motion of skyrmion lattices in transverse oscillating field becomes possible.

Part I

Magnetism, Topology and Disorder

1 Topology in Magnetism

> "I rely heavily on the reader's firm intuitive grasp of the notion of continuity. (...) Bridges would not be safer if only people who knew the proper definition of a real number were allowed to design them."
>
> N. D. Mermin, *Topological theory of defects* [17]

Skyrmions, studied in this Thesis, are part of a larger family of localised topological defects in ordered phases of matter. Topology is a powerful tool which helps to classify and provide predictions for the robustness of states even without the full knowledge of the free-energy surface, details of which are often unknown in experiment or complicated to study, e.g. due to disorder. A key to it is a topological invariant called the winding number, which does not change whatever continuous transformations are applied to the system.

We start this Chapter with a short introduction to the concept of topological protection for continuous magnetisation fields. We proceed to present topological defects for a few low-dimensional systems, introduce skyrmions and define the corresponding winding numbers. Further, we discuss how topological protection is realised through energetic stability for magnetic systems. Review articles, which have been used to create this Chapter: [3, 18, 19]. Moreover, the book [20] covers skyrmions in condensed matter systems in great depth.

1.1 Topological Protection

In mathematics the field of topology aims to describe and classify the properties of objects under continuous deformations (for example, bending or twisting) without cutting them. If two objects can be transformed into each other by a continuous deformation, they are called **homeomorphic** to each other. One can build equivalence classes of objects based on this property and associate topological invariants to them, which can tell if two given objects lie in the same or different topological classes. A coffee cup and a ring doughnut, both having one loop, can be smoothly transformed into each other and are therefore homeomorphic, while an apple and a doughnut are not (see Fig. 1).

Excitingly, there exist deep connections between the rather abstract field of topology

(a) (b)

Figure 1: In the prototypical example, a torus (a model for a doughnut) cannot be transformed into a sphere (a model for an apple) under any smooth transformations. In contrast, a cup and a torus are homeomorphic as both objects have one hole. Here the symbol $\cong$ encodes the property of being homeomorphic.

in mathematics and observed phenomena in nature. Topology helps to categorise the robustness of classical or quantum states under smooth deformations and predict their static and dynamic properties [18]. In the context of solid-state physics, one of the first well-studied topological excitations have been singular, localised lattice defects, such as dislocations and disclinations. They play an important role in material science, the study of superconducting vortices, liquid crystals, and many other branches of physics [21]. A huge breakthrough was a discovery by V. Berezinskii, D. J. Thouless and J. M. Kosterlitz of a new mechanism for phase transitions in 2D due to topological defects (vortex-antivortex pairs), which can be realised in the 2D XY model (awarded the Nobel Prize in physics in 2016) [22, 23]. More recently, topology has proven to be especially useful to predict, engineer, and characterise exotic phases of matter [24].

Topology studies continuous objects, but magnetic systems are built from discrete spins. Sometimes, however, it can be a good approximation to consider a smooth magnetisation field instead. Defects in ordered magnetic textures, which cannot be removed under continuous deformations of the magnetisation field and are thus very stable, are called **topological defects**. At first sight, it might be a non-trivial task to tell whether or not a defect in a complex magnetic texture can be removed under continuous deformation. That's exactly where ideas of topology can be of help. If a state is topologically inequivalent (has different topological invariant) to the uniform state (state without a defect), a state with a topological defect is said to be **topologically protected**. From the mathematics point of view, such two states cannot be connected by any continuous transformation, therefore the word "protected". Topologically protected states which appear in magnetism can have different nature: some are localised smooth configurations (like domain walls and single skyrmions), while others are extended textures of ordered phases (like the periodic lattice of skyrmions). A Néel domain wall is an example of a localised smooth configuration, which separates two different magnetic orderings (see Fig. 2).

Note that the energetics of a particular magnetic system will determine whether states with non-trivial topological properties are stable. In real magnetic systems, it might be more energetically favourable for a system to go to a state with a lower winding number by creating singularities (for further discussion, see Sec. 1.3). In the next Section, we proceed to define the topological invariant and study a few important examples of non-trivial topological states in low dimensions.

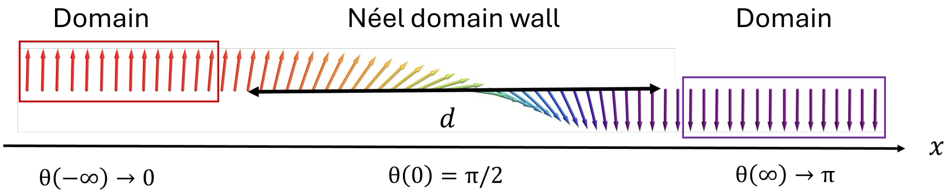

Figure 2: A Néel domain wall with a typical length d, smoothly interpolating between two domains. A spin direction is parametrised by the angle $\theta(x)$.

1.2 Topological Invariants: Skyrmions

In this Section our focus is on topologically non-trivial, real-space localised defects that appear in magnetism. We discuss a topological invariant called the winding number, which helps to study such states systematically. We then proceed further to introduce so-called hedgehogs and skyrmions.

Ordered phases of matter are characterised by order parameter space. A magnetisation field can be seen as a mapping between two spaces: real space to order-parameter space

$$\boldsymbol{r} \in \mathbb{R}^d \text{ position (base space)} \mapsto \boldsymbol{M} \in \mathbb{R}^t \text{ magnetisation (target space)}\,. \tag{1.1}$$

Here d and t are the dimensions of the base and target space, respectively. The length of the magnetisation vector is constant in a broad temperature range, which is why we switch to the unit vector in the direction of the local magnetisation, $\hat{\boldsymbol{M}} = \frac{\boldsymbol{M}}{M}$. Therefore, we can further simplify the target space to a unit sphere of dimension $d' = t - 1$

$$\boldsymbol{r} \in \mathbb{R}^d \longmapsto \hat{\boldsymbol{M}} \in S^{d'}\,. \tag{1.2}$$

Note that the dimensions of the base and target space are generally independent and are fixed by the physical problem at hand. Depending on the dimensions of these two spaces, a large zoo of different topologically non-trivial magnetic defects can appear [25].

We start the discussion by considering a 1D system with the target dimension $d' = 1$. In this case, a topological defect is given by a configuration built out of two (Néel) domain walls with a constant angular progression, depicted in Fig. 3c. We parameterise the position by the coordinate $x \in \mathbb{R}^1$ (because of the periodic boundary conditions equivalent to the circle S^1, see Fig. 3b) and the spin direction by the angle $\theta(x)$. The corresponding

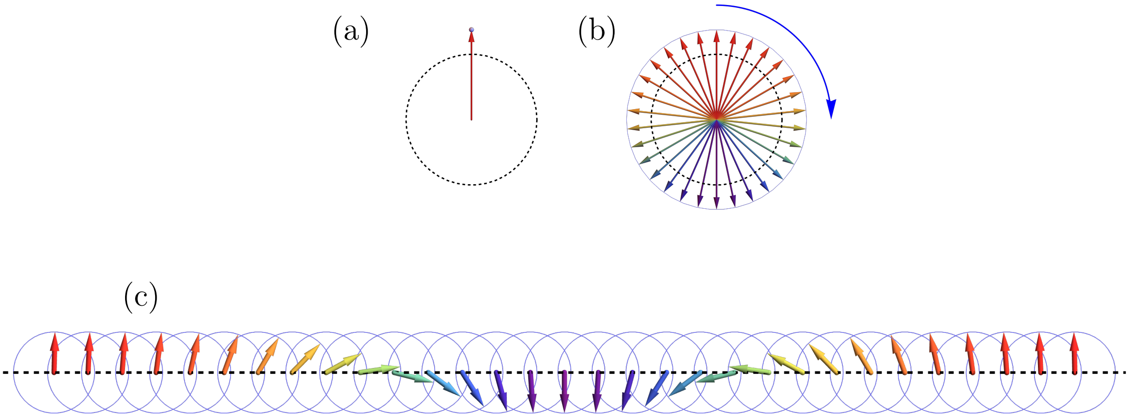

Figure 3: (a) A topologically trivial state with all spins pointing in one direction $\theta(x) = 0$. (b) and (c) A pair of Néel domain walls with constant angular progression.

map f is then given by

$$f : \boldsymbol{r} \in S^1 \;\longmapsto\; \hat{\boldsymbol{M}} \in S^1 \ . \tag{1.3}$$

The group of such mappings consisting of equivalence classes of maps which can be continuously deformed into each other is called a homotopy group. In the case at hand, the homotopy group is the fundamental group $\pi_1(S^1)$, which is isomorphic to the group $\mathbb{Z}$ of integers. The winding number $N \in \mathbb{Z}$, which classifies these mappings, is given by

$$\oint dx \frac{d\theta(x)}{dx} = 2\pi N,\; N \in \mathbb{Z}\,, \tag{1.4}$$

and counts the number of times the target space is covered as one follows a curve through the position space. The winding number depends on the orientation of this curve: it is negative if the direction of the curve is clockwise and positive otherwise. For the state presented on Fig. 3c, spins rotate around the circle once, corresponding to the winding number $N = -1$. This state is homotopically distinct from a trivial state ($N = 0$) with all spins pointing in one direction ($\theta(x) = \text{const.}$), corresponding to a single point on the target manifold (Fig. 3a). Different winding numbers signify that deforming this state back to the trivial state is impossible without creating singularities.

One important topologically non-trivial excitation is given by a vortex defect, which appears, for example, in XY magnets [22]. In 3D with the target space dimension $d' = 2$ a defect called **hedgehog** (or a **Bloch point**) appear, created by arrows pointing in the radial direction (the top part of Fig. 4a). The corresponding mapping f is given by

$$f :\; \boldsymbol{r} \in S^2 \text{ (a sphere) } \;\longmapsto\; \hat{\boldsymbol{M}} \in S^2 \text{ (a sphere)}\,. \tag{1.5}$$

Both spheres can be parametrised with the help of spherical angles $f : \boldsymbol{r}(\varphi, \theta) \mapsto \hat{\boldsymbol{M}}(\phi, \vartheta)$. The corresponding homotopy group of this map is then $\pi_2(S^2)$, which as in the first example, is isomorphic to the group $\mathbb{Z}$ of integers. The winding number Q can be defined as

$$\oiint d\Omega_b \frac{d\Omega_t}{d\Omega_b} = 4\pi Q,\; Q \in \mathbb{Z}\,. \tag{1.6}$$

Here Ω_t and Ω_b are the solid angles of the target and base spaces, respectively. As the total solid angle is 4π, this topological invariant counts the number of times the target space covers the sphere. It is a non-trivial fact that any continuous transformation of the vector field will not change this invariant. One may rigorously prove this result in the coordinate-independent formalism of differential forms [2]. For example, if we tilt all spins in the azimuthal direction as depicted on the top part of Fig. 4b, the winding number will not change, as it is a homotopic deformation. For both structures, the target sphere is covered once, $Q = 1$. The mapping between two spheres can be parametrised

---

[2] It is a deep insight from mathematics, that the integral $\frac{1}{\mathrm{Vol}(S^2)} \int_{S^2} f^*\omega$, where $\omega = xdy \wedge dz + ydz \wedge dx + zdx \wedge dy$ is the volume form of S^2, takes values in $\pi_2(S^2)$, i.e. computes the winding number of $\boldsymbol{M}$. In fact, every closed integral over closed differential forms is invariant under homotopic deformations of $\boldsymbol{M}$.

as $\vartheta = \theta, \phi = Q\varphi + \gamma$, where Q is sometimes called vorticity and is fixed by the topology, while γ is the helicity, representing the azimuthal rotation of all spins ($\gamma = 0$ or π for the spin structure on the left, $\gamma = \pm\pi/2$ on the right).

If we squash the hedgehog flat by stereographic projection (black arrows on Fig. 4a and b), it can be accommodated into the 2D space. The resulting topological defect is called a **skyrmion**. On the left, a so-called Néel skyrmion is depicted (named so because if one considers a one-dimensional cut through the diameter of a skyrmion, one obtains a Néel domain wall, see Fig. 4c). On the right, a Bloch skyrmion is depicted. In both cases, skyrmions are embedded in a uniform state with the following boundary condition: in the middle, the magnetisation is kept anti-parallel to the direction of the uniform field at infinity.

In Cartesian coordinates, the integral for the winding number Q can be rewritten to yield the expression

$$Q = \frac{1}{4\pi} \iint dxdy\, \boldsymbol{M} \cdot \left(\frac{\partial \boldsymbol{M}(x,y)}{\partial x} \times \frac{\partial \boldsymbol{M}(x,y)}{\partial y} \right). \tag{1.7}$$

The quantity which is being integrated is called the **skyrmion density**.

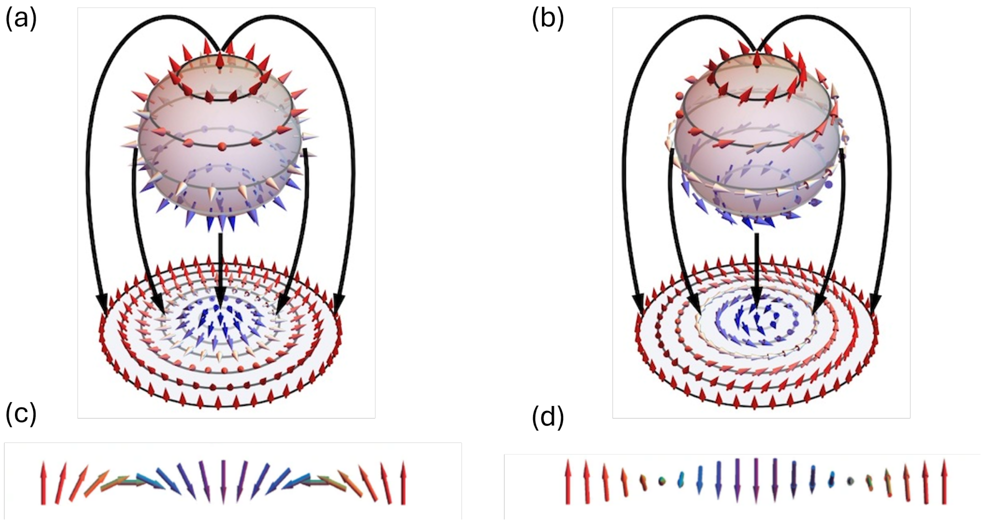

Figure 4: (a) A spherical projection of a spin configuration, called a hedgehog (or a Bloch point) with all spins pointing in the radial direction gives a Néel-skyrmion. (b) A spin configuration, obtained from a hedgehog by rotating all spins in the azimuthal direction. Spherical projection yields a Bloch skyrmion. (c) a Néel and (d) a Bloch domain wall, created by a 1D cut of corresponding skyrmions in the radial direction. Picture credits (a) and (b) from Ref. [26], (c) and (d) from Ref. [27].

1.3 Energetic Stability

In the previous Section, we introduced skyrmions and the associated winding number. Topological protection, introduced in Section 1.1, means that the system, described by the continuous magnetisation field, cannot go to the state with a lower winding number under any continuous transformations without creating singularities. The first limitation is that magnetic materials are built from discrete spins. The assumption of a continuous magnetisation field is valid only if the variation of the spin structure happens over distances much larger than the distance between single atoms (which is the case, for example, for spin configurations in helical and skyrmion phases in MnSi [14]). Further, for continuous magnetisation fields topological protection in real physical systems shall be rather understood as "costing a lot of energy" but it is strictly speaking not forbidden. In fact, it might be more energetically favourable for the system to create a singularity and go to a state with a lower winding number. Moreover, topological protection breaks down near the edges of the sample [28].

Let us first explain how topological protection is manifested by a finite-energy barrier in the example of a 1D domain wall (Fig. 2). The free energy of the ferromagnetic material in the absence of an external magnetic field is symmetric with respect to the magnetisation reversal. Therefore, the regions with constant magnetisation, called domains, have the same energy. A domain wall smoothly interpolates between two such regions. Removing a domain wall and thus changing the system's state to a uniform state will cost a large energy $\propto L/2$ for a system of size L. Thus, once this excitation is created, it will typically be very stable. However, if two domain walls with the angular progression of spins in different directions meet, the total winding number is 0, and these domain walls can annihilate smoothly, emitting the spin waves [29]. Note that, in contrast to the domain wall case, the energetic barrier for skyrmion does not scale with the system size.

Skyrmions, depending on magnetic interactions in the system, can arrise as stable or unstable solutions upon minimising the free energy. There should be a mechanism which protects skyrmions from expanding or shrinking in the radial direction and eventually collapsing to a uniform state by creating a singularity. In fact, single skyrmions embedded in a ferromagnet were found to be valid solutions for the Heisenberg ferromagnets already back in 1975 [30]. However, they turned out to be only a metastable solution. As we shall see in the next Chapter, another, more sophisticated magnetic interaction is needed in order to stabilise skyrmions.

Summary and Outlook

In this Chapter, we discussed the concept of topological protection and introduced 2D Néel and Bloch skyrmions and hedgehogs. A large family of other topological excitations appear in 2D, such as merons, bimerons, etc. Moreover, skyrmions in 3D can be extended in many different ways, such as skyrmion tubes, chiral bobbers, and hedgehog lattices. Even more exotic magnetic textures, hopfions (closed loops of skyrmion strings) have been detected recently in experiments [31]. We will study the skyrmion tubes more closely, while other structures are out of scope for this Thesis. The interested reader is referred to the review article [32].

2 | The Energetics of Twists

In this Chapter, we proceed to discuss how skyrmions introduced in the previous Chapter, can be stabilised in real materials. Here we concentrate our discussion on a certain class of magnets for which the unit cell is distinguishable from its mirror image, called chiral magnets. Chirality together with a weak spin-orbit coupling give rise to an exotic spin interaction called antisymmetric exchange interaction (or DMI). The competition of DMI with the dominant exchange interaction gives rise to helical, conical, and skyrmion lattice phases in these materials.

We start this Chapter with a short review of the relevant microscopic spin interactions present for chiral magnets. Based on symmetry considerations, we proceed to find an expression for the free energy of this system in the gradient expansion of the continuous magnetisation field. Furthermore, we will then shortly introduce twisted magnetic textures, such as helical and conical, with an emphasis on the skyrmion lattice phase.

This Chapter is largely based on the review articles [18, 19].

2.1 Spin Interactions

One of the possible ways to stabilise magnetic skyrmions is chirality. Our hands are probably the simplest example of chiral objects: the left hand cannot be superposed on the right hand by any sequence of rotations and translations. This “handedness” in the world around us is omnipresent. Coils, screws, and springs appear naturally in different parts of physics, chemistry, and biology. In fact, most molecules relevant to the existence of life and for pharmaceutical products are chiral.

Crystals can be described by the periodic repetition of their elementary building blocks, called unit cells. In the context of condensed matter physics, magnetic crystals exist for which all unit cells lack a centre of inversion symmetry, called **chiral magnets**. An important subclass of them is formed by the transition-metal germanide and silicide compounds, crystallising in the cubic B20 crystal structure (examples are MnSi, FeGe, MnGe, etc.). Although they have a cubic structure, their space group $P2_13$ contains no inversion symmetry. A unit cell of MnSi, which can serve as a neat example of this property, can be found in Fig. 5 (for more details on physical properties of this material, see Refs. [33, 34]).

Spins on periodic lattice structures interact in various ways. Here, we restrict our discussion to the most relevant spin interactions for the stabilisation of topological spin textures in chiral magnets. The dominant contribution to the energy comes from the short-ranged (symmetric) **exchange interaction**. Although the microscopic origin of magnetism is quantum mechanical, magnetic spins in solids can often be considered in a **semiclassical limit**, where spins are modelled by vectors localised at lattice sites[3]. The

---

[3] This assumption is justified in the large-spin limit: in this case, the spacing between projections of the spin operator onto a given axis goes to zero as the total spin values grow.

exchange energy can be written as

$$H_{ex} = -J \sum_{\langle i,j \rangle} \boldsymbol{S}_i \cdot \boldsymbol{S}_j \ . \tag{2.1}$$

Here $\boldsymbol{S}_i$ denotes a spin localised at the lattice site i, J is the exchange coupling constant, and we sum over $\langle i, j \rangle$, the nearest-neighbour sites, reflecting the interaction's short-ranged nature. For $J > 0$ ($J < 0$), this term is minimised when neighbouring spins align parallel (antiparallel), as is the case for ferromagnetic (antiferromagnetic) materials.

One of the prominent examples of relativistic effects in solids is the spin-orbit coupling, which couples the direction of the electronic spin to the system's crystal axis and therefore, lifts the spin-direction degeneracy. In particular, this term is allowed for chiral magnets. However, the strength of spin-orbit coupling λ_{so} is typically much weaker than that of other couplings, as it is of a relativistic nature. The combination of exchange and spin-orbit couplings gives rise to the effective antisymmetric exchange coupling present in chiral magnets. I.E. Dzyaloshinskii and T. Moriya pioneered the study of this interaction [35, 36], known nowadays as **Dzyaloshinskii - Moriya interaction**, short DMI. The corresponding spin Hamiltonian is

$$H_{DM} = \sum_{\langle i,j \rangle} \boldsymbol{D}_{ij} \cdot (\boldsymbol{S}_i \times \boldsymbol{S}_j) \, . \tag{2.2}$$

The direction of the DM vector $\boldsymbol{D}_{ij}$ depends on the details of the induced orbital moments and is constrained by the symmetries of the underlying crystal system. If the system is not chiral, there is a centre of inversion symmetry between two spins and this term automatically vanishes[4]. For $\boldsymbol{D}_{ij} > 0$ ($\boldsymbol{D}_{ij} < 0$), the left-handed (right-handed) twisted

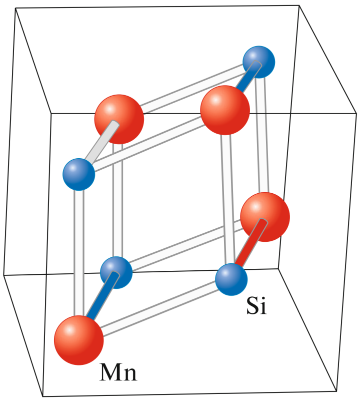

Figure 5: A unit cell of MnSi. Silicon atoms occupy four sites, forming a tetrahedron aligned along the (111) direction. Manganese atoms form a tetrahedron, inverted relative to Si atoms. Importantly, the resulting structure lacks inversion symmetry. Picture credit from [33].

---

[4] Note that this argument applies only in the bulk. An interface between two materials cannot be inverted, which gives rise to a so-called interfacial DMI (for example, at metallic ferromagnet/heavy-metal interfaces) [37].

magnetic structures are favoured, therefore introducing the sense of a preferred direction.

If one adds an external magnetic field $\boldsymbol{B}$, spins experience the **Zeeman interaction**

$$H_Z = -\sum_i \boldsymbol{S}_i \cdot \boldsymbol{B} \ , \tag{2.3}$$

which pushes them to align with the external magnetic field. This term remains invariant under the rotation of spins around the magnetic field, as well as under the simultaneous rotation of spins and magnetic field in space.

Another contribution to the energy comes from the magnetic anisotropies[5] and long-ranged dipolar interaction, which turn out to be relatively weak for skyrmion crystals. Thus, we omit the detailed discussion of these interactions here.

Competition of the exchange and DMI terms in chiral magnets leads to the formation of twisted spin structures, which we will discuss in more detail in Section (2.3). The symmetric exchange interaction is generally much stronger than DMI, causing spins to point roughly in the same direction when considered locally but start to precess around a common axis when viewed on large length scales over many unit cells due to the DMI.

Before we proceed to the next Section, we shall introduce one more approximation. Generally, a microscopic description of a magnetic material based on a single-spin picture is complicated and material-dependent. The variation of the direction of magnetic spins, leading to the effects we are interested in, happens over distances much larger than the separation of atoms. In order to capture the long-wavelength physics one can "coarse-grain" the lattice of discrete spins and switch to the continuum picture. To achieve this, a standard procedure is to average over a region much larger than the lattice spacing (therefore containing a large number of spins) but still much smaller in comparison to the full size of the system to be able to resolve structures like domain walls and skyrmions. The information about the smoothly varying spin texture is then encoded in a continuous vector field, called **local magnetisation $\boldsymbol{M}(\boldsymbol{r})$**, which is given by the average of the elementary spins in the vicinity of the point $\boldsymbol{r}$ (an approximation called **micromagnetic limit**). In the next Section we will proceed to write the free energy of chiral magnets in terms of the continuous magnetisation density.

2.2 On the Free Energy of Chiral Magnets

The standard tool to describe (thermal) phase transitions is the Ginzburg-Landau theory. Close to the critical temperature, the divergence of the correlation length leads to the universal behaviour of systems, largely independent of the microscopic details. One can

---

[5] Typically, the magnetocrystalline anisotropy is being considered, which describes the effect that spins favour certain directions in space depending on the symmetry of the crystalline structure due to the spin-orbit interaction. However, this is a higher-order effect in the spin-orbit interaction compared to the DMI for cubic chiral magnets. Anisotropies can also arise close to the surface or on interfaces, as well as locally in bulk from crystal imperfections.

then classify systems based on their dimensionality and symmetries. This leads to the idea of universality classes, a central concept in modern condensed matter physics.

For magnetic materials, the relevant order parameter is magnetisation. In the disordered (paramagnetic) phase, above the critical temperature T_c, the magnetisation is zero on average, while for low temperatures $T < T_c$, the order parameter develops a non-zero value and the system is in the ferromagnetic phase. The critical temperature T_c is determined by the (ferromagnetic) exchange interaction J, the largest energy scale of the problem. For chiral magnets, the ferromagnetic state is, however, unstable towards a helical spiral modulation, resulting in different types of ordering below T_c. In order to discuss them, we first derive the expression for the free energy for such systems based on the knowledge of relevant symmetries.

A partition sum is a central object needed to study the thermodynamic properties of a system. It is the integral over all possible magnetisation configurations, weighted with the respective value of the free energy

$$Z = \int D\boldsymbol{M}(\boldsymbol{r}) e^{-\mathcal{F}[\boldsymbol{M}(\boldsymbol{r})]} \,. \tag{2.4}$$

This functional integral, however, is a very complicated object to calculate. The conventional method in order to find an approximate solution in the thermal equilibrium is the saddle-point approximation, also known as a **mean-field theory**. This method incorporates a large simplification which, however, still allows useful predictions about the system to be made. The free energy is therefore minimised by a magnetisation configuration $\boldsymbol{M}_0$, which can be found as a minimum of the free energy functional with respect to varying the magnetisation $\boldsymbol{M}$

$$Z \approx e^{-\mathcal{F}[\boldsymbol{M}_0(\boldsymbol{r})]} \,, \quad \mathcal{F}[\boldsymbol{M_0}(\boldsymbol{r})] = \min_{\boldsymbol{M}(\boldsymbol{r})} \mathcal{F}[\boldsymbol{M}(\boldsymbol{r})] \,. \tag{2.5}$$

The next order of expansion, where quadratic fluctuations around the mean-field value are considered, is called **Gaussian approximation**.

Based on the symmetries of the system, we can fix a form of the free energy $\mathcal{F}[\boldsymbol{M}(\boldsymbol{r})]$, which must obey the same symmetries as the underlying system. We start by considering the system with the highest symmetry, neglecting DMI and crystal anisotropies (in other words, in the zeroth order approximation in terms of small relativistic spin-orbit coupling λ_{so}). This theory is well-known as it accurately describes (itinerant) ferromagnets in the absence of an external magnetic field and higher-order effects. The free energy is written in terms of a space-dependent local magnetisation $\boldsymbol{M}(\boldsymbol{r})$ and its gradients must be:

1) invariant under rotations of the magnetisation field around an arbitrary axis $\boldsymbol{M} \to \boldsymbol{R}_n \boldsymbol{M}$,

2) translation and rotation symmetric in space and invariant under spatial inversion $\boldsymbol{r} \to -\boldsymbol{r}$.

The symmetry is lower if the system is in the non-zero external magnetic field $\boldsymbol{B}$. The free energy is then invariant under combined rotation of space and magnetisation field around an axis defined by $\boldsymbol{B}$ and simultaneous inversion of magnetisation and magnetic fields ($\boldsymbol{M} \to -\boldsymbol{M}, \boldsymbol{B} \to -\boldsymbol{B}$).

Under these symmetry constraints, one can write the free energy $\mathcal{F}[\boldsymbol{M}(\boldsymbol{r})]$ of a ferromagnet at a fixed magnetisation field $\boldsymbol{M}(\boldsymbol{r})$ in the gradient expansion (valid for slowly-varying magnetisation) as

$$\mathcal{F}[\boldsymbol{M}(\boldsymbol{r})] = \int d^3\boldsymbol{r} \left(J(\boldsymbol{\nabla M})^2 + a(\boldsymbol{M} \cdot \boldsymbol{M}) + U(\boldsymbol{M} \cdot \boldsymbol{M})^2 - \boldsymbol{BM} + \dots \right). \tag{2.6}$$

Here, J, a, and U are phenomenological, material-dependent parameters, the exact values of which are fixed by the microscopic theory. The first term $J(\boldsymbol{\nabla M})^2$ is minimised for $J > 0$, when the gradient of magnetisation is zero, corresponding to the ferromagnetic alignment of spins. The following term with $a = a_0(T - T_c)$ is, for $a_0 > 0$, positive in the paramagnetic and negative in the ferromagnetic phase. Together with the $U(\boldsymbol{M} \cdot \boldsymbol{M})^2$ term, which stems from interactions and is essential for the stability of the system at larger values of $\boldsymbol{M}$, they are responsible for the creation of the double-well potential (see Fig. 6 for magnetisation in 1D). The Zeeman term, $-\boldsymbol{BM}$, pushes the magnetisation to align with the applied magnetic field.

The symmetry of chiral magnets (such as MnSi) is even further reduced, and therefore the expression for the free energy presented above needs to be modified. A phenomenological approach is based on adding Lifshitz invariants (antisymmetric functions of the form $M_i \frac{\partial M_j}{\partial x} - M_j \frac{\partial M_i}{\partial x}$ [7,8]), which are odd under spatial inversion and linear in the first spatial derivatives, representing the DMI as discussed in the previous Section. This leads to a $D\boldsymbol{M} \cdot (\boldsymbol{\nabla} \times \boldsymbol{M})$ contribution to the free-energy potential. The most general expression for the free-energy density of chiral magnets with B20 crystal symmetry, up to second order in derivatives of $\boldsymbol{M}$ field (and forth in spin interactions), was derived by Bak and Jensen in 1980 [38]. Up to the second order in the small relativistic spin-orbit coupling λ_{so} (and

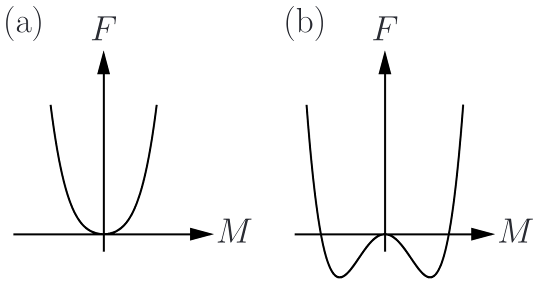

Figure 6: The free energy for 1D magnetisation field for (a) $T > T_c$ and (b) $T < T_c$. Picture credit from [19]. Below T_c, two minima appear.

neglecting anisotropy terms), the free energy then reads

$$\mathcal{F}[\boldsymbol{M}(\boldsymbol{r})] = \int d^3\boldsymbol{r}\, \big(J(\boldsymbol{\nabla M})^2 + D\boldsymbol{M}\cdot(\boldsymbol{\nabla}\times\boldsymbol{M}) + a(\boldsymbol{M}\cdot\boldsymbol{M}) + U(\boldsymbol{M}\cdot\boldsymbol{M})^2 - \boldsymbol{BM}\big)\,. \tag{2.7}$$

Competition of the first term in the Eq. (2.7), which favours colinear structures, with the second term, which gives a negative contribution for certain twisted structures, leads to the formation of the helical, conical and skyrmion phases in bulk chiral magnets, which we will discuss in more detail in the upconing section.

Let us comment on the radial stability of a single skyrmion (see Sec. 1.3). Why a magnetic field is needed to stabilise this structure, can be seen from an intuitive criterion called Derrick's theorem. The radius of the skyrmion R determines how fast the rotation of spins approaches the uniform solution (for exact solutions and schemes of determining the skyrmion radius R see, for example, Ref. [39]). In order for such a structure to be radially stable, the free energy given by Eq. (2.7) should have a minimum as a function of the skyrmion radius R. The DM term gives a negative contribution and scales as R because of the gradient, while the Zeeman term scales as R^2 (the area of a skyrmion, given by spins which do not point along the field direction). Therefore, the total energy $E \propto -a_1R + a_2R^2$, where a_1 and a_2 are positive constants, has a stable minimum with respect to R [19].

2.3 Helical, Conical, and Skyrmion Phases

In this Section, we focus our discussion on twisted spin textures, which periodically fill the medium. To study them, we apply a Fourier transformation with $\boldsymbol{M}(\boldsymbol{r}) = \sum_{\boldsymbol{q}} \boldsymbol{m_q} e^{i\boldsymbol{q}\cdot\boldsymbol{r}}$ to the free energy for chiral magnets Eq. (2.7), which leads to

$$\mathcal{F}[\boldsymbol{M}(\boldsymbol{r})] = \sum_{\boldsymbol{q}} \big[(J\boldsymbol{q}^2 + a)(\boldsymbol{m_q}\cdot\boldsymbol{m_{-q}}) + iD\boldsymbol{q}\cdot(\boldsymbol{m_q}\times\boldsymbol{m_{-q}}) - \boldsymbol{m_q}\cdot\boldsymbol{B}\big] \tag{2.8}$$

$$+U \sum_{\boldsymbol{q}_1\boldsymbol{q}_2\boldsymbol{q}_3\boldsymbol{q}_4} \big[(\boldsymbol{m}_{\boldsymbol{q}_1}\cdot\boldsymbol{m}_{\boldsymbol{q}_2})(\boldsymbol{m}_{\boldsymbol{q}_3}\cdot\boldsymbol{m}_{\boldsymbol{q}_4})\delta^{(3)}(\boldsymbol{q}_1+\boldsymbol{q}_2+\boldsymbol{q}_3+\boldsymbol{q}_4)\big]\,. \tag{2.9}$$

Note, that the Fourier components have the property $\boldsymbol{m}^*_{\boldsymbol{q}} = \boldsymbol{m}_{-\boldsymbol{q}}$. The $\boldsymbol{q} = 0$ component corresponds to the ferromagnetic magnetisation. Competition of the first two terms, quadratic and linear in $\boldsymbol{q}$, leads to the instability of the ferromagnetic state towards a helical spiral modulation.

Luckily, there is a way to directly measure Fourier components of these textures. Diffraction techniques are powerful experimental probes for ordered phases of matter, which provide complementary information to real-space and imaging techniques.

Neutrons are especially useful for studying periodic spin structures, as they have large penetration depth and do not experience Coulomb interaction and are scattered by atomic nuclei and magnetic moments only. The measured scattering Bragg intensity profile gives the Fourier components of magnetic structure: $I(\boldsymbol{q}) \propto |\boldsymbol{m}_{\boldsymbol{q}}|^2$. Probing large structures (compared to the spacing between atoms) means lower $\boldsymbol{q}$ vectors, therefore smaller scattering angles θ. Thus, this technique is called the small angle neutron scattering (SANS). For more details on this technique and on the setup, which was used to find the skyrmion phase (see Fig. 7b), the reader is referred to Ref. [14]. The phase diagram of MnSi, which is obtained with the help of this technique, is depicted in Fig. 7a. Below the critical temperature, $T_c \approx 29K$, a number of ordered phases are formed. At high magnetic field values $\boldsymbol{B}$, the field-polarised phase appears, in which all spins point in the direction of the applied field. At smaller magnetic field values, helical, conical, and skyrmion phases appear.

Helical and conical phases

In the absence of a magnetic field and below the transition temperature T_c, the competition between the first two terms in Eq. (2.9) pushes spins to twist with a constant angle and align perpendicular to the propagation vector $\boldsymbol{q}$. This phase is known as a **helical phase**. The resulting magnetisation is given by

$$\boldsymbol{M}(\boldsymbol{r}) = M_0 \frac{1}{\sqrt{2}} \left(\boldsymbol{n}_1 \cos(\boldsymbol{q} \cdot \boldsymbol{r}) + \boldsymbol{n}_2 \sin(\boldsymbol{q} \cdot \boldsymbol{r})\right). \tag{2.10}$$

Here, the length of the propagation vector $|\boldsymbol{q}| = D/J$ reflects again the competition of two energy scales and $\boldsymbol{n}_1$, $\boldsymbol{n}_2$ are orthogonal unit vectors (see Fig. 8). The length of the magnetisation vector $M_0 \equiv |\boldsymbol{M}|$ does not change in a broad temperature range and is equal to the saturation magnetisation, which is reached at low temperatures. For MnSi, the helix has a pitch of $L_h \approx 180$ Å, much larger than a unit cell parameter of $a \approx 4.56$ Å [33], which leads to a decoupling of the magnetic and atomic structures. Note that this solution is degenerate with respect to the direction of the propagation vector $\boldsymbol{q}$. In order to fix the direction of this vector, one needs to consider the neglected anisotropy terms in Eq. (2.7) [14, 39]. The propagation vector $\boldsymbol{q}$ is in fact pointing in the easy-axis direction imposed by the crystal symmetry (which is given by the [111] crystalline direction for MnSi).

Although on the mean-field level the transition from the helical to paramagnetic phase

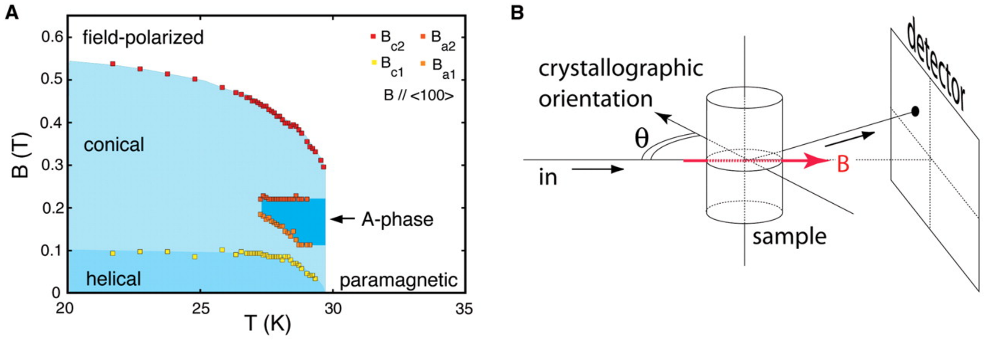

Figure 7: (A) Phase diagram of MnSi measured with the help of small angle neutron scattering (SANS). (B) SANS setup used in the [14]. Notably, the applied magnetic field **B** was directed parallel to the incident neutron beam.

for zero magnetic field is of second order, the nature of this transition is more intricate. It turns out that the interactions between the fluctuations drive a first-order transition [40] (the mechanism initially proposed by Brazovskii [41]).

In an applied magnetic field, the directional degeneracy of the propagation vector $\boldsymbol{q}$ is lifted and spins start to cant in the direction of the applied field (see Fig. 8b). This phase is known as a **conical phase**.

For these phases, two Bragg spots appear in SANS measurement at momenta $\boldsymbol{q}$ and $-\boldsymbol{q}$, parallel to the magnetic field in the conical phase and along [111] in the helical phase [15].

Skyrmion phase

In a small range of temperatures and magnetic fields between conical and paramagnetic phases, even more exotic spin textures can be stabilised, characterised by a multiple-$\boldsymbol{q}$ order, where several propagation vectors $\boldsymbol{q}_i$ coexist. In the presence of a magnetic field, one of the components in Eq. (2.9) can be set to its ferromagnetic value $\boldsymbol{q}_1 = 0$, giving the uniform component of the magnetisation $\boldsymbol{M}_f$. Then the second sum is proportional to the $\delta^{(3)}(\boldsymbol{q}_2 + \boldsymbol{q}_3 + \boldsymbol{q}_4)$ term. Such a term appears in the theory of a liquid to a crystal lattice transitions. In our case, it gives rise to the so-called **skyrmion-lattice phase** [14, 19]. The skyrmion-lattice phase is slightly higher in the free energy than the conical phase in the mean field approximation for 3D systems[6]. Therefore, the skyrmion lattice was predicted to be thermodynamically unstable in early studies [9, 10]. However, strikingly, thermal fluctuations above the mean field stabilise this solution (first calculated in Gaussian approximation in Ref. [14] and later confirmed in a non-perturbative manner using classical

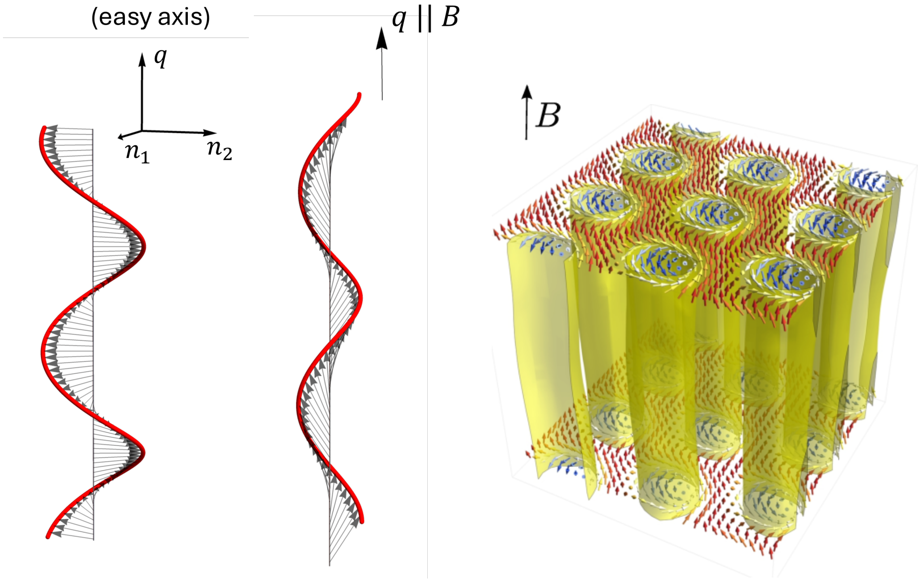

(a) (b) (c)

Figure 8: Schematics of (a) helical, (b) conical and (c) skyrmion phases (magnetisation vanishes along yellow tubes). Picture credits for subfigures (c) from [15].

---

[6] Interestingly, the situation is different for 2d films, see [42].

Monte Carlo simulations in Ref. [15]). A full calculation shows that the solution can be approximated by a superposition of three helices

$$\boldsymbol{M}(\boldsymbol{r}) \approx \boldsymbol{M}_f + \sum_{i=1}^{3} \boldsymbol{M}_{\boldsymbol{q}_i}(\boldsymbol{r} + \Delta \boldsymbol{r}) \,. \tag{2.11}$$

Here, $\boldsymbol{M}_{\boldsymbol{q}_i}(\boldsymbol{r})$ is the magnetisation of a single helix as given by Eq. (2.10) with the wave vector $\boldsymbol{q}_i$ and two unit vectors, $\boldsymbol{n}_{i1}$ and $\boldsymbol{n}_{i2}$, orthogonal to each other and the corresponding wave vector. The three propagation vectors $\boldsymbol{q_1}, \boldsymbol{q_2}, \boldsymbol{q_3}$ are of equal magnitude, have an angular separation of $2\pi/3$ and lie in the plane perpendicular to the magnetic field. All three helices have the same chirality. The resulting spin texture has hexagonal symmetry, reflected in the six Bragg spots, arranged on a regular hexagon in the plane perpendicular to $\boldsymbol{B}$ (for all directions of $\boldsymbol{B}$, meaning that the skyrmion lattice is being formed independently from the underlying crystal structure). Note that the exact solution also contains higher order modes (for example, the signature of the double wave vector $\boldsymbol{q}$ can be seen in the neutron scattering data, see Fig. 9). However, the weight of these modes decays rapidly, so this approximation remains valid. The skyrmion lattice extends to the 3D, forming elastic tube-like structures, which will be the main focus of this Thesis (see Fig. 8c). This elastic lattice resembles the one formed by superconducting vortices [43].

One can assign a topological invariant to the skyrmion lattice. A unit vector in the direction of magnetisation $\hat{\boldsymbol{M}}$, integrated over a unit cell (u.c.) of a skyrmion lattice, has the topological property

$$\frac{1}{4\pi} \iint_{\text{u.c.}} dx dy \; \hat{\boldsymbol{M}} \cdot \left(\frac{\partial \hat{\boldsymbol{M}}(x,y)}{\partial x} \times \frac{\partial \hat{\boldsymbol{M}}(x,y)}{\partial y} \right) = W \,, \tag{2.12}$$

where $W = -1$ is a winding number of a skyrmion lattice. A distinctive consequence of this topological protection is that the skyrmion lattice has a very small pinning to the

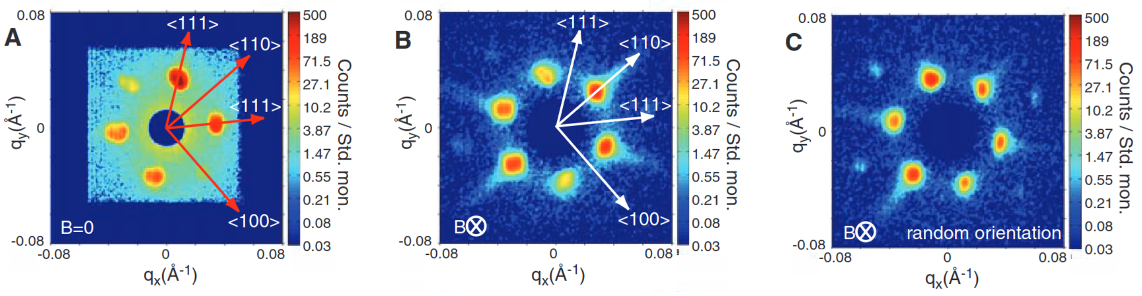

Figure 9: SANS scattering intensities data from the measurements on MnSi. (a) at $\boldsymbol{B} = 0$ and $T = 27$ K a helical phase is measured. (b) at $T = 26.77$ K a sixfold pattern appears in the plane perpendicular to magnetic field $\boldsymbol{B}$. (c) A sixfold pattern is present (in the plane perpendicular to magnetic field $\boldsymbol{B}$) for a random orientation of the sample. For (b) and (c), background measurement above T_c was subtracted. Picture credit from Ref. [14].

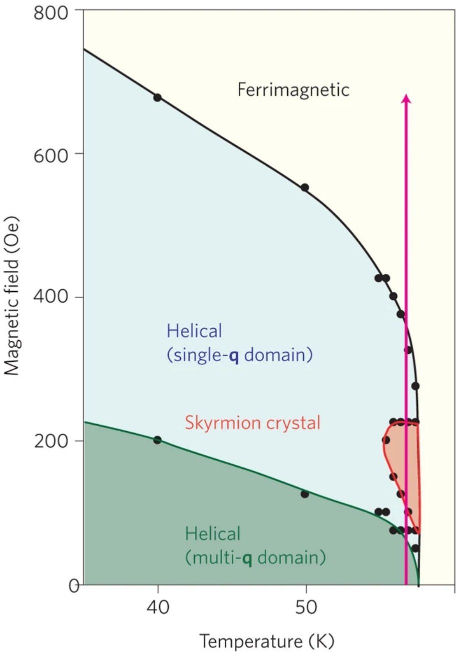

Figure 10: Temperature-magnetic field phase diagram of Cu_2OSeO_3 determined from magnetic susceptibility measurements. Magnetic field is applied along [100] direction. Picture credit from Ref. [44].

underlying lattice and, therefore, allows for easy manipulation with external current and drives, as we shall see in the next Chapter.

Summary and Outlook

In this Chapter, we considered magnets with a B20 structure in more detail, such as MnSi, FeGe, which are weak itinerant ferromagnets and have metallic properties. The origin of their chirality lies in the asymmetric exchange mechanism, due to which these materials have helimagnetic structure in the bulk and can host skyrmions. In the next Chapter, we discuss how skyrmion lattice in these materials can be driven with the help of a external current.

A high degree of universality exists in temperature-magnetic field phase diagrams across different cubic chiral magnets [45]. Note, however, that some of these compounds have very different origins to their chirality. Examples are long-ranged dipolar, frustrated exchange, or four-spin exchange interactions [46], to name just a few. One important example for this Thesis is the Mott insulator Cu_2OSeO_3. It is also chiral but predominantly ferrimagnetic (formed by two sublattices directed in opposite directions). This material can also host skyrmions, and its temperature-magnetic field phase diagram looks remarkably similar to that of MnSi (see Fig. 10). The only significant difference is that its phase diagram features an additional low-temperature skyrmion phase for magnetic fields applied along the easy crystallographic (100) directions, which is currently extensively studied [47].

Furthermore, skyrmions exist in real materials not only in the form of periodic lattices but in many different arrangements, such as single skyrmions in 2D, as a gas of skyrmions and glassy configurations [48]. However, these systems lie outside of the scope of this Thesis.

3 | Pinning and Creep

> "Owl explained about *flux pinning* and *creep*. He had explained this to Pooh and Christopher Robin once before, and had been waiting ever since for a chance to do it again, because it is a thing you can easily explain twice before anybody knows what you are talking about. "
>
> A.A. Milne, *Winnie-the-Pooh*, from [43]

The central theme of this Thesis is the pinning-depinning transition due to shaking fields and external currents. This Chapter discusses how a skyrmion lattice can be manipulated using external drives, especially by an external current for metallic systems such as MnSi. A crucial ingredient to understand and control the dynamics of skyrmion lattices under external drive is pinning. Pinning can have many different microscopic origins, which we discuss more closely.

We start this Chapter with a short introduction to the pinning-depinning transitions, which is a universal phenomenon across many physical systems. Further, we discuss how emergent electrodynamics arise for non-trivial spin textures and the skyrmion Hall effect, due to which ultralow depinning current densities were detected. In the next Section we shortly introduce the equation of motion for skyrmions as rigid particles. Moreover, we discuss the regimes of elastic and plastic depinnings of skyrmion lattices. We proceed to review several important experimental and numerical studies on the bending and breaking of skyrmion lines under external drives. At the end of this Chapter, we shortly introduce the phenomenon of creep.

Review articles, which have been used while writing this Chapter are Refs. [46, 49, 50].

3.1 Pinning - Depinning Transitions

In an analogy to second-order equilibrium phase transitions, elastic systems can undergo nonequilibrium phase transitions between different dynamical phases when subject to external drives. The study of critical exponents and universality classes of these transitions is an active research field, with a high degree of universality across many different physical systems, such as vortices in type-II superconductors [43], charge density waves [51], magnetic domain walls [52, 53] and many other (for a broad review article, see Ref. [49]).

Due to their topological stability and solitary particle-like behaviour, skyrmions can be effectively described as interacting particles (or interacting elastic strings for 3D systems). This approximation is appropriate as long as weak pinning produces only little distortion on the shape of the skyrmions (or skyrmion lines). Potential minima in the disorder landscape (called pinning sites) produce a force on the skyrmions, with the maximum value of this force called pinning strength. The nature of such pinning sites on the microscopic level can be naturally occurring atomic impurities, local anisotropy, sample thickness modulations, missing spins, holes, adatoms at the surface and many other effects. Moreover, in 3D systems, more extended defects such as grain boundaries or dislocations produce even stronger pinning forces [49].

The coupling to external drives allows to efficiently move skyrmions and opens a new area to investigate. Probably the most well-studied one is by applied current due to the spin-transfer torques for metallic systems (such as MnSi), which we discuss in detail in the next Section. This motion can be then deduced from changes in the Hall resistivity [54,55] or observed in direct imaging experiments [56–58]. Moreover, one can move skyrmions with the help of temperature gradients [59–62], spin waves [63–65], magnons [66], etc. In this Thesis, the focus of our attention is on the study of skyrmion line movement due to the external transverse magnetic fields.

A skyrmion lattice driven over a disorder potential experiences a competition of ordering effects, favouring a triangular lattice, with random pinning, which tries to disorder the lattice. This competition gives rise to a rich variety of non-equilibrium phases. Below a critical threshold F_c, skyrmions stay pinned (called the **pinned phase**), while above this threshold, particles start to move (called the **moving phase**). When skyrmions move, pinning creates **friction** for the skyrmion motion under an applied drive. For elastic depinning (which we will discuss in more depth in Sec. 3.4), the velocity-force curve takes the form $v \propto (F_d - F_c)^\beta$ where F_d is the driving force and β is a critical exponent. Depending on the value of β, different university classes can be identified. Unfortunately, the exact value of this critical exponent for the skyrmion lattice remains unknown and is a hard problem to tackle both theoretically and experimentally [50].

One of the significant breakthroughs in the field of skyrmions was a report of ultralow electric currents needed to depin the skyrmion lattice [16]. In the next Section, we will discuss closer how this phenomenon was detected.

3.2 Emergent Electrodynamics. Skyrmion Hall effect

In this Section, we discuss more closely the interplay of spin currents with skyrmion lattices. This Section is based on a review article, Ref. [46].

Consider conduction electrons passing through a spin texture in a metallic skyrmion hosting material (e.g. MnSi). We assume that conduction electrons and spins coupled ferromagnetically at each site by Hund's coupling (in the strong coupling limit). Spins of the electrons in this model align with the local magnetization direction $\hat{\boldsymbol{M}}(\boldsymbol{r})$ adiabatically. The hopping amplitude of an electron between two neighboring sites in a non-planar skyrmion structure acquires a phase factor, known as a Berry phase. It is also sometimes called geometric or topological, as it depends only on the path taken, not on time. This vector potential produces an effective electromagnetic field, which electrons will experience even in the absence of external fields. The effective fields which arise due to this effect are called **emergent electromagnetic fields**. An emergent magnetic field $\boldsymbol{B}^e$ is proportional to the local skyrmion density [54]

$$B_i^e = \epsilon_{ijk} \frac{\hbar}{2} \hat{\boldsymbol{M}} \cdot (\partial_j \hat{\boldsymbol{M}} \times \partial_k \hat{\boldsymbol{M}}) \,. \tag{3.1}$$

The magnetic flux corresponding to it is proportional to the topological winding number

$$\Phi_B = 2\pi W\,. \tag{3.2}$$

An emergent electric field $\boldsymbol{E}^e$ is given by

$$E_i^e = \hbar\, \hat{\boldsymbol{M}} \cdot (\partial_j \hat{\boldsymbol{M}} \times \partial_t \hat{\boldsymbol{M}})\,. \tag{3.3}$$

Note that the emergent electric field is absent for a static skyrmion, whereas the magnetic field is present even in the static case. For a derivation of emergent fields and more detailed discussion, see Ref. [54]. Using $\partial_t \hat{\boldsymbol{M}} = \frac{\partial x_i}{\partial t} \partial_{x_i} \hat{\boldsymbol{M}}$ one can rewrite the emergent electromagnetic field with help of the drift velocity of skyrmion crystal $\boldsymbol{v}_d$ as $\boldsymbol{E}^e = \boldsymbol{v}_d \times \boldsymbol{B}^e$.

Under applied electric $\boldsymbol{E}$ and magnetic $\boldsymbol{B}$ fields, conduction electrons will experience a Lorentz force $-e[(\boldsymbol{E} + \boldsymbol{E}^e) + \boldsymbol{v} \times (\boldsymbol{B} + \boldsymbol{B}^e)]$, where $-e$ is the charge and $\boldsymbol{v}$ is the velocity of electrons. Because of the emergent magnetic field $\boldsymbol{B}^e$, the Hall effect will occur, called the topological Hall effect (THE). Moreover, due to the spin transfer torque (STT), the skyrmion lattice will move in the transverse direction to the current, an effect referred to as **skyrmion Hall effect** (see Fig. 11). With the help of Hall resistivity measurements, the skyrmion lattice was found to depin at ultralow critical currents of $j \approx 10^6 \mathrm{A/m}^2$ [54] (see Fig. 12). Generally, the skyrmion lattice in MnSi is only weakly pinned to the local defects of the underlying lattice due to its smoothness, large skyrmion lattice constant (for MnSi skyrmion radius is $R_s \approx 200$ Å much larger than the atomic lattice constant $a \approx 4.56$ Å) and clean samples (carrier mean free paths is $l \approx 1000$ Å) [54]. This is in contrast to, for example, a helical phase, which is much more strongly pinned [55]. Moreover, the measured critical current for the skyrmion lattice in MnSi is approximately 5 orders of magnitude smaller than the one observed for magnetic domain walls, which can also be moved via

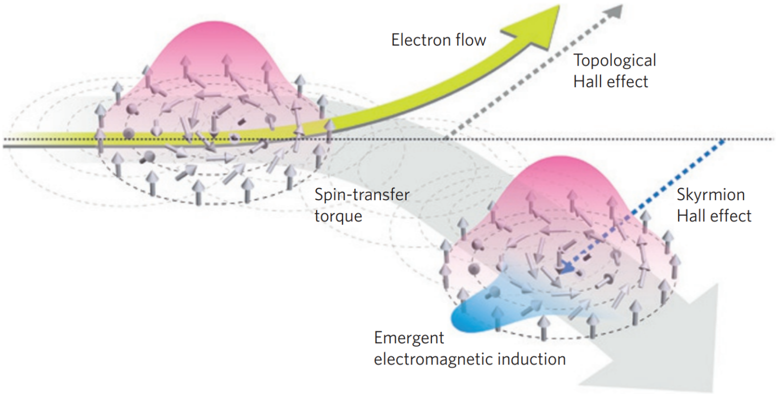

Figure 11: Under the external current, electrons are deflected by the Lorentz force due to the emergent magnetic field. Because of the spin-transfer torque mechanism, skyrmions are deflected in (almost) transverse direction to the current direction [46].

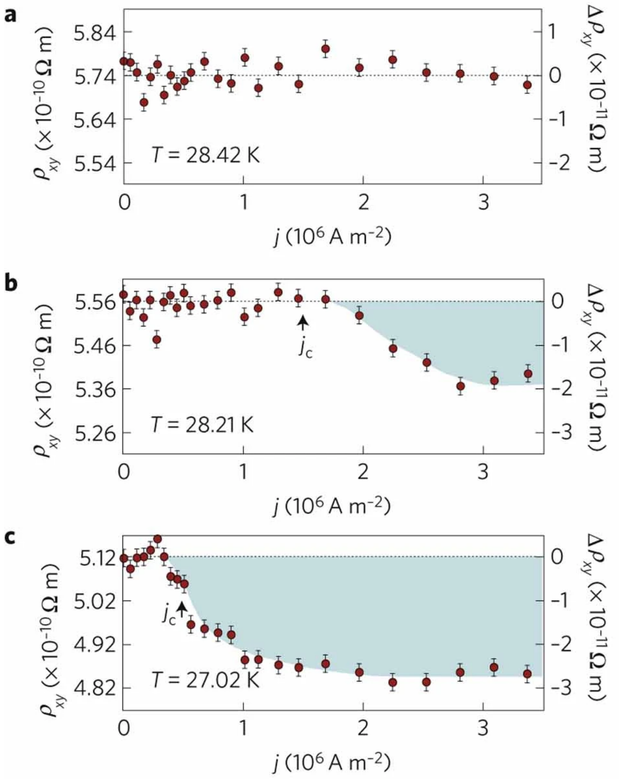

Figure 12: The change in the Hall resistivity ρ_{yx} as function of current j at $B = 250$ mT for several temperatures. The depinning of the skyrmion lattice is deduced from the change in the Hall resistivity. Picture credit from Ref. [54].

spin-transfer torques [67].

In the next Section, we proceed to discuss an effective equation for rigid skyrmion motion, which will be used extensively later in this Thesis.

3.3 Skyrmion Dynamics

A skyrmion is a large object which consists of many single spins. Instead of tracking the dynamics of each individual spin, it is, in many cases, convenient to switch to a description of skyrmion as a rigid particle. The dynamics of this rigid particle is described by the so-called Thiele equation, which we will discuss in this Section.

In the continuum approximation, the magnetisation dynamics $\boldsymbol{M}(\boldsymbol{r}, t)$ is governed by the Landau Lifshitz Gilbert equation (LLG) [68]

$$\dot{\boldsymbol{M}} = \gamma \cdot (\boldsymbol{M} \times \boldsymbol{B}_{\text{eff}}) - \gamma \frac{\alpha}{M} \cdot (\boldsymbol{M} \times (\boldsymbol{M} \times \boldsymbol{B}_{\text{eff}})) \ . \tag{3.4}$$

The free-energy density gives rise to an effective magnetic field $\boldsymbol{B}_{\text{eff}}$ defined from a variational equation $\boldsymbol{B}_{\text{eff}} = -\frac{\delta \mathcal{F}[\boldsymbol{M}]}{\delta \boldsymbol{M}}$. This field originates from all energetic contributions of the system, such as exchange interactions, Dzyaloshinskii–Moriya interaction, anisotropies, etc. (see Eq. (2.7)). The first term gives precession with the gyromagnetic ratio $\gamma = 1.76 \cdot 10^{11}\,\mathrm{T}^{-1}$, while the second term is the phenomenologically included relaxation, proportional to a dimensionless damping constant α.

An approximate analytical solution for the dynamics of the skyrmion lattice is often obtained with the help of the so-called **Thiele equation** (originally derived by A. Thiele in 1973 [69]). When subject to an external drive, magnetic moments will rearrange coherently, leading to the skyrmion lattice motion. Therefore, instead of focusing on underlying spin dynamics, one can switch to a so-called centre of mass coordinate to describe the movement of a large object (compared to the distance between single atoms) - a skyrmion. The Thiele equation can be obtained from the LLG equation by projecting the latter to the translational mode and assuming a rigidity of spin texture during the motion

$$\boldsymbol{M}(\boldsymbol{r}, t) = \boldsymbol{M}_0(\boldsymbol{r} - \boldsymbol{R}(t)) \,. \tag{3.5}$$

Here $\boldsymbol{R}(t)$ is a generalized coordinate. Using this ansatz the time derivative can be rewritten as $\dot{\boldsymbol{M}} = -(\dot{\boldsymbol{R}} \cdot \boldsymbol{\nabla}) \cdot \boldsymbol{M}$. Now we substitute this expression in Eq. (3.4), multiply it with $\partial_i \boldsymbol{M}$ and integrate over space. After some computational steps, which are omitted here (for technical details, see Ref. [70]), one finally arrives at the Thiele equation for forces

$$\boldsymbol{\mathcal{G}} \times \dot{\boldsymbol{R}} + \alpha \mathcal{D} \dot{\boldsymbol{R}} = \boldsymbol{F} \,. \tag{3.6}$$

Here $\boldsymbol{\mathcal{G}} = (0, 0, \mathcal{G})^T$ is a quantized gyrocoupling vector,

$$\mathcal{G} = m_s \int_{U.C.} d\boldsymbol{r}\; \hat{\boldsymbol{M}} \cdot (\partial_x \hat{\boldsymbol{M}} \times \partial_y \hat{\boldsymbol{M}}) = 4\pi m_s W \;, \tag{3.7}$$

where $\hat{\boldsymbol{M}}$ is the local orientation of the magnetisation, U.C. refers to the unit cell of the skyrmion lattice, W is a quantised topological charge as defined in Eq. (1.7) and m_s is the spin density (with units $\hbar$ per volume). As one can see from this equation, gyrocoupling is intimately related to the non-trivial topology of skyrmions. The gyrocoupling term (sometimes called Magnus force) pushes skyrmions perpendicular to the direction of the velocity. Further, the diagonal dissipation tensor $\mathcal{D}$ is given by

$$\mathcal{D} = \frac{m_s}{2} \int_{U.C.} d^2\boldsymbol{r} (\partial_x \hat{\boldsymbol{M}} \cdot \partial_x \hat{\boldsymbol{M}} + \partial_y \hat{\boldsymbol{M}} \cdot \partial_y \hat{\boldsymbol{M}}) \,. \tag{3.8}$$

In the Thiele equation (3.5), $\alpha\mathcal{D}$ is the friction experienced by the skyrmion, proportional to the damping constant from the LLG equation. Moreover, the force on the right-hand side can be found as $\boldsymbol{F} = -\frac{\delta \mathcal{F}}{\delta \boldsymbol{R}}$.

One can extend this equation to account for other external forces, such as those which arise from the currents and pinning. The modified Thiele equation has the form [54]

$$\boldsymbol{\mathcal{G}} \times (\boldsymbol{v}_d - \boldsymbol{v}_s) + \mathcal{D}(\alpha \boldsymbol{v}_d - \beta \boldsymbol{v}_s) = \boldsymbol{F}_p \,. \tag{3.9}$$

In this equation, $\boldsymbol{v}_d$ is the drift velocity of the skyrmion lattice and v_s is the effective spin current velocity, which is proportional to the applied current ($v_s = \frac{j_s}{n_s} \approx \frac{jp}{en_s}$, where p is the local spin polarisation, $p \approx 0.1$ for MnSi). The terms proportional to $\boldsymbol{v}_s$ describe the effect of the adiabatic and non-adiabatic spin torques. Dissipative terms are expected to be small as α, β arise mainly from spin-orbit effects and spin-flip scattering [54].

The term on the right hand side of this equation is the phenomenological pinning force $\boldsymbol{F}_p$. This is an effective force on a rigid skyrmion particle, which can have different microscopic origins, as discussed in Section 3.1. For a skyrmion lattice moving with a velocity v, the pinning force has a power-law dependence, $\boldsymbol{F}_p = -f(v)\hat{\boldsymbol{v}}$, where $\hat{\boldsymbol{v}}$ is the unit vector in the direction of velocity and $v = |\boldsymbol{v}|$. The strength of this force depends, in the general case, on the velocity v. However, the precise dependence is not known. In the limit $f(v \to 0) = f_p$, this force should give the critical force from the current needed to depin the lattice. For the limit of strong forces, a power low dependence $f(v \to \infty) = v^{-\alpha}$ is expected. In Section 5.4, we continue this discussion and introduce the pinning model used within our theory.

In this Thesis, most of our theoretical results have been obtained within Thiele approach in the elastic depinning regime. In the next Section, we discuss 3D skyrmion lines in disorder potentials and consider the regimes of both elastic and plastic depinning.

3.4 Skyrmion Lines in Disorder Potentials

On the theoretical level, pinning effects for 3D skyrmion lattices are not easy to study. It is clear, however, that the critical force needed to depin the lattice is determined from the competition between the strength of the pinning potential and the elasticity of the skyrmion lattice.

If the strength of disorder is weak, above the transition all skyrmions start moving, preserving the triangular lattice symmetry without breaking the lines and generation of topological defects, the regime called **elastic depinning**. For MnSi, the lattice is built out of 1D skyrmion strings, which can be modelled in the case of weak pinning by a collection of harmonic springs. A somewhat similar system to skyrmions in which depinning under applied currents is probably most extensively studied is the vortex lattice in type-II superconductors. The crucial difference to skyrmion systems comes from the fact that the dynamics is overdamped (the gyrocoupling term is much weaker than the dissipation in Thiele equation 3.9). Because of the gyrocoupling term, a single skyrmion can move around a point pinning site [46], see Fig. 13. A more detailed study of a skyrmion interacting with a hole showed a combination of a longer-range repulsion with a short-range attraction [71].

A so-called **collective pinning limit** (which is believed to be relevant for MnSi [50]) is realised when pinning is relatively weak, and a large number of pinning sites act collectively so that one can efficiently approximate pinning by a disordered substrate with Gaussian character [50, 72].

Let us start the discussion by considering a single skyrmion line. Here we follow the

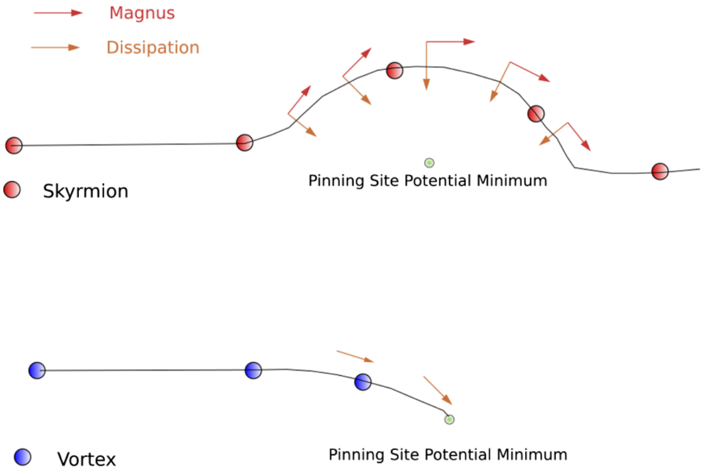

Figure 13: Skyrmion (upper panel) and superconducting vortex (bottom panel) interacting with an attractive point pinning site (green dot). Picture credit from [49].

ideas developed for superconducting vortices in Ref. [43]. Counter-intuitively, infinitely stiff lines cannot be pinned at all. A minimal lengthscale the skyrmion core is able to resolve in the transverse direction is the effective correlation length ξ, which is of the order of skyrmion radius R_s (see Fig. 14). Here, we consider only pinning due to the point defects on a scale smaller than the effective correlation length ξ. The strength and the directions of random pinning forces sum up so that only the fluctuations in the density and force of the defects will pin the skyrmion line. Assuming a density of individual pins acting on the vortex line to be n_i, the mean force from one pinning site f_{pin}, the total pinning force acting on a segment of length L is given by $F_{pin}(L) \approx (f_{pin}^2 n_i \xi^2 L)^{1/2}$. This force competes with the force from current, which grows linearly, see Eq. (3.9)

$$\boldsymbol{F}_c \approx -L\left(\boldsymbol{\mathcal{G}} \times \boldsymbol{v}_s\right). \tag{3.10}$$

For the dimensional estimate, we neglect the relatively small α and β in the Thiele equation 3.9. From the equation above, one can see that for long lines, the force from the current always wins, and the critical current vanishes in this limit.

However, in reality, lines can bend to find the best position for the pining potential. For a line $\boldsymbol{u}(z)$, the elastic energy of deformation is simply determined by

$$E_{el} = \frac{\epsilon}{2}\int_{-L/2}^{L/2} (\partial_z \boldsymbol{u})^2 dz\,. \tag{3.11}$$

Here, ϵ is the skyrmion line tension. Therefore, a line of length L with deviation $|\boldsymbol{u}| \approx \xi$ will have an elastic energy $E_{el} \propto \epsilon(\xi/L)^2 L$.

The idea of Larkin for vortices in type-II superconductors was to introduce the domains of correlated regions with characteristic collective pinning length scale L_c [73]. These domains interact elastically with the pinning potential and compete independently with

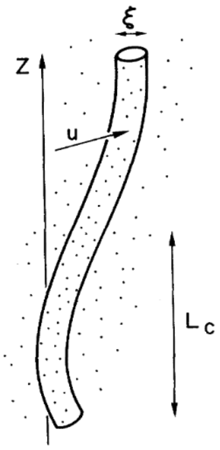

Figure 14: A skyrmion line (or a vortex line) pinned in the collective pinning limit by many weak pinning centers. The transverse length scale, which skyrmion line is able to resolve is given by ξ. The collective pinning length is denoted by L_c. Picture credit from [43].

the force from the current. The length scale L_c is obtained from the competition of elastic energy with the pinning energy $E_{pin} \approx F_{pin}(L)\xi$. From this, one can find the size of the regions L_c

$$E_{el}(L_c) = E_{pin}(L_c) \quad \Rightarrow \quad L_c \approx \left(\frac{\epsilon^2}{f_{pin}^2 n_i} \right)^{\frac{1}{3}} . \tag{3.12}$$

Each of the pieces of length L_c competes as an independent unit with the force from the current, $F_c \approx F_{\text{pin}}$. From this condition, we find

$$v_{s,c} = \frac{\epsilon\, \xi}{\mathcal{G} L_c^2} = \frac{\xi}{\mathcal{G}} \left(\frac{f_{pin}^4 n_i^2}{\epsilon} \right)^{1/3} . \tag{3.13}$$

We see that the critical current $j_c \propto v_{s,c}$ depends inversely on ϵ and goes to zero for infinitely stiff lines.

In order to make an estimate for the skyrmion string lattice, one needs to include the elastic constants of the skyrmion lattice. Here we assume again that the effective correlation length and skyrmion lattice constant are of the same order, $\xi \sim a_0$. Following Ref. [74], we define a collective pinning volume $V_{\text{pin}} = \ell_{\text{pin}} \varrho_{\text{pin}}^2$, where ℓ_{pin} and ϱ_{pin} are longitudinal and transversal dimensions, respectively. From Ref. [43] they can be found from

$$\ell_{\text{pin}} \approx \eta \frac{L_{\text{pin}}^3}{a_0^2} , \qquad \varrho_{\text{pin}} \approx \sqrt{\eta} \frac{L_{\text{pin}}^3}{a_0^2} . \tag{3.14}$$

Here $\eta = c_{44}/c_{66}$ is the ratio of the bend (c_{44}) and shear (c_{66}) elastic constants of the skyrmion lattice. Further, we rewrite the Thiele equation for the volume element V

$$-\boldsymbol{\mathcal{G}}^V \times \boldsymbol{v}_s = \boldsymbol{F}_{\text{pin}}^V . \tag{3.15}$$

Here $\boldsymbol{\mathcal{G}}^V = \boldsymbol{\mathcal{G}}\ell_{\rm pin}\varrho_{\rm pin}^2/a_0^2$ is the net gyrovector of $V_{\rm pin}$. The pinning force acting on the volume V can be found from the pinnning force acting on the single line using the relation [43],

$$F_{\rm pin}^V \sim F_{\rm pin}\eta\frac{L_{\rm pin}^4}{a_0^4}\,. \tag{3.16}$$

Finally, we obtain

$$v_{s,\rm c} \approx \frac{\epsilon\,\xi}{\mathcal{G}\eta}\frac{a_0^4}{L_{\rm pin}^6}\,. \tag{3.17}$$

We see again that the spin velocity depends inversely on the ratio η of elastic constants.

Upon increasing the strength of the disorder or, for example, in the presence of more extended objects such as grain boundaries or dislocations[7] (especially strong in thin-film systems, leading to a critical current much stronger than in bulk systems such as MnSi [57]) the next level of complexity occurs: the system might undergo an (irreversible) **plastic depinning**. In this case, some portion of skyrmions might remain stuck, while others can flow around them (as observed in thin films [76]). Moreover, significant lattice distortions are produced (for example, topological defects might appear, see the next Section). This plasticity remains generally a hard problem to tackle. It is not fully clear if it possesses universal features, with possibly different types of criticality occurring between single skyrmions and between emergent topological defects [49].

3.5 Bending and Breaking of Skyrmion Lines

In this Section, we review several important numerical and experimental studies on skyrmion lines in 3D disorder potentials.

Although for 2D skyrmions in disorder potentials there exists a huge body of literature, either based on the Thiele equation [77–79] or more precise micromagnetic approaches [80], the situation is different for 3D systems. Although perfectly stiff 3D skyrmion lines can be theoretically treated with 2D models, a fully 3D system exhibits much richer phenomena, as skyrmion lines are emergent objects that can bend or be broken apart. However, the numerical expense for simulating 3D systems with pinning is large; that's why most numerical simulations for 3D systems are performed on rather small systems, modelling thin films.

Already early theoretical studies have suggested that skyrmion lines can break into pieces by forming singular three-dimensional topological defects known as Bloch points, identified with emergent monopoles/antiminopoles [81, 83] (see the left panel of Fig. 15). In the experimental study in Ref. [82], the metastable skyrmion lattice in bulk MnSi was studied under repeated electric current pulses by measuring the Hall resistivity ρ_{yx}. It was found that, at low current densities $j \approx 10^6 \mathrm{A}/m^2$, the lattice is in the elastic (reversible) pinning regime, while for larger currents $j \approx 3\cdot 10^6 \mathrm{A}/m^2$ it undergoes irreversible processes,

---

[7] For a detailed discussion on collective pinning regime along with a strong pinning regime in thin films, see for example Ref. [75]

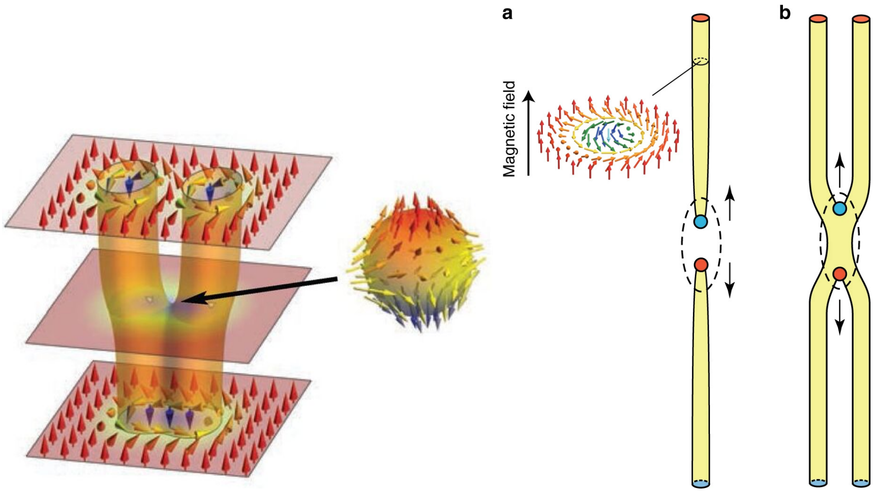

Figure 15: Left panel: the merging of two skyrmion lines. The defect which is created is an emergent magnetic antimonopole. Right panel: monopoles/antimonopoles (represented by coloured circles) resulting from partial pinching off/merging of two skyrmion strings. Picture credits from Refs. [81], [82].

which was attributed to the topological unwinding at higher current densities (see the right panel of Fig. 15). In numerical studies of skyrmion depinning using micromagnetic simulations, pinning is often introduced by easy axis anisotropy at randomly selected sites [55]. It was shown that when a segmented string (with a monopole on one of the sides) starts to move above the threshold applied current, the length of the skyrmion string shortens, and the skyrmion strings disappear eventually. Therefore, it was argued that the length of the skyrmion string is an important parameter to consider when studying current-induced motion. Although it remains not fully clear how exactly these results relate to the thermodynamically stable phase in MnSi, one can say for sure that the dynamics of monopole-like excitations, as well as Dirac stringlike excitations (emergent object where there is a monopole and antimonopole pair at the two ends) are important factors to consider [84, 85]. Generally, extended defects such as Bloch points or grain boundaries are more effective than point defects (considered in the previous Section) in pinning skyrmion lines [49].

These results have been followed by micromagnetic simulations in Ref. [86] of current-driven dynamics of a skyrmion string in pinning potential as a function of the thickness of the sample L_z versus the applied current. Authors identified the pinned, depinned regions and regions where the annihilation of skyrmion string happens (see Fig.16). It is more difficult to pin longer than shorter strings, which is also supported by lower critical currents in bulk samples as compared to the thin films [54, 57].

There are several experimental studies on the bending of skyrmion lines under external currents and temperature gradients. In Ref. [87] the nonreciprocal nonlinear Hall response in MnSi thin plates under external current was studied. It was found from different responses to positive and negative currents $\pm j$ in the second-harmonic complex resistivity under applied low-frequency sine-wave AC current. It was argued that this signal, which emerges above the threshold current only in the skyrmion phase, stems from the current-induced deformation dynamics of skyrmion strings due to disorder. Under stronger drives, skyrmions become straighter, and the effect is reduced. The resulting dynamical phase diagram is shown in Fig. 17, where a pinned phase below the threshold current j_{th}, bent to straight transition j_{co} can be found as a function of current density and temperature. Interestingly, we find a bending of skyrmion lines under the application of external currents within our theory as well (see Sec. 7.1). Further, the effective bending of skyrmion strings in bulk MnSi in orthogonal thermal gradients was recently measured using small angle neutron scattering [88].

Moreover, the small-angle neutron scattering experiments of the moving magnetic skyrmion lattice in bulk MnSi under electric current [89] showed a spatially inhomoge-

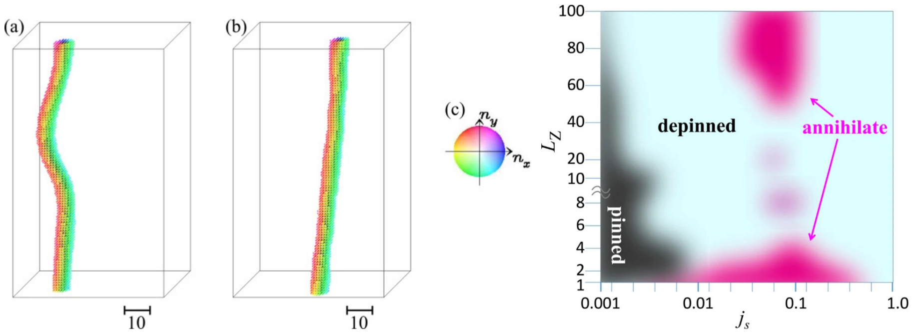

Figure 16: Right panel: numerically simulated phase diagram for current-driven skyrmion string in the disordered system. L_z is the thickness of system, j_s is the current density. Left panel: two snapshots of skyrmion line movement for $L_Z = 100$ and (a) $j_s = 0.04$, (b) $j_s = 1.0$ using the colour scheme depicted in (c) for an in-plane magnetic moment. Both pictures are taken from Ref. [86].

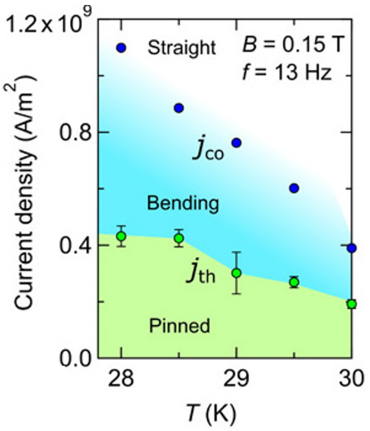

Figure 17: Phase diagram of skyrmion lattice subject to external current. For a description see the text. Picture credit from Ref. [87].

neous rotation of the skyrmion lattice for current densities greater than a threshold value as well as significant friction near the sample edges due to pinning. The effect of edges was further studied in a recent micromagnetic simulation of skyrmion strings near a tilted surface, which showed that the strings contort towards the surfaces of their confining crystals [90].

The recent development of high-precision experimental techniques, such as holographic vector-field electron tomography [91] with a sub-10-nanometre resolution and resonant magnetic x-ray imaging [92] foster further understanding of the three-dimensional magnetic texture, depinning and bending of skyrmion lines under external drives. In the next Section we will briefly introduce another important effect, which appears because of thermal fluctuations.

3.6 Creep

An important effect, which is not captured in the traditional mean-field picture, is the disorder in the form of thermal fluctuations. The interplay between the static (discussed in the previous Sections) and thermal disorder is, in general, a hard problem to tackle. Thermal disorder reduces the effectiveness of the static disorder potential so that skyrmion lines can move due to the thermally activated jumps over the pinning barriers at the values of the force (e.g. due to the external current) lower than the critical (the process known as a **thermal depinning**).

In Fig. 18, one can see a schematic picture of skyrmion lattice velocity v as a function of external current. For $T = 0$ a well-defined depinning transition exists at j_c (blue curve). At finite temperatures, the motion can start already at much lower values at f_c*. In Fig. 18c, a (distorted) skyrmion lattice is shown, pinned to static pinning centres (blue shaded areas). In the absence of the current, the potential is given by $V(x)$. It becomes tilted under an external current. Depending on the strength of the applied current, three phases exist: for $j > j_c$, the energy barrier ΔU vanishes and skyrmions fully depin. For $j \ll j_c$, the skyrmion has an orbital trajectory. For intermediate currents $j_c* \leq j \leq j_c$, creep might occur. If a skyrmion becomes depinned at some point of time, it will be trapped by the next pinning centre. The escape rate due to the thermal fluctuations is given by $\Gamma \propto \exp\left(\frac{-\Delta U}{k_B T}\right)$, where k_B is the Boltzmann constant.

Creep was predicted using particle models for skyrmions in metallic chiral magnets [93] and observed for single skyrmions in thin films [94]. However, only recently thermal creep was detected for bulk skyrmion lattice at ultra-low current densities using resonant ultrasound spectroscopy—a probe highly sensitive to the coupling between skyrmion and atomic lattices. It was shown that in MnSi, depinning occurs at j_c^* that is only 4% of the known critical current j_c [95]. These results have been in good agreement with the Anderson-Kim model for creep, introduced originally for superconducting vortices [96]. It was found that the local pinning potential vanishes linearly with current $\Delta U = \beta(j - j_c^*)$. The measured stiffening of the skyrmion lattice F (for the details of its definition, see

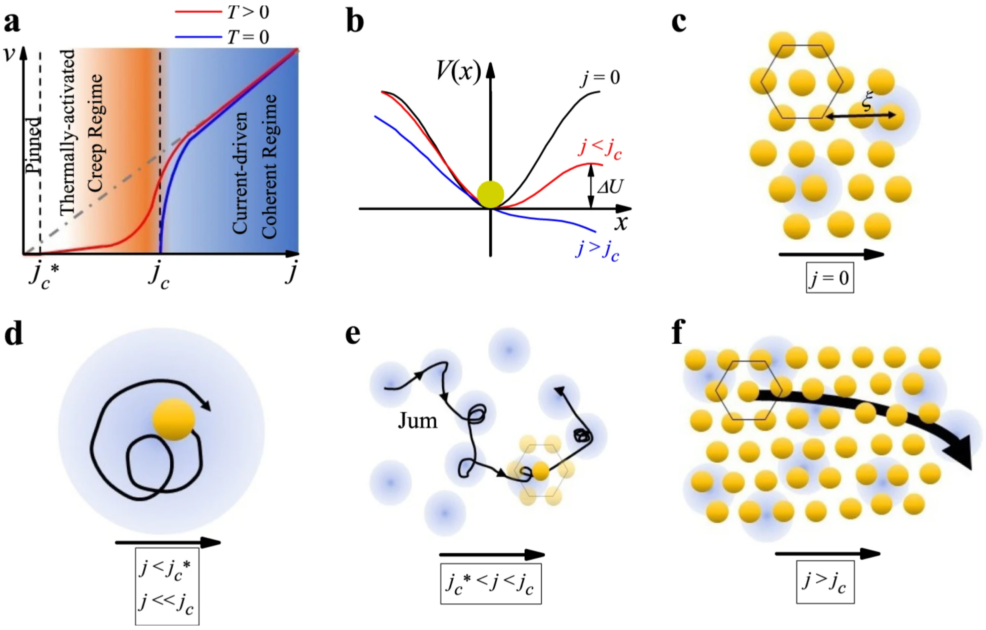

Figure 18: Creep in bulk skyrmion lattices. For the description, see the text. Picture credit from [95].

Ref. [95]) was found to obey the following law

$$\Delta F(j) - \Delta F(j = 0) \propto \exp\left(-\frac{\beta(j - j_c^*)}{k_B T}\right), \tag{3.18}$$

where β is a material-dependent prefactor.

Further, if thermal fluctuations are strong, they can (partially) disorder the system. However, in this Thesis we are not interested in this regime.

Summary and Outlook

In the center of this Chapter is the pinning-depinning transition of the skyrmion lattice under external drives. We considered closer how emergent electric and magnetic fields arise and why skyrmion lattices can be efficiently driven with external currents. Further, we discussed the microscopic mechanisms of skyrmion lattice pinning and several regimes, such as elastic and plastic depinning. Notably, both from theoretical and experimental points of view, it is clear that an important role in the skyrmion lattice pinnings is played by defects in the skyrmion lattice structure, such as Bloch points. Moreover, we discussed several experimental studies in which the bending of skyrmion lines was detected. In the last Section, we shortly introduced the important phenomenon of thermal creep.

On a microscopic level there are many effects, which contribute to the pinning of skyrmion lines in bulk materials and it remains one of the outstanding problems on the way to useful spintronic devices. However, in this Thesis we instead use a simplified, phenomenological model of pinning, which we introduce and study in the next Chapters.

Part II

Skyrmion Lattice Under External Drives

4 | Skyrmion Lattices under Slow AC-Drives

In this Chapter, we consider more closely skyrmion lattices under slow periodic drives. Such drives can be applied either parallel or perpendicular to the static magnetic field, needed to stabilize the skyrmion lattice. Several different probes can be used to experimentally investigate such systems. We start with introducing the first important experiment, namely the measurement of AC susceptibilities in MnSi. Further, we discuss the second experiment, namely the Time-Involved Small-Angle Neutron Scattering Experiment (TISANE). These are two important experiments, which we will use to validate our theory in the next Chapters.

This work was conducted in collaboration with a group of Prof. C. Pfleiderer and is currently in preparation for publication [97]. Experimental results presented in the first Section of this Chapter are measured by Dr. F. Rucker and in the second by Dr. D. Mettus.

4.1 Transverse AC Magnetic Susceptibility

A powerful experimental technique to study magnetic materials is the application of small, periodic magnetic fields. This driving field shall be added along with a static magnetic field needed to stabilize different phases in MnSi.

At a constant temperature of $T \approx 28$ K, MnSi undergoes several phase transitions in a static magnetic field (see Sec. 2.3). The first transition from helical to conical phase happens at the critical field value B_{c1}. At the second critical field value B_{c2}, a transition from a conical to a field-polarized state occurs. Moreover, in a small temperature range, the skyrmion phase is observed with the critical field values B_{a1} and B_{a2} [14,48].

When both static magnetic field $\boldsymbol{H}$ and small oscillating field $\partial \boldsymbol{H}_{\mathrm{ac}}$ are applied, two possible configurations exist. One possible case is when the driving field is applied in the direction of the static field. The susceptibility measured in this case is referred to as **longitudinal susceptibility** $\chi_{\parallel}$ (see Fig. 19a)

$$\chi_{\parallel} = \frac{\partial M_i}{\partial H_{ac,j}} \quad \text{with} \quad i, j, k \in \{x, y, z\} \text{ and } i = j \parallel k\,. \tag{4.1}$$

Here $\boldsymbol{M}$ is the measured magnetisation. This configuration is well-studied, and the measurements on longitudinal susceptibility existed even before the discovery of the skyrmion phase [99–101].

If the driving field is applied in the direction of the static field, the total field changes the amplitude but not the direction. Therefore, deep in the ordered phases (helical, conical or skyrmion states), the direction is fixed and the small changes in the amplitude of the applied field do not have a large effect on the magnetic order as measured by $\chi_{\parallel}$ [102–104]. The situation is drastically different close to the phase transitions at B_{c1}, B_{a1} and B_{a2}, where pronounced maxima in $\chi_{\parallel}$ are observed when the driving frequencies are small [102,105].

Another configuration is realised, when the driving field is applied perpendicular to the direction of the static field. In this case, the response of the magnetic order to small changes in the field orientation instead of the amplitude is being probed. The susceptibility, measured in this case is called **transverse susceptibility** $\chi_\perp$ (see Fig. 19b):

$$\chi_\perp = \frac{\partial M_i}{\partial H_{ac,j}} \quad \text{with } \ i,j,k \in \{x,y,z\} \text{ and } i = j \perp k\,. \tag{4.2}$$

This configuration is much less studied. To the best of our knowledge, the transverse susceptibility in MnSi was measured for the first time by Dr. F. Rucker [98]. It was done by means of a bespoke susceptometer comprising a primary coil with a balanced pair of secondary coils. The sample which was used for this measurement is depicted in Fig. 19c. In Fig. 20, the susceptibility data for a small oscillating field of $\nu = 120$ Hz is depicted for a range of transverse magnetic field strengths B_{AC} between 0.03 mT and 12.6 mT. Remarkably, all phases show strong response under applied transverse magnetic field.

In their work, Dr. F. Rucker and co-authors identified two limits. The first one is the limit for small magnetic fields B_{AC}. Before reaching the critical value of the transverse field $B_{\mathrm{AC}} \approx 0.63$ mT, almost no change is observed in the real part of the transverse susceptibility. This limit is identified with the pinned phase (denoted as the limit B, see Fig. 20). We will discuss this statement more closely in the next Chapter. Strikingly, the depinning starts already at tiny transverse magnetic field values. Further, for large magnetic fields, the real part of the susceptibility asymptotically approaches another limit, denoted as the limit A. In this limit, data points in the skyrmion and conical phases nicely

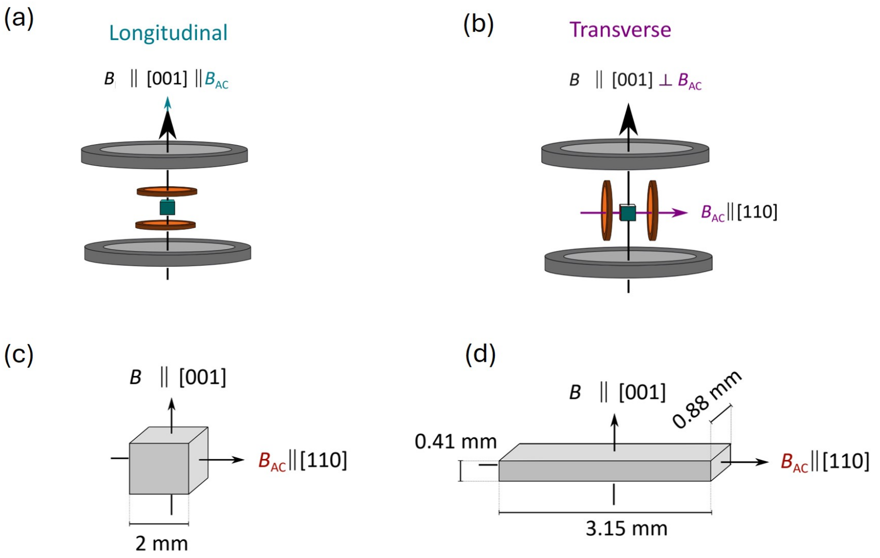

Figure 19: Schematics of longitudinal and transverse susceptibility for MnSi. Picture credit from [98].

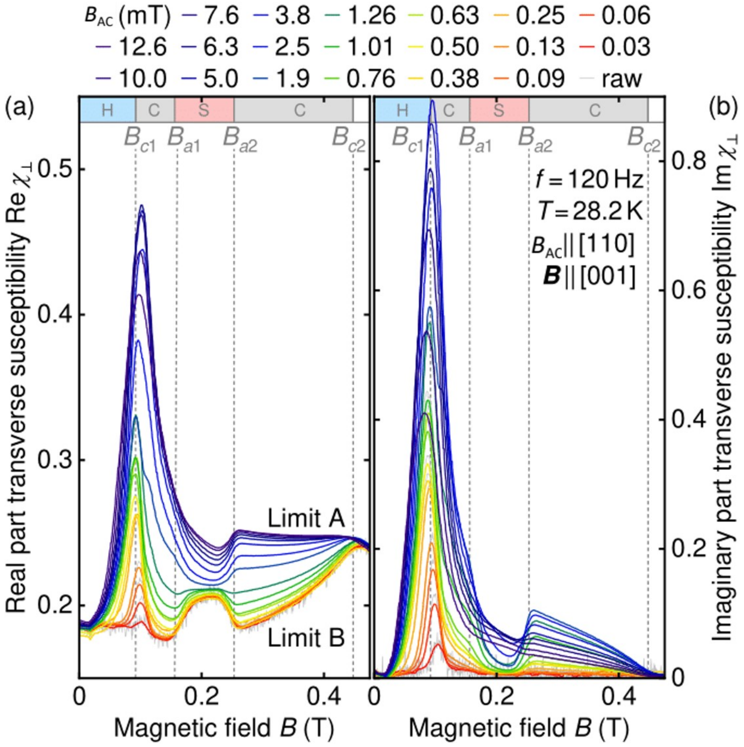

Figure 20: Real and imaginary parts of the transverse susceptibility for varying strength of the transverse oscillating field B_{AC}. Measured by Dr. F. Rucker [98].

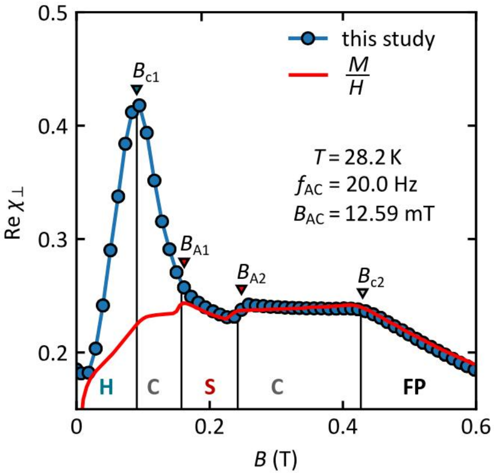

Figure 21: Real part of the transverse susceptibility in MnSi in the static magnetic field $B(T)$ and a strong value of the oscillating magnetic field $B_{\mathrm{AC}} = 12.59$ mT. Here H, C, S, FP refers to helical, conical, skyrmion and field-polarized phases, respectively. Picture credit from [98].

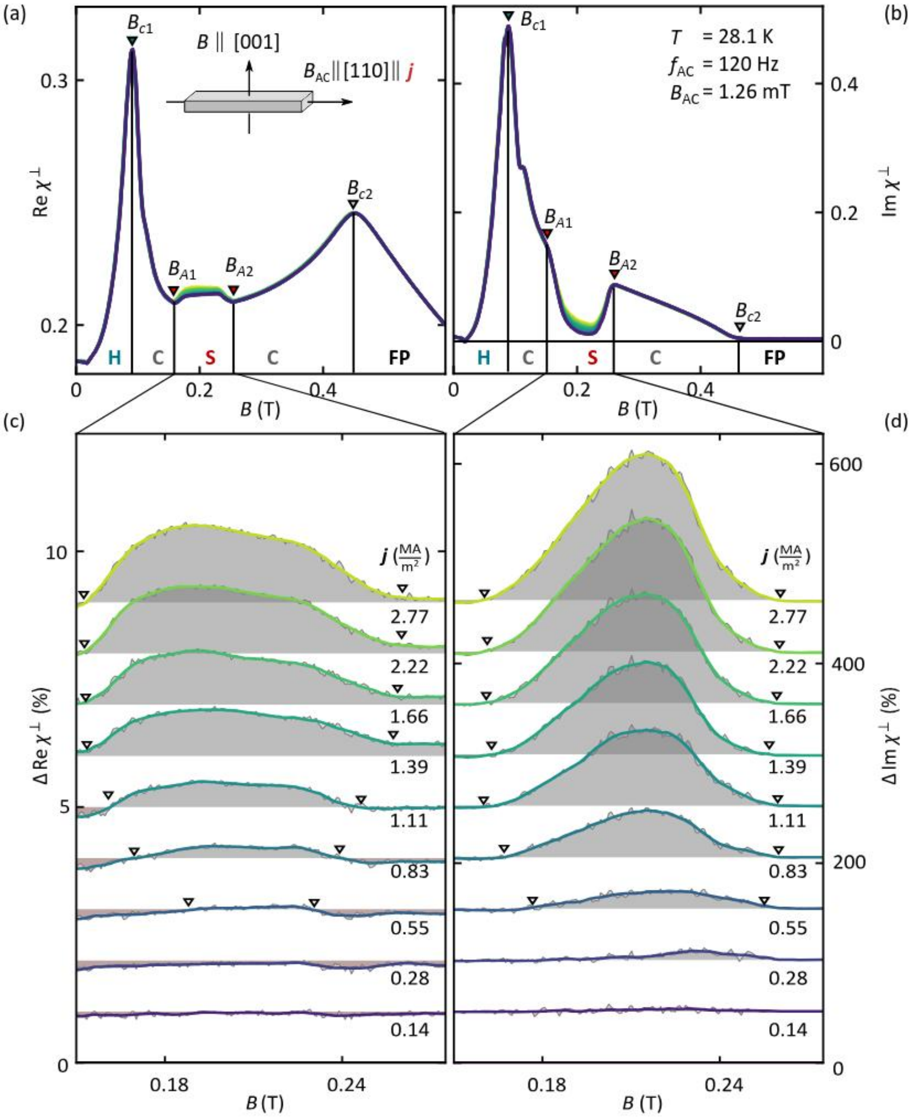

Figure 22: Real and imaginary parts of transverse susceptibility in static field $B(T)$ and oscillating field B_{AC} for varying strength of the current j. Measured by Dr. F. Rucker [98].

match the saturation limit

$$\mathrm{Re}\chi_\perp = \frac{M}{H} , \tag{4.3}$$

as can be seen in Fig. 21. This result is consistent with the statement that for strong transverse magnetic fields, the whole skyrmion lattice follows the applied magnetic field. We will discuss it more closely in the next Chapter.

In addition a combined effect of oscillating transverse magnetic field and external electric current was studied, see Fig. 22. The geometry which was used for this measurement is depicted in Fig. 19d. The external current was applied parallel to the direction of the oscillating field and perpendicular to the direction of the DC field. Because of heating effects, a complex temperature correction was performed (for the details, see Ref. [98]). As one can see, only the skyrmion phase shows a response in real and imaginary parts of the magnetic susceptibility.

In the next Chapter, we will develop a theoretical model, which we will use later on to explain the observed phenomena in transverse susceptibilities in Chapters 6 and 7.

4.2 Time-Resolved SANS and TISANE

A powerful experimental technique to probe periodic magnetic textures, such as a skyrmion lattice, is the small-angle neutron scattering (SANS) as discussed in Section 2.3. Being a momentum space technique, SANS provides complementary information to the direct real-space imaging techniques, such as Lorentz transmission electron microscopy [48]. Already the first neutron scattering experiments have shown that due to the magnetic Bragg scattering, a six-fold scattering pattern in the skyrmion phase appears. The skyrmion lattice is being formed in a plane perpendicular to the direction of the applied magnetic field $\boldsymbol{B}$, independent from the underlying atomic crystal for all orientations of $\boldsymbol{B}$ [14].

A number of techniques has been developed on the base of SANS to study dynamic response of skyrmion lattices under applied oscillating magnetic fields. Using the conventional SANS setup with a continuous neutron beam, one can resolve changes in the scattering pattern for slow drives, a technique called **time-resolved SANS**. In the ideal case, where neutrons have a fixed velocity, the time dependence of the detector follows the time dependence of the sample modulation. Therefore, these two systems shall be synchronised so that their periods match. The data is then being recorded at the detector over many oscillation periods and binned with the period T_d. However, in reality, the velocity selector produces a continuous beam with wavelength λ and wavelength spread $\Delta\lambda/\lambda$, which results in the distribution of neutron velocities. Due to this distribution, the detector signal will be smeared. Therefore, the time resolution of SANS is limited by this wavelength spread.

A technique called **TISANE** (time-involved small-angle neutron scattering experiment) was introduced to improve the resolution in time-resolved SANS [107]. The TISANE measurements on the depinning of skyrmion lattices used in this Thesis were performed at the instrument SANS-I at the FRM-II in Garching, Germany, by Dr. D. Mettus, group of

Prof. C. Pfleiderer. As these measurements provide important experimental evidence to support the theoretical model, we explain the setup here in a bit more detail (see Fig. 23).

Instead of using a continuous neutron beam as in the time-resolved SANS, a pulsed beam is used in TISANE. These periodic neutron pulses are generated by a chopper system. The system uses the unpolarized incident neutrons with a mean wavelength of $\lambda = 6\,\text{Å}$ and a wavelength broadening of $\Delta\lambda/\lambda \sim 10\,\%$ (FWHM). After this, the neutrons pass through the sample, which is subject to an AC magnetic field (typical frequencies used $\nu \approx 400$ Hz). Finally, neutrons are recorded at a detector with a period of time binning. The resulting data is, therefore, binned into a discrete number of time frames. An important trick which is used in TISANE to achieve better time resolution and a larger range of accessible sample frequencies is called the TISANE condition. This condition is a relation between periods of neutron pulses T_C, sample modulation T_S and detector signal binning T_D depending on the distances L_{CS} between pulses of chopper system and sample and L_{SD} between chopper

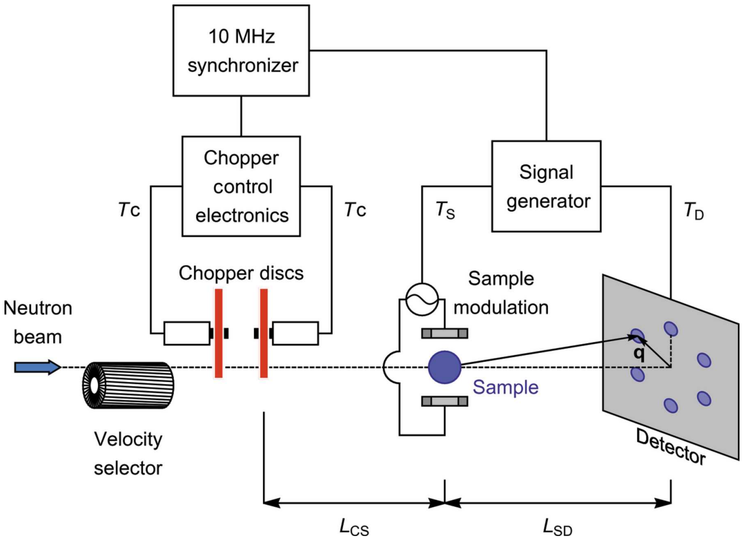

Figure 23: The schematic depiction of the experimental setup, used for TISANE measurements. Picture credit from Ref. [106].

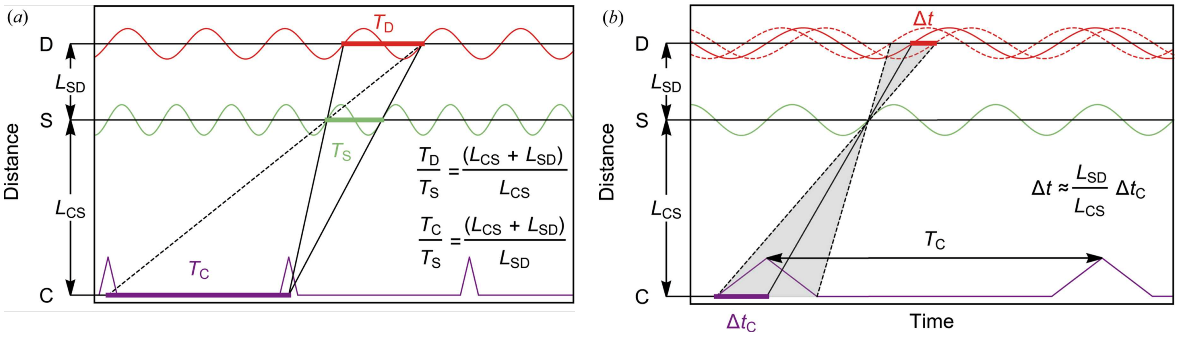

Figure 24: (a) Schematic of TISANE. Chopper, sample and detector are denoted with C, S and D. (b) Because of the finite chopper pulse width, the signal will be smeared. Picture credit from Ref. [106].

system and detector (see Fig. 24)

$$\frac{T_D}{T_S} = \frac{L_{CS} + L_{SD}}{L_{CS}} \quad \text{and} \quad \frac{T_C}{T_S} = \frac{L_{CS} + L_{SD}}{L_{SD}}\,. \tag{4.4}$$

In this case, neutrons from different chopper pulses that arrive at the sample at the same point of time will reach the detector within the same phase independently of their wavelengths [106]. This requires extremely precise synchronization of all parts of the setup, which is achieved by the master trigger unit. Technical details on all parts of this system can be found in Ref. [106].

Limitations on the precision of the experimental data of TISANE comes from the finite width of the chopper pulses (Δt_c on Fig. 24b), as well as the finite flight time of the neutrons across the sample. For the data, presented in this and the next Chapter, spherical samples were used to ensure rotational invariance and minimise demagnetisation effects. For MnSi, data was measured at temperature $T = 28.0$ K, static magnetic field $B_{\mathrm{dc}} = 170$ mT, oscillation frequency $\nu = 403$ Hz and sample radius of 5.8 mm.

The TISANE procedure is as follows: First, the oscillating field is applied, and the intensity of scattering for each orientation of the static field with respect to the neutron beam, called rocking angle ω (at each detector time frame) is measured (see Fig. 25). Six spots are being detected because of the hexagonal symmetry of the skyrmion lattice. For each time step, intensities from two out of six peaks (dubbed Box 1 and Box 2, see left panel of Fig. 26) are added to obtain a larger intensity (which has a benefit of smaller mean deviation) and average over a possible error because of the non-perfect alignment of the detector with respect to the incoming neutron beam.

The resulting rocking curves contain information about the skyrmion lattice response to

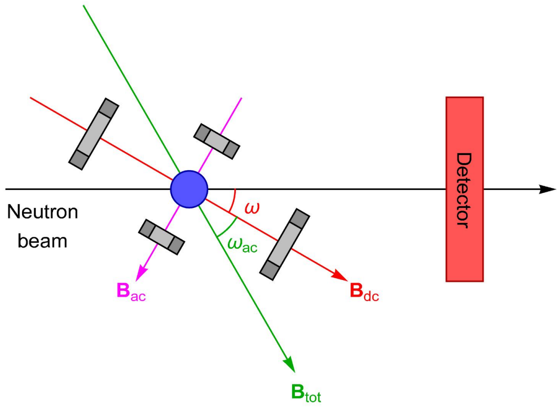

Figure 25: The schematic picture of the setup, used for TISANE measurements. The static magnetic field $\boldsymbol{B}_{dc}$ and the oscillating magnetic field $\boldsymbol{B}_{ac}$ together constitute the total magnetic field $\boldsymbol{B}_{tot}$. The orientation of this field with respect to the static magnetic field is denoted by ω_{ac}, while the orientation of the static field with respect to the neutron beam is the rocking angle ω. Picture credit from Ref. [106].

the applied drive. The position of the rocking scan peak gives roughly a general direction of the skyrmion lattice. As the area remains constant over time, one can assume that the total skyrmion lattice volume, which responds to the drive, remains unchanged. We can track the motion of the skyrmion lattice by tracking the movement of the rocking peak. The experimental rocking curves are being fitted with the Gaussian distribution. In the absence of the transverse oscillating magnetic field, the intensity as a function of the angle ω is plotted on the right panel of Fig. 26. The rocking peak centre position was found to be slightly off from the perfect alignment at $\omega_0 \approx -1.275°$. This angle was subtracted from all measurements at non-zero driving field values.

Using this scheme, one obtains time-dependent intensities at fixed rocking angles (see Fig. 27), which are often presented in the form of the time-resolved rocking angle maps (see, e.g., Fig. 39 in the next Section). We will discuss in more detail the resulting curves in Section 5.8.

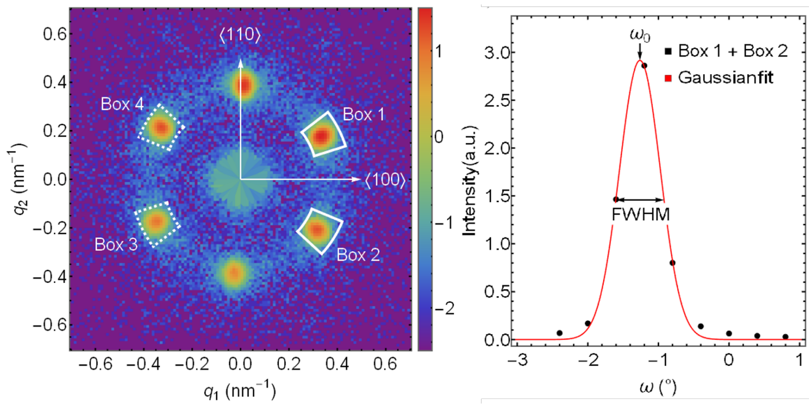

Figure 26: Left panel: typical SANS intensity pattern of the skyrmion lattice in MnSi in the absence of driving transverse field. Right panel: Gaussian fit to the summed measured intensity from Boxes 1 and 2. Picture credit from Ref. [106].

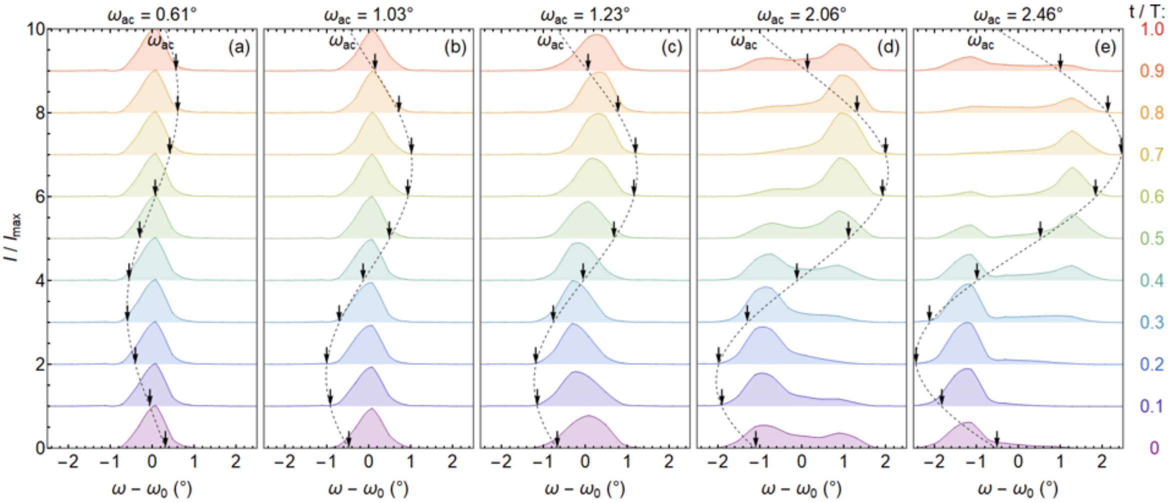

Figure 27: Time-resolved rocking curves, measured by Dr. Denis Mettus on MnSi sample for several tilting angles ω_{ac}. Dotted line: the corresponding value of ac magnetic field.

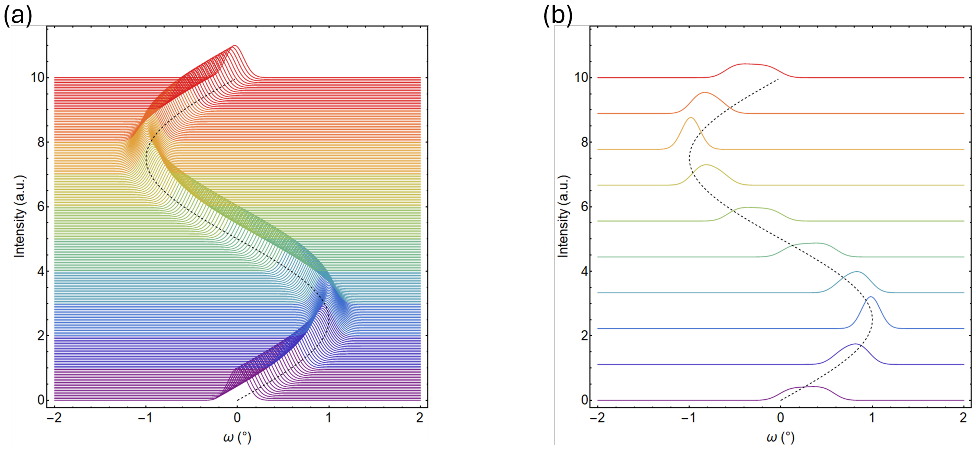

Figure 28: Effects of time bining. Picture credit by Dr. D. Mettus.

Note that time bins are not precise cuts in time. Although, in reality, the peak centre moves continuously (Fig. 28a), the measured data will be sorted in a finite number of time bins. Therefore, the measured intensity contains the integrated intensity over a finite time, which leads to smearing effects (Fig. 28b). We will discuss these effects more closely in the next Chapter.

5 | Unpinning Skyrmion Lattices with Shaking Fields

> "God made solids, but surfaces were the work of the devil."
> W. Pauli [108]

As discussed in the previous Chapter, already tiny transverse oscillating fields of approximately $1\ \mathrm{mT}$ are enough to unpin the skyrmion lattice in MnSi. In this Chapter, we develop a mean-field description of bulk skyrmion-hosting magnets under slowly oscillating (up to a few hundred Hz) tilted magnetic fields (dubbed as "shaking fields"). Instead of two phases (pinned and depinned) of a skyrmion lattice under external current, we predict that at least three phases exist in the shaking field. Further, we find both transitions and a high degree of universality in unpinning processes across different materials.

We start this Chapter with an introductory Section about the dynamics of skyrmion lines in tilted magnetic fields. We formulate a model of the low-energy collective excitations of the skyrmion lattice in terms of an elastic skyrmion string and proceed to derive the corresponding gradient expansion of the free energy. Further, we introduce a phenomenological pinning force using the effective slip-stick model to account for disorder in our system. Importantly, we differentiate between the bulk and surface pinnings and show that including surface pinning is crucial to explain the experimental data. We use the Thiele equation to find the rescaled parameters of dynamics of the elastic skyrmion lattice and provide an analytic solution to it in the adiabatic limit. Depending on the strength of the applied magnetic field, we predict that three dynamic phases appear: pinned, central pinned, and depinned. Results obtained from this effective model qualitatively reproduce all experimental findings from the time-resolved small-angle neutron scattering (TISANE) measurements for MnSi, doped samples $\mathrm{Mn}_{1-x}\mathrm{Fe}_x\mathrm{Si}$ (with x $= 0.02, 0.04$ and 0.06) and insulator $\mathrm{Cu_2OSeO_3}$.

This work was conducted in collaboration with the group of Prof. C. Pfleiderer and is currently in preparation for publication [109]. Experimental results presented in this Chapter are measured by Dr. D. Mettus.

5.1 Skyrmion Lines Under Tilted Magnetic Fields

Skyrmions in three spatial dimensions are smooth, line-like magnetic textures. Before we start the discussion of their dynamics in shaking fields, let us quickly recall how they respond to static tilted magnetic fields. For Bloch skyrmions, found in cubic helimagnets, the magnetisation is perpendicular to the radial direction. The free energy for cubic helimagnets (derived in Sec. 2.2) is isotropic, and the pinning to the underlying lattice due to anisotropies were found to be very small in experiments [14]. Therefore, the skyrmion lines always align parallel to the applied magnetic field, largely independent of the relative direction of the magnetic field with respect to the crystalline structure, as depicted in Fig. 29. Note that this is not the case for the skyrmion line of Néel skyrmions and antiskyrmions (see Ref. [110] for more details). Therefore, we constrain our discussion to cubic helimagnets in tilted oscillating fields in the following.

Let us consider the case of a skyrmion lattice subject to a shaking field. It has two components: the first one is the static magnetic field B_z in z direction, needed to sta-

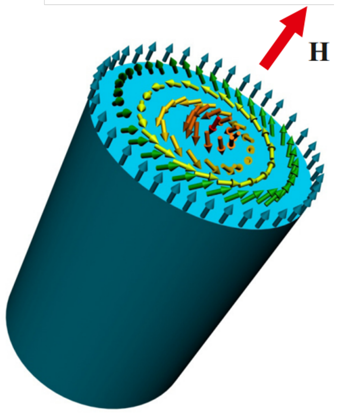

Figure 29: A skyrmion line subject to the external tilted magnetic field aligns parallel to the direction of the field (in the absence of pinning and demagnetisation effects). Picture credit from Ref. [110].

bilise the skyrmion phase in the bulk skyrmion hosting materials (recall Fig. 7 for the exemplary MnSi phase diagram). The second one is a tiny transverse oscillating field in x direction, $B_x(t) = b\cos(\nu t)$ with $b \ll B_z$. The total magnetic field is then given by $\boldsymbol{B}(t) = (B_x(t), 0, B_z)$. Depending on the oscillation frequency of the external field ν, very different phenomena may occur: for frequencies in the GHz regime, internal excitations of the skyrmion line or magnon excitations can be created [111, 112]. For example, for MnSi the internal frequency is $\frac{\nu^{\text{int}}}{2\pi} = 16.7$ GHz [112]. In this Thesis, we consider much lower frequencies of around a few Hz to a few kHz. In this regime, the low energy excitation due to the driving tilted field is a collective lattice excitation, as depicted in Fig. 30b.

Since we constrain our discussion to the regime where $b \ll B_z$, the direction of the total field $\boldsymbol{B}(t)$ changes only slightly, maximally a few degrees in the relevant experiments, $\delta\theta_B \ll 1$. These angles might, at first, seem tiny. However, let us consider skyrmion lines which follow the direction of the applied magnetic field (Fig. 30b). In this case, skyrmions need to move a long distance of order $z\delta\theta_B$, where $-\frac{L}{2} \leq z \leq \frac{L}{2}$ is a coordinate along the skyrmion string. For example, for a cubic sample with 2mm length under a tilted magnetic field of the order of $\delta\theta_B = 1^\circ = 0.017$ from the experiments, the end of the skyrmion line would need to move $\Delta x = 0.03$ mm, a gigantic distance compared to the typical skyrmion distance of $d \approx 20$ nm [14]. This cannot happen instantaneously for long skyrmion strings with the length of the order of the sample size, as skyrmions would need to move with speed $\propto z\partial_t\delta\theta_B$. Thus, we expect skyrmion lines to bend.

In order to describe this bending, we focus on the low-energy collective excitation of the skyrmion lattice. If $\boldsymbol{M}_0(\boldsymbol{r})$ describes the magnetisation of the undistorted periodic skyrmion lattice in equilibrium, we assume that the magnetisation of the distorted lattice is approximately described by

$$\boldsymbol{M}(\boldsymbol{r}, t) \approx \boldsymbol{M}_0(\boldsymbol{r} - \boldsymbol{u}(z, t)) + \delta\boldsymbol{M}(\boldsymbol{r}, t)\,. \tag{5.1}$$

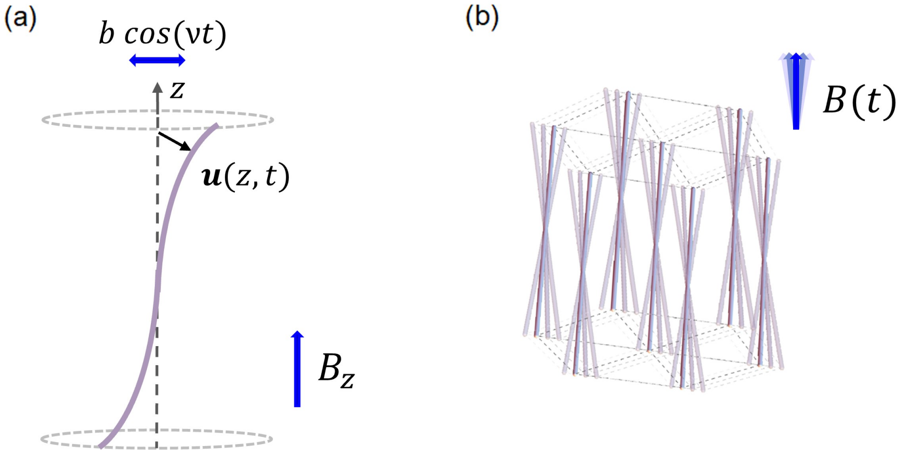

Figure 30: Skyrmion lines subject to the external magnetic field $\boldsymbol{B}(t) = (B_x(t), 0, B_z)$. (a) The lateral distortion of each skyrmion line in a periodic skyrmion lattice is parametrised by the function $\boldsymbol{u}(z, t)$. (b) In the absence of pinning, skyrmion lines follow the direction of the applied magnetic field $\boldsymbol{B}(t)$.

Further, we introduce a parametrisation of the skyrmion lattice by a displacement function

$$\boldsymbol{u}(z, t) = \begin{pmatrix} u_x(z, t) \\ u_y(z, t) \\ z \end{pmatrix} . \tag{5.2}$$

This function depends only on z and t and describes the lateral distortion of each skyrmion line in a periodic skyrmion lattice (see Fig. 30a). Crucially, although skyrmions travel large distances of order $z \cdot \delta\theta_B$, so that $\boldsymbol{u}$ can be much larger than the typical skyrmion distance and $\boldsymbol{M}(\boldsymbol{r}, t) - \boldsymbol{M}_0(\boldsymbol{r})$ may be very large, corrections to this collective excitation $\delta\boldsymbol{M}(\boldsymbol{r}, t)$ remain tiny. These corrections include several effects such as a shape deformation of single skyrmions and a distortion of the skyrmion lines in the z direction among others. However, we expect that these effects are negligible for the discussion of the low-energy dynamics of the skyrmion lattice. Therefore, we can formulate an effective theory in terms of $\boldsymbol{u}(z, t)$, which encodes the tilting, the bending and the motion of the skyrmion lattice up to small local corrections.

Note that Eq. (5.1) does not take into account that the effective distance of skyrmions may change in the distorted skyrmion lattice. However, it turns out that this effect gives only higher-order corrections to the energy. Consider a skyrmion lattice distorted by a small angle γ (see Fig. 31). We denote the distance between skyrmion lines h ($\tilde{h}$) for the undistorted (distorted) skyrmion lattice. The change of this distance can be estimated from the geometric considerations

$$h - \tilde{h} = h - h\cos(\gamma) \approx h(\partial_z u_x)^2 . \tag{5.3}$$

Here we used a Taylor expansion in the small angle γ and approximated it with a derivative

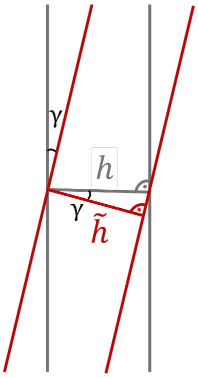

Figure 31: A lattice of undistorted (gray) and distorted (red) skyrmion lines.

of the displacement function of the distorted lattice in x direction, $\gamma \approx \partial_z u_x$. As the free energy should be quadratic in terms of $h - \tilde{h}$, we conclude that this effect will give only higher-order corrections to the energy ($\propto (\partial_z \boldsymbol{u})^4$) and is therefore ignored in the following.

5.2 Free Energy of Skyrmion Lines in External Oscillating Field

In this Section, we proceed to derive the free-energy functional for the skyrmion lattice subject to a shaking field in the absence of pinning.

We parametrise the collective motion of the skyrmion lattice by the unit vector $\hat{\boldsymbol{n}}$, oriented parallel to the skyrmion tubes and perpendicular to the plane of the skyrmions. In the absence of a drive, when only the static field B_z is applied, the uniform magnetisation per volume is given by $\boldsymbol{m}_0 = m_0 \hat{\boldsymbol{n}}$, where m_0 is the average magnetisation density of skyrmions in the internal background field B_0, oriented parallel to $\hat{n}$. This corresponds to an external field $B_z = B_0 + N_z m_0$ when the demagnetisation factor N_z, encoding the sample shape, is considered.

We derive the free energy for the most general case when the oscillating transverse magnetic fields in both x and y directions are applied, $\boldsymbol{B}(t) = (B_x(t), B_y(t), B_z)$. The orientation of the skyrmion lattice will deviate slightly from the z axis, $\hat{\boldsymbol{n}} = (\delta n_x, \delta n_y, n_z)$. Because transverse magnetic fields B_x, B_y are much smaller compared to the static field in the z direction, $B_x, B_y \ll B_z$, the bending of the skyrmion lattice in transverse directions δn_x, δn_y is expected to be small. Thus, we find the z component of this vector $n_z = \sqrt{1 - \delta n_x^2 - \delta n_y^2} \approx 1 - \frac{\delta n_x^2}{2} - \frac{\delta n_y^2}{2}$.

When a sample is subject to external field $\boldsymbol{B}$, a demagnetisation field appears, which reduces the internal effect of the applied field. The exact strength of this field depends on the shape of the sample [113]. The change of the free-energy density f of a skyrmion lattice in a fixed magnetic field $\boldsymbol{B}$ and a fixed magnetisation configuration $\boldsymbol{m}$ can be found in a Taylor expansion around the uniform magnetisation $\boldsymbol{m}_0$. Taking the demagnetisation effecs into account and expanding the change of the free-energy density up to quadratic order, we obtain

$$f = (\boldsymbol{m} - \boldsymbol{m}_0) \cdot \left.\frac{df_0}{d\boldsymbol{m}}\right|_{\boldsymbol{m}=\boldsymbol{m}_0} + \frac{1}{2\chi_{\parallel}^{00}}(\boldsymbol{m} - \boldsymbol{m}_0)^2 + \frac{1}{2\chi_{\perp}^{00}}(\boldsymbol{m}_\perp)^2 + \sum_{i=x,y,z} \frac{N_i m_i^2}{2} - \boldsymbol{m}\boldsymbol{B} \,. \tag{5.4}$$

Here f_0 is the free-energy density in the absence of both the external field and demagnetisation factors, $\boldsymbol{m}_\perp$ is the transverse component of the magnetisation, N_i are the demagnetisation factors encoding the sample shape, and $\chi_{\perp/\parallel}^{00}$ are the bare (static) susceptibilities of the skyrmion lattice for a parallel/perpendicular magnetic field (in the absence of demagnetisation fields), which can be found from measurements.

For the free-energy density in the absence of both the external field and demagnetisation factors, we find

$$\left.\frac{df_0}{d\boldsymbol{m}}\right|_{\boldsymbol{m}=\boldsymbol{m}_0} = B_0 \hat{n} \,. \tag{5.5}$$

We search for the magnetisation configuration $\boldsymbol{m}^*$, which minimises the density functional f with respect to the magnetisation vector $\boldsymbol{m}$ (the mean-field approximation, see Eq. (2.5) in Sec. 2.2). We find this minimum by demanding that derivatives of the free energy with respect to the three components of the magnetisation vector vanish. Moreover, we are interested in the total free energy, which can be found by integrating the free-energy density functional over the volume of our system at the previously found point $\boldsymbol{m}^*$

$$\mathcal{F} = \min_{\boldsymbol{m}} F = \int f|_{\boldsymbol{m}=\boldsymbol{m}^*} \, d^3\boldsymbol{r} \,. \tag{5.6}$$

The integral over x, y is straightforward, as the integrand does not depend on these variables and yields the area per skyrmion A_s. The remaining z integral runs over the whole length of the skyrmion line. Further, we switch from the description through the unit vector $\hat{n}$ to the description through the displacement function $\boldsymbol{u}(z,t)$. Locally, the direction of magnetisation in the transverse direction is given by the derivative of the displacement function $\boldsymbol{u}(z,t)$

$$\boldsymbol{m} = m_0 \frac{1}{\sqrt{1 + (\partial_z \boldsymbol{u}(z,t))^2}} \left(\partial_z \boldsymbol{u}(z,t), 1\right)^T \,. \tag{5.7}$$

Finally, after some algebraic manipulations (see Appendix A for more details), we arrive at the exact formula for the free energy of our system in the lowest order of the gradient expansion

$$\mathcal{F} = -\sum_{i=x,y} \frac{\gamma_i}{2} B_i(t)^2 + \int_{-L/2}^{L/2} dz \sum_{i=x,y} \frac{\epsilon_{0,i}}{2} \left(\partial_z u_i(z,t) - \frac{B_i(t)}{B'_{z,i}}\right)^2 \,. \tag{5.8}$$

Here, several important notations have been introduced. The first one is the effective z

field

$$B'_{z,i} = B_z + m_0(N_i - N_z) \ , \tag{5.9}$$

which accounts for corrections from demagnetisation factors for non-spherical samples. At large applied transverse fields and small frequencies, when the pinning is negligible, $B'_{z,i}$ provides the saturation value of the susceptibility. Thus, the skyrmion lattice simply follows the external field:

$$\chi_i^\infty = \frac{m_0}{B_{z,i}} = \frac{m_0}{B_z + m_0(N_i - N_z)} \, . \tag{5.10}$$

The susceptibility in the pinned phase, when $\partial_z u_i = 0$, is given by

$$\chi_i^0 = \frac{\chi_\perp^{00}}{1 + N_i \chi_\perp^{00}} \, . \tag{5.11}$$

Finally, we introduce the two remaining constants

$$\gamma_i = V_s \chi_i^\infty, \ \ \epsilon_{0,i} = A_s(\chi_i^\infty - \chi_i^0) B'^2_{z,i} \, . \tag{5.12}$$

Here $A_s \approx 230\,\mathrm{nm}^2$ is the area per skyrmion as introduced earlier and $V_s = A_s L$ is the corresponding volume of one skyrmion line. Furthermore, ϵ_0 has dimensions energy/length and has the meaning of the elastic constant of the skyrmion lattice. Importantly, for MnSi, we can calculate all these constants from the experimentally available data on magnetisation measurements and uniform susceptibilities of skyrmion lattices, presented in Section 4.1. In these experiments the transverse oscillating magnetic field was applied only in the x direction. In this case we obtain $\chi_x^0 \approx \frac{0.2}{\mu_0}$ and $\chi_x^\infty \approx \frac{0.3}{\mu_0}$, where μ_0 is the magnetic permeability, and

$$\epsilon_{0,x} \approx 4 \cdot 10^{-13} \frac{\mathrm{J}}{\mathrm{m}} \approx 30\,\mathrm{K}\frac{k_B}{\mathrm{nm}} \approx 600\,\mathrm{GHz}\frac{2\pi\hbar}{\mathrm{nm}} \, . \tag{5.13}$$

Note that Eq. (5.8) was derived under the assumption of smooth and small skyrmion lattice deformations, hence including only the lowest gradient term. The corrections to this formula include two types of terms. The first group of correction terms involve higher powers of $\partial_z \boldsymbol{u}$. These terms are much smaller than the main contribution as we are working using the assumption of the weakly distorted skyrmion lattice, $|\partial_z \boldsymbol{u}| \ll 1$. Other correction terms include higher derivatives of the displacement function $\boldsymbol{u}$. Let us, for example, consider the bending energy of skyrmion lines, described by

$$\mathcal{F}_B = \int_{-L/2}^{L/2} dz \, \alpha_0 \left[(\partial_z^2 u_x(z,t))^2 + \left(\partial_z^2 u_y(z,t)\right)^2 \right] \, . \tag{5.14}$$

Here, a prefactor α_0 can be found from a dimension of analysis to be of the order of $\epsilon_0 R_s^2$, where R_s is the skyrmion radius (the typical length scale of our system in the direction perpendicular to the applied static field). Now we make a substitution $z = \tilde{z}L$ in the integral and get

$$\mathcal{F}_B \approx \frac{\epsilon_0 R_s^2}{L^3} \int_{-1/2}^{1/2} d\tilde{z} \, \left[(\partial_{\tilde{z}}^2 u_x(\tilde{z},t))^2 + \left(\partial_{\tilde{z}}^2 u_y(\tilde{z},t)\right)^2 \right] . \tag{5.15}$$

In the assumption of a weakly distorted skyrmion lattice, the variations of $\boldsymbol{u}$ occur on the scale of a fraction of the length of the skyrmion string. The term $\mathcal{F}_B$ is therefore suppressed by $(R_s/L)^2 \ll 1$, compared to the leading order term presented in the Eq. (5.8). From similar considerations, we can also neglect other higher derivative corrections to Eq. (5.8) in this Chapter.

Note that the expression for the free energy is translation invariant with respect to translations in x and y directions. It is also invariant with respect to space inversion ($\boldsymbol{r} \to -\boldsymbol{r}$, $\boldsymbol{u}(\boldsymbol{r}) \to -\boldsymbol{u}(-\boldsymbol{r})$ and the magnetic field $\boldsymbol{B}$ is invariant under inversion). However, the underlying crystal structure is chiral. We will consider the corrections needed to restore the underlying chirality of the skyrmion lattice in Chapter 8.

In the absence of pinning, the minimum of the free energy, Eq. (5.8), can be easily obtained. In this case, the skyrmion line is straight and follows the effective magnetic field (see Fig. 30b):

$$\partial_z u_x(z,t) = \frac{B_x(t)}{B'_{z,x}}, \ \partial_z u_y = \frac{B_y(t)}{B'_{z,y}} \ \Rightarrow \ u_x(z,t) = z \, \frac{B_x(t)}{B'_{z,x}}, \ u_y(z,t) = z \, \frac{B_y(t)}{B'_{z,y}} . \tag{5.16}$$

After calculating the expression for the free energy of the skyrmion lines in a shaking field in the absence of pinning, we can now proceed to introduce the resulting equation of motion and find the elastic forces acting on the skyrmion line.

5.3 Equation of Motion and Elastic Forces

The expression of the free energy found in Section 5.2 describes the change of energy of the skyrmion line due to elastic bending in the absence of pinning. However, in real systems, the dynamics of the skyrmion lines is determined by the competition of the elastic force with Magnus, dissipative, and pinning forces. Our starting point to find the equation of motion is the Thiele equation (see Sec. 3.3), which accurately describes the motion of skyrmions as rigid objects in the presence of weak forces. The skyrmion line is built from single skyrmions. Therefore, instead of using the 2D version of the Thiele equation, $\boldsymbol{M}(\boldsymbol{r},t) = \boldsymbol{M}_0(\boldsymbol{r} - \boldsymbol{R}(t))$, for the 2D skyrmion coordinate $\boldsymbol{R}(t)$ we identify, for each z, the coordinate $\boldsymbol{R}(t)$ with the respective coordinate of the displacement function $\boldsymbol{u}(z,t)$. Therefore, in the absence of an external current, we can write the Thiele equation as

$$\boldsymbol{\mathcal{G}} \times \dot{\boldsymbol{u}}(z,t) + \alpha \mathcal{D} \dot{\boldsymbol{u}}(z,t) = -\frac{\delta \mathcal{F}}{\delta \boldsymbol{u}(z,t)} + \boldsymbol{F}^p . \tag{5.17}$$

Here $\boldsymbol{\mathcal{G}}$ is a gyrocouping vector, given by $\boldsymbol{\mathcal{G}} \approx 4\pi m_s W \hat{\boldsymbol{z}}$, where m_s is the spin density (with units $\hbar$ per volume). This vector is oriented parallel to the skyrmion orientation $\hat{n}$. However, we neglect this higher-order effect by setting $\hat{n} = \hat{z} + O(\partial_z \boldsymbol{u})$. Moreover, $W = -1$ is the winding number per unit cell, reflecting the non-trivial topology of skyrmions. Further, $\mathcal{D}$ is the dissipative tensor computed from $\mathcal{D} = \frac{m_s}{2}\int_{UC} d^2r(\nabla \hat{\boldsymbol{M}})^2$. Here, $\hat{\boldsymbol{M}}$ is the local orientation of the magnetisation, and one integrates over the unit cell of the skyrmion lattice. We will discuss the last term, the pinning force $\boldsymbol{F}^p$ in the next Section.

We constrain the further discussion to the transverse field acting only in the x direction and take $N_x = N_y = N_z = N$, valid for spherical samples, used for experiments discussed in this Chapter. Further, we drop the index x for γ_x and $\epsilon_{0,x}$ so that the free energy functional reads

$$\mathcal{F} = -\frac{\gamma}{2}B_x(t)^2 + \int_{-L/2}^{L/2} dz\, \frac{\epsilon_0}{2}\left[\left(\partial_z u_x(z,t) - \frac{B_x(t)}{B_z'}\right)^2 + (\partial_z u_y(z,t))^2\right] . \tag{5.18}$$

We proceed to evaluate the elastic force $-\frac{\delta \mathcal{F}}{\delta \boldsymbol{u}(z,t)}$ in Eq. (5.17) from the expression of the free energy. To find the force, which acts in the x direction at the point $z = z_0$ at a moment of time t, we calculate a functional derivative of the free-energy functional with respect to $u_x(z_0, t)$ via partial integration

$$-\frac{\delta \mathcal{F}[u_x(z,t), u_y(z,t)]}{\delta u_x(z_0,t)} = -\epsilon_0 \left[\delta(z - z_0)\left(\partial_z u_x - \frac{B_x(t)}{B_z'}\right)\Bigg|_{z_0=-L/2}^{z_0=L/2} - L\, \partial_z^2 u_x\Big|_{z=z_0}\right] . \tag{5.19}$$

A similar calculation gives the force acting in the y direction. Finally, we obtain that the **elastic force** (per length) acting in the bulk is given by

$$\boldsymbol{F}^{el,b} = -\frac{1}{L}\frac{\delta \mathcal{F}}{\delta \boldsymbol{u}} = \epsilon_0\, \partial_z^2 \boldsymbol{u} , \tag{5.20}$$

and the **elastic force on the surface** is

$$\boldsymbol{F}^{el,s} = -\epsilon_0 \left(\partial_z \boldsymbol{u} - \frac{B_x(t)}{B_z}\hat{\boldsymbol{x}}\right) . \tag{5.21}$$

We can write these two forces in a compact form with the help of two delta functions

$$-\frac{\delta \mathcal{F}}{\delta \boldsymbol{u}(z,t)} = \epsilon_0\, \partial_z^2 \boldsymbol{u} - \epsilon_0 \left[\delta\left(z - \frac{L}{2}\right) - \delta\left(z + \frac{L}{2}\right)\right]\left(\partial_z \boldsymbol{u} - \frac{B_x(t)}{B_z'}\hat{\boldsymbol{x}}\right) . \tag{5.22}$$

Note that the elastic force in the bulk is defined as a force per length in contrast to the surface force; therefore, these two forces have different dimensions.

The driving field, counter-intuitively, enters only as a boundary condition within the approximations of our theory, so that the ends of the line tend to align parallel to it. This fact will dramatically affect the depinning and motion of the skyrmion lines, as we shall see later. In the next Section, we proceed to introduce the effective model for the other remaining ingredient of the Thiele equation: the pinning force.

5.4 Pinning Force

Pinning forces from defects in the material or from defects in the skyrmion lattice structure, are crucial to correctly capture the observed phenomena for skyrmion lattices under external drives, e.g. depinning due to the applied current (see Sec. 3.1 for a more in-depth discussion). However, these forces substantially complicate the theoretical description. Within the mean-field theory discussed here, the function $\boldsymbol{u}(z)$ will be, in general, replaced by a field $\boldsymbol{u}(\boldsymbol{r})$ with complicated dynamics, especially close to the depinning transition. Moreover, the exact form of the pinning force and critical exponents of the depinning transition are unknown [49].

Based on this observations, we use a simple phenomenological model initially proposed in Ref. [54] to capture the most important disorder effects within the Thiele approach. This model is consistent with the observed finite critical current $j_c \approx 10^6 \mathrm{A}/m^2$ needed to depin the skyrmion lattice, as well as linear velocity dependence on current strength at larger currents (see Sec. 3.2). Firstly, skyrmions do not move if the force $\boldsymbol{F}(z,t)$ acting on them is smaller than a critical value, the so-called **depinning force**, F_c^p, which is defined as the force per skyrmion and per length needed to depin the skyrmion lattice. In this case, the pinning force cancels exactly other forces and skyrmions do not move. Secondly, when skyrmions start to move upon reaching this threshold value, they experience a **frictional force** oriented anti-parallel to the direction of motion of the skyrmion. The strength of this force is again given by F_c^p to ensure the continuity of pinning force (Fig. 32). Together, these two conditions can be written as

$$\boldsymbol{F}^p = \begin{cases} -\boldsymbol{F} & \text{for } F \leq F_c^p \,, \\ -F_c^p \frac{\dot{\boldsymbol{u}}(z,t)}{|\dot{\boldsymbol{u}(z,t)}|} & \text{for } F > F_c^p \,. \end{cases} \tag{5.23}$$

In the pinned regime, it is valid that $\boldsymbol{F}^p + \boldsymbol{F} = 0$, so that skyrmions are stuck. At first sight the form of the pinning force might seem quite simple. However, it is a highly non-linear, implicit function of the forces on the skyrmion and the skyrmion velocity. When the line is depinned, it travels the macroscopic distances $z\theta_B$, which is much larger than the skyrmion lattice constant. Therefore, F_c^p can be understood as a resulting friction force per length, averaged over many microscopic disorder realisations.

This model was initially proposed to explain the experiments on depinning by a current. From this, one can estimate the strength of the bulk pinning (see Sec. 7.1).

Now we want to expand this pinning model by introducing the pinning at the ends of the line $z = \pm\frac{L}{2}$, dubbed as **surface pinning** $\boldsymbol{F}^{p,s}$. The total pinning force is given by

$$\boldsymbol{F}^p = \boldsymbol{F}^{p,b} + \left[\delta\left(z - \frac{L}{2}\right) + \delta\left(z + \frac{L}{2}\right)\right] \boldsymbol{F}^{p,s} \,. \tag{5.24}$$

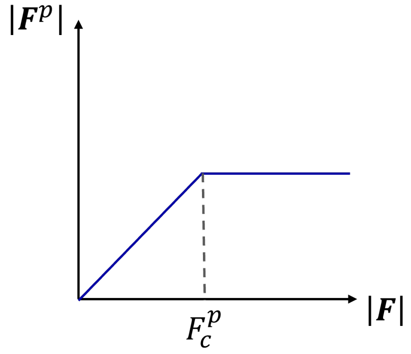

Figure 32: The pinning force $\boldsymbol{F}^p$ has the same strength and is directed anti-parallel to the applied force $\boldsymbol{F}$ until the force strength reaches the critical value F_c^p. After this, the pinning force $\boldsymbol{F}^p$ has a constant value F_c^p and is directed anti-parallel to the direction of the motion.

Here $\boldsymbol{F}^{p,b}$ and $\boldsymbol{F}^{p,s}$ denote a bulk and a surface pinning, respectively. Each of these forces follow Eq. (5.23) and are again non-linear functions of z and t, which depend on applied forces and the local skyrmion velocity. Note that the bulk pinning has units of force per length, while the surface pinning has a unit of force (to match the dimensions of elastic forces introduced in Sec. 5.3). The dimensionless parameter $\tilde{F}^{p,s} = \frac{F^{p,s}}{LF^{p,b}}$ characterises the relative strength of surface-to-bulk pinnings. Later in this Chapter, we will find the value of this parameter from measurements.

The motivation for including the surface pinning on the level of the mean-field theory is simple: it is crucial to correctly capture a finite strength of the transverse magnetic drive, $b_c \approx 1\,\mathrm{mT}$, needed to depin the skyrmion lattice in MnSi by the shaking field (see Sec. 4.1). We recall that the driving field $B_x(t)$ enters only at the surface (see Eq. (5.22)). In the pinned phase $\partial_z \boldsymbol{u}(z,t) = 0$, $\partial_z^2 \boldsymbol{u}(z,t) = 0$ and the surface pinning force exactly cancels the magnetic drive as depicted in Fig. 33. Only when the magnetic drive strength overcomes the critical value of the depinning force on the surface

$$F_c^{p,s} = \epsilon_0 \frac{b_c}{B_z'} \ , \tag{5.25}$$

the line starts to depin.

Microscopically, there are several mechanisms in which surface pinning might arise. Currently, no experimental data is available to determine if skyrmion lines are going through the whole sample or if they are breaking within the sample. If skyrmion lines end at the surface of the sample, pinning forces arise from surface roughness and surface defects. In contrast to the atoms inside the solid, which are surrounded by other atoms forming the crystal structure, surface atoms interact with other atoms from the environment. Therefore, the surface properties of a solid are quite different from its properties in the bulk. If skyrmion lines end in the bulk of the material, a Bloch point is formed at the end of the line (identified with an emergent magnetic monopole in Ref. [81]). Such

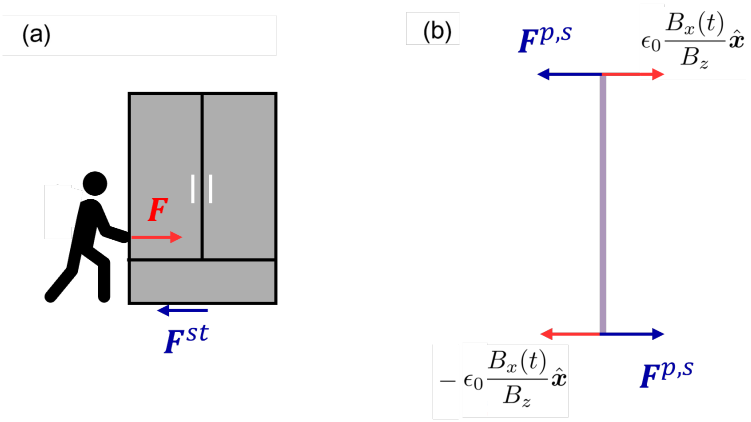

Figure 33: (a) Somewhat similar to our model, the static friction force $\boldsymbol{F}^{st}$ prevents the cupboard from moving under the applied force $\boldsymbol{F}$, $\boldsymbol{F}^{st} = -\boldsymbol{F}$. (b) The surface pinning force $\boldsymbol{F}^{p,s}$ prevents the line from movement under the driving field for $\epsilon_0 \frac{b}{B_z} \leq F_c^s$.

large topological defects (compared to the lattice constant) bind much stronger to local defects in the material in comparison to smooth skyrmion textures where such forces are suppressed by factors of $(a/R_s)^2$. Here a is the lattice constant and R_s is the skyrmion radius [70].

Note that the proposed effective pinning model cannot correctly capture critical exponents of the depinning transition or effects like thermal creep. Moreover, our theory does not capture the partial depinning of skyrmion lattice when some parts are depinned, while other parts remain stuck, the effect which was observed for skyrmion lattices (see Sec. 3.5). Despite this, the simple model can be used to successfully understand the main experimental features semi-quantitatively.

5.5 Rescaled Thiele Equation

After calculating the elastic as well as the pinning forces, we return to the Thiele equation, which governs the motion of the skyrmion line in our effective theory. In the presence of both bulk and surface pinnings, this equation has the form:

$$\boldsymbol{\mathcal{G}} \times \dot{\boldsymbol{u}}(z,t) + \alpha \mathcal{D} \dot{\boldsymbol{u}}(z,t) = -\frac{\delta \mathcal{F}}{\delta \boldsymbol{u}(z,t)} + \boldsymbol{F}^{p,b} + \left[\delta\left(z - \frac{L}{2}\right) + \delta\left(z + \frac{L}{2}\right)\right] \boldsymbol{F}^{p,s} . \tag{5.26}$$

The elastic force $-\frac{\delta \mathcal{F}}{\delta \boldsymbol{u}(z,t)}$ was calculated in Section 5.3. In order to reduce the number of independent parameters, we rewrite this equation in rescaled, dimensionless variables

$$\tilde{\boldsymbol{u}} = \tilde{\boldsymbol{u}}(\tilde{z},\tilde{t}) = \frac{\epsilon_0}{F^{p,b} L^2} \boldsymbol{u}(z,t), \quad \tilde{z} = \frac{1}{L} z, \quad \tilde{t} = \frac{\epsilon_0}{L^2 \mathcal{G}} t \, . \tag{5.27}$$

The rescaling of time performed here is equivalent to the rescaling $\tilde{\nu} = \frac{\nu}{\nu_0}$, $\nu_0 = \frac{\epsilon_0}{L^2 \mathcal{G}}$ of frequency. The coordinate $\tilde{z}$ is bounded as $-\frac{1}{2} \leq \tilde{z} \leq \frac{1}{2}$. Interestingly, the squared length of the skyrmion line enters both the rescaling of the frequency ν and the rescaling of the displacement field $\boldsymbol{u}(z,t)$. The resulting **rescaled Thiele equation** reads

$$\hat{\boldsymbol{z}} \times \dot{\tilde{\boldsymbol{u}}} + \frac{\alpha\mathcal{D}}{\mathcal{G}}\dot{\tilde{\boldsymbol{u}}} = \partial_{\tilde{z}}^2\tilde{\boldsymbol{u}} - \left[\delta\left(\tilde{z} - \frac{1}{2}\right) - \delta\left(\tilde{z} + \frac{1}{2}\right)\right] \left(\partial_{\tilde{z}}\tilde{\boldsymbol{u}} - \delta\tilde{B}\cos(\tilde{\nu}\tilde{t})\hat{\boldsymbol{x}}\right) + \tilde{\boldsymbol{F}}^p , \tag{5.28}$$

where we introduced a **rescaled pinning force $\tilde{\boldsymbol{F}}^p$** and a **rescaled driving field $\delta\tilde{B}$**

$$\begin{aligned} \tilde{\boldsymbol{F}}^p &= \frac{\boldsymbol{F}^{p,b}}{F^{p,b}} + \left[\delta\left(\tilde{z} + \frac{1}{2}\right) - \delta\left(\tilde{z} + \frac{1}{2}\right)\right] \frac{\boldsymbol{F}^{p,s}}{LF^{p,b}} , \\ \delta\tilde{B} &= \frac{\epsilon_0}{LF^{p,b}}\frac{b}{B'_z} . \end{aligned} \tag{5.29}$$

Note that in the rescaled coordinates the modulus of the depinning force in the bulk is equal to one. In addition, although the tilting angles of the magnetic field θ_B are small in the experiments, $\delta\theta_B \ll 1$, the parameter $\delta\tilde{B}$ does not need to be small as it has a (potentially) not small prefactor $\frac{\epsilon_0}{LF^{p,b}}$, as we shall see later from the experiments.

Therefore, our model has the following (fitting) parameters to be determined from the experiment:

$$\frac{\nu}{\nu_0} = \frac{\mathcal{G}L^2\nu}{\epsilon_0} , \qquad \tilde{\epsilon}_0 = \frac{\epsilon_0}{LF^{p,b}} = \frac{L_p}{L} , \qquad \tilde{F}_c^{p,s} = \frac{F^{p,s}}{LF^{p,b}} . \tag{5.30}$$

Here, the second parameter $\tilde{\epsilon}_0$ can be rewritten with the help of a parameter with dimensions of length $L_p = \frac{\epsilon_0}{F^{p,b}}$. We call this parameter a typical pinning length.

In the present Chapter, we concentrate on the limit of very slow drives, which is sufficient to explain the main observed effects in the TISANE experiment. We proceed to discuss intermediate frequencies in the next Chapter.

5.6 Dynamic Phases in the Adiabatic Limit

In general, it is not an straightforward task to find analytic solution for the displacement function $\tilde{\boldsymbol{u}}(\tilde{z},\tilde{t})$ for every driving frequency $\tilde{\nu}$ from the rescaled Thiele equation (5.28). As experiments operate in the regime of few Hz to few kHz, we start by considering the limit of slow drives, which we call the **adiabatic limit**. In this Section, we derive a fully analytic solution for the displacement function $\tilde{\boldsymbol{u}}(\tilde{z},\tilde{t})$ and three dynamic phases as a function of (rescaled) driving field strength $\delta\tilde{B}$ in the adiabatic limit.

The key to this solution is the realisation that, as the field changes very slowly, elastic forces and pinning forces in the bulk and at the surface exactly compensate each other at any given point in time

$$\partial_{\tilde{z}}^2\tilde{\boldsymbol{u}}(\tilde{z},\tilde{t}) = \frac{\boldsymbol{F}^{p,b}(\tilde{t})}{F_c^{p,b}} , \qquad \left(\partial_{\tilde{z}}\tilde{\boldsymbol{u}}(\tilde{z},\tilde{t}) - \delta\tilde{B}\cos(\tilde{\nu}\tilde{t})\hat{\boldsymbol{x}}\right)\Big|_{\tilde{z}=\frac{1}{2}} = \tilde{\boldsymbol{F}}^{p,s}(\tilde{t}) . \tag{5.31}$$

Based on these equations, we observe that the skyrmion line only moves in the direction of the applied drive. Because of the invariance under $\tilde{\boldsymbol{u}}(\tilde{z},\tilde{t}) = -\tilde{\boldsymbol{u}}(-\tilde{z},\tilde{t})$ we restrict our analysis to the interval $\tilde{z} \in [0, \frac{1}{2}]$ and then directly obtain the solution for the remainding interval by inversion.

If the strength of the rescaled driving field $\delta\tilde{B}$ is smaller than the maximal value of the surface pinning force $\tilde{F}_c^{p,s}$, the skyrmion line will stay pinned. As we have defined in Eq. (5.23), in this regime, the surface pinning force $\tilde{\boldsymbol{F}}^{p,s}(t)$ exactly cancels the driving force, which is given by the driving field $\boldsymbol{B}_x(t)$ at the end of the line

$$\tilde{\boldsymbol{F}}^{p,s}(t) + \delta\tilde{B}\cos(\tilde{\nu}\tilde{t})\hat{\boldsymbol{x}} = 0 \;\Rightarrow\; \partial_{\tilde{z}}\tilde{\boldsymbol{u}} = 0\,. \tag{5.32}$$

We call this phase the **fully pinned** phase. The critical value of the rescaled driving field $\delta\tilde{B}_{c,1}$ (which corresponds to the critical tilting angle $\frac{b_{c,1}}{B_z'}$ in unscaled coordinates), at which the driving field becomes stronger than the surface pinning, is given by

$$\delta\tilde{B}_{c,1} = \tilde{F}_c^{p,s} \;\Rightarrow\; \frac{b_{c,1}}{B_z'} = \frac{F_c^{p,s}}{\epsilon_0}\,. \tag{5.33}$$

After crossing this critical treshhold, the end of the line starts to depin. As the driving force acts only at the surface, depinning begins from the end of the line. Note that this transition exists only for a non-zero surface-pinning force. Moreover, the value of the first critical field $\delta\tilde{B}_{c,1}$ is independent of the frequency of the drive ν and length of the lines L within our theory.

We firstly direct our attention to the equation for the derivative at the surface $\partial_{\tilde{z}}\tilde{\boldsymbol{u}}$, in the regime where the line starts to depin, Eq. (5.31). The maximal strength of the surface pinning is given by $\tilde{F}_c^{p,s}$ so that it is allowed to switch between the two blue dotted lines in Fig. 34. The direction of this force is always anti-parallel to the direction of the driving force, if the line is pinned or antiparallel to the direction in which the line is moving. When the strength of the field is maximal (at $\tilde{t} = 0$), the line is at the point of its largest deviation (depicted in the most left picture of Fig. 35). For the finite time $\Delta\tilde{t}_0$, the surface pinning force compensates for the change in the driving force so that the derivative stays constant and the line does not move (we label this part of the period by P). A fraction of the period during which a skyrmion line stays pinned is given by

$$\frac{\Delta\tilde{t}_0}{\tilde{T}} = \frac{1}{2\pi}\arccos\left(1 - \frac{2\tilde{F}_c^{p,s}}{\delta\tilde{B}}\right) \quad \text{for} \;\; \delta\tilde{B} \geq \tilde{F}_c^{p,s}\,. \tag{5.34}$$

After time $\Delta\tilde{t}_0$, the tip of the skyrmion line starts to depin and follow the magnetic field (this part of the period is denoted as M) until the strength of the field reaches its maximal value at the point $\tilde{t} = T/2$ and the line is pinned again. Notably, it is the ratio $\frac{\tilde{F}_c^{p,s}}{\delta\tilde{B}}$ that controls which part of the period the line stays pinned.

Until now, we have only discussed the equation for the derivative at the surface. In order to find the solution for the whole line, we need to consider the first equation in Eq. (5.31).

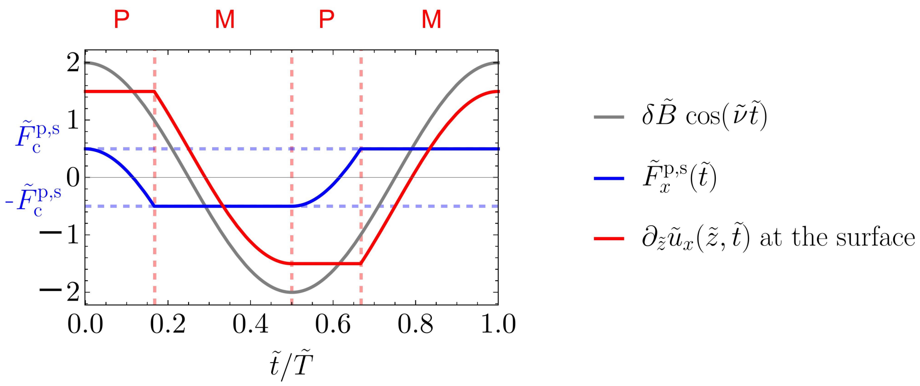

Figure 34: Schematic picture of the driving field, $\delta\tilde{B}\cos(\tilde{\nu}\tilde{t})$, time-dependent surface pinning $\tilde{F}^{p,s}(\tilde{t})$ (the maximum strength of which is $\tilde{F}_c^{p,s}$) and derivative of the displacement function $\partial_{\tilde{z}}\tilde{\boldsymbol{u}}$ at the surface ($\tilde{z} = \frac{1}{2}$) for the rescaled surface pinning $\tilde{F}_c^{p,s} = 0.5$ and the amplitude of the field $\delta\tilde{B} = 2$. At $t = 0$, when the amplitude of the field is the strongest, the surface pinning force exactly compensates the driving field, and the line is pinned (P). When the maximal value of the surface pinning force is reached, the line starts to move (M) until it is pinned again (P) at the extremum of the driving field.

The right-hand side of this equation, $\frac{\boldsymbol{F}^{p,b}(\tilde{t})}{F_c^{p,b}}$, can only have two values 1 or -1 depending on the direction of the movement. If the driving field strength is slightly larger than the critical value $\delta\tilde{B}_{c,1}$, at first, only a finite fraction of the line up to a point $\tilde{z}_0 \in (0, \frac{1}{2})$ (which depends on the strength of the driving field $\delta\tilde{B}$), becomes depinned, while the rest of the line remains pinned towards the static field B_z. The solution for the depinned part of the line at the point of largest deviation (at $\tilde{t} = 0$) must obey $\partial_{\tilde{z}}^2\tilde{u}_x(\tilde{z},\tilde{t}) = 1$ (or -1 at the point of largest deviation in the other direction). Therefore, the solution in this case is

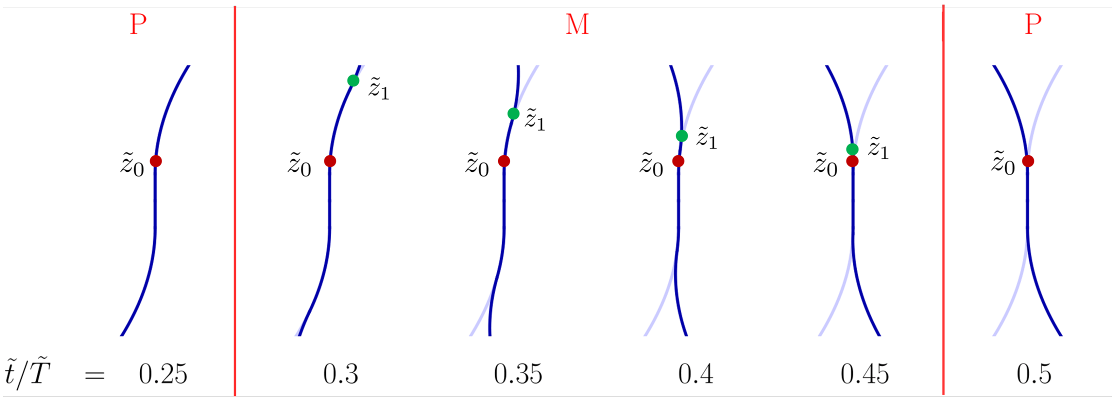

Figure 35: Stroboscopic pictures of the movement of the line over one-fourth of the period with a time step $\Delta\tilde{t} = 0.05$ for the rescaled surface pinning $\tilde{F}_c^{p,s} = 0.5$ and the amplitude of the field $\delta\tilde{B} = 0.9$ (in the central pinned phase). When the amplitude of the external field is the strongest, the central piece of line with $|\tilde{z}| \leq \tilde{z}_0$ is pinned. During the period of oscillation, the line is pinned up to the point $|\tilde{z}| \leq \tilde{z}_1(t)$.

simply given by the quadratic function

$$\tilde{u}_x(\tilde{z},\tilde{t}) = \frac{1}{2}\left(\tilde{z}-\tilde{z}_0\right)^2 . \tag{5.35}$$

The position of the point $\tilde{z}_0$ can be found by matching the derivative at the surface

$$\tilde{z}_0 = \frac{1}{2} + \tilde{F}^{p,s} - \delta\tilde{B} \tag{5.36}$$

and depends on the relative strength of surface pinning and driving fields.

In order to find a solution for the rest of the period, we notice again that the depinning beginns from the end of the line. The line becomes depinned up to a point $\tilde{z}_0 \leq \tilde{z}_1(\tilde{t}) \leq \frac{1}{2}$, which itself depends on the time (see Fig. 35). We separate the solution into two parts,

$$\tilde{u}_x(\tilde{z},\tilde{t}) = \begin{cases} \tilde{u}^{>}(\tilde{z},\tilde{t}) & \text{for } z \geq z_1 \\ \tilde{u}^{<}(\tilde{z},\tilde{t}) & \text{for } 0 \leq z < z_1 \,. \end{cases} \tag{5.37}$$

The pinned part $\tilde{u}^{<}(\tilde{z},\tilde{t})$ is given by Eq. (5.35). From the continuity of the displacement function $u(\tilde{z},\tilde{t})$ and the first derivatives at the point $\tilde{z}_1$ we find conditions

$$\tilde{u}^{>}(\tilde{z}_1,\tilde{t}) = \tilde{u}^{<}(\tilde{z}_1,\tilde{t}) \quad \text{and} \quad \partial_{\tilde{z}}\tilde{u}^{>}(\tilde{z}_1,\tilde{t}) = \partial_{\tilde{z}}\tilde{u}^{<}(\tilde{z}_1,\tilde{t})\,. \tag{5.38}$$

The depinned part should satisfy $\partial_{\tilde{z}}^2\tilde{u}^{>}(\tilde{z},\tilde{t}) = -1$. The general solution of this equation is given by $\tilde{u}^{>}(\tilde{z},\tilde{t}) = -\tilde{z}^2 + a(\tilde{t})\tilde{z} + b(\tilde{t})$. Moreover, we again demand that the equation on the derivative at the surface is satisfied. From these conditions, we find the functions $a(\tilde{t})$ and $b(\tilde{t})$. The resulting stroboscopic pictures of the movement of the line are depicted in Fig. 35b. As a finite fraction of the line stays pinned during the whole period, we call this phase the **central pinned** phase.

The full depinning of the skyrmion line happens after crossing the second critical field $\delta\tilde{B}_{c,2}$ (or tilting angle $\frac{b_{c,2}}{B_z}$ in the unrescaled coordinates). We call this phase **depinned** phase (see the upper panel on Fig. 36c for the corresponding stroboscopic picture of the skyrmion line movement). To find the second critical field, we demand that in the solution above, the parameter $\tilde{z}_0$ becomes zero

$$\delta\tilde{B}_{c,2} = \frac{1}{2} + \tilde{F}_c^{p,s} \implies \frac{b_{c,2}}{B'_z} = \frac{LF_c^{p,b}}{2\epsilon_0} + \frac{F_c^{p,s}}{\epsilon_0}\,. \tag{5.39}$$

Note that the second transition exists even in the absence of the surface pinning. The dimensionless combination $\frac{LF^{p,b}}{2\epsilon_0}$ has the meaning of the angle of the second critical field in the absence of surface pinning and characterises the competition between bulk pinning and elastic energy. Moreover, the following interesting relations hold

$$\frac{1}{2}\frac{B'_z}{\left(b_{c,2}-b_{c,1}\right)} = \tilde{\epsilon}_0 \quad \text{and} \quad \frac{1}{2}\frac{b_{c,1}}{\left(b_{c,2}-b_{c,1}\right)} = \tilde{F}_c^{p,s}\,. \tag{5.40}$$

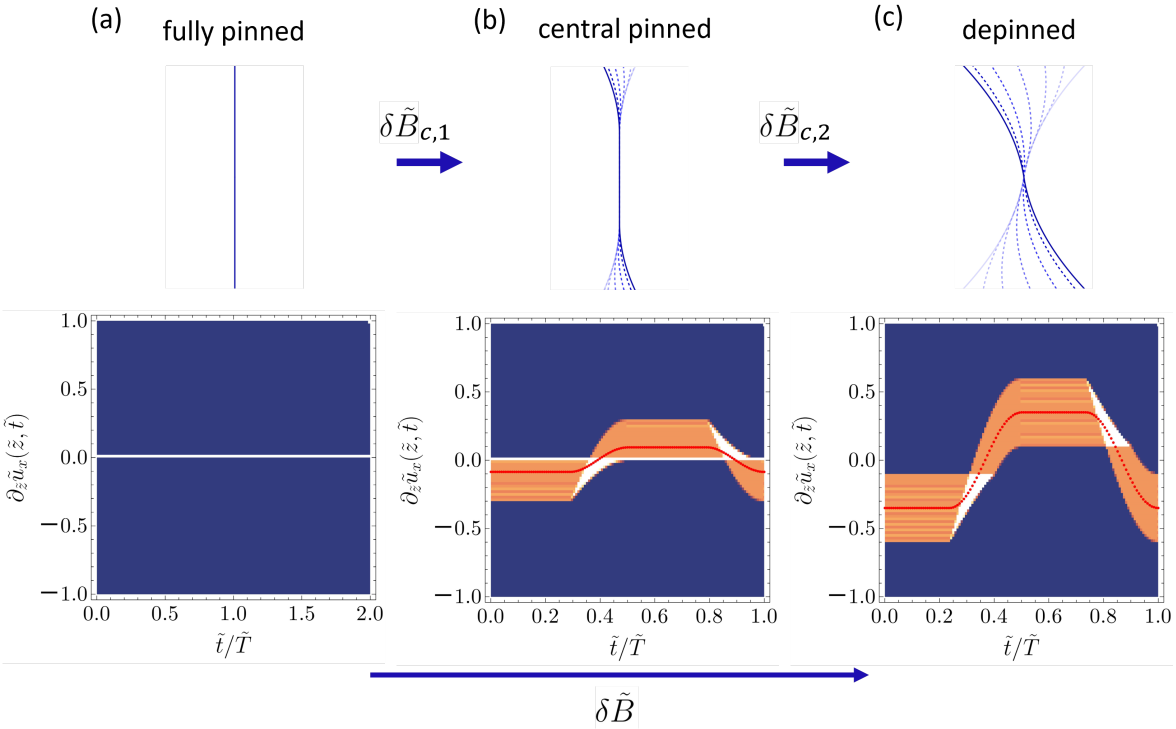

Figure 36: Upper panel: stroboscopic pictures of the skyrmion line movement in three different phases in increasing strength of the driving field $\delta\tilde{B}$. Here (a) is the fully pinned phase, (b) the central pinned phase and (c) the depinned phase. The two critical fields at which these transitions happen are $\delta\tilde{B}_{c,1}$ and $\delta\tilde{B}_{c,2}$. Lower panel: the corresponding rocking angle maps and (in red) the averaged value of the rocking angle at every time step. Parameters used to produce this plot: $\tilde{F}_c^{p,s} = 0.5$, $\Delta\tilde{z} = 0.0025$, $\Delta\tilde{t} = 0.008$ and (a) $\delta\tilde{B} = 0.4$, (b) $\delta\tilde{B} = 0.8$, (c) $\delta\tilde{B} = 1.1$. Note that the time axis was shifted by $\tilde{t}_0 = \frac{T}{2}$ as compared to Fig. 34.

Using these relations and the data on TISANE measurements of two critical fields $b_{c,1}, b_{c,2}$ one can estimate two dimensionless parameters in our model: $\tilde{\epsilon}_0 = \frac{\epsilon_0}{LF^{p,b}}$ and $\tilde{F}^{p,s} = \frac{F^{p,s}}{LF^{p,b}}$, which control the relative strength of elastic energy to bulk pinning and surface to bulk pinning respectively. From these relations we find the universal scaling parameter

$$\delta\tilde{B} - \tilde{F}_c^{p,s} = \frac{1}{2}\frac{b - b_{c,1}}{(b_{c,2} - b_{c,1})}\,. \tag{5.41}$$

After shifting and rescaling the strength of the magnetic field using this formula, we expect the bulk skyrmion-hosting materials to follow a universal behaviour.

Interestingly, a very similar mean-field solution for depinning the elastic vortex line in resonant superconducting radio-frequency cavities was found in Ref. [114]. Normally, the dynamics of skyrmions under applied forces differs from vortices in superconductors because of the much stronger gyrocoupling forces, which have their origins in the topological nature of skyrmions. Because of these forces, the direction of the skyrmion movement is perpendicular to the direction of an applied force. However, in the adiabatic limit the skyrmion line moves in the direction of the applied forces as described by Eq. (5.31). This fact gives rise to the similarity between vortex and skyrmion line movements.

In the next Section, we propose how to determine the critical fields $b_{c,1}, b_{c,2}$ from the experimentally available data on rocking curve measurements.

5.7 Experimental Signatures of Critical Fields

In the previous Section, we presented an analytical solution for the skyrmion line movement and found three dynamical phases in the adiabatic limit: the pinned, central pinned and depinned phase. In this Section, we propose how the critical fields can be tracked with the help of TISANE rocking angle measurements.

The intensity of TISANE rocking curves is proportional to the fraction of the skyrmion lattice, which is aligned with the respective angle. We expect small tilting angles of the skyrmion line because of the tiny oscillating fields $b \ll B_z$. Within our theory, the tilting angle of a line is locally approximated by its partial derivative

$$\omega(z,t) = \arctan(\partial_z \boldsymbol{u}(z,t)) \approx \partial_z \boldsymbol{u}(z,t) = \frac{1}{\tilde{\epsilon}_0} \partial_{\tilde{z}} \tilde{\boldsymbol{u}}(\tilde{z},\tilde{t})\,. \tag{5.42}$$

Using the analytical solution for the displacement function $\tilde{\boldsymbol{u}}(\tilde{z},\tilde{t})$ from the Section above, we calculate numerically the rocking angle maps in every phase. To do so, we numerically compute the partial derivative of the displacement function with respect to $\tilde{z}$ for every

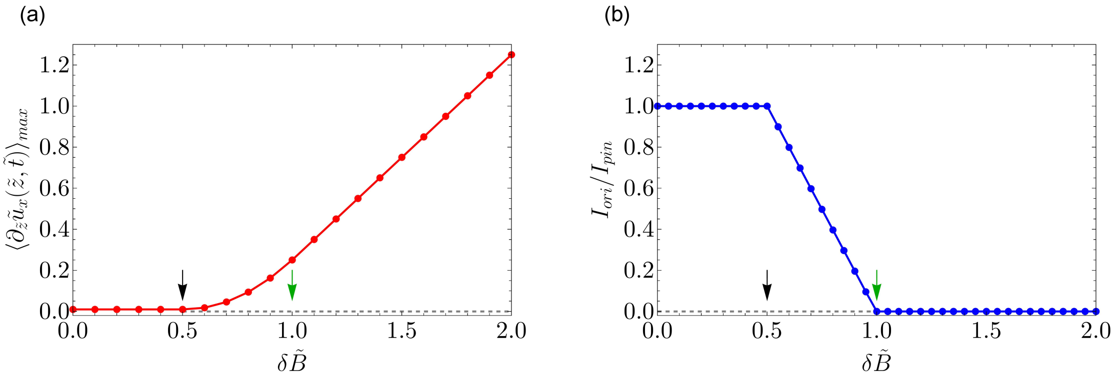

Figure 37: (a) The average angle of the rocking angle $\langle \partial_{\tilde{z}} \tilde{u}_x(\tilde{z},\tilde{t}) \rangle_{\max}$ and the relative intensity at the origin $\frac{I_{ori}}{I_{pin}}$ as functions of the driving field strength $\delta\tilde{B}$. In the pinned phase, the rocking angles are zero, and the intensity at the origin is maximal. The first transition (from pinned to central pinned phase) happens at the critical field strength $\delta\tilde{B}_{c,1} = 0.5$ (denoted by the black arrow). After crossing this value, the average rocking angle grows, and the intensity at the origin drops linearly. At the second transition from the central pinned to the depinned phase at $\delta\tilde{B}_{c,2} = 1$ (denoted by the green arrow), the intensity at the origin drops to zero. Here we used $\tilde{F}_c^{p,s} = 0.5$, $\Delta\tilde{z} = 0.0025$, $\Delta\tilde{t} = 0.008$.

$\tilde{t}_0 \in [0, T]$ (with the step Δt) and $\tilde{z}_0 \in \left[-\frac{1}{2}, \frac{1}{2}\right]$ (with the step $\Delta\tilde{z}$) using the finite-difference method

$$\partial_{\tilde{z}}\tilde{u}_x(\tilde{z}_0, \tilde{t}_0) \approx \frac{\tilde{u}_x\left(\tilde{z}_0 + \frac{\Delta\tilde{z}}{2}, \tilde{t}_0\right) - \tilde{u}_x\left(\tilde{z}_0 - \frac{\Delta\tilde{z}}{2}, \tilde{t}_0\right)}{\Delta\tilde{z}}\,. \tag{5.43}$$

Further, we calculate the number of elements of data whose values lie in successive bins $[\partial_{\tilde{z}}\tilde{u}_x - \frac{\Delta\partial_{\tilde{z}}\tilde{u}_x}{2}, \partial_{\tilde{z}}\tilde{u}_x + \frac{\Delta\partial_{\tilde{z}}\tilde{u}_x}{2}]$. The resulting data is being presented for all three phases in the form of the heat map, see Fig. 36, lower panel. For the remainder of this Thesis we call these maps “rocking angle maps”.

In the pinned phase, $\partial_{\tilde{z}}\tilde{u}_x(\tilde{z}, \tilde{t}) = 0$ at any point of the line, leading to the straight line at the corresponding rocking angle map. In the central pinned phase, a fraction of the line is depinned. However, during the whole period the finite fraction of the line remains pinned, resulting in the non-zero values at $\partial_{\tilde{z}}\tilde{u}_x(\tilde{z}, \tilde{t}) = 0$. In the depinned phase on the contrary, it hold that during the whole period $\partial_{\tilde{z}}\tilde{u}_x(\tilde{z}, \tilde{t}) \neq 0$. Moreover, the fraction of the period when the line is stuck (the flat part of the curve) becomes smaller at increasing values of the driving field.

We propose two quantities with the help of which we track the two transitions, from pinned to the central pinned and from the central pinned to depinned phase, experimentally. First, we consider the weighted average of the derivative $\partial_{\tilde{z}}\tilde{u}_x(\tilde{z}, \tilde{t})$ at every point of time during the oscillation period $\langle\partial_{\tilde{z}}\tilde{u}_x\rangle$ (red lines in Fig. 36). The quantity of interest then is $\langle\partial_{\tilde{z}}\tilde{u}_x\rangle_{\max}$, the largest weighted average value of the derivative over the period (reached at the point, when the line has the largest deviation). This quantity is equal to zero if the strength of the driving field is lower than $\delta\tilde{B}_{c,1}$, denoted by the black arrow on Fig. 37a. Above this value, the skyrmion line is in the central pinned regime and this quantity starts to grow. As such, it provides a great tool to track the first transition. After reaching the second critical value $\delta\tilde{B}_{c,2}$ (marked with the green arrow), the growth is approximately linear (in the limit of the strong driving field, the line follows the shaking field). For large values of driving field $\delta\tilde{B} \gg \tilde{F}_c^{p,s}$, the solution is an approximately straight line, as can be

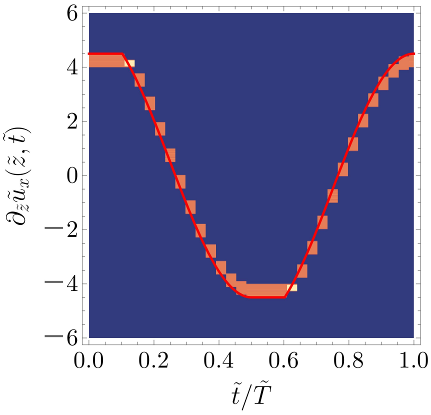

Figure 38: Rocking angle map and (in red) the weighted averaged value of the rocking angle for large value of driving field $\delta\tilde{B} \gg \tilde{F}_c^{p,s}$ at every time step. Parameters used to produce this plot: $\tilde{F}_c^{p,s} = 0.5$, $\Delta\tilde{z} = 0.0025$, $\Delta\tilde{t} = 0.008$, $\delta\tilde{B} = 5$.

seen from the rocking angle map in Fig. 38. Mathematically, this is the case because the first derivative grows linearly with increasing the driving field $\partial_{\tilde{z}}\tilde{u}_x(\tilde{z},\tilde{t}) \approx \delta\tilde{B}\cos(\tilde{\nu t})$ (see the boundary condition in Eq. (5.31)), while the absolute value of the second derivative $|\partial^2_{\tilde{z}}\tilde{u}_x(\tilde{z},\tilde{t})| = 1$ stays constant. Therefore, the derivative is almost constant along the line and is proportional to the **amplitude of the skyrmion line motion**. Importantly, even at strong values of the driving field, the line is stuck for a finite time during each period (flat region of the curve at Fig. 38). We will discuss the consequences of this fact in the next Chapter.

The second quantity of interest is the **intensity at the origin** (relative to the maximum intensity at the pinned phase), $\frac{I_{ori}}{I_{pin}}$. Within the theoretical description, this quantity is equal to 1 in the pinned phase. We predict that it has a drop at $\delta\tilde{B}_{c,1}$ (denoted again with the black arrow) and then linearly decreases until $\delta\tilde{B}_{c,2}$ (denoted with the green arrow), at the transition from the central pinned to the depinned phase. This linear dependence can be easily explained with the help of Eq. (5.36).

In the next Section, we find both transition fields $b_{c,1}, b_{c,2}$ from the TISANE measurements in MnSi, as well as the fitting parameters of our theory $\tilde{\epsilon}_0$ and $\tilde{F}^{s,p}$.

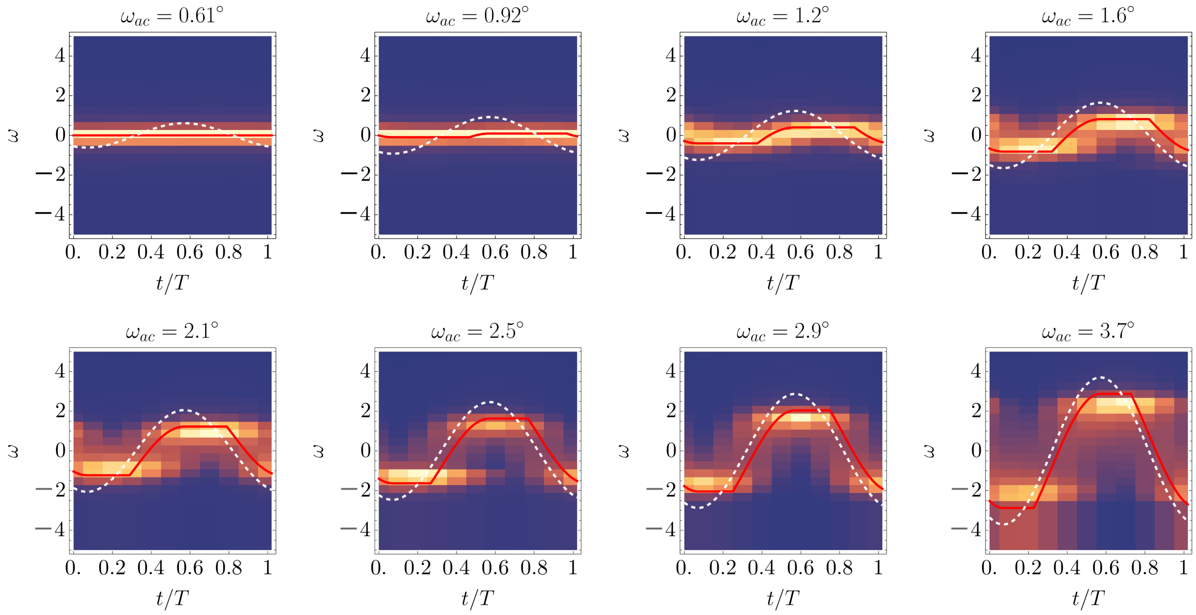

Figure 39: Time-resolved rocking angle maps at selected values of angles of the tilted driving field ω_{ac} as found from TISANE measurements on MnSi. The dashed line is the time-dependent angle of the magnetic field at the corresponding time step, and the red line is the theoretically calculated derivative at the surface $\partial_{\tilde{z}}\tilde{u}(\tilde{z},\tilde{t})$. For the white dashed and red lines, parameters are: shift in time $\Delta\phi = 0.57$ and $\tilde{F}^{p,s}_c/\tilde{\epsilon}_0{=}0.8^{\circ} \approx 0.0014$.

5.8 Tracking Dynamic Phase Transitions with TISANE

Excitingly, the two phase transitions described in the previous Sections can be tracked from the experimentally available data on TISANE (see Sec. 4.2 and Ref. [106] for more details on this technique). This data was measured by Dr. D. Mettus in the group of Prof. C. Pfleiderer.

The data on time-resolved rocking curves for MnSi at $B_z = 170$ mT, $T = 28$ K and frequency of 404 Hz for a few selected tilting fields is presented in Fig. 39 (note that angles are given in degrees $\omega_{\rm ac} = \frac{b}{B_z'}\frac{180}{\pi}^{\circ}$). We subtracted the angle $\omega_0 = -1.275°$, at which the skyrmion lattice is directed in the absence of driving field from all measurements (see Sec. 4.2). We observe that the angle of the skyrmion lattice tilting is always smaller than the angle of the driving field $\omega_{\rm ac}$ for the measured range. Moreover, at small driving field amplitudes, all intensity is concentrated at the origin and the rocking curves do not change with the increasing driving field strengths, meaning that the skyrmion lattice is pinned. The rocking peaks start moving just above the tiny tilting angle $\omega_{\rm ac}^{c,1} \approx 1°$. For example, for $\omega_{\rm ac}^{c,1} = 1.2°$, a finite intensity is still concentrated at the origin, meaning that a finite fraction of the skyrmion lattice is still pinned, while the finite intensity away from the origin signifies that a fraction of the lattice is depinned. At even higher values of the driving field, the whole lattice is depinned during the entire period of oscillation. Finally, at high applied magnetic fields, the rocking peak splits into two peaks (motion of skyrmion lattice develops bimodal character), see the rocking scans for $\omega_{\rm ac} = 2.46°$ in Fig. 40a. In TISANE, the changes over time are partially smeared out due to the finite chopper opening time. It turns out that this smearing in time is enough to explain the bimodal distribution in the observed rocking scans and they are considered to be an instrumental artifact (see the next Section and Ref. [106] for more details). Moreover, we observe that flat regions exist for all measured driving fields, meaning that the skyrmion lattice is stuck for a finite time during each oscillation period.

The exact phase of the magnetic field (corresponding to the time shift on the t/T axis) is unknown. We find a fit, both for the shift in time $\Delta\phi = 0.57$ and the rescaled parameter $\tilde{F}_c^{p,s}/\tilde{\epsilon}_0 = 0.8^{\circ}$ from our model. In Fig. 39, the white dotted line denotes the resulting angle of the applied magnetic field over one oscillation period, while the red line is the theoretically calculated derivative at the surface $\partial_{\tilde{z}}\tilde{u}(\tilde{z},\tilde{t})$ (note that it is governed by a single parameter $\tilde{F}_c^{p,s}/\tilde{\epsilon}_0$). Although we can already capture some trends such as flat parts of the distribution and an increase in the amplitude, it is clear that skyrmion lines are not straight in the experiment but rather have a more complicated spatial distribution.

In order to explain this data further, we use our theoretical model which includes two phase transitions, introduced in the previous Sections. We find the rocking peak position and intensity at the centre of motion from the measured rocking curves. The rocking peak position is the angle corresponding to the point of maximum intensity of the rocking curve at every time step (denoted by arrows at the Fig. 40a for the data set at $\omega_{\rm ac} = 2.46°$). It measures the angle at which the largest fraction of the skyrmion lattice is directed at a given time step. Further, we define the **amplitude of motion**, ω_{SL}, as the maximum rocking peak position angle over time. This quantity is presented in red as a function of ω_{ac} on Fig. 40b. The onset of ω_{SL} indicates the first transition, as discussed in the previous Section. For the experimental data, we define the first critical field $\omega_{\mathrm{ac}}^{c,1}$ as the first data point, where the value of ω_{SL} is larger than the experimental error. For MnSi, we find $\omega_{\mathrm{ac}}^{c,1} = 0.83°$, which corresponds to $b_{c,1} = 2.45$ mT. We recall that until the skyrmion line is pinned due to the surface pinning until reaching the first critical field with the corresponding angle $\omega_{\mathrm{ac}}^{c,1}$. After crossing this threshold value the motion starts at the surface, while the skyrmion string stays pinned at its centre (pinned to the central pinned transition). At larger values of the driving field, ω_{SL} grows approximately linearly, as predicted by the theory. Interestingly, from the experimental data, one can see that the slope of the curve is less than unity even far from the transition (compared it to the slope of the dashed red line $\omega_{\mathrm{SL}} = \omega_{\mathrm{ac}}$, which serves as a guide to the eye).

In order to track the second transition (from central pinned to depinned phase), we first find I_{ori}, the **intensity at the origin** (at the point when $\omega = \omega_0$) for every time step (see Fig. 40a). This quantity measures the phase volume of skyrmions aligned towards the static field B_z. We are, however, interested in the value of the minimal intensity I_{ori}

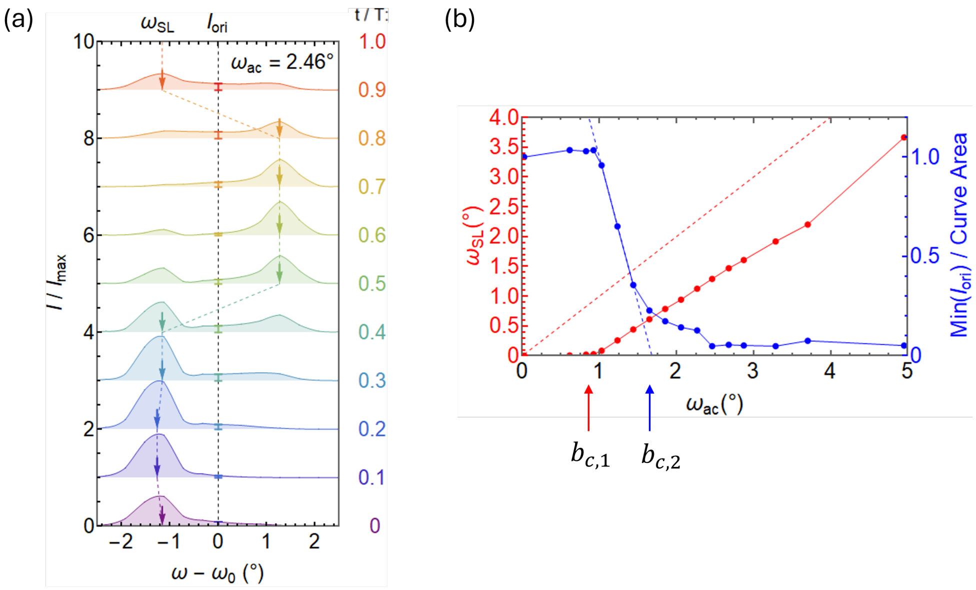

Figure 40: (a) Rocking scans for $\omega_{\mathrm{ac}} = 2.46°$ over the oscillation period T as function of the angle ω. For every time step, we find the angle ω_{SL} in which the largest fraction of the skyrmion lattice is directed. Moreover, from the intensity at $\omega = \omega_0$, we find the fraction of the line directed towards the applied static field I_{ori}. (b) For every ω_{SL}, we plot the maximum angle ω_{SL} and the minimal value of the intensity at the origin I_{ori} (normalised by the corresponding curve area) over the oscillation period. Two critical fields, at which the transition from the pinned to central pinned to depinned phase happens, are denoted as B_{c1} and B_{c2}, respectively.

over the period, denoted as Min(I_{ori}). The minimal value of the intensity over the period Min(I_{ori}) gives the volume fraction of the skyrmion lattice, which remains pinned towards B_z during the whole period of driving field oscillation, therefore presenting a perfect tool to determine the second phase transition. The found value of Min(I_{ori}) at every angle of the tilting field ω_{ac} is normalised by the total area under the rocking curve in order to compensate for the loss of the skyrmion phase volume at higher values of tilting angles. The observed dependence of this quantity on the tilting angle ω_{ac} is depicted in blue in Fig. 40b. It starts to decrease after reaching the first transition at $\omega = \omega_{\text{ac}}^{c,1}$ and decreases towards larger values of magnetic fields. In theory, however, its dependence on the magnetic field is predicted to be a straight line and after the second transition at $\omega = \omega_{\text{ac}}^{c,2}$ it shall drop to zero (compare to Fig. 37b). However, as one can see in the data, the drop of Min(I_{ori}) is not linear but instead shows a prolonged tail towards larger values of the tilting fields. In order to capture the critical value of the second transition, we make a linear fit to the curve region with the steepest slope directly after the transition $\omega_{\text{ac}}^{c,1}$, as depicted by the blue dotted line. After that we extrapolate this line to cross with the x axis (point of zero intensity). We propose to find the second transition from the corresponding value of the tilting field, which gives $\omega_{\text{ac}}^{c,2} = 1.7°$ ($b_{c,2} = 5$ mT) for MnSi. The reasons for finding $\omega_{\text{ac}}^{c,2}$ using this scheme are explained in the next Section.

The tail in Min(I_{ori}) for higher angles of the driving field in experimental data can be caused by several effects. In the next Section we discuss how the distribution of skyrmion line lengths and time binding effects might explain the deviation of experimental data from the theory prediction.

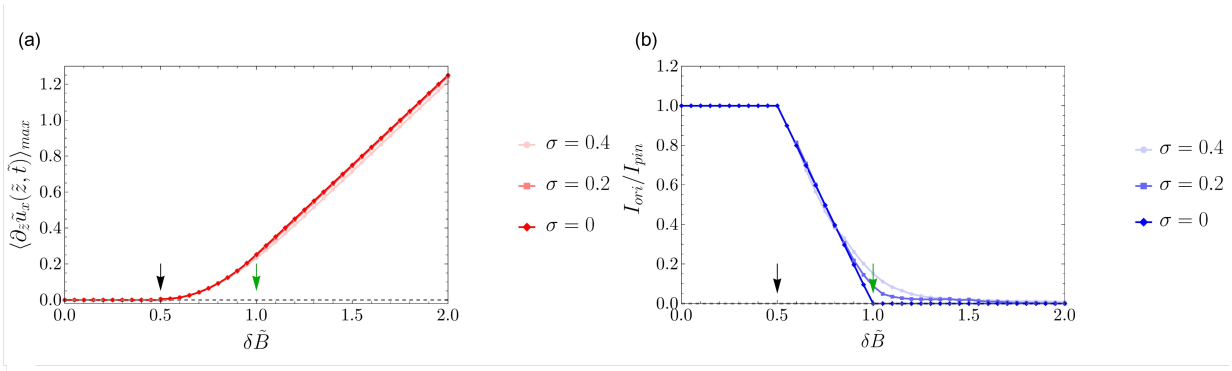

Figure 41: (a) The weighted average angle of the rocking angle $\langle \partial_{\tilde{z}} \tilde{u}_x(\tilde{z},\tilde{t}) \rangle_{\max}$ and (b) the relative intensity at the origin $\frac{I_{\text{ori}}}{I_{\text{pin}}}$ as functions of the driving field strength $\delta\tilde{B}$ for a few values of σ. Parameters used $\tilde{F}_c^{p,s} = 0.5$, $\Delta\tilde{z} = 0.0025$, $\Delta\tilde{t} = 0.008$.

5.9 Effects of Time Binning and Domain Length Distribution

In our theory of skyrmion lattices in tilting fields discussed in this Chapter, we made a number of approximations. One of the approximations was that all skyrmion lines (which describe the deviation of every line in the skyrmion lattice) have the same length L. This approximation corresponds to having a single domain in the material. However, we do not know if this condition is satisfied in the experiments. Therefore, we make a rough estimation here on the effect of domain length distribution on the two phase transitions.

To do so, we take the lengths of the lines to be Gaussian distributed with parameters μ and σ: $\mathcal{N}(\mu, \sigma^2)$. Further, the measured intensity of the signal at a given angle will be proportional to the product of the probability density function of the skyrmion line having certain length times the number of bins in the interval $\left[\partial_{\tilde{z}}\tilde{u}_x - \frac{\Delta\partial_{\tilde{z}}\tilde{u}_x}{2}, \partial_{\tilde{z}}\tilde{u}_x + \frac{\Delta\partial_{\tilde{z}}\tilde{u}_x}{2}\right]$. From this data, we calculate again the weighted average angle of the rocking angle $\langle\partial_{\tilde{z}}\tilde{u}_x(\tilde{z}, \tilde{t})\rangle_{\max}$ and the relative intensity at the origin $\frac{I_{\mathrm{ori}}}{I_{\mathrm{pin}}}$ as functions of the driving field strength $\delta\tilde{B}$ for a few values of σ. This data is depicted in Fig. 41. We observe almost no change in $\langle\partial_{\tilde{z}}\tilde{u}_x(\tilde{z}, \tilde{t})\rangle_{\max}$. However, a prominent difference is present in $\frac{I_{\mathrm{ori}}}{I_{\mathrm{pin}}}$. Similar to experiments, we see a broadening around the second critical field (denoted with the green arrow). At values just after the first critical field (denoted with the black arrow), almost no change is observed. Therefore, we propose to find the value of the second phase transition from fitting the values after the transition with a linear fit and extrapolating these curves to the x axis, as was done in the Section above.

Moreover, because of the details of the experiment, the curve for $\mathrm{Min}(I_{\mathrm{ori}})$ will be even more smeared out. We recall that although in reality the movement of the peak centre during the experiment is continuous, the measured intensity is sorted into ten time bins (see Sec. 4.2). Every single of these time bins contains a time-integrated intensity over one-tenth part of the period of oscillation. We call this effect **time smearing**. Experimentally, the time smearing originates from the finite chopper pulse width Δt_c. The parameter D_c, which is called a chopper duty cycle, characterises the ratio of chopper pulse width to the repetition time of chopper T_c

$$D_c = \frac{\Delta t_c}{T_c} \ , \tag{5.44}$$

see Fig. 24 for a graphical representation. The value of the parameter D_c in the TISANE experiment, presented in this Thesis, is $D_c = 0.352$. The effect on TISANE rocking intensities (modelled as Gaussian curves that follow a sinusoidal driving field) due to binning for different values of D_c was simulated in Ref. [106] and is depicted in Fig. 42. As can be seen from this Figure, a broadening of rocking curves occurs for higher values of D_c. Moreover, for $D_c = 0.35$ a bimodal distribution is observed. Intuitively, one can understand this artifact from Fig. 43a. A normalised sum of Gaussian intensity profiles originating at different times within the pulse results in the black line, which will be measured in the TISANE experiment. For more details of this effect, see Ref. [106].

Although the effects of time smearing were simulated for Gaussian curves that follow a sinusoidal driving field in the paper above, we believe that it has a similar influence on the movement of the line with pinning. Therefore, the bimodal distribution, observed in Fig. 40 is considered to be an experimental artifact. Moreover, we include the effects of time smearing in our model and produce corresponding plots of the amplitude of motion ω_{SL} and intensity at the origin, I_{ori}. These are depicted in Fig. 44. This data was produced by Dr. D. Mettus and is currently prepared for publication in joint work (Ref. [109]). As one can see, although the parameter D_c has almost no influence on the amplitude of the motion ω_{SL}, the intensity at the origin, $\mathrm{Min}(I_{\mathrm{ori}})$, is strongly affected. This quantity does not reach zero even for large values of the applied driving field. Moreover, we observe the angle of the curve directly after the first transition is affected.

Time smearing and domain length distribution considerably influence intensity at the origin $\mathrm{Min}(I_{\mathrm{ori}})$. Therefore, we conclude that we can successfully explain the discrepancies between the experimental data on TISANE and our theoretical model. In the next Section, we compare the unpinning processes across different materials.

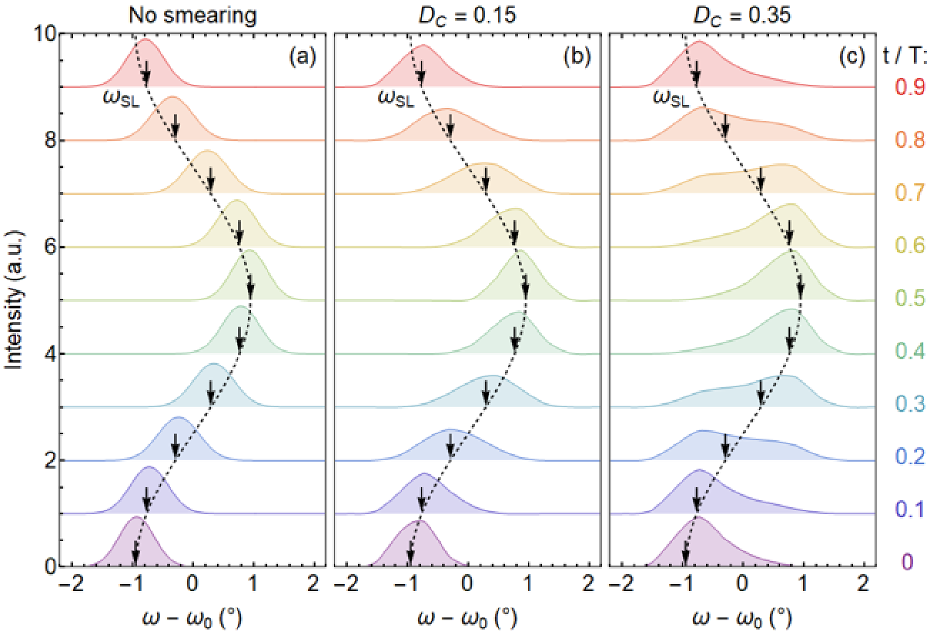

Figure 42: Simulated TISANE rocking intensities (Gaussian curves that follow a sinusoidal driving field) due to binning for different duty cycles (a) $D_c = 0$, (b) $D_c = 0.15$ and (c) $D_c = 0.15$. The effect of time smearing becomes prominent for high values of the duty cycle. Picture credit from Ref. [106]

.

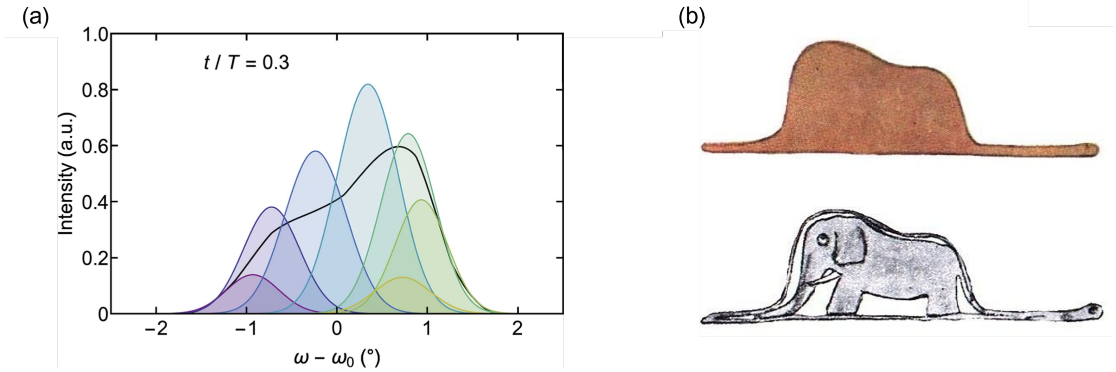

Figure 43: (a) Sum of Gaussian intensity profiles that originate at different times for one time frame at $t/T = 0.3$. Picture credit from [106]. (b) The shape of the observed rocking curve (black line) is not what we thought it was. “My drawing was not a picture of a hat. It was a picture of a boa constrictor digesting an elephant. Then, I drew the inside of the boa constrictor so that the grownups could see it clearly. They always need to have things explained.” Taken from "The Little Prince" by Antoine de Saint Exupéry. Picture credit from Ref. [115].

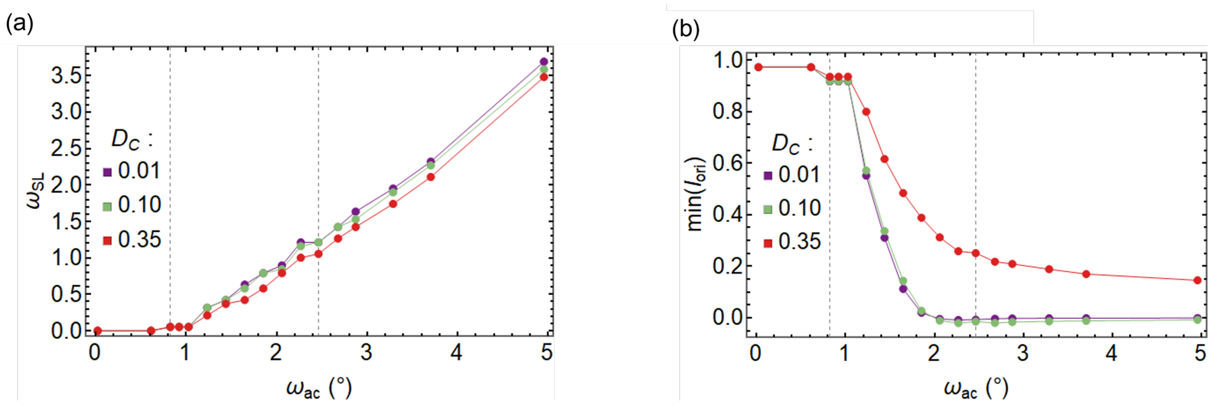

Figure 44: Effects of the time bining (controlled by the parameter D_c) on the simulated amplitude of motion ω_{SL} and intensity at the origin $\mathrm{Min}(I_{\mathrm{ori}})$. Produced by Dr. D. Mettus.

5.10 Universality of Depinning Transitions in Different Materials

Apart from the conductor MnSi, the unpinning transition was tracked in the doped systems $Mn_{1-x}Fe_xSi$ (with $x = 0.02, 0.04$ and 0.06) and in the insulator Cu_2OSeO_3. For Cu_2OSeO_3, a high-temperature skyrmion phase was probed. Every material was brought into the skyrmion lattice phase by applying a corresponding static magnetic field B_z and temperature T. The observed values of the amplitude of motion, ω_{SL} and the minimal intensity at the origin over the period, $\mathrm{Min}(I_{\mathrm{ori}})$, normalised by the curve area, can be found in the upper panel of Fig. 45 (different colours indicate different materials). From ω_{SL} one can see directly that larger tilted magnetic field amplitudes ($\omega_{\mathrm{ac}}^{c,1} \approx 3°$ for doped systems $Mn_{1-x}Fe_xSi$ and $\omega_{\mathrm{ac}}^{c,1} \approx 8°$ for Cu_2OSeO_3) are needed to depin the skyrmion lattice. These larger threshold amplitudes indicate stronger surface pinning forces. For doped systems one possible explanation is that Fe atoms act as pinning centres. However, the dependence on the doping concentration x is rather unintuitive, as shown in Fig. 59 in the next Chapter.

Moreover, when one compares two measurements of the same sample $Mn_{98}Fe_{02}Si$ but different oscillation frequencies (403 Hz and 377 Hz), one can see that the depinning field for these samples is slightly different. This signifies that the depinning might depend not only on material properties but also on the frequency of the applied driving field. However, the data was recorded only for two different frequencies. Therefore, further experimental

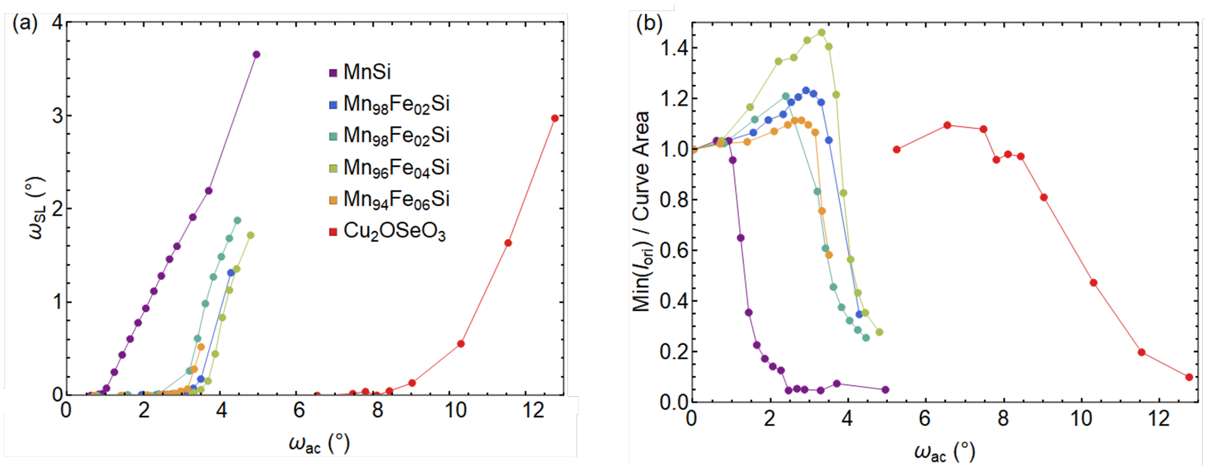

Figure 45: Comparison of unpinning transitions in different materials. (a) The amplitude of the rocking peak motion ω_{SL} and (b) intensity as the origin as a function of the angle of the tilted field ω_{ac}. MnSi was measured at driving field frequency 404 Hz, static magnetic field $B_z = 170$ mT and temperature $T = 28$ K, the blue line is $Mn_{0.98}Fe_{0.02}Si$ with 404 Hz, $B_z = 180$ mT, $T = 20.5$ K, the green line is $Mn_{0.98}Fe_{0.02}Si$ at 377 Hz, $B_z = 180$ mT, $T = 20.5$ K, $Mn_{0.96}Fe_{0.04}Si$ at 404 Hz, $B_z = 190$ mT, $T = 14$ K, $Mn_{0.94}Fe_{0.06}Si$ at 404 Hz, $B_z = 200$ mT, $T = 9$ K, Cu_2OSeO_3 at 409 Hz, $B_z = 200$ mT, $T = 9$ K, $B_z = 17$ mT, $T = 57$ K.

studies are needed. Note that this effect is not captured within our mean-field theory: if the maximal strength of the force from the magnetic field at the ends of the line is less than the critical value, proportional to the surface pinning, the line will stay pinned.

Interestingly, the minimal intensity at the origin $\mathrm{Min}(I_{\mathrm{ori}})$ increases before and just after the first transition at $\omega = \omega_{\mathrm{ac}}^{c,1}$ for all samples, but is especially strong for the doped samples. This implies that the skyrmion lattice volume fraction towards the direction of the static field increases with the application of an oscillating field. This effect also cannot be captured within our mean-field theory. Arguably, it can be explained with the help of the following considerations. Because of the pinning, skyrmion lines are trapped in the metastable state. Doped samples generally exhibit a more complicated energy landscape with many local minima. During the motion under the oscillating field, skyrmion lines move through many disorder configurations. Effectively this corresponds to averaging over the disorder. Therefore, applying a driving field helps the skyrmion lattice to order even faster at or around the first transition.

The measured strength of the driving field for most samples is, unfortunately, less or just above the critical value for the second transition $\omega_{\mathrm{ac}}^{c,2}$. Therefore, we cannot comment on the effects of time binning and domain length distribution for other materials.

From the measurements of two critical fields, we can finally find the two dimensionless parameters which control our theory in the adiabatic limit, namely $\tilde{\epsilon}_0$ and $\tilde{F}_c^{p,s}$ using Eq. 5.40. This data is plotted in Fig. 46a and Fig. 46b, respectively. Remarkably, one can see that the parameter $\tilde{\epsilon}_0$, which measures the relative strength of the pinning length $L_p = \frac{\epsilon_0}{F^{p,b}}$ to the length of skyrmion lines L, turns out to be much larger than unity for all materials, $\tilde{\epsilon}_0 \gg 1$. Because of this, tiny transverse magnetic fields suffice to depin the skyrmion lattice. Moreover, we observe that the value of $\tilde{\epsilon}_0$ is an order of magnitude

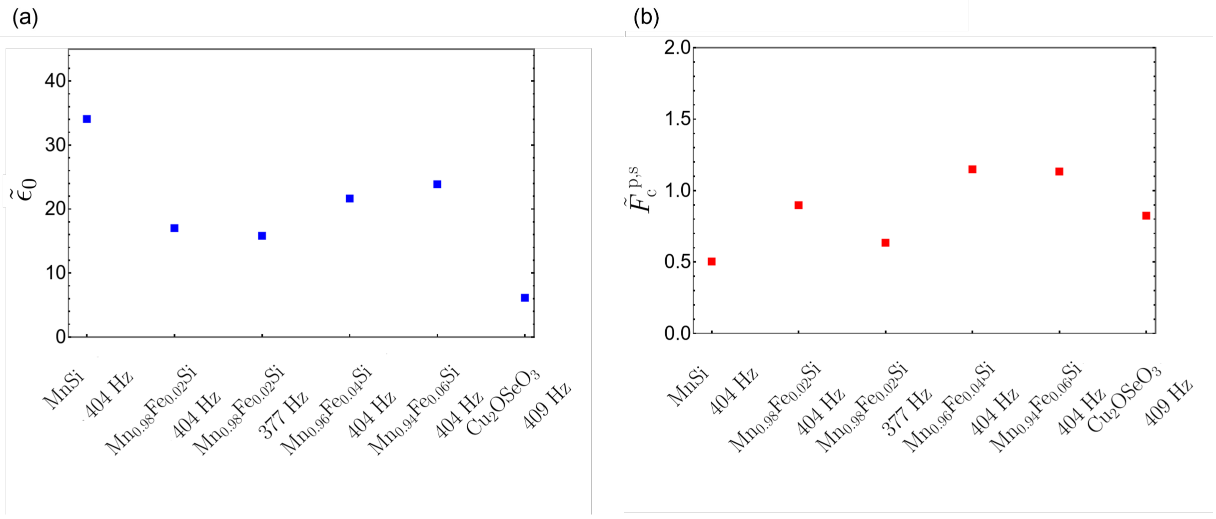

Figure 46: Fit of two parameters, (a) $\tilde{\epsilon}_0$ and (b) $\tilde{F}_c^{p,s}$, which control our theory. These parameters have been found from the critical fields $b_{c,1}$ and $b_{c,2}$ for the respective materials using the fitting scheme described in the previous Sections.

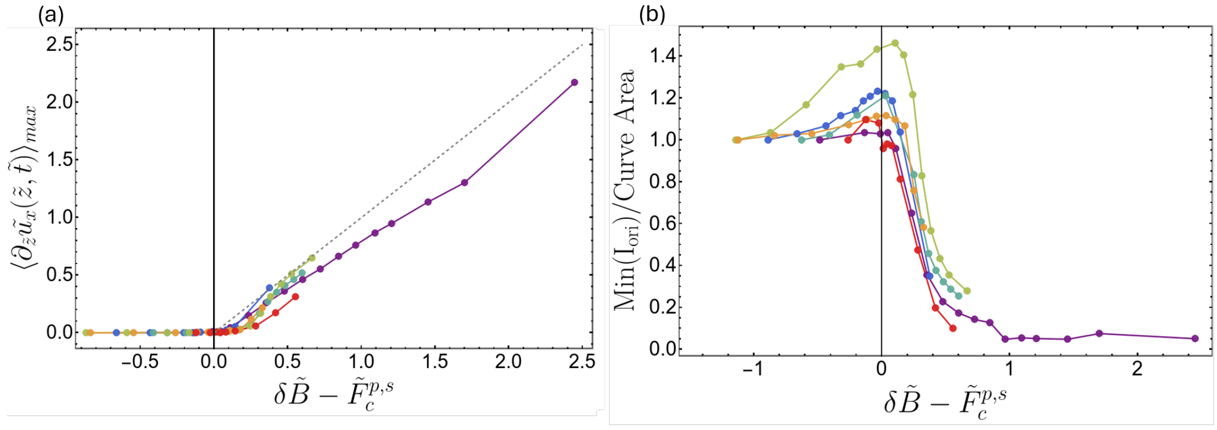

Figure 47: Universal behaviour of unpinning transitions in different materials using the rescaling procedure from our theory (see the text). The colour code and experimental parameters are the same as in the Figure above.

different for MnSi and Cu_2OSeO_3. At the same time, the ratio of surface pinning to bulk pinning, $\tilde{F}_c^{p,s}$, is of order one for all materials. More precisely, we obtain $\tilde{F}_c^{p,s} \approx 0.5$ for MnSi and $\tilde{F}_c^{p,s} \approx 0.85$ for Cu_2OSeO_3. We conclude that including surface pinning is crucial to capture the observed unpinning processes in the tilting field correctly.

Further, using Eq. 5.41 for the rescaling of the magnetic field and Eq. 5.42 for the rescaling of the rocking angle ω, we plot the data for unpinning transitions in different materials in the rescaled coordinated in Fig. 47. We observe that the unpinning transition has a universal character for these materials, as predicted by our theory.

Summary and Outlook

In this Chapter, we developed a Thiele-like description for the unpinning of skyrmion lattices with slow oscillating magnetic fields in bulk chiral magnets. We consider the collective response of the lattice, where we concentrate on a single skyrmion line, which encodes the distortion of every skyrmion line within the lattice. Contrary to what one might intuitively expect, we find that a magnetic field only enters at the ends of the line. We use a simple yet effective phenomenological slip-stick model for pinning, where we treat bulk and surface pinnings separately. In the limit of very slow drives (adiabatic limit), we find an exact solution for the movement of the line and three dynamic phases in the increasing tilting field: fully pinned, central pinned, and depinned. Our theory in this adiabatic limit is controlled by two dimensionless parameters: the relative strengths of surface to bulk pinnings and elastic to bulk pinnings (equivalently, the ratio of the typical pinning length to the length of the line). We explained the main features observed in the TISANE data for MnSi and identified the critical fields for both transitions.

Moreover, we compare the unpinning processes in different materials, namely doped samples $Fe_{1-x}Co_xSi$ for $x = 0, 0.02, 0.04, 0.06$ and the insulator Cu_2OSeO_3 and observe a high degree of universality across these samples. From the critical fields, we find that the ratio of surface to bulk pinnings is roughly of order one for all measured materials, while the ratio of the typical pinning length to the length of the line varies across the materials. Because of the very weak pinning of the skyrmion lattice, already tiny tilting fields are enough to depin the skyrmion lattice as measured in the experiment.

Although our theory successfully captured the main experimental phenomena, it has several limitations. First of all, it is a mean-field result and does not describe critical properties close to the depinning transition. We describe a single domain while, in reality, skyrmion hosting materials may contain several domains with possibly different lengths of skyrmion lines. Therefore, the measured data contains, in fact, an average of signals from domains of various lengths, which affects both the resonance frequency and the depinning field. Furthermore, our theory does not describe the possible fragmentation of the domains under oscillating fields. Our elastic theory is written only to the lowest order of the gradient expansion and does not correctly capture elastic constants for compression, tilt, and shear of the skyrmion lattice.

Despite these limitations, the simple yet effective universal model, which we have developed for the skyrmion lattice depinning and motion under shaking fields, correctly captures the main observed phenomena from TISANE measurements.

6 | Slow and Fast Shaking

> "An expert is a person who has found out by his own painful experience all the mistakes that one can make in a very narrow field."
>
> N. Bohr [116]

In the previous Chapter we presented an exact solution of skyrmion lattice motion in shaking fields in the adiabatic limit. Moreover, we discovered three dynamic phases: a pinned, a central pinned, and a depinned phase. However, in reality the shaking of skyrmion lines happens at finite, even though small frequencies. In this Chapter, we study the regime of intermediate frequencies more closely and find a new wave-like solution for a skyrmion-line motion for large frequencies, for which we predict the appearance of additional resonances. Moreover, we compare the transverse susceptibility data for MnSi for theory and experiment. In order to account for the observed discrepancies, we introduce an anisotropic surface pinning to our model and study a resulting rich phase diagram.

6.1 On a Search for Solution of Thiele's Equation

In the previous Chapter, we discussed how the solution of the Thiele equation can be obtained fully analytically in the adiabatic limit (limit of small frequencies) which is governed by two dimensionless parameters $\tilde{\epsilon}_0 = \frac{\epsilon_0}{LF^{p,b}}$ and $\tilde{F}^{p,s} = \frac{F^{p,s}}{LF^{p,b}}$. In this Chapter, we aim to find the dynamics of the skyrmion line in the shaking field for arbitrary frequencies. Note that from now on we denote the frequency of the transverse field oscillation with ω instead of ν, $B_x(t) = b\cos(\omega t)$. We recall that the rescaled Thiele equation with pinning is given by

$$\hat{\boldsymbol{z}} \times \dot{\tilde{\boldsymbol{u}}} + \frac{\alpha\mathcal{D}}{\mathcal{G}}\dot{\tilde{\boldsymbol{u}}} = \partial_{\tilde{z}}^2 \tilde{\boldsymbol{u}} - \left[\delta\left(\tilde{z} - \frac{1}{2}\right) - \delta\left(\tilde{z} + \frac{1}{2}\right)\right] \left(\partial_{\tilde{z}}\tilde{\boldsymbol{u}} - \delta\tilde{B}\cos(\tilde{\omega}\tilde{t})\hat{\boldsymbol{x}}\right) + \tilde{\boldsymbol{F}}^{p}, \tag{6.1}$$

$$\tilde{\boldsymbol{F}}^{pin} = \frac{\boldsymbol{F}^{p,b}}{F^{p,b}} + \left[\delta\left(\tilde{z} + \frac{1}{2}\right) + \delta\left(\tilde{z} - \frac{1}{2}\right)\right] \frac{\boldsymbol{F}^{p,s}}{LF^{p,b}},$$

see Section 5.5 for a detailed discussion. Pinning forces in bulk and at the surface are defined in Eq. (5.23) and depend on the applied forces and local skyrmion velocity. In order to simplify the notation, in this Section we will write $\boldsymbol{F} = \boldsymbol{F}^{el}$. More precisely, $\boldsymbol{F} = \boldsymbol{F}^{el}$ has two components: $\boldsymbol{F}^{b} = \partial_{\tilde{z}}^2 \tilde{\boldsymbol{u}}$ in the bulk and $\boldsymbol{F}^{s} = \mp\left(\partial_{\tilde{z}}\tilde{\boldsymbol{u}} - \delta\tilde{B}\hat{\boldsymbol{x}}\right)$ on the top and bottom of the surfaces, respectively. If, at a given time, the elastic forces $\boldsymbol{F}$ are locally not strong enough to depin the line ($F^{b} \leq 1$ in the bulk and $F^{s} \leq \tilde{F}_c^{p,s}$ at the surface in rescaled coordinates), its velocity at this moment is equal to zero. If it is larger than the respective critical value, the line starts to depin. Locally, the velocity of a line as function of elastic forces can be found analytically from the Thiele equation and is given by ($\dot{\tilde{u}}_x = v_x$, $\dot{\tilde{u}}_y = v_y$, $\frac{\alpha \mathcal{D}}{\mathcal{G}} = \tilde{\alpha}$)

$$v_x = \frac{K(F)F_x - F_y}{1 + K(F)^2}\,\theta(F - \tilde{F}_c^p) \quad , \quad v_y = \frac{F_x + K(F)F_y}{1 + K(F)^2}\,\theta(F - \tilde{F}_c^p)\,. \tag{6.2}$$

Here $\theta(F - \tilde{F}_c^p)$ is the Heaviside-step-function ($\tilde{F}_c^p = 1$ in the bulk and $\tilde{F}_c^p = \tilde{F}_c^{p,s}$ on the surface) and $K(F)$ is a non-linear function of the force $\boldsymbol{F}$. $K(F)$ can be found in the bulk as a solution of the equation

$$(F^2 - 1)K^2 - (2\tilde{\alpha}F^2)K + \tilde{\alpha}^2 - 1 = 0\,. \tag{6.3}$$

Note that $K(F)$ depends only on the modulus of the applied force but not on its direction. Plots for velocity $\boldsymbol{v}$ as a function of F_x for several values of F_y can be found in Fig. 48. Depinning happens always at the point $F_x = \sqrt{1 - F_y^2}$. The dynamics just after the transition is strongly nonlinear, but at large values of F_x, shows an almost linear behaviour.

Let us discuss two limits of Eq. (6.2), which can be treated analytically. If the acting force is large ($F \gg F_c^p$), one can neglect pinning, and we obtain a well-known solution of the Thiele equation in the limit of strong forces

$$v_x = \frac{\tilde{\alpha}F_x - F_y}{1 + \tilde{\alpha}^2},\ v_y = \frac{F_x + \alpha F_y}{1 + \tilde{\alpha}^2}\,. \tag{6.4}$$

The resulting velocity is directed approximately perpendicular to the direction of the force. These equations are linear and therefore one can obtain an analytic solution for a small damping constant $\tilde{\alpha}$, which will be given in Section 6.2.

Another limit, for when K is very large, corresponds to the case when forces are just enough to depin the skyrmion ($F^2 \approx 1$ or $F^2 \approx \tilde{F}_c^{p,s}$). This case is realised, for example, in the adiabatic limit (treated analytically in Sec. 5.6). The formula for velocities in the bulk then simplifies to

$$\boldsymbol{v} = \boldsymbol{F}\left(\sqrt{F^2(1 + \tilde{\alpha}^2) - 1} - \tilde{\alpha}\right). \tag{6.5}$$

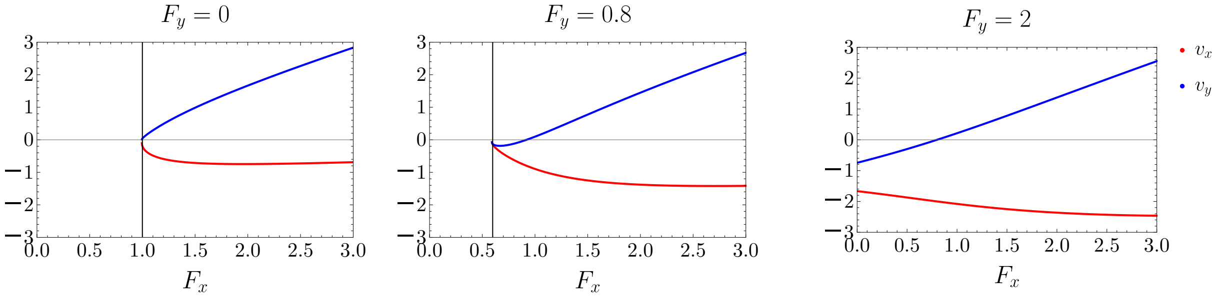

Figure 48: Velocities v_x and v_y as functions of x component of the force force F_x for several values of F_y. Parameters used: $\tilde{F}_c^p = 1$, $\tilde{\alpha} = 0.1$.

From this equation we see that in this limit where K becomes large, the velocity is parallel to the direction of the applied force, in contrast to the other limit we considered. However, in this case, finding an analytic solution is quite tricky because of the $F\sqrt{F^2-1}$ term.

As argued in the previous Chapter, pinning is essential in order to capture the main experimental observations. With pinning, Eq. 6.2 is a highly nonlinear equation in partial derivatives of the displacement function $\tilde{\boldsymbol{u}}(\tilde{z},\tilde{t})$. We therfore aim to find its solution numerically. The basic idea is to discretise both $\tilde{z}$ and $\tilde{t}$ variables such that, instead of a continuous line, we are dealing with a set of N points with coordinates $\tilde{u}_n^i$ ($i = x, y$ and $n = 1 \dots N$). The goal is to find the positions of these points for every time step (N_{step} updates in time in total). The spatial derivatives in Thiele's equation are then approximated with the help of finite-difference formulas (where the error of derivatives is $\propto \frac{1}{N^2}$). Furthermore, we solve Eq. (6.2) using Heun's method (also called the two-stage Runge–Kutta method) for solving ordinary differential equations. Note, that the presence of non-analytic forces make it necessary not to use a standard one-stage Runge–Kutta method [117]. The chosen initial value is simply given by the deviation of every point of the line from being zero. The error of time truncation is expected to be of the order of $\left(\frac{1}{N_{steps}}\right)^2$ [118]. In our code, we typically use $N_{steps} = 10^6$, $N = 60$ and wait around 20 periods to obtain a periodic solution in the long-time limit (when all initial effects have vanished). More details on the numerical implementation can be found in the Appendix B.

In the next Section, we consider more closely the regime of strong forces given by Eq. (6.4), which is, as we shall see, realised for large frequencies.

6.2 Exact Solution for Large Frequencies

In order to get some intuition for the dependence of the skyrmion line motion on the driving frequency, we first consider the case when both pinning and damping constants are absent. Practically, this case is realised if elastic forces are much larger than pinning, $\boldsymbol{F}^{el} \gg \boldsymbol{F}^{p}$. Damping is, however, always present in real materials. We will discuss the influence of damping on our results later. The Thiele equation for the bulk can be written in unscaled coordinates as

$$\begin{cases} \mathcal{G}\frac{\partial u_y(z,t)}{\partial t} &= \varepsilon_0 \frac{\partial^2 u_x(z,t)}{\partial z^2} \\ -\mathcal{G}\frac{\partial u_x(z,t)}{\partial t} &= \varepsilon_0 \frac{\partial^2 u_y(z,t)}{\partial z^2} \end{cases} . \tag{6.6}$$

The boundary equation on the (top) of the line is given by

$$\begin{cases} \mathcal{G}\left.\frac{\partial u_y(z,t)}{\partial t}\right|_{z=L/2} &= -\frac{\varepsilon_0}{L}\left.\left(\frac{\partial u_x(z,t)}{\partial z} - \frac{b}{B_z'}\cos(\omega t)\right)\right|_{z=L/2} \\ -\mathcal{G}\left.\frac{\partial u_x(z,t)}{\partial t}\right|_{z=L/2} &= -\frac{\varepsilon_0}{L}\left.\frac{\partial u_y(z,t)}{\partial z}\right|_{z=L/2} \end{cases} . \tag{6.7}$$

Note that the $\frac{1}{L}$ prefactor on the boundary appears because of the delta function on the boundary. Under the assumption that for both functions $u_x(z,t)$ and $u_y(z,t)$ continuity conditions are satisfied, we can partially differentiate the second equation in Eq. (6.6) with respect to t and exchange the order of derivatives in z and t

$$-\mathcal{G}\frac{\partial^2 u_x(z,t)}{\partial t^2} = \varepsilon_0 \frac{\partial^2}{\partial z^2}\frac{\partial u_y(z,t)}{\partial t}\,. \tag{6.8}$$

Now we partially differentiate the first equation twice with respect to z and substitute $\frac{\partial^2}{\partial z^2}\frac{\partial u_y(z,t)}{\partial t}$ from the second equation. After doing so, we finally obtain

$$\frac{\partial^2 u_x(z,t)}{\partial t^2} + \frac{\epsilon_0^2}{\mathcal{G}^2}\frac{\partial^4 u_x(z,t)}{\partial z^4} = 0\,. \tag{6.9}$$

This allows us to reduce a system of coupled equations in partial derivatives to a set of decoupled equations. Because the drive is periodic, the movement of the line will also be periodic in time. Thus, we solve the equation with the help of the Fourier transform in time $u_x(z,t) = \sum_{n=1}^{\infty}(A(z,\omega)\sin(n\omega t) + B(z,\omega)\cos(n\omega t))$. Here, the zeroth coefficient does not appear because our system is inversion symmetric. Furthermore, we introduce a new variable $\beta = \sqrt{\frac{\mathcal{G}\omega}{\varepsilon_0}}$ and obtain

$$\frac{\partial^4 A(z,\omega)}{\partial z^4} - n^2\beta^4 A(z,\omega) = 0, \quad \frac{\partial^4 B(z,\omega)}{\partial z^4} - n^2\beta^4 B(z,\omega) = 0\,. \tag{6.10}$$

The normal modes of the equation are the functions $\sin(\sqrt{n}\beta z), \cos(\sqrt{n}\beta z), \sinh(\sqrt{n}\beta z)$ and $\cosh(\sqrt{n}\beta z)$. Moreover, based on equations, we know that the solution has the property $\boldsymbol{u}(z,t) = -\boldsymbol{u}(-z,t)$. Because of this condition, the coefficients of $\cos(\sqrt{n}\beta z)$ and $\cosh(\sqrt{n}\beta z)$ vanish. We finally obtain the solution of Eq. (6.6) in the bulk

$$\begin{cases} u_x(z,t) = \sum_{n=1}^{\infty}\left(c_1^{(n)}\sin(kz) - c_2^{(n)}\sinh(kz)\right)\sin(n\omega t) + \left(c_4^{(n)}\sin(kz) + c_3^{(n)}\sinh(kz)\right)\cos(n\omega t)) \\ u_y(z,t) = \sum_{n=1}^{\infty}\left(c_3^{(n)}\sinh(kz) - c_4^{(n)}\sin(kz)\right)\sin(n\omega t) + \left(c_1^{(n)}\sin(kz) + c_2^{(n)}\sinh(kz)\right)\cos(n\omega t)). \end{cases} \tag{6.11}$$

Here $k = \sqrt{n}\beta$. We can see that the higher time harmonics vanish by substituting this equation to the boundary condition, Eq. (6.7). From matching the solution at the boundary, we find

$$\begin{cases} u_x(z,t) = -\frac{1}{2\beta}\frac{b}{B_z'}\left(\frac{\sinh(\beta z)}{\cosh(L\beta/2)+L\beta\sinh(L\beta/2)} + \frac{\sin(\beta z)}{\cos(L\beta/2)-L\beta\sin(L\beta/2)}\right)\cos(\omega t) \\ u_y(z,t) = -\frac{1}{2\beta}\frac{b}{B_z'}\left(\frac{\sinh(\beta z)}{\cosh(L\beta/2)+L\beta\sinh(L\beta/2)} - \frac{\sin(\beta z)}{\cos(L\beta/2)-L\beta\sin(L\beta/2)}\right)\sin(\omega t)\,. \end{cases} \tag{6.12}$$

For every fixed value of z in Eq. (6.12), the trajectory of a skyrmion line in the x, y plane is an ellipse. To see this, we rewrite $u_x(z,t) = S(z)\cos(\omega t)$, $u_y(z,t) = H(z)\sin(\omega t)$ and obtain a parametric equation of an ellipse

$$\left(\frac{u_x(z,t)}{S(z)}\right)^2 + \left(\frac{u_y(z,t)}{H(z)}\right)^2 = 1\,. \tag{6.13}$$

This ellipse has a major axis $2G(z)$ and a minor axis $2H(z)$, both proportional to the strength of the applied transverse magnetic field b and inversely proportional to β.

Note that this equation has in general infinitely many resonant frequencies. Two different regimes exist depending on the value of the parameter $\frac{L\beta}{2}$. For $\frac{L\beta}{2} \ll 1$, the leading order of the solution for u_x coordinate is given by $u_x(z,t) \approx b\cos(\omega t)z$ (where the lines are following the shaking field) and remain suppressed for another coordinate $u_y \propto \beta^2 z^3$. For $\frac{L\beta}{2} \geq \frac{\pi}{2}$ instead of following a magnetic field, the skyrmion line forms a wave in z direction with a wave vector $\frac{2\pi}{\beta}$.

We think this solution becomes relevant for our model with pinning in the limit of large magnetic fields b and large oscillation frequencies ω (since in this limit the elastic force $\partial_z^2 u \propto \omega$ is much larger than the pinning force and Eq.6.6 is valid). Stroboscopic pictures of the movement of the line in this limit are depicted in Fig. 49. For a model with pinning we find resonant frequencies at $\cos\left(\frac{L\beta}{2}\right) = 0$, which corresponds to $\frac{L\beta}{2} = \frac{N\pi}{2}$ (or $\frac{\omega}{\omega_0} = (N\pi)^2$, where $N \in \mathbb{N}$), see Section 6.4 for a further discussion.

One might follow a similar procedure as described above, in order to obtain an analytic solution in the bulk for the case of non-zero damping. When doing so, we however find that the solution is a highly complicated expression (see Appendix C).

6.3 Transverse Susceptibility

A standard technique to probe the response of magnetic systems are magnetic transverse susceptibility measurements. In this Section, we discuss, in more detail, how these transverse susceptibilities can be obtained within our theory.

The magnetisation of the skyrmion lattice under transverse oscillating field $B_x(t) = b\cos(\omega t)$ in the direction of an applied oscillating field for small amplitudes b can be expressed in a

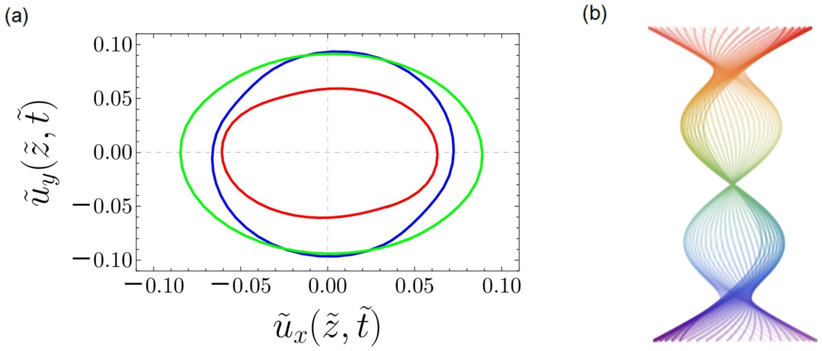

Figure 49: (a) The trajectories of the skyrmion line in the $\tilde{u}_x(\tilde{z},\tilde{t})$ plane for $\tilde{z} = 0.17$ (green), $\tilde{z} = 0.25$ (blue) and $\tilde{z} = 0.33$ (red). (b) Stroboscopic pictures of displacement $\boldsymbol{u}(z,t)$ of the skyrmion line. The following parameters have been used: $\omega/\omega_0 = 60$, $\alpha\mathcal{D}/\mathcal{G} = 0.1$, $F^{p,st}/(LF^{p,b}) = 0.2$.

Fourier expansion

$$m^{\perp}(\omega,t)=\sum_{n=1}^{\infty}\big(\operatorname{Re} m_n^{\perp}\cos(n\omega t)+\operatorname{Im} m_n^{\perp}\sin(n\omega t)\big)=b\sum_{n=1}^{\infty}\big(\operatorname{Re}\chi_n^{\perp}\cos(n\omega t)+\operatorname{Im}\chi_n^{\perp}\sin(n\omega t)\big)\,. \tag{6.14}$$

Here $\chi_n^{\perp}$ are the (complex) susceptibilities. With the help of the magnetisation, the real and imaginary parts can then be found to be

$$\operatorname{Re}\chi_n^{\perp}=\frac{1}{\pi b}\int_0^{2\pi} m_n^{\perp}\cos(n\omega t)\,d(\omega t),\quad \operatorname{Im}\chi_n^{\perp}=\frac{1}{\pi b}\int_0^{2\pi} m_n^{\perp}\sin(n\omega t)\,d(\omega t)\,. \tag{6.15}$$

The higher harmonics ($n \geq 2$) of the complex susceptibility are often referred to as **nonlinear susceptibilities**.

Going further, we recall that the expression of the free energy which describes the displacement of the skyrmion lines due to the slowly oscillating shaking field $\boldsymbol{B}=(B_x(t),0,B_z)$ can be written as

$$\mathcal{F}=-\frac{\gamma}{2}B_x(t)^2+\int_{-L/2}^{L/2}dz\,\frac{\epsilon_0}{2}\left[\,]\left(\partial_z u_x(z,t)-\frac{B_x(t)}{B'_z}\right)^2+\left(\partial_z u_y(z,t)\right)^2\right]\,. \tag{6.16}$$

For a derivation see Section 5.2. From this expression we can easily obtain the transverse magnetization, $m^{\perp}$ per volume

$$\begin{aligned} m^{\perp}(t) &= -\frac{1}{V_s}\frac{d\mathcal{F}}{dB_x(t)}=\frac{\gamma}{V_s}B_x(t)+\frac{\epsilon_0}{V_s B'_z}\int_{-L/2}^{L/2}dz\,\partial_z u_x(t)\\ &= \chi_{\perp}^{0}B_x(t)+(\chi_{\perp}^{\infty}-\chi_{\perp}^{0})B'_z\,\frac{u_x(L/2,t)-u_x(-L/2,t)}{L}\,. \end{aligned} \tag{6.17}$$

Remarkably, the transverse magnetisation is obtained from the displacement of the ends of the skyrmion line only. Transverse susceptibility can be found from this expression by integrating the transverse magnetisation over one oscillation period $T=2\pi/\omega$, see Eq. (6.15)

$$\chi_n^{\perp}=\frac{2}{Tb}\int_{t_0}^{t_0+T} m_n^{\perp}(t)e^{in\omega t}\,dt\,.$$

Here t_0 is an arbitrarily chosen point in time[8]. Rewritten in dimensionless variables $\tilde{\boldsymbol{u}}(\tilde z,t)=\frac{\epsilon_0}{F^{p,b}L^2}\boldsymbol{u}(z,t)$, $\tilde z=\frac{z}{L}$, $\tilde t=\frac{\epsilon_0 t}{L^2\mathcal{G}}, \delta\tilde B=\frac{\epsilon_0}{LF^{p,b}}\frac{b}{B'_z}$ (for a detailed discussion, see Sec. 5.5) we find the complex transverse susceptibility within our theory to be

$$\chi_n^{\perp}=\chi_{\perp}^{0}+(\chi_{\perp}^{\infty}-\chi_{\perp}^{0})\frac{2}{\tilde T}\int_{\tilde t_0}^{\tilde t_0+\tilde T}\frac{\tilde u_x\left(\frac{1}{2},\tilde t\right)-\tilde u_x\left(-\frac{1}{2},\tilde t\right)}{\delta\tilde B}e^{in\tilde\omega\tilde t}d\tilde t\,. \tag{6.18}$$

---

[8] For the numerical implementation, it is important to wait sufficiently long until all initial state effects have vanished.

For the regime where the skyrmion lattice is pinned, one obtains a transverse susceptibility $\chi^0_\perp$ as expected. We define

$$\Delta_{b\to 0}\chi^\perp_n = \chi^\perp_n - \chi^0_\perp\,, \tag{6.19}$$

as the **increase of susceptibility**, which is due to the oscillating field compared to the pinned phase. In the limit of an infinitely strong transverse magnetic field, the skyrmion lattice will follow the driving field $\tilde{u}_x = z\,\delta\tilde{B}(\tilde{t}) = z\tilde{B}\cos(\omega t)$. In this case the change of the real part of the linear susceptibility $\mathrm{Re}\,\Delta_{b\to 0}\chi^\perp_1$ reaches the saturation value $\chi^\infty_\perp$, while the imaginary part $\mathrm{Im}\,\Delta_{b\to 0}\chi^\perp_1$ and all nonlinear susceptibilities vanish. For the intermediate driving magnetic field strength, higher harmonics will appear in the solution (see Sec. 6.6 for further discussion).

In the next Section, we compare the data on the increase of linear susceptibility available from experiments on MnSi with data produced using our theoretical model. For the remainder of this thesis, we drop the index for linear susceptibility unless stated otherwise and simply write $\Delta_{b\to 0}\chi^\perp$.

6.4 Transverse Susceptibility in the Case of Isotropic Pinning

The data on the increase of the linear transverse susceptibility $\Delta_{b\to 0}\chi^\perp$ in MnSi, was measured by Dr. F. Rucker and published in his PhD thesis [98]. This data for an oscillation frequency of $\omega = 120$ Hz, applied static magnetic field of $B_z = 0.22$ T and temperature of $T = 28$ K as a function of the strength of transverse magnetic field b, is depicted on a semi-logarithmic scale on Fig. 50a. Measurements were conducted on a cubic sample with an edge length of 2 mm.

The increase of linear transverse susceptibility $\Delta_{b\to 0}\chi^\perp$ from the experimental data on $\chi^\perp$ was obtained using the following procedure. Firstly, we performed a fit with a horizontal line for points with $b \leq 0.5$ mT in order to account for the measurement errors in the pinned phase. From this we found $\mathrm{Re}\chi^0_\perp = 0.205$ and $\mathrm{Im}\chi^0_\perp = 0.005$. Secondly, we subtracted this value from all measured $\chi^\perp$. As shown in Fig. 50a, the real part of transverse susceptibility is approximately equal to zero before reaching the critical strength $b_c \approx 0.5$ mT of the transverse field. It then increases monotonically and approaches a saturation value at strong values of the driving field. The imaginary part of transverse susceptibility starts to increase approximately at the same value of $b_c \approx 0.5$ mT, has a pronounced peak at $b \approx 5$ mT and decreases with a steep slope after this value. Strikingly, the imaginary part of transverse susceptibility is stronger than the real part for all measured data points.

In order to compare this data to our theoretical prediction, we solve the rescaled Thiele equation (7.3) using Heun's method of finding numerical solutions to ordinary differential equations (see Appendix B for more details on numerical technique and implementation). Using the numerically found solution for the skyrmion line $\tilde{\boldsymbol{u}}(\tilde{z},\tilde{t})$ we are able to find with the help of Eq. (6.18) the transverse magnetic susceptibility.

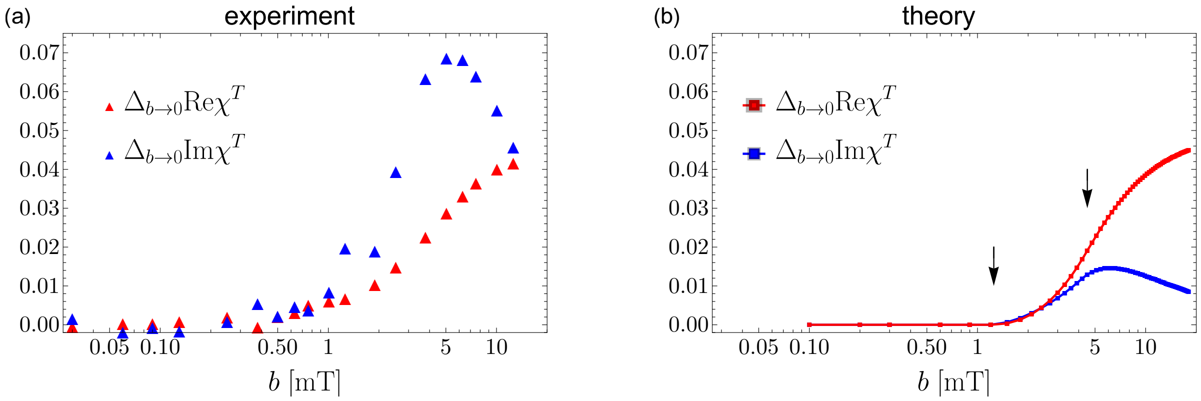

Figure 50: Change of the real (red) and imaginary (blue) parts of transverse susceptibility in the bulk of MnSi as a function of the amplitude of the oscillating field b as found from (a) experiment and (b) our theoretical model. The experimental data was measured by F. Rucker. The experiment was conducted at $B_z = 0.22$ T and temperature $T = 28$ K; for further details on experimental measurements, see Ref. [98]. For the theoretical model, the following parameters have been used: $\omega/\omega_0 = 1.26$, $\alpha\mathcal{D}/\mathcal{G} = 0.1$, $F^{p,st}/(LF^{p,b}) = 0.2$.

From the data of the magnetisation we calculated $\chi_\perp^\infty = 0.254$, which leads to the saturation value of $\Delta_{b\to 0}\mathrm{Re}\chi^\perp = 0.049$. The real and imaginary parts of the transverse susceptibility as a function of the rescaled magnetic field $\tilde{B}$, which we calculated, are presented on the semi-logarithmic scale in Fig. 51. We plot these quantities for a few values of the rescaled surface pinning $\tilde{F}^{p,s} = 0.2, 2, 10$. We identify the signatures of both phase transitions, found in Section 5.6, in the susceptibility data. As one can see from Fig. 51, there exists a general trend for all values of the rescaled surface pinning $\tilde{F}^{p,s}$. Before reaching the critical value of the transverse field $\delta\tilde{B}_{c,1} = \tilde{F}^{p,s}$ (the first arrow), both susceptibilities are zero, corresponding to the pinned phase. After the depinning, the skyrmion lines enter the central-pinned phase and both susceptibilities start to grow. Shortly after reaching the second value of the critical field, $\delta\tilde{B}_{c,2}$, the imaginary part of the susceptibility peaks and then decreases. In the limit of very strong transverse magnetic fields, the skyrmion line simply follows the magnetic field $u_x(z,t) \approx z\, b\cos(\omega t)$ and the imaginary part of the susceptibility decreases, while the real part approaches its saturation value. Moreover, we observe that at the point of the second transition, the second derivative of the real part of the susceptibility changes its sign. Importantly, the relative distance between first and second transitions, which is the same in rescaled and unrescaled coordinates $\frac{\delta\tilde{B}_{c,2}-\delta\tilde{B}_{c,1}}{\delta\tilde{B}_{c,1}} = \frac{b_{c,2}-b_{c,1}}{b_{c,1}}$, decreases for stronger surface pinnings. From this, we deduce that the data from the experiment is in the regime of lower values of $\tilde{F}^{p,s}$.

In order to quantitatively compare the theoretical data with data from measurements, we recall that our theory posesses in general three fitting parameters (for a detailed discussion, see Sec. 5.5), which can be found by fitting the experimental data

$$\frac{\omega}{\omega_0} = \frac{\mathcal{G}L^2\omega}{\epsilon_0}\,, \quad \tilde{\epsilon}_0 = \frac{\epsilon_0}{LF^{p,b}} = \frac{L_p}{L}\,, \quad \tilde{F}^{p,s} = \frac{F^{p,s}}{LF^{p,b}}\,. \tag{6.20}$$

The second scaling parameter, $\tilde{\epsilon}_0$, simply gives the rescaling of the x axis $\delta\tilde{B} = \tilde{\epsilon}_0\frac{b}{B'_z}$. Rescaling of the frequency ω_0 has a more complicated influence on the dynamics, which we will discuss at the end of this Section. We find the best fit for the following parameters: $\omega/\omega_0 = 1.26$, $\tilde{\epsilon}_0 = 36.7$, $\tilde{F}^{p,s} = 0.2$. The corresponding transverse susceptibility is plotted in Fig. 50. These values are in good agreement with values found from TISANE on MnSi ($\tilde{\epsilon}_0 = 34, \tilde{F}^{p,s} = 0.5$, see the Sec. 5.10). Note, however, that the measurements of transverse susceptibilities and TISANE have been performed on two different samples with different sizes and shapes. Therefore, we found that the parameters are slightly different.

Using these three parameters, we can estimate the typical length of skyrmion lines in MnSi. From our fit, we obtain a size of domains, $L \approx 0.2$ mm, which is approximately an order of magnitude smaller than the sample size.

Within our theory, we are able to explain the overall shape of the real part of transverse susceptibility as found from measurements quite well. The only difference is that in the experiment, depinning starts already for slightly lower values of the driving field. This can be explained through a number of different effects. The first possible explanation is that due to thermal creep (which is not included in our theory, see Sec. 3.6), depinning starts

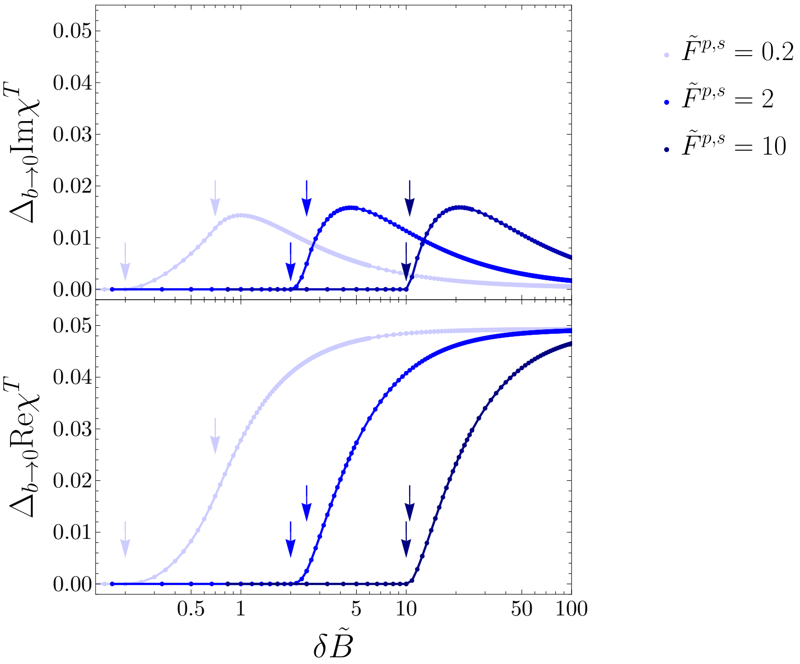

Figure 51: Change of real and imaginary parts of the transverse susceptibility as a function of the rescaled amplitude of the oscillating field δB for different strengths of anisotropic surface pinning (parameters used $\omega/\omega_0 = 0.63, \alpha D/\mathcal{G} = 0.1$).

already at a bit lower values of the shaking field. Moreover, real materials posses a domain structure. Thus, instead of having a single value of a length of domain L and a surface pinning parameter $\tilde{F}^{p,s}$, the measured data contains an averaged value of a distribution of domains with different parameters. It is therefore natural to expect that depinning might start at slightly lower values in the applied field than those predicted by our single-domain theory.

Moreover, our theory correctly captures the overall shape and peak of the imaginary part of the transverse susceptibility. There is, however, a significant difference, as the magnitude of the imaginary part found from the presented theory is approximately 5 times lower than the one found in experiment. Note that there are effects, for example caused by heating, which contribute to the measured imaginary part, which lie outside the realm of our theory. We did find that one possible explanation lies within the anisotropic surface pinning. We will discuss this effect and the new phases which appear in this case in the next Section.

Let us now discuss the frequency dependence of $\mathrm{Re}\,\Delta_{b\to 0}\chi^{\perp}$ and $\mathrm{Im}\,\Delta_{b\to 0}\chi^{\perp}$ within our theory. The data for $\tilde{F}^{p,s} = 0.2$ is presented on the right panel in Fig. 52. First of all, we

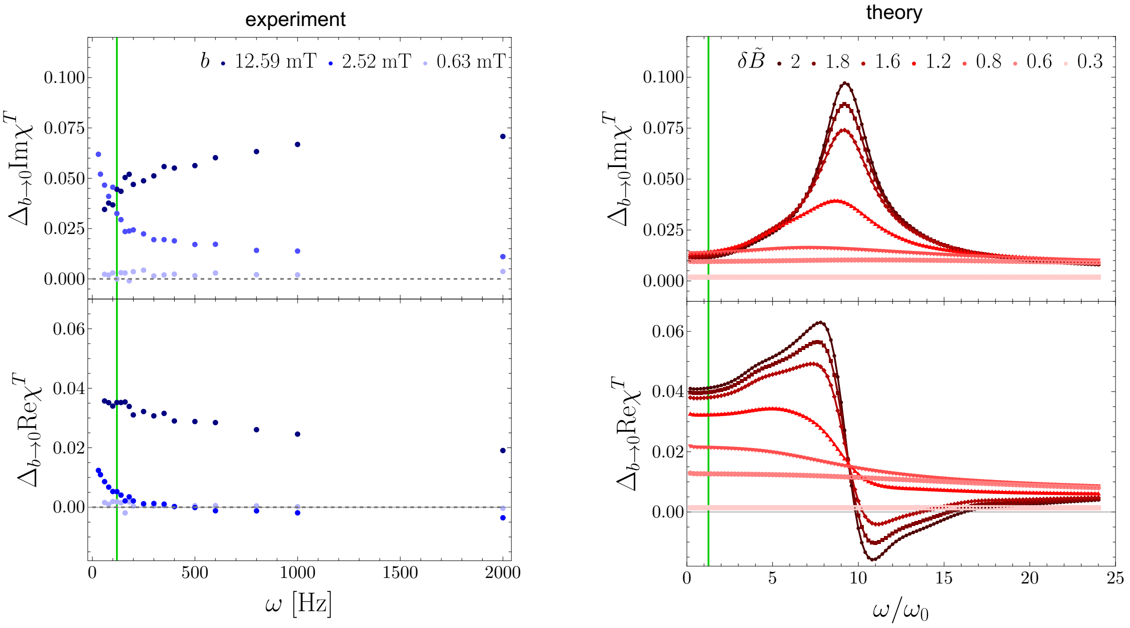

Figure 52: Frequency dependence of $\Delta_{b\to 0}\chi^{\perp}$ as measured in experiments on MnSi and found from our theory. The green line on the left panel denotes the frequency at which experimental data, presented in Fig. 50, was measured. The experimental data was measured by F. Rucker. The experiment was conducted at $B_z = 0.22$ T and temperature $T = 28$ K; for further details on experimental measurements, see Ref. [98]. For the plot on the right we used $\alpha\mathcal{D}/\mathcal{G} = 0.1$, $F^{p,st}/(LF^{p,b}) = 0.2$. Here, the green line denotes the frequency at which the transverse susceptibility was calculated in Fig. 50.

see that at larger values of the driving field $\delta\tilde{B} \gtrsim 1.2$, the resonant frequency $\omega/\omega_0 \approx \pi^2$ found in the previous Section for the clean limit, becomes very prominent. For smaller applied driving fields $\delta\tilde{B} \lesssim 1.2$ almost no resonance is observed, instead we observe a small gradual decrease in $\mathrm{Re}\,\Delta_{b\to 0}\chi^{\perp}$ and almost no change in $\mathrm{Im}\,\Delta_{b\to 0}\chi^{\perp}$. We therefore conclude that the resonance is pronounced in the regime where the driving field is much stronger than the surface pinning.

There exist two limits that can be treated analytically. For small driving frequencies, $\frac{\omega}{\pi^2\omega_0} \to 0$, the solution found in the adiabatic limit is valid, see Sec. 5.6. For strong driving fields far away from the depinning transition, $\delta\tilde{B} \gg \tilde{F}^{p,s}$, the real part of the susceptibility asymptotically reaches its saturation value $\mathrm{Re}\,\Delta_{b\to 0}\chi^{\perp} \approx 0.05$, while the imaginary part $\mathrm{Im}\,\Delta_{b\to 0}\chi^{\perp}$ decreases. For large driving frequencies, $\frac{\omega}{\pi^2\omega_0} \gg 1$ the solution found in the previous Section for the clean limit is valid. We plot the data for larger frequencies in Fig. 53. We see that, in addition, resonances at higher frequencies of $\frac{\omega}{\pi^2\omega_0} \approx 3^2, 5^2, \ldots$ appear. We note, however, that when frequencies are close to the GHz regime, other phenomena become more relevant and our theory loses its validity. Interestingly, we predict that slightly negative values of $\mathrm{Re}\,\Delta_{b\to 0}\chi^{\perp}$ might occur just after the resonance for stronger driving fields.

In order to find the correct regime for the rescaled frequency $\frac{\omega}{\omega_0}$ in which our experiments are operating, we compare this data with the data obtained from experiments. On the left panel of Fig. 52 the measured dependence of $\mathrm{Re}\,\Delta_{b\to 0}\chi^{\perp}$ and $\mathrm{Im}\,\Delta_{b\to 0}\chi^{\perp}$ on the driving frequency ω is presented for a few values of the driving field b. The green vertical line shows the frequency at which the data discussed earlier in this Section (Fig. 50) was measured. Unfortunately, the frequency dependence was recorded only for three selected values of b. We can therefore not find the corresponding values of the depinning field for each frequency. What we can see, however, is that at $b = 0.63$ mT there is almost no change in $\mathrm{Re}\,\Delta_{b\to 0}\chi^{\perp}$ or $\mathrm{Im}\,\Delta_{b\to 0}\chi^{\perp}$ for all measured frequencies. Therefore, we conclude that the skyrmion lattice is pinned at this value of the driving field. Looking at the data

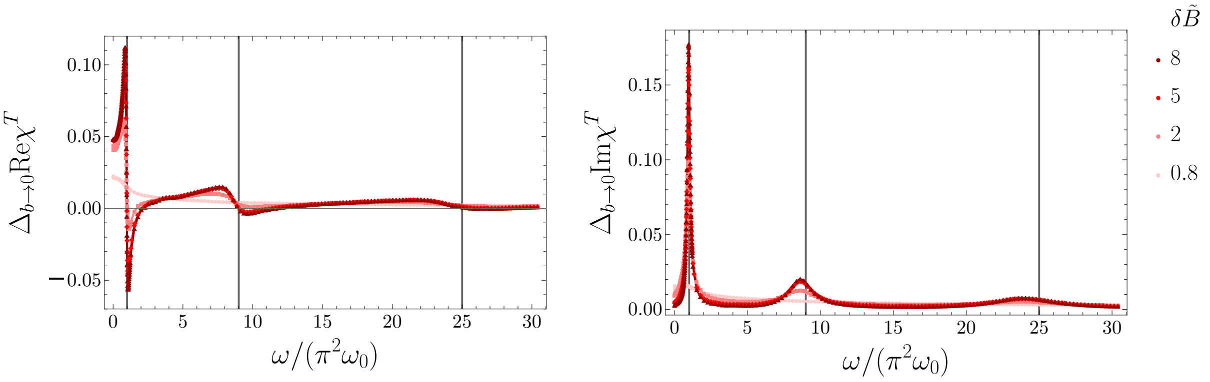

Figure 53: Frequency dependence of $\Delta_{b\to 0}\chi^{\perp}$ at higher frequencies. Here we used $\alpha\mathcal{D}/\mathcal{G} = 0.1$, $F^{p,st}/(LF^{p,b}) = 0.2$.

for $b = 12.59$ mT, we see a slight decrease in the $\mathrm{Re}\,\Delta_{b\to 0}\chi^{\perp}$ and an increase in $\mathrm{Im}\,\Delta_{b\to 0}\chi^{\perp}$. This behaviour can be explained within our theory for the values of the rescaled field at $\delta\tilde{B} \approx 1.2$. Furthermore, the $b = 2.52$ mT data shows more complicated behaviour. At frequencies $\omega \lesssim 120$ Hz there is a strong upturn in both $\mathrm{Re}\,\Delta_{b\to 0}\chi^{\perp}$ and $\mathrm{Im}\,\Delta_{b\to 0}\chi^{\perp}$. As this value of the depinning field is still rather close to the depinning transition, we expect that, at slow frequencies, it might be strongly affected by creep. This effect is not captured within our mean-field theory. Moreover, we observe that $\mathrm{Re}\,\Delta_{b\to 0}\chi^{\perp}$ has slightly negative values at frequencies above $\omega \approx 500$ Hz.

We do not find signatures of resonance in the experiment. One possible explanation of this comes from the fact that the resonance frequency $\omega = \pi^2\omega_0$ is proportional to L^2. A distribution of domains with different lengths L in real materials contributes to the signal. Therefore, the resonance frequency will be smeared. From the absolute values of the measured $\mathrm{Re}\,\Delta_{b\to 0}\chi^{\perp}$ or $\mathrm{Im}\,\Delta_{b\to 0}\chi^{\perp}$ we conclude that experiment operates at small values of the parameter $\frac{\omega}{\pi^2\omega_0}$. In the fit above, we used a value $\frac{\omega}{\omega_0} = 1.26$ (green line on the right panel of Fig. 52). Moreover, we see again that at the measured frequency $\omega = 120$ Hz, the absolute value of $\mathrm{Im}\,\Delta_{b\to 0}\chi^{\perp}$ is much higher than predicted by our theory. One possible explanation is anisotropic surface pinning, which we will introduce in the next Section.

6.5 Anisotropic Surface Pinning

In the previous Chapter, we introduced an effective slip-stick model for pinning, which takes into account that pinning forces at the end of a skyrmion line can be different from bulk pinning forces (see Sec. 5.4). With the help of the isotropic surface pinning model, we could already explain the main features in the transverse susceptibility data. However, the magnitude of the change of the imaginary part of surface pinning found in experiments is approximately 5 times larger than that from theory (see Fig. 50). In this Section, we propose extending our model to account for anisotropic surface pinning, which might explain the mismatch between measured and theoretical values.

For a crystal on a substrate, for example, the pinning on the top and bottom surface will generally be very different. Furthermore, as was observed in experiments, skyrmion lines may break within the sample, see Sec. 3.5. A Bloch point is being formed at the end of the line (identified with an emergent magnetic monopole, see Ref. [81]). In this case, we expect that, while one end of the line experiences pinning from surface roughness and surface defects at the sample boundary, another end might have a completely different strength of pinning force. We thus introduce different pinnings at the top and at the bottom of the line (dubbed as **anisotropic surface pinning**) in our phenomenological pinning theory

$$\tilde{\boldsymbol{F}}^{p} = \frac{\boldsymbol{F}^{p,b}}{F^{p,b}} + \delta(\tilde{z}+1/2)\,\frac{\boldsymbol{F}^{p,st}}{LF^{p,b}} + \delta(\tilde{z}-1/2)\,\frac{\boldsymbol{F}^{p,sb}}{LF^{p,b}}\,. \tag{6.21}$$

Let us assume in the following (without the loss of generality) that a bottom of line has a weaker pinning, compared to the top, $F^{p,sb} \leq F^{p,st}$. The parameter, which quantifies the asymmetry of the surface pinnings is

$$A_{SP} = \frac{F^{p,st}}{F^{p,st} + F^{p,sb}} \,. \tag{6.22}$$

For a symmetric pinning $F^{p,st} = F^{p,sb}$ we obtain $A_{SP} = \frac{1}{2}$. Note, that for strong asymmetry $F^{p,st} \gg F^{p,sb}$ this parameter goes to one.

For this asymmetric case, we obtain five phases (depending on the strength of asymmetry and the strength of an effective magnetic field) instead of three phases in the case of symmetric pinning. Skyrmion strings are in the fully-pinned phase (FP) for weak fields, as depicted in Fig. 54A. Starting from the critical field, one (or both) ends of the string start to move, while some part (or just one point) of the line remain pinned. We find three different pinned phases, depending on where the pinned region lies. The first pinned phase is the center-pinned phase (dubbed as PP.C). In this phase, both ends of the line are depinned; however, a finite fraction remains pinned. This phase was already present for symmetric pinning and depicted with yellow (see Fig. 54C for stroboscopic pictures). If the asymmetry is higher, only one end of the line is depinned, while the finite fraction of the line and the other end is pinned. We call this phase partially pinned at one end (PP.E). This phase is depicted with a blue colour (stroboscopic pictures depicted in Fig. 54B). Furthermore, if both the magnetic field and the asymmetry are high, only one point of the line remains pinned during the whole oscillation period. We call this phase partially pinned at one endpoint (PP.1EP), depicted in pink (stroboscopic pictures depicted on Fig. 54E). If the line is depinned during the whole period of oscillations, we call this phase depinned or walking (W) for reasons which we will make clear later (see Fig. 54D). The characteristic signatures of each of the phases, which we used to determine them numerically, are

	top of SL moving	bottom of SL moving	SL moving (up to one point)
fully-pinned (FP)	-	-	-
center-pinned (PP.C)	+	+	-
partially-pinned at one end (PP.E)	-	+	-
partially-pinned at one endpoint (PP.1EP)	-	+	+
walking (W)	+	+	+

Table 1: Dynamic phases of skyrmion line (SL) movement with anisotropic surface pinning.

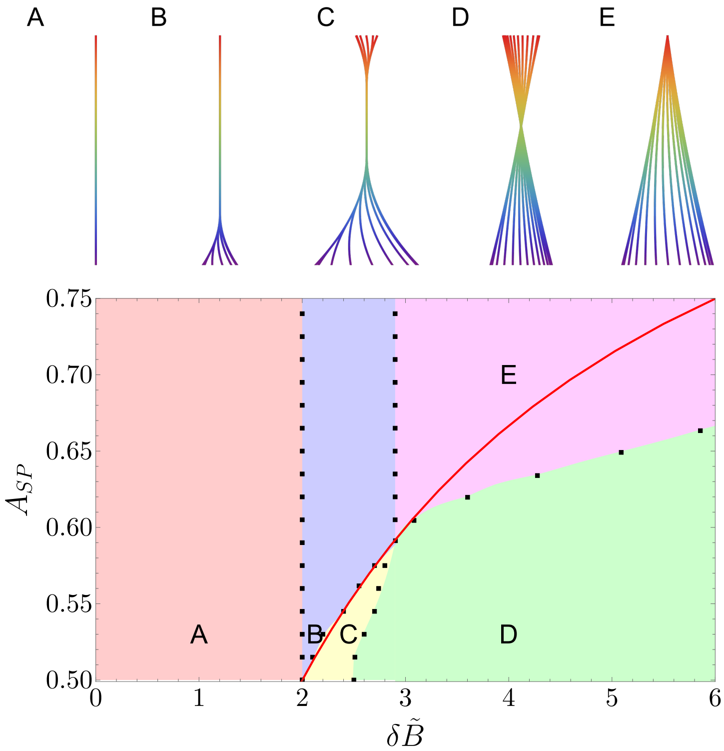

Figure 54: Bottom panel: phase diagram for the case of anisotropic pinning. Depending on the strength of asymmetry, quantified by the parameter A_{SP} and strength of transverse magnetic field $\delta\tilde{B}$, a number of phases appear. Upper panel: stroboscopic pictures of skyrmion line movement in different phases (positions of the letters inside of the phase diagram denote the values used to produce these pictures). Fully pinned phase (A), (B) partially pinned at one end, (C) center-pinned, (E) partially pinned at one endpoint and (D) depinned. Parameters $\omega/\omega_0 = 2.32$, $\alpha\mathcal{D}/\mathcal{G} = 0.1$, $F^{p,st}/(LF^{p,b}) = 0.7$.

summarised in Table 1.

Several transition lines can be found analytically. First of all, the phase transition from FP to PP.C phase and from FP to PP.E (the first vertical line) happens at a critical field $\delta\tilde{B}_{c,1} = \tilde{F}^{p,sb}$. Furthermore, the critical value for the transition from PP.E to PP.1EP phase (the second vertical line) can be found from Eq. (5.36) to be at $\delta\tilde{B}_{c,2} = \tilde{F}^{p,sb} + 1$ (by setting $z_0 = -\frac{1}{2}$). Moreover, the transition line from PP.C to PP.E (red line on Fig. 54) can be found by demanding $\delta\tilde{B}_{c,2} = \tilde{F}^{p,st}$

$$A_{SP}^{cr} = \frac{\delta\tilde{B}}{\delta\tilde{B} + F^{p,sb}} \,. \tag{6.23}$$

The real and imaginary transverse susceptibilities for the case of anisotropic pinning are depicted in Fig. 55. The red dashed line marks the transition from FP to PP.E phase, while the arrows point to the rescaled magnetic field value at PP.1EP to W transition. We observe that while the real part of transverse susceptibility has only a slight change, even

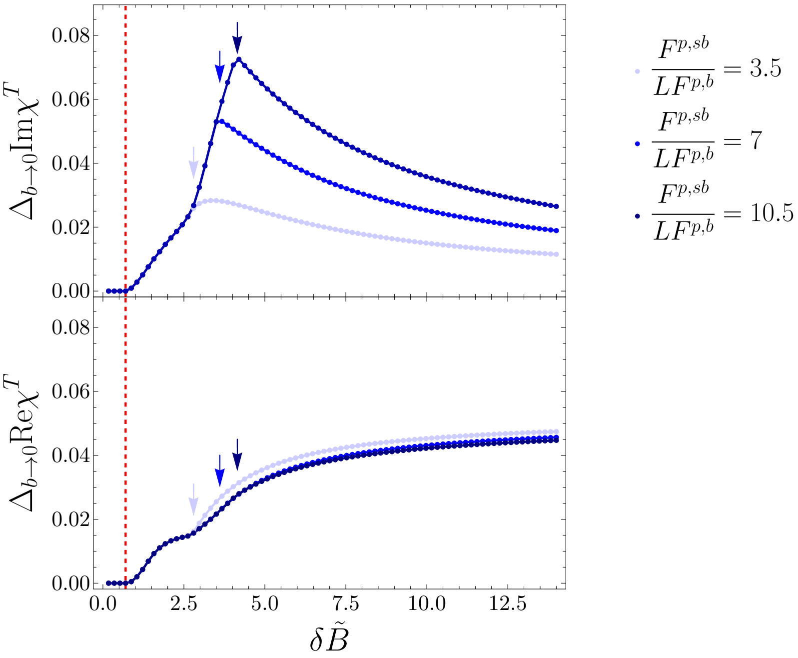

Figure 55: Change of the real and imaginary parts of the susceptibility as a function of the rescaled amplitude of the oscillating field $\delta\tilde{B}$ for a different strength of anisotropic surface pinning. The red dashed line marks the transition from FP to PP.E phase (Fig. 54 A→B). Arrows point to the corresponding value of the rescaled magnetic field value at PP.1EP to W transition (Fig. 54 E→ D). The colours of the arrows encode the values of anisotropic surface pinnings. Parameters, used to produce this plot $\omega/\omega_0 = 2.32$, $\alpha\mathcal{D}/\mathcal{G} = 0.1$, $F^{p,st}/(LF^{p,b}) = 0.7$, $\beta\mathcal{D}/\mathcal{G} = 0.07$.

for strong surface pinning anisotropy, the imaginary part experiences a dramatic increase. We recall that a similar trend can be seen in the experimental data (Fig. 50a). We find the best fit for stronger values of assymetry $\omega/\omega_0 = 2.32$, $\alpha\mathcal{D}/\mathcal{G} = 0.1$, $F^{p,st}/(LF^{p,b}) = 0.7$, $F^{p,sb}/(LF^{p,b}) = 10.5$ ($\tilde{\epsilon}_0 = 190$). The corresponding plot can be found in Fig. 56. Therefore, we believe it might be a strong indication that surface pinning in MnSi has an anisotropic nature. Note, however, that the observed peak in experiments is much more smeared. We expect this might be a consequence of a domain structure (see the discussion in the previous Section).

With this, we conclude our discussion on the linear susceptibilities in MnSi. In the next Section, we briefly discuss the nonlinear susceptibilities.

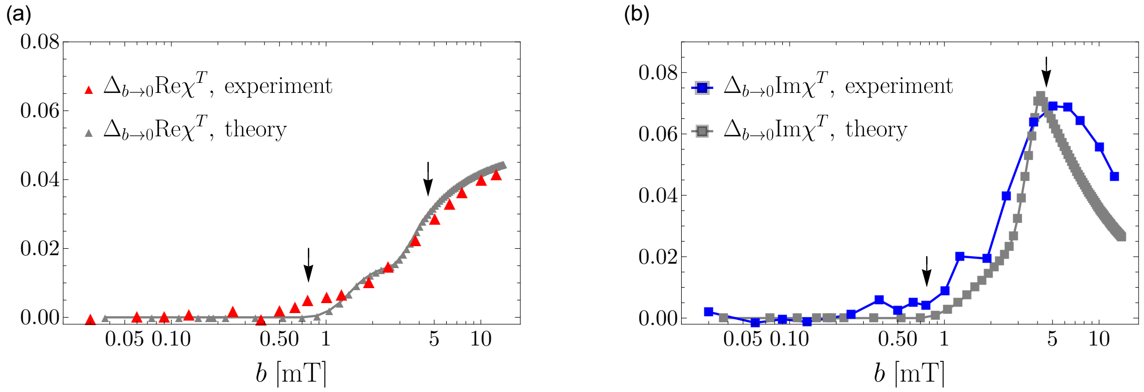

Figure 56: (a) The change of the real parts of transverse susceptibility as a function of the amplitude of the oscillating field b as measured in bulk MnSi (red) and from our anisotropic pinning model (grey). (b) The change of the imaginary part of transverse susceptibility as a function of the amplitude of the oscillating field b is measured in bulk MnSi (blue) and calculated from our theory (grey). The experimental data was measured by Dr. F. Rucker. The experiment was conducted at $B_z = 0.22$ T and temperature $T = 28$ K; for further details on experimental measurements, see Ref. [98]. For theoretical model, the following parameters have been used: $\omega/\omega_0 = 2.32$, $\alpha\mathcal{D}/\mathcal{G} = 0.1$, $F^{p,st}/(LF^{p,b}) = 0.7$, $F^{p,sb}/(LF^{p,b}) = 10.5$.

6.6 Non-Linear Susceptibilities

So far we have discussed only the linear susceptibilities. However, one may also ask if non-linear pinning force leads to interesting signatures of dynamic phases in the nonlinear susceptibilities.

We start the discussion with even nonlinear susceptibilities $\Delta_{b\to 0}\chi^{\perp}_{2m}$, where $m \geq 1$. The equations of motion are invariant under simultaneous rotation around z axis by π and shift in time by $T/2$, $\boldsymbol{u}\left(z, t+\frac{T}{2}\right) = -\boldsymbol{u}\left(z,t\right)$ (for a derivation and discussion see the Chapter 8). We now split the integral in Eq. 6.18 in two parts and obtain

$$\int_{\tilde{t}_0}^{t_0+\tilde{T}/2} \left(\frac{\tilde{u}_x(\frac{1}{2},\tilde{t}) - \tilde{u}_x(-\frac{1}{2},\tilde{t})}{\delta\tilde{B}} \right) e^{i2N\tilde{\omega}\tilde{t}} d\tilde{t} + \int_{t_0}^{t_0+\tilde{T}/2} \left(\frac{\tilde{u}_x(\frac{1}{2},\tilde{t}+\frac{\tilde{T}}{2}) - \tilde{u}_x(-\frac{1}{2},\tilde{t}+\frac{\tilde{T}}{2})}{\delta\tilde{B}} \right) e^{i2N\tilde{\omega}\tilde{t}} d\tilde{t} = 0. \tag{6.24}$$

Therefore, all even nonlinear susceptibilities $\chi^{\perp}_{2m}(\omega)$ vanish.

However, we do expect strong uneven nonlinear susceptibilities $\chi^{\perp}_{2m+1}(\omega)$ to appear. Let us consider the limit of strong but finite transverse magnetic field strengths. From the solution in the adiabatic limit, we find that the line is almost straight. The corresponding time-dependent direction of the line is given by the derivative at the surface $\partial_{\tilde{z}}u_x(\tilde{z},\tilde{t})|_{\tilde{z}=\frac{1}{2}}$ (red line on the Fig. 38). In Fig. 57, one can see the plots for $\partial_{\tilde{z}}u_x(\tilde{z},\tilde{t})$ for two different strengths of the applied magnetic field. Interestingly, the skyrmion line stays stuck for

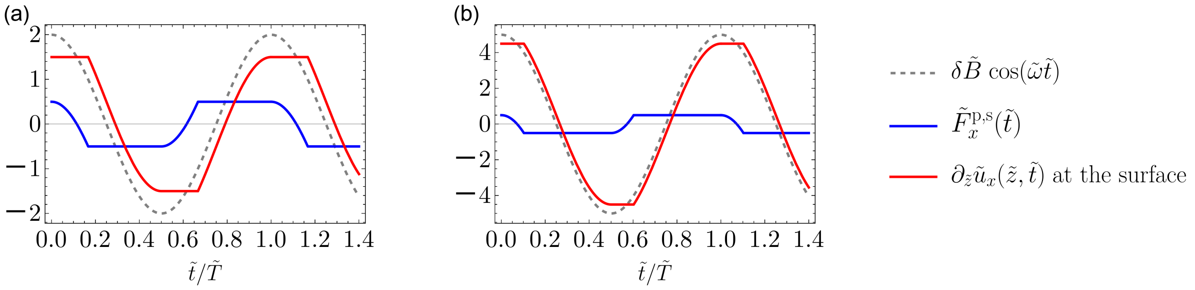

Figure 57: Schematic picture of the driving field, $\delta\tilde{B}\cos(\tilde{\omega}\tilde{t})$, time-dependent surface pinning $\tilde{F}^{p,s}(\tilde{t})$ (the maximum strength of which is $\tilde{F}_c^{p,s}$) and derivative of the displacement function $\partial_{\tilde{z}}\tilde{\boldsymbol{u}}$ at the surface ($\tilde{z}=\frac{1}{2}$) for two different strength of magnetic field $\delta\tilde{B}=2$, $\delta\tilde{B}=5$ in the adiabatic limit. Here $\tilde{F}_c^{p,s}=0.5$.

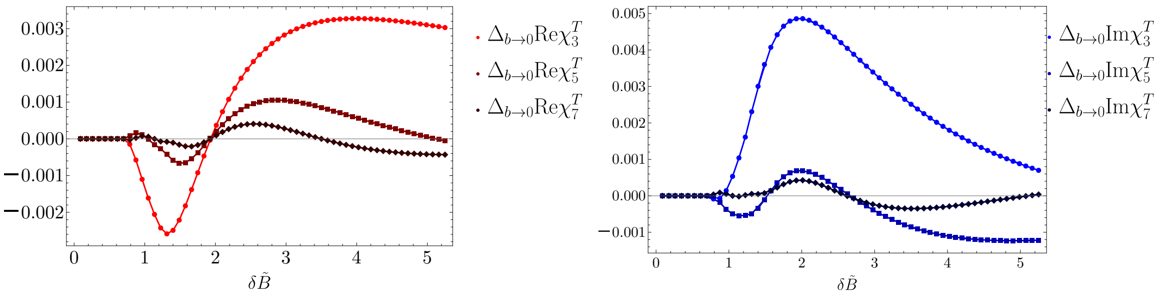

Figure 58: Real and imaginary parts of nonlinear susceptibilities for MnSi. Parameters used $\omega/\omega_0=1.26$, $\alpha\mathcal{D}/\mathcal{G}=0.1$, $F^{p,st}/(LF^{p,b})=0.7$.

a finite time even for large magnetic field strengths $\delta\tilde{B}\gg\tilde{F}_c^{p,s}$. This time is given by Eq. (5.34) in the previous Chapter. Because the line is stuck for a finite amount of time during every period of oscillation, even for arbitrarily large but finite values of the applied driving field, we expect strong signatures in the nonlinear susceptibility.

In Fig. 58, we present the nonlinear susceptibilities for the parameters from MnSi. As discussed earlier, even nonlinear susceptibilities vanish, so we are left with only uneven susceptibilities. We find that the strongest amplitude of the third harmonic relative to the linear one is of order $\frac{\Delta_{b\to0}\mathrm{Re}\chi_3^\perp}{\Delta_{b\to0}\mathrm{Re}\chi_1^\perp}\approx 7.5\%$ and $\frac{\Delta_{b\to0}\mathrm{Im}\chi_3^\perp}{\Delta_{b\to0}\mathrm{Im}\chi_1^\perp}\approx 28\%$. We predict that this strong response can be measured with the help of nonlinear susceptibility measurements. Moreover, it would be interesting to investigate closer in the future why the negative relative nonlinear susceptibilities appear.

Summary and Outlook

In this Chapter, we studied the unpinning process of skyrmion lattices under shaking fields for different frequencies using transverse susceptibility. We compared results from our theory with the data from measurements on MnSi and found an overall good agreement with some limitations, which we discuss below. The found values for the (rescaled) surface pinning $\delta\tilde{B}$ and the ratio of pinning length to the length of skyrmion $\tilde{\epsilon}_0$ agree well with the values from TISANE measurements. Moreover, based on the susceptibility data, we propose an extension of our model with anisotropic surface pinning, which might explain the higher observed values of the increase in imaginary susceptibility. Furthermore, we predict that strong signatures in nonlinear susceptibility will appear.

Similar to the previous Chapter, a number of effects cannot be captured with our mean-field description. For the measured real part of transverse susceptibility, depinning starts already at lower values of applied field b. The imaginary part of transverse susceptibility has a higher and more smeared peak compared to the theoretically found one. Moreover, no clear indication of the resonance peak is observed. We attribute all these effects to the limitations of our mean-field theory. First of all, our theory describes only a single domain of length L. In reality, a measured signal is an average of domains of varying widths, which affect the resonance frequency (which scales $\propto L^2$) and depinning fields. Moreover, our theory does not describe the domain fragmentation, e.g. for different frequencies. Furthermore, with our theory, we cannot capture correctly critical properties, which might be of importance close to transition. In addition, we do not include the effects of temperature, such as thermal creep. Despite these, we have been able to capture the main observed effects using our phenomenological model.

7 | Pushing and Shaking

In the previous Chapters we have studied how skyrmion lattices respond to shaking fields. In this Chapter, we study the dynamics of a skyrmion lattice under simultaneous application of a shaking field together with the "pushing" by an electric current. Already the first studies yielded a very low critical current $j_c \approx 10^6$ A/m^2, needed to depin the skyrmion lattice [16]. Under the applied current we find in total five phases with only two (dubbed as "walking" and "running" for reasons explained later in this Chapter) showing a net translational velocity. With the help of this phase diagram we explain the striking experimental observation that the critical current, needed to depin the skyrmion lattice, vanishes at tiny transverse field amplitude of $b \approx 5$ mT.

We start this Chapter with a discussion on the phases of elastic skyrmion lattices under external current in the absence of a shaking field. We proceed with a discussion on phases under pushing and shaking for isotropic and anisotropic surface pinnings. We compare the dependence of depinning currents on applied transverse field for all of these cases.

This work was conducted in collaboration with the group of Prof. C Pfleiderer and is currently in preparation for publication [119]. Experimental results presented in this Chapter are measured by Dr. F. Rucker and can be found in his PhD thesis [98].

7.1 Skyrmion Lattice Under External Current

In this Section, we discuss how the electric current enters the Thiele equation and which phases exist for skyrmion lattice with surface pinning.

An electric current gives rise to a spin current with velocity $\boldsymbol{v}_s$, oriented approximately parallel (or antiparallel) to the external current. The modified Thiele equation for the skyrmion lattice subject to both a shaking field and a current takes the form

$$\boldsymbol{\mathcal{G}} \times (\dot{\boldsymbol{u}}(z,t) - \boldsymbol{v_s}) + \mathcal{D}(\alpha \dot{\boldsymbol{u}}(z,t) - \beta \boldsymbol{v_s}) = -\frac{\delta \mathcal{F}}{\delta \boldsymbol{u}(z,t)} + \boldsymbol{F}^p \,. \tag{7.1}$$

See Sec. 3.3 for a more detailed discussion of this equation. The forces on the right hand side of this equation are defined in Sec. 5.3 and Sec. 5.4. In the absence of an oscillating field and in the absence of surface pinning, only two phases exist: the pinned and depinned phase. In the first phase, the strength of the applied current is not strong enough to depin the lattice. In the second phase, skyrmion lines flow without bending. The critical value of the current needed to depin the lattice can be found from

$$|\boldsymbol{\mathcal{G}} \times \boldsymbol{v_s}| = F^{p,b} \,. \tag{7.2}$$

Here we neglected a relatively small non-adiabatic term, proportional to β. For MnSi, the value of the critical current is $j_c \approx 10^6$ A/m^2. From it, we estimate $v_s \approx 1.6 \cdot 10^{-4}$ m/s and $F^{p,b} \approx 3 \cdot 10^{-10}\,$N/m.

From the formula above, we see that the critical current and the bulk pinning are proportional to each other, $j_c \propto F^{p,b}$. Using our theory and data on two critical fields from TISANE measurements (see Section 5.10), we can obtain an estimate for the relative

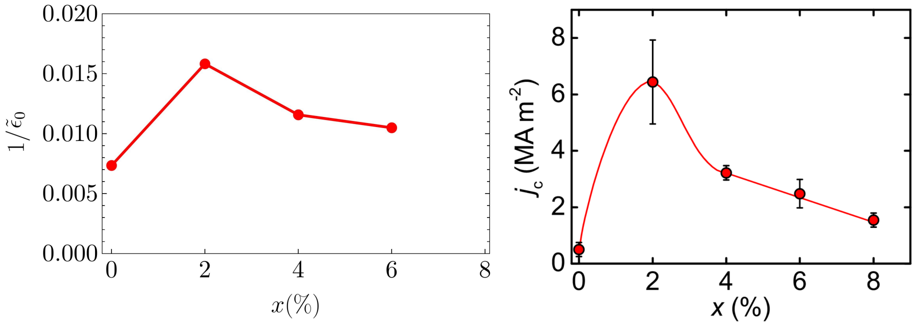

(a)

(b)

Figure 59: Left panel: $\frac{1}{\tilde\epsilon_0} = \frac{LF^{p,b}}{\epsilon_0}$ as found from TISANE mesaruments (see Sec.4.2). Right panel: measurements of the critical current with the help of Hall resistivity measurements in these materials from Ref. [120]

strength of the bulk pinning $\frac{1}{\tilde\epsilon_0} = \frac{LF^{p,b}}{\epsilon_0}$ for different concentrations of Fe doping x in MnSi ($\mathrm{Mn}_{1-x}\mathrm{Fe}_x\mathrm{Si}$ with $x = 0, 0.02, 0.04$ and 0.06). This data is presented in Fig. 59a. For comparison, the critical current j_c measured in these materials by Dr. C. Schnarr is presented on the right hand side of Fig. 59b [120]. Both quantities exhibit a similar trend, which agrees well with Eq. (7.2). For $x = 0.02$, the value of critical current and bulk pinning are higher than the one for MnSi. At higher values of dopping, we observe a drop in both quantities. Note, however, that one needs to take into account that the lengths of lines and elasticity constants might change depending on the doping.

In order to find the dynamics in the presence of (isotropic) surface pinning, we write the rescaled Thiele equation in the dimensionless variables $\tilde{\boldsymbol{u}} = \tilde{\boldsymbol{u}}(\tilde z, \tilde t) = \frac{\epsilon_0 \boldsymbol{u}}{F^{p,b}L^2}$, $\tilde z = \frac{z}{L}$, $\tilde t = \frac{\epsilon_0 t}{L^2 \mathcal{G}}$

$$\hat{\boldsymbol{z}} \times \dot{\tilde{\boldsymbol{u}}} + \frac{\alpha\mathcal{D}}{\mathcal{G}}\dot{\tilde{\boldsymbol{u}}} = \tilde{\boldsymbol{v}}_s + \partial_{\tilde z}^2\tilde{\boldsymbol{u}} - \left[\delta\left(\tilde z - \frac{1}{2}\right) - \delta\left(\tilde z + \frac{1}{2}\right)\right]\left(\partial_{\tilde z}\tilde{\boldsymbol{u}} - \delta\tilde B\cos(\tilde\omega\tilde t)\hat{\boldsymbol{x}}\right) + \tilde{\boldsymbol{F}}^p, \tag{7.3}$$

$$\tilde{\boldsymbol{F}}^p = \frac{\boldsymbol{F}^{p,b}}{F^{p,b}} + \left[\delta\left(\tilde z + \frac{1}{2}\right) + \delta\left(\tilde z - \frac{1}{2}\right)\right]\frac{\boldsymbol{F}^{p,s}}{LF^{p,b}}\,,$$

with

$$\tilde{\boldsymbol{v}}_s = \frac{1}{F^{p,b}}\left(\boldsymbol{\mathcal{G}} \times \boldsymbol{v}_s + \beta\mathcal{D}\boldsymbol{v}_s\right),\ \delta\tilde B = \frac{\epsilon_0}{LF^{p,b}}\frac{b}{B'_z}\,. \tag{7.4}$$

For a detailed discussion on Thiele equation see Section 5.5. Pinning forces in the bulk and at the surface are defined in Eq. 5.23 and depend on applied forces (an elastic force and a force from external current) and the local skyrmion velocity.

In the absence of a magnetic field but in the presence of (isotropic) surface pinning we already obtain three phases under external current instead of two, see Fig. 60. If the current is smaller than a critical value $\tilde{\boldsymbol{v}}_s^{c,1} = 1$, the line is fully pinned due to the bulk pinning (phase A). At stronger values of $\tilde{\boldsymbol{v}}_s$, a new phase appears: the middle of the skyrmion becomes depinned, while both ends of the line are still pinned (phase B). This

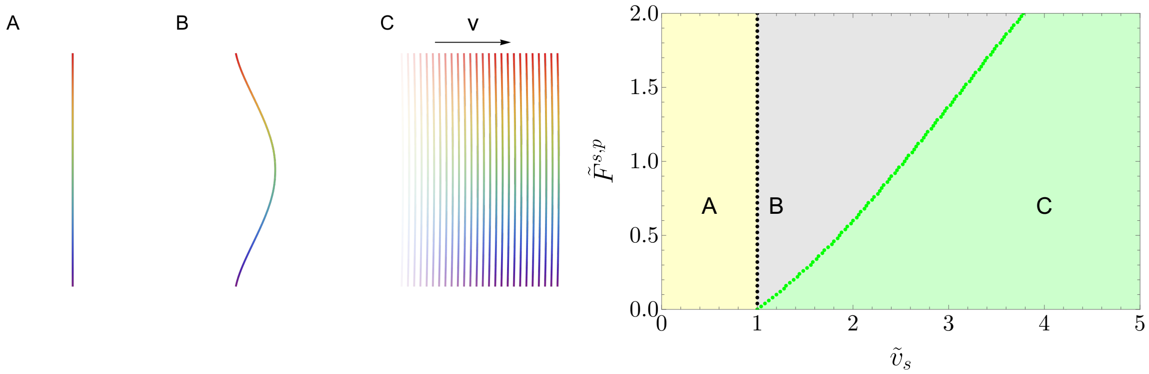

Figure 60: Phases of skyrmion lattice in the presence of current, but in the absence of shaking field with our model. The right panel: stroboscopic pictures of the skyrmion lattice movement. Positions of letters on the phase diagram signifies the values of respective parameters. Here $\alpha\mathcal{D}/\mathcal{G} = 0.1$, $\beta\mathcal{D}/\mathcal{G} = 0.07$.

is a static configuration, i.e. no dependence on time for the displacement function $\tilde{\boldsymbol{u}}(\tilde{z})$ is present. In the bulk we obtain $\partial^2_{\tilde{z}}\tilde{\boldsymbol{u}} + \tilde{\boldsymbol{v}}_s = \frac{\boldsymbol{F}^{p,b}}{F^{p,b}}$, while at the ends of the line surface pinning $\tilde{F}^{p,s}$ keeps the line pinned $\mp\partial_{\tilde{z}}\tilde{\boldsymbol{u}}\big|_{z=\pm\frac{1}{2}} = \frac{\boldsymbol{F}^{p,s}}{LF^{p,b}}$. In this phase the solution is given by quadratic function

$$\tilde{\boldsymbol{u}}(\tilde{z}) = \frac{\boldsymbol{a}(\tilde{\boldsymbol{v}}_s)}{2}\left(\tilde{z} - \frac{1}{2}\right)\left(\tilde{z} + \frac{1}{2}\right) . \tag{7.5}$$

The dependence of the depinning current on the surface pinning is approximately linear, see the right panel of Fig. 60.

In the third phase, the line is moving at every point in time with a net translational velocity $v \propto \tilde{v}_s$. We call this phase a **running phase**. In the next Section, we discuss how a shaking field affects each of these phases.

7.2 Phases Under Pushing and Shaking: Isotropic Surface Pinning

In this Section, we explore phases of skyrmion lattices under simultaneous application of shaking field and external current, when both are applied perpendicular to the direction of the static magnetic field B'_z (see Fig. 22 for the schematic picture of the experiment).

We start our discussion with the phase diagram in the absence of a surface pinning, depicted in Fig. 61. If surface pinning is absent, arbitrarily weak magnetic oscillating fields depin the ends of the skyrmion line. Therefore, only two phases exist: central pinned and depinned (see Sec. 5.6). These two phases have very different responses to the applied current. In the central pinned phase, a finite fraction of the line is still pinned. Under application of the weak current the line will stay pinned and a (partially) pinned phase (depicted with yellow) appears on the phase diagram for weak fields and weak currents. In the depinned phase, the skyrmion line is fully depinned during the part of the oscillation

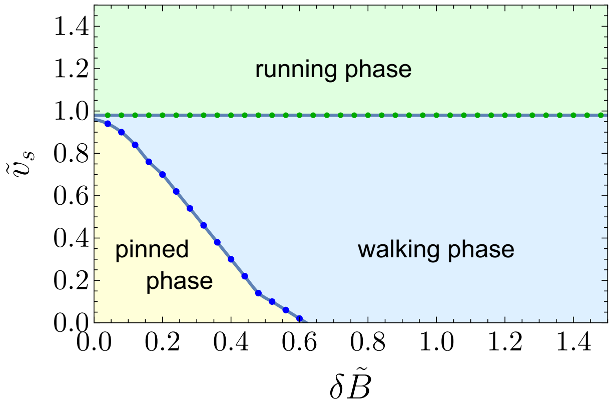

Figure 61: Theoretical phase in the absence of surface pinning (parameters $\omega/\omega_0 = 2.32$, $\alpha\mathcal{D}/\mathcal{G} = 0.1$, $\tilde{F}^{p,s} = 0$, $\beta\mathcal{D}/\mathcal{G} = 0.07$). In this case, we predict a pinned (yellow), walking (blue), and running (green) phase.

period and remains stuck when local forces become smaller than the depinning force. In contrast to the center-pinned phase, during the part of the period where the full skyrmion line moves, the application of an arbitrarily weak current will be enough to set the skyrmion line to move with a net translational velocity $\boldsymbol{v}$. The skyrmion line, however, will remain stuck during the other part of the period. We call this phase the **walking phase** as "walking" (in contrast to "running") implies that at least one foot is always on the ground (and thus not moving). This phase is depicted in blue in the phase diagram. If the force from the current is larger than the strength of the bulk pinning, $\tilde{v}_s \geq 1$, the line will never be pinned during the oscillation period independently of the strength of the magnetic field and a **running phase** emerges (color green in the phase diagram).

For the case of a finite surface pinning, which is present in real materials as we have argued in the previous Chapters, we obtain five phases instead of three phases under both the current and shaking field. The phase diagram for this case with parameter values obtained from fitting the increase of real and imaginary susceptibilities for MnSi (see Sec. 6.4) is presented in Fig. 62. Instead of one (partially) pinned phase in the absence of surface pinning, here we obtain three (partially) pinned phases: (A) trivial fully pinned phase, (B) both ends pinned, while bulk part depinned due to the current phase and (C) central pinned phase. Moreover, we again obtain walking (D) and running phases (E), in which the skyrmion line moves with a net velocity $\boldsymbol{v}$. We predict that the critical current j_c, needed to depin the skyrmion lattice, will drop along the phase transition from the pinned to the walking phase (blue line).

The quantity of interest is the relative increase of real and imaginary parts of magnetic susceptibility as compared to the value of a given magnetic field in the absence of a current

$$\Delta_{j=0}\chi^T(b,j)(\%) = \frac{\chi^T(b,j) - \chi^T(b,j=0)}{\chi^T(b,j=0)}\,. \tag{7.6}$$

We predict that (partially) pinned phases show fundamentally different response to the

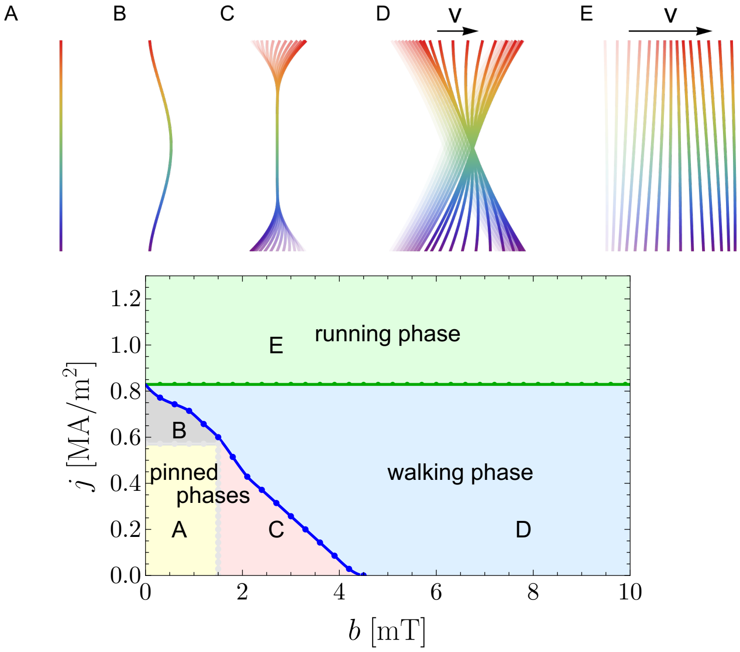

Figure 62: Lower panel: phases of skyrmion lattice under driving field b and an electrical current density j, applied perpendicular to the skyrmion lines. Upper panel: stroboscopic pictures of skyrmion line movement (illustrated by decreasing color saturation). Position of letters on the phase diagram denote the values of b and j used to produced the pictures. (A) - (C) phases are pinned phases with no net velocity. In (D) and (E) phases, a net translational velocity v is observed. Parameters used: $\omega/\omega_0 = 1.26$, $\tilde{\epsilon}_0 = 36.67$, $F^{p,st}/(LF^{p,b}) = 0.2$, $\alpha\mathcal{D}/\mathcal{G} = 0.1$ and $\beta\mathcal{D}/\mathcal{G} = 0.07$.

application of an electric current when compared to the walking or running phases. Fully pinned and both-ends pinned phases are static and will show no response in magnetic susceptibility. In the central pinned phase, the ends of the skyrmion line do move. However, in this phase, the current causes a static deformation $\Delta\tilde{\boldsymbol{u}}(\tilde{z})$, which satisfies $\partial_{\tilde{z}}^2\Delta\tilde{\boldsymbol{u}}(\tilde{z}) = \tilde{v}_s$. This deformation is time-independent even in the presence of an oscillating magnetic field. Therefore, the difference $\chi^T(b,j) - \chi^{\perp}(b,j=0)$, vanishes exactly in this phase. Only in the walking (or running) phase, the response measured by $\Delta_{j=0}\chi^T(b,j)$ is affected by the current. Therefore, $\Delta_{j=0}\chi^T(b,j)$ can be used as a tool to identify the transition from (partially) pinned into the walking phase. The corresponding plot of $\Delta_{j=0}\chi^T(b,j)$ for several values of b, obtained from our theory is shown in the right panel of Fig. 63. As one can see, the increase of the transverse susceptibility (marked with red triangles) coincides with the values of pinned to the walking phase transition from the phase diagram in Fig. 62.

In order to probe this phase diagram experimentally, $\Delta_{j=0}\chi^T(b,j)$ has been measured by Dr. F. Rucker in MnSi (Ref. [98]). This data is depicted on the left panel of Fig. 63 as a function of the current strength j for several measured values of a driving field b. As one can see from this Figure, $\Delta_{j=0}\mathrm{Re}\,\chi^T(b,j)$ has an increase at the value of current, denoted with red triangles (for the detailed explanation how these values have been determined from the measured data see Ref. [98]). This increase is associated with the depinning of the skyrmion lattice. The critical current j_c, at which this depinning happens, is depicted in the left panel of Fig. 64. As one can see, strikingly, the critical current drops to zero at the critical value of the applied driving field $b \approx 5$ mT. On the right panel of Fig. 64, we see the theoretically calculated plot for the critical current j_c, which shows a similar drop at $b \approx 5$ mT. Note, however, that the decrease of the critical current, calculated from our model is much more gradual than the abrupt drop in the experiment. Because of this, it is harder to determine the value of j_c at which the depinning starts from the experiment.

Although our theory successfully explains the drop of the critical current, there are a few significant differences in $\Delta_{j=0}\chi^T(b, j)$ between theory and experment. First of all, as we have already noted, the drop is much more steep in the experiment. Note that the increase of $\Delta_{j=0}\chi^T(b, j)$ is predicted to be very gradual, therefore, the values of j_c which we estimated from the experiment most probably are larger than the real values. Secondly, we observe non-analytic behaviour of $|j|$ type for $\Delta_{j=0}\chi^T(b, j)$ at higher values of b in experimental data. This effect cannot be captured within our mean-field theory. One possible explanation for it may lie in the fact, that under applied current some parts of the skyrmion lattice are moving, while others are not (see Sec. 3.5 for a discussion).

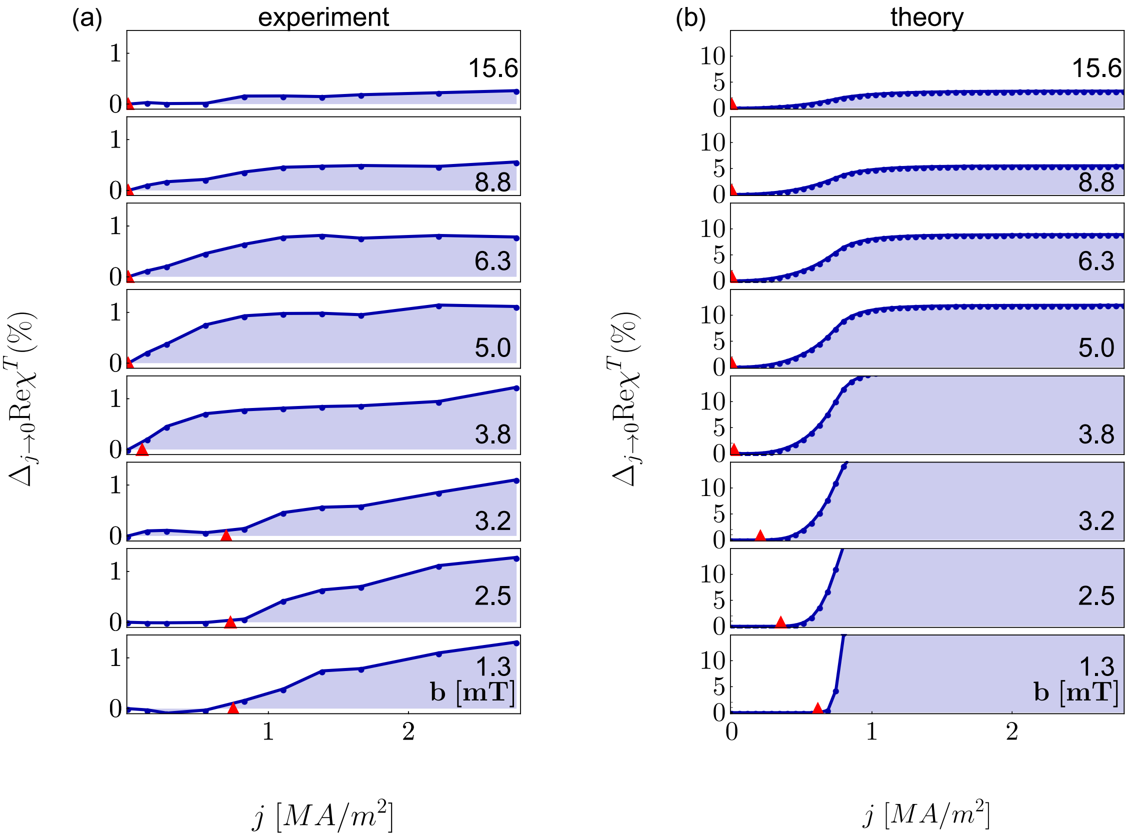

Figure 63: $\Delta_{j=0}\chi^T(b, j)(\%)$ found from experiment (left panel) and from theory (right panel) for several values of transverse magnetic field strength b. Here we used $\omega/\omega_0 = 1.26$, $\tilde{\epsilon}_0 = 36.67$, $F^{p,st}/(LF^{p,b}) = 0.2$, $\alpha\mathcal{D}/\mathcal{G} = 0.1$ and $\beta\mathcal{D}/\mathcal{G} = 0.07$.

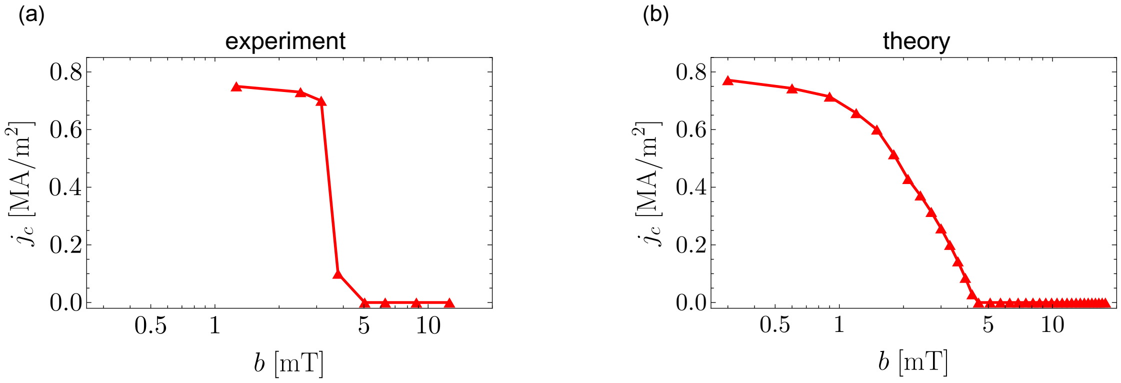

Figure 64: Drop of the critical current j_c as function of applied trasverse magnetic field b as (a) measured in MnSi (b) calculated theoretically. Parameters used for theory plot $\omega/\omega_0 = 1.26$, $\tilde{\epsilon}_0 = 36.67$, $F^{p,st}/(LF^{p,b}) = 0.2$, $\alpha\mathcal{D}/\mathcal{G} = 0.1$ and $\beta\mathcal{D}/\mathcal{G} = 0.07$.

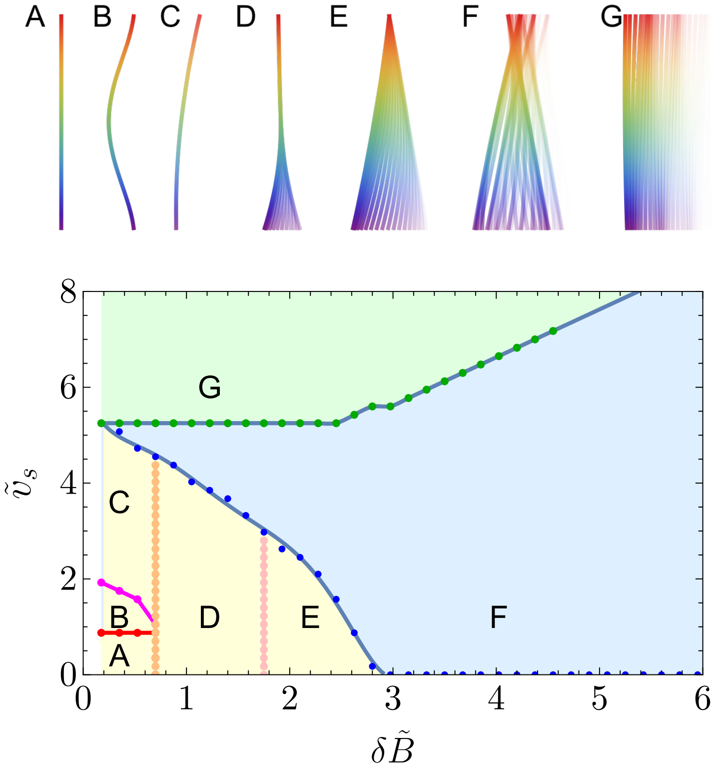

Figure 65: Panel A-G shows the stroboscopic pictures of $u_x(t)$ at times $t = n\delta t$. The theoretical phase diagram (parameters $\omega/\omega_0 = 2.32$, $\alpha\mathcal{D}/\mathcal{G} = 0.1$, $F^{p,sb}/(LF^{p,b}) = 0.7, F^{p,st}/(LF^{p,b}) = 3.5$, $\beta\mathcal{D}/\mathcal{G} = 0.07$). The position of letters on the phase diagram correspond to the parameters chosen for panel A-G.

7.3 Phases Under Pushing and Shaking: Anisotropic Surface Pinning

In this Section, we study the phases of a skyrmion lattice under simultaneous application of the shaking field and pushing with a current for an anisotropic surface pinning model. We recall that in this case, the surface pinning acquires the form

$$\boldsymbol{F}^{\boldsymbol{p}} = \boldsymbol{F}^{p,b} + \boldsymbol{F}^{p,s} = \boldsymbol{F}^{p,b} + \delta(z + L/2)\ \boldsymbol{F}^{p,st} + \delta(z - L/2)\ \boldsymbol{F}^{p,sb}\ , \tag{7.7}$$

where $\boldsymbol{F}^{p,b}$ denotes a bulk, $\boldsymbol{F}^{p,st}$ a top surface and $\boldsymbol{F}^{p,sb}$ a bottom surface pinning. The dimensionless parameters $\tilde{F}^{p,st} = \frac{F^{p,st}}{LF^{p,b}}$, $\tilde{F}^{p,sb} = \frac{F^{p,sb}}{LF^{p,b}}$ characterise the relative strengths of the surface to bulk pinnings.

Instead of five phases, which we obtained for the isotropic surface pinning, for the anisotropic pinning case we obtain seven different phases. Five of them are (partially) pinned phases, see panels A-G in Fig. 65. Phases A and B we have already encountered for the symmetric pinning case. We do have, however, new phases C-E. In the phase C, the skyrmion line is pinned at the original position (zero deviation) for one end, but it has a non-zero, although static, deviation for the rest of the line. Note that since this phase is static it will show no response in the transverse susceptibility. Phase D is similar to the phase C from the symmetric pinning case, with the only difference being that only one end is moving instead of both ends moving. Although a finite fraction of the line remains pinned in this phase, it will have a non-zero response in the transverse susceptibility $\chi^T(b, j)$. Finally, in phase E, one end remains to be pinned, while the rest of the line oscillates back and forth. Even under the application of an infinitesimally small current, this phase will remain pinned. However, it is different for the walking (F) and running phases (G), which are similar to the symmetric pinning model. In this phases the skyrmion lattice has net velocity $\boldsymbol{v}$. Therefore, a non-zero increase of the $\Delta_{j=0}\chi^T(b, j)$ will be measured for a (partially) pinned to walking phase transition.

In Fig. 66 we show how the asymmetric pinning affects the current dependence of $\Delta_{j=0}\chi^T(b, j)$ for two different strengths of the surface pinning ($F^{p,st}/(LF^{p,b}) = 3.5$ and $F^{p,st}/(LF^{p,b}) = 10.5$ for the left and right panels, respectively). Comparing the plot in Fig. 66a shows only minor changes in comparison to the case of symmetric pinning (Fig. 63). However, for stronger values of the asymmetry, as depicted on Fig. 66b, $\Delta_{j=0}\chi^T(b, j)$ develops a negative sign, which is not confirmed in experiments. The resulting drop of critical current is depicted on Fig. 67. In this case, we obtain a much steeper decrease at around 5 mT in comparison to the symmetric surface pinning model. Therefore, we argue, that one further possible reason for a steeper decrease of the critical current observed in experiments might be due to the coexistence of domains with stronger anisotropic pinnings.

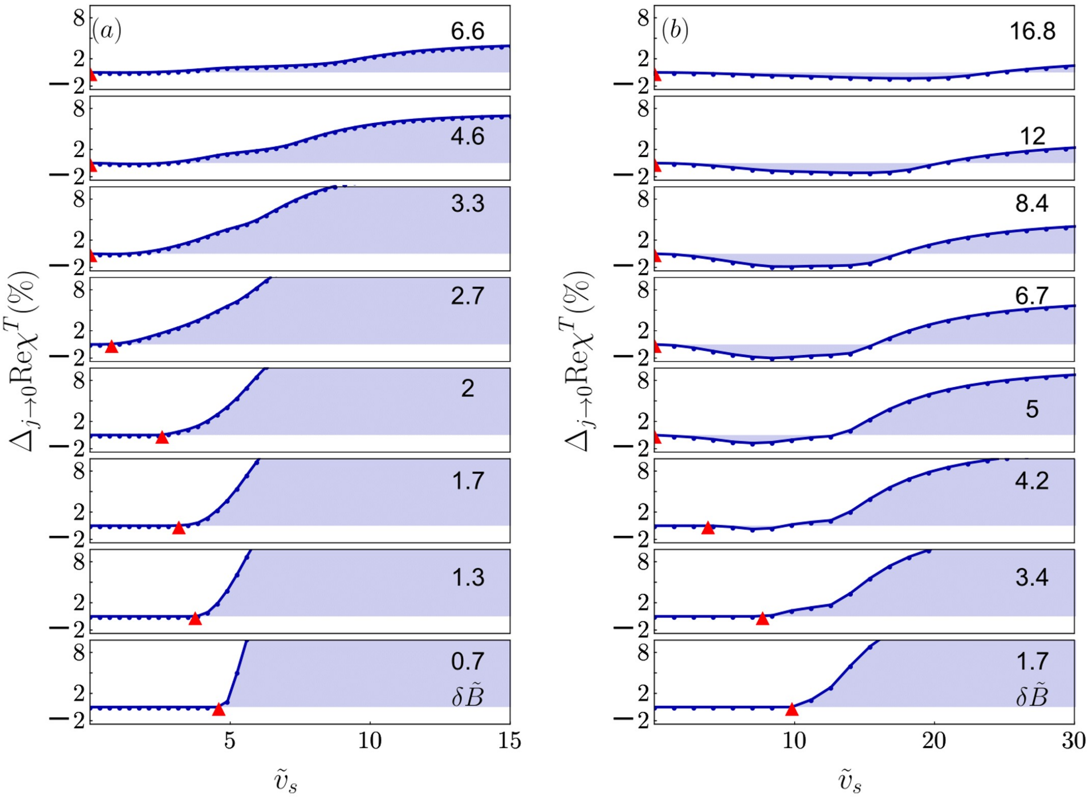

Figure 66: Relative change of the real part of the transverse susceptibility in the case of asymmetric surface pinning as a function current density j for different $\delta\tilde{B}$. Left panel: $F^{p,st}/(LF^{p,b}) = 3.5$. Right panel: $F^{p,st}/(LF^{p,b}) = 10.5$. Parameters used: $\omega/\omega_0 = 2.32$, $\alpha\mathcal{D}/\mathcal{G} = 0.1$, $F^{p,sb}/(LF^{p,b}) = 0.7$, $\beta\mathcal{D}/\mathcal{G} = 0.07$.

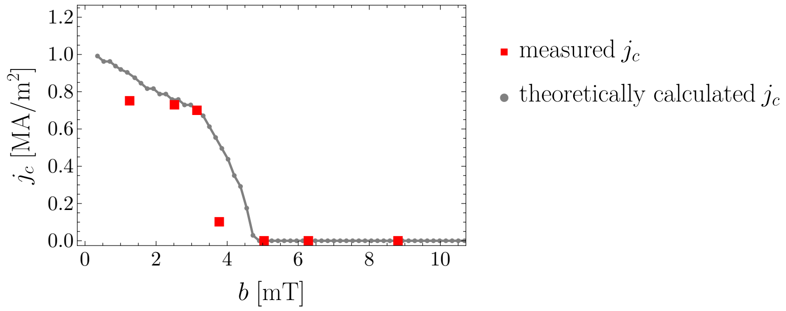

Figure 67: Drop of the critical current for the anisotropic surface pinning model. Red squares denote the experimental data taken from Ref. [98], grey circles is the theoretical data with parameters $F^{p,st}/(LF^{p,b}) = 10.5$, $\omega/\omega_0 = 2.32$, $\alpha\mathcal{D}/\mathcal{G} = 0.1$, $F^{p,sb}/(LF^{p,b}) = 0.7$, $\beta\mathcal{D}/\mathcal{G} = 0.07$.

Summary and Outlook

In this Chapter, we have thoroughly studied the rich non-equilibrium phase diagram of a skyrmion lattice under simultaneous application of a shaking field and external current. We show that because of the shaking pinning is effectively gone so the depinning current for the translational motion of a skyrmion lattice vanishes. In order to explain this striking phenomenon theoretically, we used an effective slip–stick model for the bending and motion of the skyrmion lines, which turns out to be sufficient to explain the main experimental findings. We predict the existence of walking and running phases, in which skyrmion lines are depinned due to the shaking field. It is for this reason, that the critical current drops to zero in these phases. We compare our findings with the measurements on the increase of the real part of transverse susceptibility in MnSi. Although we can qualitatively capture the drop of the critical current, the exact shape of the transverse susceptibility at small currents does not match our predictions. More precisely, a non-analyticity of $|j|$ type appears. This effect lies outside our mean-field description, so further theoretical and experimental studies are needed to better understand this phenomenon.

Part III

Net Motion Under Oscillating Fields

8 | Onset of a Net Motion Under Oscillating Fields

> "Nothing happens until something moves."
>
> Albert Einstein

In the last Chapters, we have modelled the motion of the skyrmion line under the inversion-symmetric part of the free energy for the displacement of elastic lines. Therefore, no directed motion of the skyrmion line was possible within this theory even in the unpinned phase. One may, however, ask if it is possible to make use of the intrinsic non-reciprocity of the skyrmion-hosting materials to make skyrmions walk under the applied oscillating magnetic fields. In this Chapter, we find the conditions under which such motion becomes possible, therefore paving the way for the creation of a non-reciprocal dynamic state of matter. Further, we argue that the non-linearity of the Thiele equation is crucial for this motion to exist. This nonlinearity can be implemented with the help of either higher-order gradient terms or with the help of pinning. We claim that motion due to pinning is, rather unintuitively, more efficient than motion due to higher-order gradient terms. Therefore, pinning turns out to be a friend instead of being a foe.

Some parts of the work presented in this Chapter has been conducted in collaboration with Hannah Dürschmidt in the context of her Bachelor Thesis, co-supervised by the author of this Thesis.

8.1 Symmetries of the Skyrmion Lattice

When speaking about symmetries of the skyrmion lattice, we need to be careful to differentiate between symmetries of the free energy (which must respect the symmetries of underlying microscopic Hamiltonian) and symmetries of the equations which describe dynamics, in our case the Thiele equation. The first relevant symmetry is the translation invariance: if the skyrmion lattice moves in space, the energy shall remain unchanged. It is a Goldstone mode of the system. Due to this constraint, solely terms including only derivatives of the displacement function, such as $\partial_z \boldsymbol{u}(z,t), \partial_z^2 \boldsymbol{u}(z,t), \dots$, are allowed. Moreover, the microscopic Hamiltonian is invariant under combined rotations of real and spin spaces around the z-axis [121]. Furthermore, in the presence of a transverse magnetic field the combined application of rotation around the y axis by π and time reversal is a valid symmetry.

Importantly, the complete expression of the free energy is not invariant under the inversion symmetry for chiral magnets. However, both the free energy functional in the lowest gradient expansion, as well as the respective equations of motion (see Sec. 5.5) are invariant under inversion for the case of isotropic pinning. This can be seen via direct computation by substituting $\boldsymbol{r} \to -\boldsymbol{r}$, $\boldsymbol{u} \to -\boldsymbol{u}$:

$$\boldsymbol{\mathcal{G}} \times \dot{\boldsymbol{u}}(z,t) + \alpha D \dot{\boldsymbol{u}}(z,t) = -\frac{\delta \mathcal{F}(\boldsymbol{u}(z,t), \boldsymbol{B}(t))}{\delta \boldsymbol{u}(z,t)} + \boldsymbol{F}^p(\boldsymbol{u}(z,t))$$

$$\xrightarrow{\text{Inversion}} \boldsymbol{\mathcal{G}} \times (-\dot{\boldsymbol{u}}(-z,t)) + \alpha D(-\dot{\boldsymbol{u}}(-z,t)) = -\frac{\delta \mathcal{F}(-\boldsymbol{u}(-z,t), \boldsymbol{B}(t))}{\delta(-\boldsymbol{u}(-z,t))} + \boldsymbol{F}^p(-\boldsymbol{u}(-z,t)) \,.$$

We treat the terms on the right hand side of this equation separately. The free energy is unchanged, as can be shown via direct calculation

$$\begin{aligned} -\frac{\delta \mathcal{F}(-\boldsymbol{u}(-z,t), \boldsymbol{B}(t))}{\delta \boldsymbol{u}(-z,t)} &= \epsilon_0 \frac{\partial^2(-\boldsymbol{u})}{\partial(-z)^2} - \epsilon_0 \left[\delta\left(-z - \tfrac{L}{2}\right) - \delta\left(-z + \tfrac{L}{2}\right)\right] \left(\frac{-\partial \boldsymbol{u}}{-\partial z} - \frac{\boldsymbol{B}_x(t)}{B_z}\right) \\ &= -\frac{\delta \mathcal{F}(\boldsymbol{u}(z,t), \boldsymbol{B}(t))}{\delta \boldsymbol{u}(z,t)} \,. \end{aligned}$$

We use the expression for the pinning force in the bulk from Eq. (5.24) and use the definition $\boldsymbol{F}^{p,b}(\boldsymbol{u}(z,t)) = -F_c^{p,b} \frac{\dot{\boldsymbol{u}}(z,t)}{|\dot{\boldsymbol{u}}(z,t)|}$ to obrain

$$\boldsymbol{F}^{p,b}(-\boldsymbol{u}(-z,t)) = -\boldsymbol{F}^p(\boldsymbol{u}(z,t)) \,. \tag{8.1}$$

The total pinning force can then be found from

$$\begin{aligned} \boldsymbol{F}^p(-\boldsymbol{u}(-z,t)) &= -\boldsymbol{F}^p(\boldsymbol{u}(-z,t)) \\ &= -\left(\boldsymbol{F}^{p,b} + \delta\left(-z - \tfrac{L}{2}\right) \boldsymbol{F}^{p,s} + \delta\left(-z + \tfrac{L}{2}\right) \boldsymbol{F}^{p,s}\right) \\ &= -\left(\boldsymbol{F}^{p,b} + \delta\left(z + \tfrac{L}{2}\right) \boldsymbol{F}^{p,s} + \delta\left(z - \tfrac{L}{2}\right) \boldsymbol{F}^{p,s}\right) \\ &= -\boldsymbol{F}^p(\boldsymbol{u}\,(z,t)) \,. \end{aligned} \tag{8.2}$$

Thus, every term in the Thiele equation receives a minus sign. After canceling this minus sign we obtain the original Thiele equation. Because of this inversion symmetry, no directed motion of skyrmion lines in space is possible in the case of an isotropic pinning. For anisotropic pinning, inversion symmetry is explicitly broken, because the two ends of the line experience different pinning. Still, even in this case there is no directed motion possible under $\cos(\omega t)$ drive, as we shall see in the upcoming Section. We proceed to define the velocities of the directed motion of skyrmion lines and reveal one additional symmetry which hinders its motion.

8.2 Directed Motion of Skyrmion Lines

In the previous Section we have shown, that the equation of motion for skyrmion lines is invariant under inversion for the case of symmetric pinning, so that no net motion in space is possible. In order to examine when such motion becomes possible, we introduce two definitions of the average velocity, $\langle \boldsymbol{v} \rangle$, of a line for a general drive with period T. The first one is the local velocity

$$\langle \boldsymbol{v} \rangle_t = \lim_{t_0 \to \infty} \frac{1}{T} \int_{t_0}^{t_0+T} \boldsymbol{v}(z,t)\, dt\,. \tag{8.3}$$

Here t_0 is an arbitrarily chosen point of time[9]. If this quantity is non-zero for every point of the line, a skyrmion line will move in space. Another definition of the average velocity $\langle \boldsymbol{v} \rangle_2$ is given by

$$\langle \boldsymbol{v} \rangle_{z,t} = \lim_{t_0 \to \infty} \frac{1}{T} \int_{t_0}^{t_0+T} dt\, \frac{1}{L} \int_{-\frac{L}{2}}^{\frac{L}{2}} \boldsymbol{v}(z,t)\, dz\ , \tag{8.4}$$

where we integrate both over one period and length of a skyrmion line. In the following we consider the average velocity separately for the case of (i) isotropic and (ii) anisotropic pinnings.

(i) Isotropic surface pinning

From our previous discussion it is already clear, that if the dynamics of the line is invariant under inversion $\boldsymbol{r} \to -\boldsymbol{r}$ and $\boldsymbol{u}(z,t) \to -\boldsymbol{u}(-z,t)$ (note that magnetic field does not change under inversion $\boldsymbol{B}(t) \to \boldsymbol{B}(t)$), the directed motion of the line is impossible. We show explicitly with the help of direct calculation that the average velocity in the second definition, given by Eq. (8.4), vanishes:

$$\int_{-\frac{L}{2}}^{\frac{L}{2}} \boldsymbol{v}(z,t)\, dz = \int_{-\frac{L}{2}}^{0} \boldsymbol{v}(z,t)\, dz + \int_{0}^{\frac{L}{2}} \boldsymbol{v}(z,t)\, dz = \int_{-\frac{L}{2}}^{0} \boldsymbol{v}(z,t)\, dz - \int_{-\frac{L}{2}}^{0} \boldsymbol{v}(-z,t)\, d(-z) = 0\,.$$

$$\Longrightarrow \langle \boldsymbol{v} \rangle_{z,t} = \frac{1}{T} \int_{t_0}^{t_0+T} dt\, \frac{1}{L} \int_{-\frac{L}{2}}^{\frac{L}{2}} \boldsymbol{v}(z,t)\, dz = 0\,.$$

We therefore conclude that for the case of symmetric pinning, no motion of the skyrmion line in space is possible.

(ii) Anisotropic pinning

Anisotropic pinning explicitly breaks the inversion symmetry. However, even in this case no directed motion under $\cos(\omega t)$ drive is possible due to a hidden symmetry of the equation of motion. This symmetry is a rotation with π around z axis $\mathcal{R}_{z,\pi}$, together with a translation in time with a half period $\frac{T}{2}$, $\mathcal{T}_{t,\frac{T}{2}}$. Let us check, if the Thiele equation obeys this symmetry.

---

[9] For the numerical implementation, it is important to wait sufficiently long until all initial state effects have vanished, hence $\lim_{t_0 \to \infty}$.

After rotation with π around z axis $\mathcal{R}_{\pi,z}$ we obtain from the Thiele equation

$$\boldsymbol{\mathcal{G}} \times (-\dot{\boldsymbol{u}}(z,t)) + \alpha D(-\dot{\boldsymbol{u}}(z,t)) = -\frac{\delta \mathcal{F}(-\boldsymbol{u}(z,t), \boldsymbol{B}(t))}{\delta(-\boldsymbol{u}(z,t))} - \boldsymbol{F}^p(-\boldsymbol{u}(z,t)) \,.$$

Using the previously discussed relations Eq (8.1) we find

$$\boldsymbol{\mathcal{G}} \times \dot{\boldsymbol{u}}(z,t) + \alpha D\dot{\boldsymbol{u}}(z,t) = -\frac{\delta \mathcal{F}(-\boldsymbol{u}(z,t), \boldsymbol{B}(t))}{\delta \boldsymbol{u}(z,t)} - \boldsymbol{F}^p(\boldsymbol{u}(z,t)) \,.$$

The free energy can be dealt with separately. First, we notice $\mathcal{F}(-\boldsymbol{u}(z,t), \boldsymbol{B}_x(t)) = \mathcal{F}(\boldsymbol{u}(z,t), -\boldsymbol{B}_x(t))$ and then calculate

$$\begin{aligned}\mathcal{F}(\boldsymbol{u}(z,t), -\boldsymbol{B}(t)) &= -\frac{\gamma}{2}(-\boldsymbol{B}_x(t))^2 + \frac{\epsilon}{2}\int_{-\frac{L}{2}}^{\frac{L}{2}} dz \left(\partial_z \boldsymbol{u}(z,t) - \frac{(-\boldsymbol{B}_x(t))}{B_z'}\right)^2 \\ &= -\frac{\gamma}{2}\left[\boldsymbol{B}_x\left(t+\frac{T}{2}\right)\right]^2 + \frac{\epsilon}{2}\int_{-\frac{L}{2}}^{\frac{L}{2}} dz \left(\partial_z \boldsymbol{u}(z,t) - \frac{\boldsymbol{B}_x(t+\frac{T}{2})}{B_z'}\right)^2 .\end{aligned}$$

Thus, we obtain

$$\boldsymbol{\mathcal{G}} \times \dot{\boldsymbol{u}}(z,t) + \alpha D\dot{\boldsymbol{u}}(z,t) = -\frac{\delta \mathcal{F}(\boldsymbol{u}(z,t), \boldsymbol{B}(t+\frac{T}{2}))}{\delta \boldsymbol{u}(z,t)} - \boldsymbol{F}^p(\boldsymbol{u}(z,t)) \,.$$

If the magnetic field has the property $\boldsymbol{B}_x(t) = -\boldsymbol{B}_x\left(t+\frac{T}{2}\right)$, we conclude that the free energy is invariant under the combined transformation $\mathcal{R}_{z,\pi} \cdot \mathcal{T}_{t,\frac{T}{2}}$.

Furthermore, if the magnetic field has this property, the velocity obeys

$$\boldsymbol{v}\left(z, t+\frac{T}{2}\right) = -\boldsymbol{v}(z,t) \,. \tag{8.5}$$

Then one can prove using the first definition of average velocity $\langle \boldsymbol{v} \rangle_t$ that a net motion is not possible:

$$\begin{aligned}\int_{t_0}^{t_0+T} \boldsymbol{v}(z,t)\,dt &= \int_{t_0}^{t_0+\frac{T}{2}} \boldsymbol{v}(t)\,dt + \int_{t_0}^{t_0+\frac{T}{2}} \boldsymbol{v}(z,t-\frac{T}{2})\,dt \\ &= \int_{t_0}^{t_0+\frac{T}{2}} \boldsymbol{v}(z,t)\,dt + \int_{t_0}^{t_0+\frac{T}{2}} \boldsymbol{v}(z,t+\frac{T}{2})\,dt = 0 \\ \Longrightarrow \langle \boldsymbol{v} \rangle_1 &= \frac{1}{T}\int_{t_0}^{t_0+T} \boldsymbol{v}(z,t)\,dt = 0 \,.\end{aligned}$$

Therefore, the net movement in space is possible only if this symmetry is broken. This can be achieved if the magnetic field $\boldsymbol{B}_x B(t)$ has non-zero higher harmonics. The simplest example of such field is the oscillation field of the form $\boldsymbol{B}_x(t) = b_1 \cos(\omega t) + b_2 \cos(2\omega t)$, which we will use later in Section 8.5 to find numerically a movement of the line.

Note that for the rest of this Chapter, we concentrate only on the case of isotropic pinning.

8.3 Higher Order Terms in the Free Energy

As was shown in the previous Section, if one considers only the lowest gradient term of the free energy, no net motion in space is possible because of the inversion symmetry for the isotropic pinning case. However, there are higher-order terms in the free energy expansion, which break the inversion symmetry. Some of the higher-order terms have been already introduced in Section 5.2. However, it was argued that they are suppressed by the powers of large length of skyrmions L. In this Section, we find the form of the low-order non-linear terms and find their scaling with L.

To find all symmetry-allowed terms for higher gradient expansion of the free energy, there are two possible paths one can take. The first path is based on searching the invariants and the second path is from the microscopic Hamiltonian. In both cases, the higher order terms should obey the symmetries of the underlying Hamiltonian.

The first path in order to find the higher order terms in free energy expansion, is based on finding all the quantities, which do not change under the symmetry transformations, discussed earlier in Sec. 8.1. We recall, that we have chosen a parametrisation of the displacement of the skyrmion lines $\boldsymbol{u}(z,t)$ given by

$$\begin{pmatrix} u_x(z) \\ u_y(z) \\ z \end{pmatrix} = \boldsymbol{u}(z) \in \mathbb{R}^3 \,. \tag{8.6}$$

Equivalently, one can choose another parametrization of the line, such as $\boldsymbol{u}(\lambda)$. Geometric invariants, such as length, curvature, etc. do not change under different parametrisations. Our goal is to find the geometric invariants, which obey the symmetries of the underlying spin system. Note however, that we will not be able to find the exact value of prefactors using this method, but rather the general form of these terms.

1. The first invariant is the length of the line. For two different parametrisations $\boldsymbol{u}(\lambda)$, $\boldsymbol{u}(\lambda')$ we obtain

$$\int \sqrt{\left(\frac{\partial \boldsymbol{u}}{\partial \lambda}\right)^2} d\lambda = \int \sqrt{\left(\frac{\partial \boldsymbol{u}}{\partial \lambda'}\frac{\partial \lambda'}{\partial \lambda}\right)^2} \frac{\partial \lambda}{\partial \lambda'}\, d\lambda' = \int \sqrt{\left(\frac{\partial \boldsymbol{u}}{\partial \lambda'}\right)^2} d\lambda' \,. \tag{8.7}$$

Therefore, this term is invariant under change of parametrization. For the parametrisation given by Eq. (8.6) one gets

$$\int \sqrt{1+(u_x')^2+(u_y')^2}\,dz \approx \int \left(1+\frac{1}{2}\left(u_x'^2+u_y'^2\right)-\frac{1}{8}\left(u_x'^2+u_y'^2\right)^2\right)dz\,. \tag{8.8}$$

Here it is important to differentiate a single skyrmion line versus a lattice of skyrmion lines. For a single skyrmion line, this term will produce a tension for non-spherical samples: under an applied magnetic field, competition between a line following the magnetic field and one returning to the position of zero deviation will be created. The length, rather counter-intuitively, is not an invariant for a lattice of skyrmion lines. If the lattice, for example, rotates under the applied shaking field, the length of skyrmion lines changes. This will produce a change in the energy density, which breaks the rotational invariance. We therefore believe that this term is not present for bulk skyrmion lattices.

2. The second invariant is the total magnetisation

$$\int \boldsymbol{B}\frac{\partial \boldsymbol{u}}{\partial \lambda}\,d\lambda = \boldsymbol{B}(\boldsymbol{u}_t-\boldsymbol{u}_b)\,, \tag{8.9}$$

where $\boldsymbol{u}_t$ and $\boldsymbol{u}_b$ are the positions of the top and at the bottom of the line. As one can see, this term produces only a surface term.

3. The third important invariant is given by

$$\int \frac{\left(\boldsymbol{B}\frac{\partial \boldsymbol{u}}{\partial \lambda}\right)^2}{\sqrt{\left(\frac{\partial \boldsymbol{u}}{\partial \lambda}\right)^2}}\,d\lambda\,. \tag{8.10}$$

For the parametrisation given by Eq. (8.6) and $B_y=0$ we obtain

$$\int \frac{\left(\boldsymbol{B}\frac{\partial \boldsymbol{u}}{\partial \lambda}\right)^2}{\sqrt{\left(\frac{\partial \boldsymbol{u}}{\partial \lambda}\right)^2}}\,d\lambda \approx \int (B_x(t)u_x'+B_z)^2\left(1-\frac{1}{2}|\boldsymbol{u}'|^2\right)dz\,. \tag{8.11}$$

This invariant produces the free energy at lowest order which was derived in Sec. 5.2.

4. The forth invariant is related to the curvature of the line

$$\int \frac{\sqrt{\left(\frac{\partial \boldsymbol{u}}{\partial \lambda}\times\frac{\partial^2 \boldsymbol{u}}{\partial \lambda^2}\right)^2}}{\sqrt{\left(\frac{\partial \boldsymbol{u}}{\partial \lambda}\right)^2}}d\lambda\,. \tag{8.12}$$

It is invariant because of the property

$$\frac{\partial^2 \boldsymbol{u}}{\partial \lambda^2} = \frac{\partial}{\partial \lambda}\left(\frac{\partial \boldsymbol{u}}{\partial \lambda'}\frac{\partial \lambda'}{\partial \lambda}\right) = \frac{\partial^2 \boldsymbol{u}}{\partial \lambda'^2}\frac{\partial \lambda'}{\partial \lambda} + \frac{\partial \boldsymbol{u}}{\partial \lambda'}\frac{\partial^2 \lambda'}{\partial \lambda^2}\,. \tag{8.13}$$

The cross product with the second term vanishes. Using the parametrisation from Eq. (8.6) we obtain

$$\int \frac{\sqrt{\left(\frac{\partial \boldsymbol{u}}{\partial \lambda} \times \frac{\partial^2 \boldsymbol{u}}{\partial \lambda^2}\right)^2}}{\sqrt{\left(\frac{\partial \boldsymbol{u}}{\partial \lambda}\right)^2}} d\lambda \approx \int |\boldsymbol{u}''|^2 dz\,. \tag{8.14}$$

5. The fifth invariant is given by

$$\int \frac{\boldsymbol{B}\left(\frac{\partial \boldsymbol{u}}{\partial \lambda} \times \frac{\partial^2 \boldsymbol{u}}{\partial \lambda^2}\right)}{\sqrt{\left(\frac{\partial \boldsymbol{u}}{\partial \lambda}\right)^2}} d\lambda\,. \tag{8.15}$$

For $B_y = 0$ and Eq. (8.6) we get

$$\int \left(-B_x u_y'' + B_z(u_x' u_y'' - u_y' u_x'')\right) dz = \int \left(-B_x u_y'' + B_z \hat{\boldsymbol{z}} \cdot (\boldsymbol{u}' \times \boldsymbol{u}'')\right)\, dz\,. \tag{8.16}$$

From the invariants above we conclude that up to quadratic order, terms of the form $|\boldsymbol{u}'|^2$, $[\boldsymbol{u}' \times \boldsymbol{u}'']_z$ and $|\boldsymbol{u}''|^2$ will appear. Using these invariants we may also predict the general form of the nonlinear terms. Up to fourth order, the increase of the free energy due to a bending in the shaking field reads

$$\mathcal{F} = \pi \cdot \int_{-L/2}^{L/2} \left(F^{(1)} + F^{(2)} + F^{(3)} + F^{(4)} + \ldots\right) dz\,, \tag{8.17}$$

$$\begin{aligned}
F^{(1)} &= \tilde{b}(c_{11} u_x' + c_{12} u_y'')\,,\\
F^{(2)} &= c_{21}|\boldsymbol{u}'|^2 + c_{22}[\boldsymbol{u}' \times \boldsymbol{u}'']_z + c_{23}|\boldsymbol{u}''|^2\,,\\
F^{(3)} &= \tilde{b}(c_{31} u_x' |\boldsymbol{u}'|^2 + c_{32} u_y'' |\boldsymbol{u}'|^2 + c_{33} u_x' [\boldsymbol{u}' \times \boldsymbol{u}'']_z)\,,\\
F^{(4)} &= -c_{41}|\boldsymbol{u}'|^4 - c_{42}|\boldsymbol{u}'|^2[\boldsymbol{u}' \times \boldsymbol{u}'']_z\,.
\end{aligned}$$

Note that this free energy contains all terms allowed by symmetry for skyrmion lines. In the equations before it holds that $\tilde{b} = \frac{b}{B_z'}$. From $F^{(1)}$ we only obtain surface terms after integration, while all other terms produce the forces in the bulk. Moreover, in the absence of a transverse magnetic field, the resulting expression has only the second and fourth order terms. This can be explained by the symmetry of the Hamiltonian with respect to arbitrary rotations within the xy-plane. If the magnetic field is present, this symmetry is broken. The leading fourth order term has a negative sign, as can be seen, for example, from fluctuations of the stiffness in second-order perturbation theory [121].

Note that the presence of inversion-symmetry-breaking terms, such as $[\boldsymbol{u}' \times \boldsymbol{u}'']_z$, reflects the non-reciprocity of the skyrmion lattice [121, 122]. It was predicted theoretically [123] and observed experimentally [124], for example in magnon dispersion. It thereby provides a direct way to determine the strength of the DMI in non-centrosymmetric magnets.

Interestingly, one can obtain the same expansion using the approach taken in Ref. [122]. In this paper, the nonlinear terms for a single skyrmion line dynamics has been studied. The idea is to derive this terms starting from magnetic interactions present for cubic chiral magnets. For the precise form of the coefficients obtained using this method, see Appendix D.

In the next Section, we investigate if net motion of the lattice under oscillating magnetic fields is possible due to nonliner terms in the free energy without pinning.

8.4 Net motion Without Pinning

In this Section, we discuss the motion of skyrmion lattices in transverse oscillating magnetic field in the absence of pinning.

Let us first consider only the second-order terms in the free energy

$$\mathcal{F} = -\frac{\gamma}{2}\boldsymbol{B}_x(t)^2 + \int_{-\frac{L}{2}}^{\frac{L}{2}} dz \left[\frac{\epsilon_0}{2}\left(\partial_z \boldsymbol{u} - \frac{\boldsymbol{B}_x(t)}{B_z}\right)^2 + \epsilon_3 \hat{z} \cdot \left(\partial_z \boldsymbol{u} \times \partial_z^2 \boldsymbol{u}\right) + \epsilon_4 (\partial_z^2 \boldsymbol{u})^2\right]. \quad (8.18)$$

Here the second term $\hat{z} \cdot (\partial_z \boldsymbol{u} \times \partial_z^2 \boldsymbol{u})$ explicitly breaks the inversion symmetry. In the absence of pinning, the resulting equations of motion are linear. To see this, we calculate first the functional derivative $-\frac{\delta \mathcal{F}(\boldsymbol{u}(z,t)}{\delta \boldsymbol{u}(z,t)}$. The corresponding forces are presented in the second column of Table 2. The Thiele equation then reads

$$\boldsymbol{\mathcal{G}} \times \dot{\boldsymbol{u}}(z,t) + \alpha \mathcal{D} \dot{\boldsymbol{u}}(z,t) = 2c_{21}\boldsymbol{u}'' + 2c_{22}\hat{\boldsymbol{z}} \times \boldsymbol{u}^{(3)} - 2c_{23}\boldsymbol{u}^{(4)}. \quad (8.19)$$

Here $\boldsymbol{u}^{(3)}$ and $\boldsymbol{u}^{(4)}$ denote the third and fourth derivative with respect to z, respectively. The resulting equation is linear in $\boldsymbol{u}(z,t)$. Therefore, under the external periodic drive $\boldsymbol{B}_x(t) = \sum_n b^{(n)} e^{in\omega t}\hat{x}$, the solution will be given by $u_x(z,t) \propto \sum_n u_x^{(n)} e^{in\omega t}$, $u_y(z,t) \propto \sum_n u_y^{(n)} e^{in\omega t}$ and no directed motion is space is possible.

Therefore, we need some form of non-linearity in order to make skyrmion lines move in space. Let us first consider all non-linear terms which appear in Eq. (8.17). The resulting forces in the bulk can be found again in the second column of the Table 2. However, not all terms are equally important. To see this, we introduce the following rescaling of variables $u = u_0\tilde{u}$, $z = L\tilde{z}$. The resulting prefector of each term is given in the third column of Table 2. The variables $\tilde{u}$ and $\tilde{z}$ are dimensionless. From equating the prefactors before the terms which come from the leading second order force $|\boldsymbol{u}'|^2$ and the leading forth order force

Term	Force in the bulk	Prefactor	$u_0 = \sqrt{\frac{c_{21}}{2c_{41}}}L$
$\lvert \boldsymbol{u}' \rvert^2$	$2c_{21}\boldsymbol{u}''$	$2c_{21}\frac{u_0}{L^2}$	$c_{21}\sqrt{\frac{2c_{21}}{c_{41}}}\frac{1}{L}$
$[\boldsymbol{u}' \times \boldsymbol{u}'']_z$	$2c_{22}\hat{\boldsymbol{z}} \times \boldsymbol{u}^{(3)}$	$2c_{22}\frac{u_0}{L^3}$	$c_{22}\sqrt{\frac{2c_{21}}{2c_{41}}}\frac{1}{L^2}$
$\lvert \boldsymbol{u}'' \rvert^2$	$-2c_{23}\boldsymbol{u}^{(4)}$	$-2c_{23}\frac{u_0}{L^4}$	$-c_{23}\sqrt{\frac{2c_{21}}{2c_{41}}}\frac{1}{L^3}$
$u'_x \lvert \boldsymbol{u}' \rvert^2$	$\tilde{b}c_{31}\left((3u'^2_x + u'^2_y)'\hat{\boldsymbol{x}} + 2(u'_x u'_y)'\hat{\boldsymbol{y}}\right)$	$2\tilde{b}c_{31}\frac{u_0^2}{L^3}$	$\tilde{b}c_{31}\frac{c_{21}}{c_{41}}\frac{1}{L}$
$u''_y \lvert \boldsymbol{u}' \rvert^2$	$2\tilde{b}c_{32}(u'_x\hat{\boldsymbol{z}} \times \boldsymbol{u}'')'$	$2\tilde{b}c_{32}\frac{u_0^2}{L^4}$	$\tilde{b}c_{32}\frac{c_{21}}{c_{41}}\frac{1}{L^2}$
$u'_x[\boldsymbol{u}' \times \boldsymbol{u}'']_z$	$3\tilde{b}c_{33}(u'_x\hat{\boldsymbol{z}} \times \boldsymbol{u}'')'$	$3\tilde{b}c_{33}\frac{u_0^2}{L^4}$	$\tilde{b}c_{33}\frac{3c_{21}}{2c_{41}}\frac{1}{L^2}$
$\lvert \boldsymbol{u}' \rvert^4$	$-4c_{41}(\boldsymbol{u}'\lvert \boldsymbol{u}' \rvert^2)'$	$-4c_{41}\frac{u_0^3}{L^4}$	$-4c_{41}(\frac{c_{21}}{2c_{41}})^{3/2}\frac{1}{L}$
$\lvert \boldsymbol{u}' \rvert^2[\boldsymbol{u}' \times \boldsymbol{u}'']_z$	$-4c_{42}(\hat{\boldsymbol{z}} \times \boldsymbol{u}''\lvert \boldsymbol{u}' \rvert^2)'$	$-4c_{42}\frac{u_0^3}{L^5}$	$-4c_{42}(\frac{c_{21}}{2c_{41}})^{3/2}\frac{1}{L^2}$

Table 2: Nonlinear terms from the expression of the free energy. In the third column the prefactor after rescaling is given.

$|\boldsymbol{u}'|^2$, we obtain the relation $u_0 = \sqrt{\frac{c_{21}}{2c_{41}}}L$. Using this relation, we obtain a final prefactor for every term in the fourth column of Table 2. For long skyrmions lines, most of the terms will be suppressed in higher powers of $\frac{1}{L}$. The three leading order terms are the terms proportional to $\frac{1}{L}$. Furthermore, the third-order term is suppressed with $\tilde{b}$. Therefore, we finally obtain

$$\hat{\boldsymbol{z}} \times \dot{\tilde{\boldsymbol{u}}}(\tilde{z}, \tilde{t}) + \frac{\alpha D}{\mathcal{G}}\dot{\tilde{\boldsymbol{u}}}(\tilde{z}, \tilde{t}) = \tilde{\boldsymbol{u}}'' - (\tilde{\boldsymbol{u}}'|\tilde{\boldsymbol{u}}'|^2)' \,.$$

Here we used the rescaling of time $t_0 = \frac{\mathcal{G}L^2}{2c_{21}}$. This equation defines the dynamics of skyrmions for long skyrmion strings. Surprisingly, no net motion of the skyrmion lattice is possible only with the help of nonlinearities, which come from terms of the free energy of the form $-\frac{\delta\mathcal{F}(\boldsymbol{u}(z,t)}{\delta\boldsymbol{u}(z,t)}$. The fundamental reason for this is that in this case, the total momentum of the skyrmion lattice is conserved. In Ref. [125] we find the following expression for the momentum

$$\boldsymbol{P}^{\text{skyr}}_{\alpha} = \frac{4\pi\hbar}{a^2}\epsilon_{0\alpha\beta}\boldsymbol{R}_{\beta} \,. \tag{8.20}$$

Here $\boldsymbol{R}$ is the skyrmion coordinate and a is a typical distance between the magnetic moments. The Thiele equation (without the pinning) can be rewritten in the following form

$$\dot{\boldsymbol{P}}^{\text{skyr}} = \boldsymbol{F}, \tag{8.21}$$

where $\boldsymbol{F}$ describes the forces, which act on the skyrmions. However, there is no flow of momentum to the skyrmion lines because of the terms produced from the free energy from oscillating magnetic field. Thus, we again conclude that in this case any directed motion is prohibited.

To set skyrmions into motion, we require another type of nonlinearity. Let us consider the nonlinearity, which comes from the gyroscopic $\boldsymbol{\mathcal{G}}$ and dissipation $\mathcal{D}$ tensors. These corrections are functionals of $\boldsymbol{u}'(z,t)$ and $\boldsymbol{u}''(z,t)$, multiplied by the velocity $\dot{\boldsymbol{u}}(z,t)$ in the Thiele equation. The exact form of these corrections can be found in Ref. [122]. We argue that, although a net motion will be possible in this case, the nonlinearity, which comes from the third and fourth order of the gradient expansion, will be relatively weak and it is suppressed by powers of $\frac{1}{L}$. On the contrary, a net motion in the theory with pinning is possible already for terms of second order of the free energy, as we will see in the next Section.

8.5 Numerical Results for the Net Motion

In this Section, we present numerical evidence for the net motion of the skyrmion line under an oscillating transverse magnetic field in a system with phenomenologically included pinning.

We return to Eq. (8.19) and consider the second order terms only. In addition we now introduce pinning to this equation. In rescaled variables $\tilde{\boldsymbol{u}} = \frac{\epsilon_0 F^{p,b}}{L^2}\boldsymbol{u}$, $\tilde{\omega} = \omega\frac{L^2\mathcal{G}}{\epsilon_0}$ the Thiele equation in the bulk up to second order reads

$$\hat{\boldsymbol{z}} \times \dot{\tilde{\boldsymbol{u}}} + \frac{\alpha D}{\mathcal{G}}\dot{\tilde{\boldsymbol{u}}} = \tilde{\boldsymbol{u}}'' + \epsilon_3 \hat{\boldsymbol{z}} \times \tilde{\boldsymbol{u}}^{(3)} - \epsilon_4 \tilde{\boldsymbol{u}}^{(4)} - \frac{\dot{\tilde{\boldsymbol{u}}}}{|\dot{\tilde{\boldsymbol{u}}}|}\,. \tag{8.22}$$

Here $\epsilon_3 = \frac{2c_{22}}{\epsilon_0 L}$ and $\epsilon_4 = \frac{c_{23}}{\epsilon_0 L^2}$. The drive again only enters at the boundary with a $\partial_{\tilde{z}}\tilde{\boldsymbol{u}} - \delta\tilde{B}\cos(\tilde{\omega}\tilde{t})\hat{\boldsymbol{x}}$ term. Here the rescaled field is $\delta B = \frac{\epsilon_0}{LF^{p,b}}\frac{B_x(t)}{B_z}$. Note, that there are also other more complicated boundary terms, which come from $-\frac{\delta\mathcal{F}(\boldsymbol{u}(z,t))}{\delta\boldsymbol{u}(z,t)}$. They can be found in Appendix D.

We solve the dynamics of this equation numerically using the method introduced in Section 6.1. For it, we approximate the higher-order derivatives using the finite-difference method. Moreover, from the Thiele equation we see that the third and the forth derivatives terms, $\epsilon_3 = \frac{2c_{22}}{\epsilon_0 L}$ and $\epsilon_4 = \frac{c_{23}}{\epsilon_0 L^2}$ are suppressed by powers of $\frac{1}{L}$. This does not come as a surprise since we have already seen this in Table 2. Thus, we choose a small numerical value for both ϵ_3 and ϵ_4.

We define the step of the skyrmion line in one period as $\Delta\tilde{u} = \sqrt{\Delta\tilde{u}_x^2 + \Delta\tilde{u}_y^2}$, where $\Delta\tilde{u}_x$ and $\Delta\tilde{u}_y$ indicate how far the skyrmion line is moved in one period. Because of the broken inversion symmetry due to the term proportional to ϵ_3, a movement of the line is possible even for symmetric surface pinning. For our numerical implementation, we set the surface pinning to zero, $\frac{F^{p,st}}{LF^{p,b}} = \frac{F^{p,sb}}{LF^{p,b}} = 0$. Furthermore, we use $\frac{\alpha\mathcal{D}}{\mathcal{G}} = 0.1$, number of descretisation points in z direction $N = 50$ and number of time steps N_{steps} from $2\cdot 10^6$ to

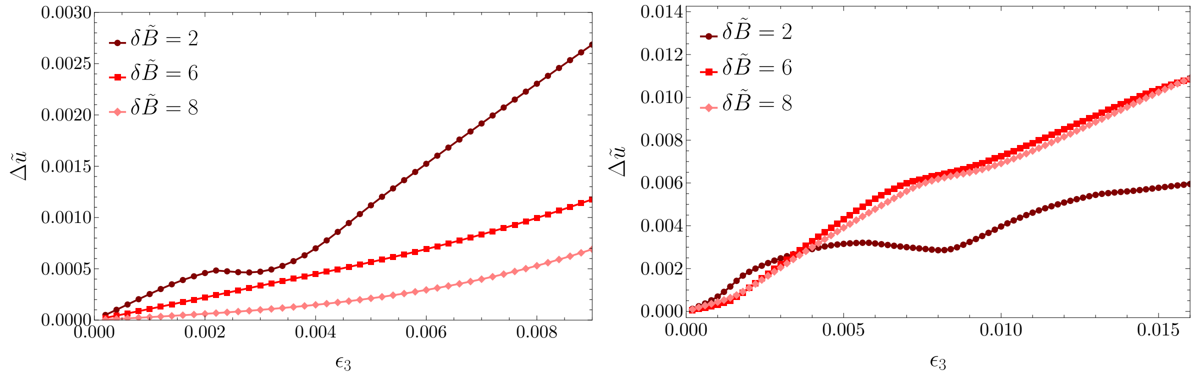

(a) (b)

Figure 68: Dependence of step $\Delta\tilde{u}$ for the driving function (a) $\delta\tilde{B}\left(\sin(\tilde{\omega}\tilde{t}) + \sin(2\tilde{\omega}\tilde{t})\right)$ and (b) $\delta\tilde{B}\left(\frac{\sin(\tilde{\omega}\tilde{t})}{2+\sin(\tilde{\omega}\tilde{t})}\right)$ for several values of magnetic field. Here $\epsilon_4 = 0.0002$, $\frac{\omega}{\omega_0} = 1.26$.

$4 \cdot 10^6$ (see Appendix B for more details on the convergence). Moreover, we note that the term proportional to ϵ_4 is crucial in order to avoid the instability in dispersion of $c_2k^2 + c_3k^3$ type for large k.

We used two different functions to model the the time drive. The first function is simply $\delta\tilde{B}(\sin(\tilde{\omega}\tilde{t}) + \sin(2\tilde{\omega t}))$, while the second function is $\delta\tilde{B}\left(\frac{\sin(\tilde{\omega}\tilde{t})}{2+\sin(\tilde{\omega}\tilde{t})}\right)$. The first function has only non-zero second harmonics, while the second has infinitely many higher harmonics. The step per period $\Delta\tilde{u}$ as a function of the inversion-breaking parameter ϵ_3 for several magnetic fields is depicted in Fig. 68 (left for the first function and right for the second). In the absence of the inversion-symmetry-breaking term ($\epsilon_3 = 0$), no motion is observed ($\Delta\tilde{u} = 0$) for both driving fields. For non-zero values of ϵ_3 we observe approximately linear behaviour with $\Delta\tilde{u} \approx 0.25\epsilon_3$ for the first drive and much larger $\Delta\tilde{u} \approx 1.5\epsilon_3$ for the second.

Further, in Fig. 69 we plot the dependence of steps in x and y directions, as well as the total step $\Delta\tilde{u}$ for varying strength of magnetic field $\delta\tilde{B}$ under the first drive. Although the form of the free energy is different from the one discussed in Sec. 5.6, there exist central

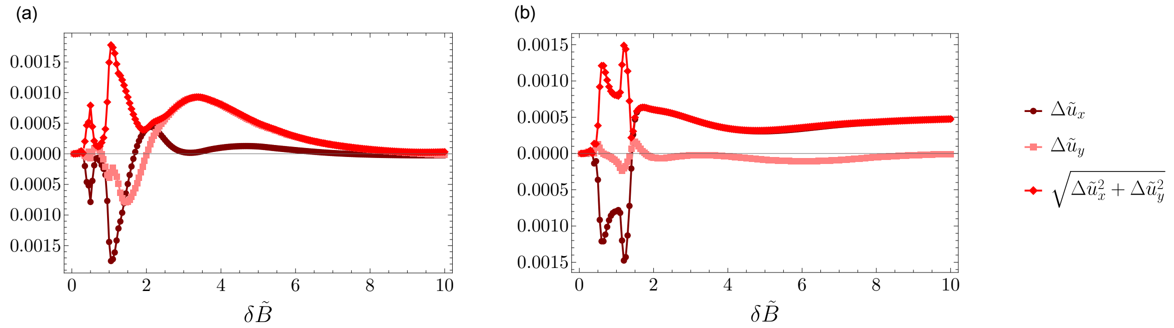

Figure 69: Dependence of steps $\Delta\tilde{u}_x$, $\Delta\tilde{u}_y$ and $\Delta\tilde{u}$ for the drive $\delta\tilde{B}\left(\sin(\tilde{\omega}\tilde{t}) + \sin(2\tilde{\omega}\tilde{t})\right)$ for (a) $\omega/\omega_0 = 1.26$ (b)$\omega/\omega_0 = 0.63$. Parameters used: $\epsilon_3 = 0.0025$ and $\epsilon_4 = 0.0001$.

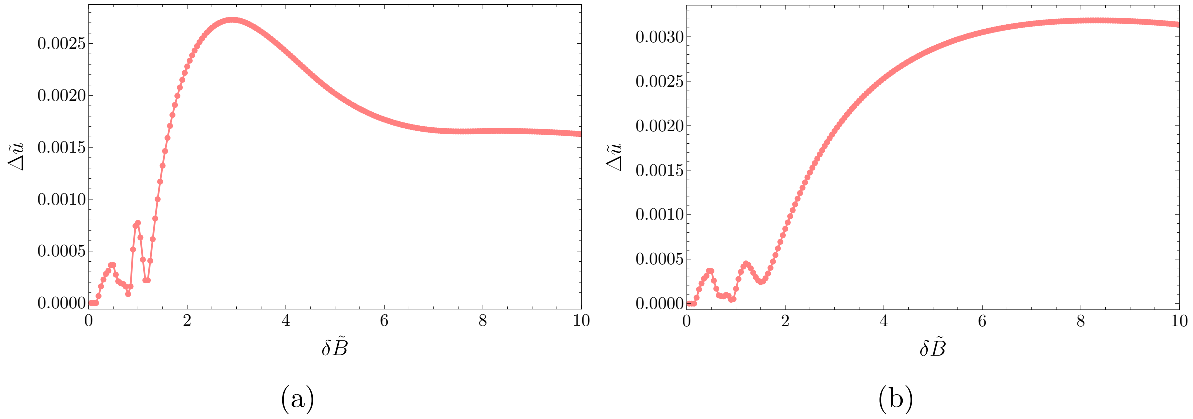

(a) (b)

Figure 70: Dependence of step $\Delta\tilde{u}$ for the drive $\delta\tilde{B}\left(\frac{\sin(\tilde{\omega}\tilde{t})}{2+\sin(\tilde{\omega}\tilde{t})}\right)$ for (a) $\frac{\omega}{\omega_0} = 1.26$ (b) $\frac{\omega}{\omega_0} = 0.63$. $\epsilon_3 = 0.0025$ and $\epsilon_4 = 0.0001$.

pinned phase for small magnetic field strength $\delta\tilde{B}$. For intermediate fields the dependence is rather complicated with two sharp peaks, which might be because of the resonances in the system. However, we have not been able to develop an analytic solution for this case. Moreover, for large magnetic fields the value of $\Delta\tilde{u}$ decreases. We expect, that in this regime skyrmion lines become straighter and the effect of higher-order derivatives becomes negligible. However, the movement happens because of these terms. Therefore, we see that the step Δu decays. Moreover, we observe that for stronger fields line moves in x direction.

In Fig. 70 we present the dependence of the total step $\Delta\tilde{u}$ for varying strength of the magnetic field $\delta\tilde{B}$ for the second function. In this case, the absolute values are much larger. Moreover, we see that the general behavior is rather similar to the other drive. Although two peaks for intermediate field values are present, they are much less pronounced.

Now let us estimate the size of the step, which a skyrmion line will make in one period in the unscaled coordinates, $\Delta\tilde{u} = \frac{\epsilon_0}{F^{p,b}L^2}\Delta u$. We estimate

$$\Delta u = \Delta\tilde{u}\frac{F^{p,b}L^2}{\epsilon_0} = \frac{\epsilon_3}{\epsilon_0}\frac{\Delta\tilde{u}}{\epsilon_3}\frac{F^{p,b}L^2}{\epsilon_0} \sim \text{const.}\frac{R_s F^{p,b}L}{\epsilon_0} \approx \text{const.} \cdot 0,03 \cdot R_s \,.$$

For this estimate we replaced $\frac{\Delta\tilde{u}}{\epsilon_3}$ with a constant because of the approximately linear dependence of the step size $\Delta\tilde{u}$ on the parameter ϵ_3 (see Fig. 68). The value of this term can be estimated as $0,1\ldots1$ from the numerical simulations in the previous Section. We continue by replacing $\frac{\epsilon_3}{\epsilon_0}$ with the skyrmion radius R_s from dimensional analysis. Moreover, $\frac{F^{p,b}L}{\epsilon_0} \approx 0.03$ as found from the experimental data (see Fig. 46).

We can now compare this velocity to the velocity of the end of the line. If the line follows the magnetic field, we obtain

$$\Delta = \frac{B_x}{B_z}L\,.$$

From the rescaling $\delta\tilde{B} = \frac{\epsilon_0}{LF^{p,b}}\frac{B_x}{B_z}$ we obtain

$$\Delta = \frac{L^2 F^{p,b}}{\epsilon_0}\delta\tilde{B} \approx 0,03 \cdot L \cdot \delta\tilde{B}\,.$$

Using the parameters, found in the previous Chapter we obtain

$$\frac{\Delta u}{\Delta} \approx \text{const.}\frac{R_s}{\delta\tilde{B}L} \approx \text{const.} \cdot 10^{-5} \cdot \frac{1}{\delta\tilde{B}} \approx 10^{-3}\dots 10^{-5}\,. \tag{8.23}$$

We conclude that the velocity of the end of the line during its motion is much larger than the velocity of the net motion of the skyrmion lattice in the presence of the symmetry breaking terms.

Summary and Outlook

In order to understand when a net motion of skyrmion lines in the presence of an applied, oscillating magnetic field becomes possible, we started by analysing the symmetries of the skyrmion lattice. Apart from the inversion symmetry, which can prohibit such motion, we have found one hidden symmetry, constituted by a combination of $\pi-$rotation around the z axis and translation in time by a half period $\frac{T}{2}$. If these symmetries are broken, for example by an external magnetic field drive with higher harmonics, a net motion becomes possible. Furthermore, the Thiele equation of dynamics needs to contain nonlinear terms to activate such motion. Counter-intuitively, we argue that this motion will be more efficient with pinning due to the suppression of higher gradient terms in powers of the length of long skyrmion strings L. It will be interesting to understand the nature of the resonances, which appear for certain values of the driving field, in the future.

Conclusions

In this Thesis, we studied a new type of unpinning transition of skyrmion lattices under slowly oscillating transverse magnetic fields and external electric currents. We find that the skyrmion lattice exhibits an extremely rich non-equilibrium phase diagram already in mean-field approximation. Crucially, we find that the skyrmion lattice is in a weak pinning regime, consistent with ultralow critical current observations.

In the first Part of this Thesis, we described the low-energy collective excitation of the elastic skyrmion lattice using a Thiele-like approach to its dynamics. In doing so, we included pinning forces, due to disorder, by using a phenomenological model, as well as a surface pinning in our description of the dynamics of the skyrmion line. The surface pinning turned out to be a crucial ingredient to explaining the experimental observations of depinning with a transverse magnetic field. We have shown that within our model, the transverse magnetic field enters only at the boundary and competes with the surface pinning in order to depin the line. Already in the adiabatic limit (limit of slow drives), three phase transitions appear, the signatures of which we extracted from the experimental data from the group of Prof. Pfleiderer. The unpinning process exhibits a high degree of universality across metallic, as well as insulating skyrmion-hosting materials. Further, we speculate that the surface pinning might have an anisotropic nature.

In the second Part of this Thesis, we studied the dynamics of the skyrmion lattice in the presence of shaking fields and external currents. In this regime we have discovered two more phases, namely the walking and the running phases, where the skyrmion lattice is fully depinned and set into motion. Using our theoretical model, we successfully explained the striking observation that for a critical magnetic amplitude, the critical external current, needed to depin the skyrmion lattice via the shacking field, drops to zero.

In the third Part of the Thesis, we have shown that directed motion of skyrmion lines solely under periodic magnetic fields is possible due to intrinsic non-reciprocity of the skyrmion-hosting materials. This way an exotic non-reciprocal dynamic state of matter can be created. In order for such movement to be possible, nonlinearity needs to be present in the equations of motion. We argue that nonlinearity due to the pinning is an efficient mechanism to make such movement possible. Moreover, we discuss conditions on the periodic magnetic field for such state to exist.

Despite its success in capturing the main experimental observations in a qualitative manner, our mean-field theory has a number of limitations. First of all, our theory describes only a single domain, while in a real skyrmion-hosting material we expect that a number of domains can coexist. Our theory does not capture the possible breaking of skyrmion lines under oscillating fields and plastic depinning under strong currents. Similarly, some observed phenomena, such as the coexistence of pinned and depinned regions within the sample, are beyond the scope of this Thesis and might contribute to the observed non-analytic behaviour of the increase of the real susceptibility due to the current. Crucially, we do not include temperature effects such as creep. Temperature effects might explain the observed mismatch between the intensities at the origin for doped materials for theory and experiment. Moreover, in our theory, the critical value of the transverse magnetic field is independent of frequency, which differs from experimental observations.

Although in this Thesis we mainly discussed the regime of very slow drives, the intermediate regime of $10 - 10^5$ kHz might be of interest as well. Based on our theoretical studies we predicted the experimental observation of strong nonlinear harmonics in the skyrmion lattices. We hope that in the future, both this effect and the net motion of skyrmion lines solely due to a periodic magnetic field, will be detected in experiments.

Summarizing, during the course of this Thesis, we have been able to gain important new insights in the process of depinning of skyrmion lattices due to external drives.

References

[1] P. W. Anderson. More is different. *Science*, 177(4047):393–396, 1972.

[2] Complexity matters. *Nature Physics*, 18(8):843–843, 2022.

[3] A. N. Bogdanov and C. Panagopoulos. The emergence of magnetic skyrmions. *Physics Today*, 2020.

[4] T.H.R. Skyrme. A non-linear field theory. *Proceedings of the Royal Society of London. Series A, Mathematical and Physical Sciences*, 260(1300):127, 1961.

[5] T.H.R. Skyrme. A unified field theory of mesons and baryons. *Nucl. Phys.*, 31:556–569, 1962.

[6] N. Manton. *Skyrmions – A Theory of Nuclei.* World Scientific (Europe), 2022.

[7] I. E. Dzyaloshinskii. Theory of helicoidal structures in antiferromagnets. *Sov. Phys. JETP*, 19:960, 1964.

[8] L. D. Landau and E. M. Lifshitz. *Statistical Physics, Part 1.* Course of Theoretical Physics. Butterworth-Heinemann, Oxford, 1980.

[9] A.N. Bogdanov and D.A. Yablonskii. Thermodynamically stable "vortices" in magnetically ordered crystals. The mixed state of magnets. *Zh. Eksp. Teo. Fiz.*, 95:178–182, 1989.

[10] A. Bogdanov and A. Hubert. Thermodynamically stable magnetic vortex states in magnetic crystals. *J. Magn. Magn. Mat.*, 138:255–269, 1994.

[11] S. Tewari, D. Belitz, and T. R. Kirkpatrick. Blue quantum fog: Chiral condensation in quantum helimagnets. *Phys. Rev. Lett.*, 96:047207, 2006.

[12] I. Fischer, N. Shah, and A. Rosch. Crystalline phases in chiral ferromagnets: Destabilization of helical order. *Phys. Rev. B*, 77:024415, 2008.

[13] U. K. Rößler, A. N. Bogdanov, and C. Pfleiderer. Spontaneous skyrmion ground states in magnetic metals. *Nature*, 442(7104):797–801, 2006.

[14] S. Mühlbauer, B. Binz, F. Jonietz, C. Pfleiderer, A. Rosch, A. Neubauer, R. Georgii, and P. Böni. Skyrmion lattice in a chiral magnet. *Science*, 323:915, 2009.

[15] S. Buhrandt and L. Fritz. Skyrmion lattice phase in three-dimensional chiral magnets from Monte Carlo simulations. *Phys. Rev. B*, 88:195137, 2013.

[16] F. Jonietz, S. Mühlbauer, C. Pfleiderer, A. Neubauer, W. Münzer, A. Bauer, T. Adams, R. Georgii, P. Böni, R. A. Duine, K. Everschor, M. Garst, and A. Rosch. Spin transfer torques in MnSi at ultralow current densities. *Science*, 330:1648, 2010.

[17] N. D. Mermin. The topological theory of defects in ordered media. *Rev. Mod. Phys.*, 51:591–648, 1979.

[18] P. Mellado and R. Troncoso. *Topological Phenomena in Spin Systems: Textures and Waves*, chapter 9. IntechOpen, Rijeka, 2023.

[19] T. Lancaster. Skyrmions in magnetic materials. *Contemporary Physics*, 60(3):246–261, 2019.

[20] J. M. Han. *Skyrmions in Condensed Matter*, volume 278. Springer Tracts in Modern Physics, 2017.

[21] M. Kleman and J. Friedel. Disclinations, dislocations, and continuous defects: A reappraisal. *Rev. Mod. Phys.*, 80:61–115, 2008.

[22] J. Kosterlitz and D. Thouless. Ordering, metastability and phase transitions in two-dimensional systems. *Journal of Physics C: Solid State Physics*, 6(7):1181, 1973.

[23] V. L. Berezinsky. Destruction of long range order in one-dimensional and two-dimensional systems having a continuous symmetry group. *Sov. Phys. JETP*, 32:493–500, 1971.

[24] R. Moessner and J. E. Moore. *Topological Phases of Matter*. Cambridge University Press, 2021.

[25] X. S. Wang and X. R. Wang. *Topology in Magnetism*, pages 357–403. Springer International Publishing, Cham, 2021.

[26] Y. Shen. Topological quasiparticles of light: Optical skyrmions and beyond. *Wolfram Community*, 2022.

[27] Eunsung J., Danilo A., Dao P., and Xiao Z. Theoretical approach to predict the size of skyrmion. *Modern Concepts in Material Science*, 2(2), 2019.

[28] B. Heinrich. Skyrmion birth at the notch. *Nature Nanotechnology*, 16(10):1051–1051, 2021.

[29] S. Woo, T. Delaney, and G. S. D. Beach. Magnetic domain wall depinning assisted by spin wave bursts. *Nature Physics*, 13(5):448–454, 2017.

[30] A. A. Belavin and A. M. Polyakov. Metastable states of two-dimensional isotropic ferromagnets. *JETP Letters*, 22:503, 1975.

[31] F. Zheng, N. S. Kiselev, F. N. Rybakov, L. Yang, W. Shi, S. Blügel, and R. E. Dunin-Borkowski. Hopfion rings in a cubic chiral magnet. *Nature*, 623(7988):718–723, 2023.

[32] B. Göbel, I. Mertig, and O. A. Tretiakov. Beyond skyrmions: Review and perspectives of alternative magnetic quasiparticles. *Physics Reports*, 895:1–28, 2021. Beyond skyrmions: Review and perspectives of alternative magnetic quasiparticles.

[33] S. M. Stishov and A. E. Petrova. Itinerant chiral magnet MnSi. *Journal of Experimental and Theoretical Physics*, 131(1):201–207, 2020.

[34] J. F. DiTusa, S. B. Zhang, K. Yamaura, Y. Xiong, J. C. Prestigiacomo, B. W. Fulfer, P. W. Adams, M. I. Brickson, D. A. Browne, C. Capan, Z. Fisk, and Julia Y. Chan. Magnetic, thermodynamic, and electrical transport properties of the noncentrosymmetric $B20$ germanides MnGe and CoGe. *Phys. Rev. B*, 90:144404, 2014.

[35] T. Moriya. Anisotropic superexchange interaction and weak ferromagnetism. *Phys. Rev.*, 120:91, 1960.

[36] I. E. Dzialoshinskii. Thermodynamic theory of “weak” ferromagnetism in antiferromagnetic substances. *Sov. Phys. JETP*, 5:1259, 1957.

[37] S. Heinze, K. von Bergmann, M. Menzel, J. Brede, A. Kubetzka, R. Wiesendanger, G. Bihlmayer, and S. Blügel. Spontaneous atomic-scale magnetic skyrmion lattice in two dimensions. *Nature Physics*, 7(9):713–718, 2011.

[38] P. Bak and M. H. Jensen. Theory of helical magnetic structures and phase transitions in MnSi and FeGe. *J. Phys. C*, 13:L881, 1980.

[39] U. Rößler, A. Leonov, and A. Bogdanov. Chiral skyrmionic matter in non-centrosymmetric magnets. *Journal of Physics: Conference Series*, 303(1):012105, 2011.

[40] M. Janoschek, M. Garst, A. Bauer, P. Krautscheid, R. Georgii, P. Böni, and C. Pfleiderer. Fluctuation-induced first-order phase transition in Dzyaloshinskii–Moriya helimagnets. *Phys. Rev. B*, 87:134407, 2013.

[41] S. Brazovskii. Phase transition of an isotropic system to a nonuniform state. *Sov. Phys. JETP*, 41, 1975.

[42] J. Han, J. Zang, Z. Yang, J. Park, and N. Nagaosa. Skyrmion lattice in a two-dimensional chiral magnet. *Phys. Rev. B*, 82:094429, 2010.

[43] G. Blatter, M. V. Feigel’man, V. B. Geshkenbein, A. I. Larkin, and V. M. Vinokur. Vortices in high-temperature superconductors. *Rev. Mod. Phys.*, 66:1125–1388, 1994.

[44] Y. Onose, Y. Okamura, S. Seki, S. Ishiwata, and Y. Tokura. Observation of magnetic excitations of skyrmion crystal in a helimagnetic insulator Cu_2OSeO_3. *Phys. Rev. Lett.*, 109:037603, 2012.

[45] K. Everschor-Sitte, J. Masell, R. M. Reeve, and M. Kläui. Perspective: Magnetic skyrmions—overview of recent progress in an active research field. *Journal of Applied Physics*, 124(24):240901, 2018.

[46] N. Nagaosa and Y. Tokura. Topological properties and dynamics of magnetic skyrmions. *Nat. Nanotechnol.*, 8:899, 2013.

[47] F. Qian, L. Bannenberg, H. Wilhelm, G. Chaboussant, L. Debeer-Schmitt, M. Schmidt, A. Aqeel, T. Palstra, E. Brück, A. Lefering, C. Pappas, M. Mostovoy, and A. Leonov. New magnetic phase of the chiral skyrmion material Cu_2OSeO_3. *Science Advances*, 4(9):eaat7323, 2024.

[48] X. Z. Yu, Y. Onose, N. Kanazawa, J. H. Park, J. H. Han, Y. Matsui, N. Nagaosa, and Y. Tokura. Real-space observation of a two-dimensional skyrmion crystal. *Nature*, 465(7300):901–904, 2010.

[49] C. Reichhardt, C. J. O. Reichhardt, and M. V. Milošević. Statics and dynamics of skyrmions interacting with disorder and nanostructures. *Rev. Mod. Phys.*, 94:035005, 2022.

[50] C. Reichhardt and C. J. Olson Reichhardt. Depinning and nonequilibrium dynamic phases of particle assemblies driven over random and ordered substrates: a review. *Rep. Prog. Phys.*, 80(2):026501, 2017.

[51] G. Grüner. The dynamics of charge-density waves. *Rev. Mod. Phys.*, 60:1129–1181, 1988.

[52] S. Lemerle, J. Ferré, C. Chappert, V. Mathet, T. Giamarchi, and P. Le Doussal. Domain wall creep in an ising ultrathin magnetic film. *Phys. Rev. Lett.*, 80:849–852, 1998.

[53] S. Brazovskii and T. Nattermann. Pinning and sliding of driven elastic systems: from domain walls to charge density waves. *Advances in Physics*, 53(2):177–252, 2004.

[54] T. Schulz, R. Ritz, A. Bauer, M. Halder, M. Wagner, C. Franz, C. Pfleiderer, K. Everschor, M. Garst, and A. Rosch. Emergent electrodynamics of skyrmions in a chiral magnet. *Nat. Phys.*, 8:301, 2012.

[55] J. Iwasaki, M. Mochizuki, and N. Nagaosa. Universal current-velocity relation of skyrmion motion in chiral magnets. *Nat. Commun.*, 4(1):1463, 2013.

[56] W. Jiang, P. Upadhyaya, W. Zhang, G. Yu, M. B. Jungfleisch, F. Y. Fradin, J. E. Pearson, Y. Tserkonvyak, K. L. Wang, O. Heinonen, G. E. te Velthuis, and A. Hoffmann. Blowing magnetic skyrmion bubbles. *Science*, 349:283, 2015.

[57] S. Woo, K. Litzius, B. Krüger, M. Im, L. Caretta, K. Richter, M. Mann, A. Krone, R. M. Reeve, M. Weigand, P. Agrawal, I. Lemesh, M. Mawass, P. Fischer, M. Kläui, and G. Beach. Observation of room-temperature magnetic skyrmions and their current-driven dynamics in ultrathin metallic ferromagnets. *Nature Materials*, 15(5):501–506, 2016.

[58] S. Woo, K. M. Song, X. Zhang, Y. Zhou, M. Ezawa, X. Liu, S. Finizio, J. Raabe, N.J. Lee, S. Kim, S. Park, Y. Kim, J. Kim, D. Lee, O. Lee, J. Choi, B. Min, H. Koo, and J. Chang. Current-driven dynamics and inhibition of the skyrmion Hall effect of ferrimagnetic skyrmions in GdFeCo films. *Nature Communications*, 9(1):959, 2018.

[59] L. Kong and J. Zang. Dynamics of an insulating skyrmion under a temperature gradient. *Phys. Rev. Lett.*, 111:067203, 2013.

[60] M. Mochizuki, X. Z. Yu, S. Seki, N. Kanazawa, W. Koshibae, J. Zang, M. Mostovoy, Y. Tokura, and N. Nagaosa. Thermally driven ratchet motion of a skyrmion microcrystal and topological magnon Hall effect. *Nature Materials*, 13(3):241–246, 2014.

[61] S. Pöllath, J. Wild, L. Heinen, T. N. G. Meier, M. Kronseder, L. Tutsch, A. Bauer, H. Berger, C. Pfleiderer, J. Zweck, A. Rosch, and C. H. Back. Dynamical defects in rotating magnetic skyrmion lattices. *Phys. Rev. Lett.*, 118:207205, 2017.

[62] Z. Wang, M. Guo, H. Zhou, L. Zhao, T. Xu, R. Tomasello, H. Bai, Y. Dong, S. Je, W. Chao, H. Han, S. Lee, K. Lee, Y. Yao, W. Han, C. Song, H. Wu, M. Carpentieri, G. Finocchio, M. Im, S. Lin, and W. Jiang. Thermal generation, manipulation and thermoelectric detection of skyrmions. *Nature Electronics*, 3(11):672–679, 2020.

[63] X. Zhang, M. Ezawa, and Y. Zhou. Magnetic skyrmion logic gates: conversion, duplication and merging of skyrmions. *Scientific Reports*, 5(1):9400, 2015.

[64] X. Zhang, J. Müller, J. Xia, M. Garst, X. Liu, and Y. Zhou. Motion of skyrmions in nanowires driven by magnonic momentum-transfer forces. *New Journal of Physics*, 19(6):065001, 2017.

[65] M. Shen, Y. Zhang, J. Ou-Yang, X. Yang, and L. You. Motion of a skyrmionium driven by spin wave. *Applied Physics Letters*, 112(6):062403, 2018.

[66] C. Psaroudaki and D. Loss. Skyrmions driven by intrinsic magnons. *Phys. Rev. Lett.*, 120:237203, 2018.

[67] M. Tsoi, R. E. Fontana, and S. S. P. Parkin. Magnetic domain wall motion triggered by an electric current. *Applied Physics Letters*, 83(13):2617–2619, 2003.

[68] D.L. Landau and E. Lifshitz. On the theory of the dispersion of magnetic permeability in ferromagnetic bodies. *Phys. Z. Sowjetunion*, 8(153), 1935.

[69] A. A. Thiele. Steady-state motion of magnetic domains. *Phys. Rev. Lett.*, 30:230–233, 1973.

[70] K. Everschor, M. Garst, R. A. Duine, and A. Rosch. Current-induced rotational torques in the skyrmion lattice phase of chiral magnets. *Phys. Rev. B*, 84:064401, 2011.

[71] J. Müller and A. Rosch. Capturing of a magnetic skyrmion with a hole. *Phys. Rev. B*, 91:054410, 2015.

[72] A. I. Larkin and Yu. N. Ovchinnikov. Pinning in type II superconductors. *Journal of Low Temperature Physics*, 34(3):409–428, 1979.

[73] A. I. Larkin. Effect of inhomogeneities on the structure of the mixed state of superconductors. *ZhETF*, 58:1466–1470, 1970.

[74] S. Okumura, V. P. Kravchuk, and M. Garst. Instability of magnetic skyrmion strings induced by longitudinal spin currents. *Phys. Rev. Lett.*, 131:066702, 2023.

[75] J. Zang, M. Mostovoy, J.H. Han, and N. Nagaosa. Dynamics of skyrmion crystals in metallic thin films. *Phys. Rev. Lett.*, 107:136804, 2011.

[76] S. A. Montoya, R. Tolley, I. Gilbert, S. Je, M. Im, and E. Fullerton. Spin-orbit torque induced dipole skyrmion motion at room temperature. *Phys. Rev. B*, 98:104432, 2018.

[77] S. A. Díaz, C. Reichhardt, D. Arovas, A. Saxena, and C. Reichhardt. Fluctuations and noise signatures of driven magnetic skyrmions. *Phys. Rev. B*, 96:085106, 2017.

[78] C. Reichhardt and C. J. Olson Reichhardt. Noise fluctuations and drive dependence of the skyrmion Hall effect in disordered systems. *New Journal of Physics*, 18(9):095005, 2016.

[79] C. Reichhardt, D. Ray, and C. J. Olson Reichhardt. Quantized transport for a skyrmion moving on a two-dimensional periodic substrate. *Phys. Rev. B*, 91:104426, 2015.

[80] W. Koshibae and N. Nagaosa. Theory of current-driven skyrmions in disordered magnets. *Scientific Reports*, 8(1):6328, 2018.

[81] P. Milde, D. Köhler, J. Seidel, L. M. Eng, A. Bauer, A. Chacon, J. Kindervater, S. Mühlbauer, C. Pfleiderer, S. Buhrandt, C. Schütte, and A. Rosch. Unwinding of a skyrmion lattice by magnetic monopoles. *Science*, 340:1076, 2013.

[82] F. Kagawa, H. Oike, W. Koshibae, A. Kikkawa, Y. Okamura, Y. Taguchi, N. Nagaosa, and Y. Tokura. Current-induced viscoelastic topological unwinding of metastable skyrmion strings. *Nature Communications*, 8:1332, 2017.

[83] C. Schütte and A. Rosch. Dynamics and energetics of emergent magnetic monopoles in chiral magnets. *Phys. Rev. B*, 90:174432, 2014.

[84] S. Lin and A. Saxena. Dynamics of Dirac strings and monopolelike excitations in chiral magnets under a current drive. *Phys. Rev. B*, 93:060401, 2016.

[85] X. Zhang, A. Mishchenko, G. De Filippis, and N. Nagaosa. Electric transport in three-dimensional skyrmion/monopole crystal. *Phys. Rev. B*, 94:174428, 2016.

[86] W. Koshibae and N. Nagaosa. Dynamics of skyrmion in disordered chiral magnet of thin film form. *Sci. Rep.*, 9:5111, 2019.

[87] T. Yokouchi, S. Hoshino, N. Kanazawa, A. Kikkawa, D. Morikawa, K. Shibata, T. Arima, Y. Taguchi, F. Kagawa, N. Nagaosa, and Y. Tokura. Current-induced dynamics of skyrmion strings. *Sci. Adv.*, 4, 2018.

[88] K. Ran, W. Tan, X. Sun, Y. Liu, R. Dalgliesh, N. Steinke, G. van der Laan, S. Langridge, T Hesjedal, and S. Zhang. Bending skyrmion strings under two-dimensional thermal gradients. *Nature Communications*, 15(1):4860, 2024.

[89] D. Okuyama, M. Bleuel, J. S. White, Q. Ye, J. Krzywon, G. Nagy, Z. Q. Im, I. Živković, M. Bartkowiak, H. M. Rønnow, S. Hoshino, J. Iwasaki, N. Nagaosa, A. Kikkawa, Y. Taguchi, Y. Tokura, D. Higashi, J. D. Reim, Y. Nambu, and T. J. Sato. Deformation of the moving magnetic skyrmion lattice in MnSi under electric current flow. *Commun. Phys.*, 2:1, 2019.

[90] R. Brearton, D. M. Burn, A. A. Haghighirad, G. van der Laan, and T. Hesjedal. Three-dimensional structure of magnetic skyrmions. *Phys. Rev. B*, 106:214404, 2022.

[91] D. Wolf, S. Schneider, U. K. Rößler, A. Kovács, M. Schmidt, R. Dunin-Borkowski, B. Büchner, B. Rellinghaus, and A. Lubk. Unveiling the three-dimensional magnetic texture of skyrmion tubes. *Nature Nanotechnology*, 17(3):250–255, 2021.

[92] M. T. Birch, D. Cortés-Ortuño, L. A. Turnbull, M. N. Wilson, F. Groß, N. Träger, A. Laurenson, N. Bukin, S. H. Moody, M. Weigand, G. Schütz, H. Popescu, R. Fan, P. Steadman, J. A. T. Verezhak, G. Balakrishnan, J. C. Loudon, A. C. Twitchett-Harrison, O. Hovorka, H. Fangohr, F. Y. Ogrin, J. Gräfe, and P. D. Hatton. Real-space imaging of confined magnetic skyrmion tubes. *Nature Communications*, 11(1), 2020.

[93] S. Lin, C. Reichhardt, C. D. Batista, and A. Saxena. Particle model for skyrmions in metallic chiral magnets: Dynamics, pinning, and creep. *Phys. Rev. B*, 87:214419, 2013.

[94] W. Jiang, X. Zhang, G. Yu, W. Zhang, X. Wang, M. B. Jungfleisch, J. Pearson, X. Cheng, O. Heinonen, K. L. Wang, Y. Zhou, A. Hoffmann, and S. G.E. Velthuis. Direct observation of the skyrmion Hall effect. *Nature Physics*, 13(2):162–169, 2017.

[95] Y. Luo, S.-Z. Lin, M. Leroux, N. Wakeham, D. M. Fobes, E. D. Bauer, J. B. Betts, J. D. Thompson, A. Migliori, M. Janoschek, and B. Maiorov. Skyrmion lattice creep at ultra-low current densities. *Commun. Mater.*, 1:1, 2020.

[96] P. W. Anderson and Y. B. Kim. Hard superconductivity: Theory of the motion of abrikosov flux lines. *Rev. Mod. Phys.*, 36:39–43, 1964.

[97] F. Rucker, D. Mettus, A. Bauer, A. Bezvershenko, M. Garst, A. Rosch, and C. Pfleiderer. Amplitude and frequency dependence of the transverse AC susceptibility in MnSi. Manuscript in preparation.

[98] F. Rucker. *Transverse Susceptibility of Complex Magnetic Textures.* PhD thesis, Technische Universität München, 2017.

[99] C. N. Guy. Low field magnetic studies of a single crystal of MnSi. *Solid State Commun.*, 25:169, 1978.

[100] C. Pfleiderer, C. Thessieu, A. N. Stepanov, G. Lapertot, M. Couach, and J. Flouquet. Field dependence of the magnetic quantum phase transition in MnSi. *Physica B*, 230–232:576, 1997.

[101] M. Ohkuma, M. Mito, M. Pardo, Y. Kousaka, S. Iwasaki, K. Ohishi, J. Akimitsu, K. Inoue, V. Laliena, and J. Campo. New magnetic intermediate state, "B-phase", in the cubic chiral magnet MnSi. *APL Materials*, 10:041104, 2022.

[102] A. Bauer and C. Pfleiderer. Magnetic phase diagram of MnSi inferred from magnetization and ac susceptibility. *Phys. Rev. B*, 85:214418, 2012.

[103] L. J. Bannenberg, A. J. E. Lefering, K. Kakurai, Y. Onose, Y. Endoh, Y. Tokura, and C. Pappas. Magnetic relaxation phenomena in the chiral magnet $\mathrm{Fe}_{1-x}\mathrm{Co}_x\mathrm{Si}$: An ac susceptibility study. *Phys. Rev. B*, 94:134433, 2016.

[104] L. J. Bannenberg, F. Weber, A. J. E. Lefering, T. Wolf, and C. Pappas. Magnetization and ac susceptibility study of the cubic chiral magnet $\mathrm{Mn}_{1-x}\mathrm{Fe}_x\mathrm{Si}$. *Phys. Rev. B*, 98:184430, 2018.

[105] A. Bauer, M. Garst, and C. Pfleiderer. History dependence of the magnetic properties of single-crystal $\mathrm{Fe}_{1-x}\mathrm{Co}_x\mathrm{Si}$. *Phys. Rev. B*, 93:235144, 2016.

[106] D. Mettus, A. Chacon, A. Bauer, S. Mühlbauer, and C. Pfleiderer. Optimization strategies and artifacts of time-involved small-angle neutron scattering experiments. *J. Appl. Crystallogr.*, 55:1603, 2022.

[107] D. Kipping, R. Gähler, and K. Habicht. Small angle neutron scattering at very high time resolution: Principle and simulations of TISANE. *Physics Letters A*, 372(10):1541–1546, 2008.

[108] B. Jamtveit and P. Meakin. *Growth, Dissolution and Pattern Formation in Geosystems.* Springer Dordrecht, 1999. p.291.

[109] D. Mettus, A. Chacon, A. Bauer, S. Mühlbauer, A. Bezvershenko, L. Heinen, C. Pfleiderer, and A. Rosch. Dynamical depinning of a skyrmion lattice by oscillating magnetic fields. Manuscript in preparation.

[110] A. O. Leonov and I. Kézsmárki. Skyrmion robustness in noncentrosymmetric magnets with axial symmetry: The role of anisotropy and tilted magnetic fields. *Phys. Rev. B*, 96:214413, 2017.

[111] T. Schwarze, J. Waizner, M. Garst, A. Bauer, I. Stasinopoulos, H. Berger, C. Pfleiderer, and D. Grundler. Universal helimagnon and skyrmion excitations in metallic, semiconducting and insulating chiral magnets. *Nat. Mater.*, 14:478, 2015.

[112] M. Garst, J. Waizner, and D. Grundler. Collective spin excitations of helices and magnetic skyrmions: review and perspectives of magnonics in non-centrosymmetric magnets. *Journal of Physics D: Applied Physics*, 50(29):293002, 2017.

[113] S. B. Roy. *Demagnetization Field and Demagnetization Factor*, page 329–338. Cambridge University Press, 2023.

[114] D. B. Liarte, D. Hall, P. N. Koufalis, A. Miyazaki, A. Senanian, M. Liepe, and J. P. Sethna. Vortex dynamics and losses due to pinning: Dissipation from trapped magnetic flux in resonant superconducting radio-frequency cavities. *Phys. Rev. Appl.*, 10:054057, 2018.

[115] T. Ullman, E. Kosoy, A. Soltani, M. Siegel, J. Tenenbaum, and E. Spelke. Draping an elephant: Uncovering children's reasoning about cloth-covered objects. 2019.

[116] R. Coughlan. *Dr. Edward Teller's Magnificent Obsession.* LIFE, 1954. p.62.

[117] F. Schütte. *Skyrmions and Monopoles in Chiral Magnets Correlated Heterostructures.* PhD thesis, Universität zu Köln, 2014.

[118] E. Suli and D.F. Mayers. *An Introduction to Numerical Analysis.* Cambridge University Press, 2003.

[119] F. Rucker, A. Bezvershenko, D. Mettus, A. Bauer, L. Heinen, M. Garst, A. Rosch, and C. Pfleiderer. Pushing and shaking skyrmion lattices: Creation of non-equilibrium phases. Manuscript in preparation.

[120] C. Schnarr. *Spin-transfer torque effects in* $Mn_{1-x}Fe_xSi$ *volume crystals and epitaxial MnSi films*. PhD thesis, Technische Universität München, 2017.

[121] V. P. Kravchuk, U. K. Rößler, J. van den Brink, and M. Garst. Solitary wave excitations of skyrmion strings in chiral magnets. *Phys. Rev. B*, 102:220408, 2020.

[122] V. Kravchuk. Nonlinear dynamics of skyrmion strings. *Phys. Rev. B*, 108:144412, 2023.

[123] S. Lin, J. Zhu, and A. Saxena. Kelvin modes of a skyrmion line in chiral magnets and the associated magnon transport. *Phys. Rev. B*, 99:140408, 2019.

[124] S. Seki, M. Garst, J. Waizner, R. Takagi, N. D. Khanh, Y. Okamura, K. Kondou, F. Kagawa, Y. Otani, and Y. Tokura. Propagation dynamics of spin excitations along skyrmion strings. *Nature Communications*, 11(1):256, 2020.

[125] C. Schütte and M. Garst. Magnon-skyrmion scattering in chiral magnets. *Phys. Rev. B*, 90(9):094423, 2014.

A | Derivation of the free energy

In order to find the free energy of the elastic skyrmion line when subject to external slowly oscillating magnetic magnetic field $\boldsymbol{B}$, we substitute the expression for the orientation of the skyrmion lattice $\hat{\boldsymbol{n}} = (\delta n_x, \delta n_y, n_z)$, where $n_z = \sqrt{1 - \delta n_x^2 - \delta n_y^2} \approx 1 - \frac{\delta n_x^2}{2} - \frac{\delta n_y^2}{2}$ into the expression for the change of the free energy f, given by

$$f = (\boldsymbol{m} - \boldsymbol{m}_0) \cdot \left. \frac{df_0}{d\boldsymbol{m}} \right|_{\boldsymbol{m} = \boldsymbol{m}_0} + \frac{1}{2\chi_{\parallel}^{00}} (\boldsymbol{m} - \boldsymbol{m}_0)^2 + \frac{1}{2\chi_{\perp}^{00}} (\boldsymbol{m}_{\perp})^2 + \sum_{i=x,y,z} \frac{N_i m_i^2}{2} - \boldsymbol{m}\boldsymbol{B} \,. \tag{A.1}$$

Further, we Taylor expand this experssion with respect to δn_x, δn_y up to quadratic order and obtain

$$\begin{aligned} f =& \frac{N_z m_0^2}{2} + \sum_{i=x,y,z} \frac{N_i m_i^2}{2} - \boldsymbol{m} \cdot \boldsymbol{B} + q B_0 + m_z B_0 \left(1 - \frac{\boldsymbol{\delta n}_{\perp}^2}{2} \right) + \\ & \frac{1}{2\chi_{\perp}^{00}} \left(\boldsymbol{m}_{\perp}^2 - q^2 - 2 q m_z + \boldsymbol{\delta n}_{\perp}^2 m_z^2 \right) + \frac{1}{2\chi_{\parallel}^{00}} \left(q^2 + (m_0 - m_z)(m_0 - m_z + \boldsymbol{\delta n}_{\perp}^2 m_z - 2q) \right) , \end{aligned} \tag{A.2}$$

where we denoted $\boldsymbol{\delta n}_{\perp} = (\delta n_x, \delta n_y)$, $\boldsymbol{m}_{\perp} = (m_x, m_y)$, $q = \boldsymbol{\delta n}_{\perp} \cdot \boldsymbol{m}_{\perp}$.

The magnetisation configuration $\boldsymbol{m}^*$, which minimises the density functional f can be found by setting partial derivatives of the free energy with respect to the three components of the magnetisation vector to zero. The result is given by

$$m_j^* = \frac{B_j \chi_{\perp}^{00}}{1 + N_j \chi_{\perp}^{00}} + \delta n_{\perp,j} \frac{B_z (\chi_{\parallel}^{00} - \chi_{\perp}^{00}) + (m_0 - B_0 \chi_{\parallel}^{00})(1 + N_z \chi_{\perp}^{00})}{(1 + N_z \chi_{\parallel}^{00})(1 + N_j \chi_{\perp}^{00})} \tag{A.3}$$

for $j = x, y$ and

$$\begin{aligned} m_z^* =& \frac{m_0 \left(1 - \frac{\delta n_{\perp}^2}{2} \right) + (B_z - B_0) \chi_{\parallel}^{00}}{1 + N_z \chi_{\parallel}^{00}} - \frac{1}{1 + N_z \chi_{\parallel}^{00}} \sum_{j=x,y} \frac{\delta n_{\perp,j} (\chi_{\parallel}^{00} - \chi_{\perp}^{00})(B_z \delta n_{\perp,j} - B_j)}{1 + N_j \chi_{\perp}^{00}} - \\ & - \frac{(\chi_{\parallel}^{00} - \chi_{\perp}^{00}) \left(m_0 + (B_z - B_0) \chi_{\parallel}^{00} \right) \sum_{j=x,y} \delta n_j^2 (N_j - N_z)(1 + N_j \chi_{\perp}^{00})}{(1 + N_z \chi_{\parallel}^{00})^2 \prod_{j=x,y} (1 + N_j \chi_{\perp}^{00})} \,. \end{aligned} \tag{A.4}$$

We are interested in the total free energy, which can be found by integrating the free-energy density functional over the volume of our system at the previously found point $\boldsymbol{m}^*$:

$$\mathcal{F} = \min_{\boldsymbol{m}} F = \int f|_{\boldsymbol{m} = \boldsymbol{m}^*} \, d^3\boldsymbol{r} \,. \tag{A.5}$$

After substituting Eqs. (A.3), (A.4) in the expression (A.2) we obtain an exact formula for the free energy of our system in the lowest order of the gradient expansion

$$\mathcal{F} = -\sum_{i=x,y} \frac{\gamma_i}{2} B_i(t)^2 + \int_{-L/2}^{L/2} dz \sum_{i=x,y} \frac{\epsilon_{0,i}}{2} \left(\partial_z u_i(z,t) - \frac{B_i(t)}{B'_{z,i}} \right)^2 . \tag{A.6}$$

For the definitions of γ_i, $\epsilon_{0,i}$ and $B'_{z,i}$ see the main text.

B | Numerics

As discussed in the main text, the Thiele equation for the dynamics of the skyrmion line becomes a highly non-linear two-dimensional differential equation due to pinning. Therefore, we find its solution numerically.

In order to solve the dynamics, we parametrize the line with N points with coordinates $\tilde{u}_n^i$ ($i = x, y$ and $n = 1 \dots N$) and distance $\Delta\tilde{z} = \frac{1}{N-1}$ between them in z direction, $\tilde{z} \in \left(-\frac{1}{2}, \frac{1}{2}\right)$.

Given the positions of all points $\tilde{u}_n^i$, we use the second-order centered difference approximation (which gives error for calculation of derivatives of the order $(\frac{1}{N})^2$), to calculate the free energy functional:

$$\mathcal{F} = \sum_{i=x,y} \sum_{n=1}^{n=N-1} \frac{1}{2} \left(\frac{\tilde{u}_n^i - \tilde{u}_{n+1}^i}{\Delta\tilde{z}} - \frac{B_x(t)}{B_z'} \right)^2 \Delta\tilde{z} \,. \tag{B.1}$$

The elastic forces (per length) $f_n^i = \frac{1}{\Delta\tilde{z}} \frac{\partial\mathcal{F}}{\partial\tilde{u}_n^i}$ are given by:

$$f_1^i = \frac{1}{\Delta\tilde{z}} \left(\frac{B_x(t)}{B_z'} - \frac{\tilde{u}_1^i - \tilde{u}_2^i}{\Delta\tilde{z}} \right), \, f_N^i = \frac{1}{\Delta\tilde{z}} \left(-\frac{B_x(t)}{B_z'} + \frac{\tilde{u}_{N-1}^i - \tilde{u}_N^i}{\Delta\tilde{z}} \right), f_n^i = \frac{\tilde{u}_{n-1}^i - 2\tilde{u}_n^i + \tilde{u}_{n+1}^i}{\Delta\tilde{z}^2} \,.$$

Therefore, the elastic forces acting on each point can be found by calculating the first and the second numerical spacial derivatives (for the first/last point and all intermediate points, respectively).

In order to depinn the skyrmion line, one needs to apply the magnetic field large enough to overcome the surface pinning. If we start from the pinned skyrmion line $\tilde{u}_n^i = 0$, at the critical magnetic field $\delta\tilde{B}_1^{cr}$ (without the current) the following condition should be satisfied

$$\frac{1}{\Delta\tilde{z}} \delta\tilde{B}^{cr} = \frac{1}{\Delta\tilde{z}} \frac{F^{p,s}}{LF^{p,b}} \,, \tag{B.2}$$

giving the prefactor for the surface pinning in the descritised version.

Time is also descritized, so that during each period $T_{period} = \frac{2\pi}{\tilde{\omega}}$ of the oscillation of external magnetic field N_{steps} updates are performed, with the time step of $d\tilde{t} = \frac{T_{period}}{N_{steps}}$. Effectively the problem of solving the dynamics of the system simplifies to finding coordinates of N points at every time step, which is done by integrating the rescaled Thiele's equation. For this the Heun's method of finding numerical solutions to ordinary differential equations was used with the initial condition of straight line (zero displacement of every point).

In order to find the evolution in time of our system, we calculate total forces F_n^i acting on every point, consisting of elastic forces and forces from applied current

$$F_n^i = f_n^i + \tilde{v}_s^i \,. \tag{B.3}$$

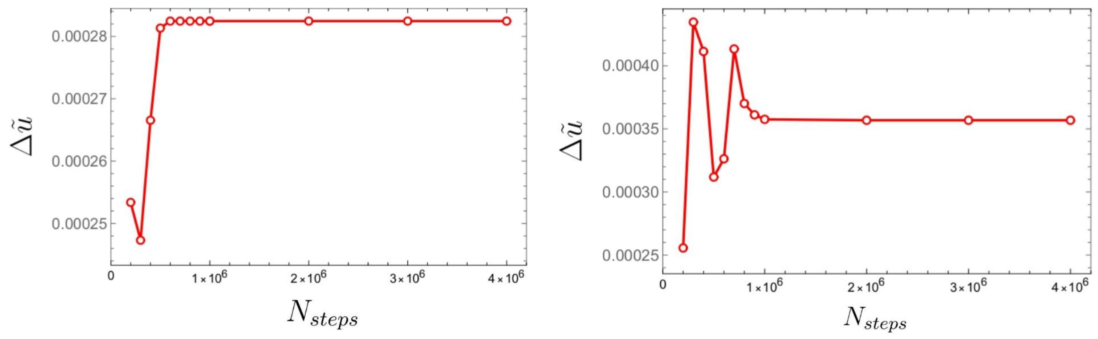

(a) (b)

Figure 71: The convergence of solution for (a) $T_p = 5$, $\delta\tilde{B} = 6$, $\epsilon_3 = 0.0025$, $\epsilon_4 = 0.0001$, (b) $T_p = 10$, $\delta\tilde{B} = 6$, $\epsilon_3 = 0.0025$, $\epsilon_4 = 0.0001$.

At the first step, we check for every point if the total force F_n acting on it is smaller than the pinning force (which is equal to 1 in rescaled variables for the points with $i = 2 \dots N-1$ and $\frac{1}{\Delta\tilde{z}}\frac{F^{p,st}}{LF^{p,b}}$, $\frac{1}{\Delta\tilde{z}}\frac{F^{p,sb}}{LF^{p,b}}$ for the first and the last point, respectively). If yes, then the point stays pinned and no update is needed.
If the total force on the point is larger than the critical pinning force value, we obtain a nonlinear equation for the velocity $v_n^i = \partial_t u_n^i$ (nonlinear due to the $1/|\partial_t \tilde{u}_n^i|$ term in the Thiele equation). Luckily, this equation can be solved analytically (see Sec.6.1), giving the velocities $\partial_t \tilde{u}_n^i$ as function of forces F_n^i acting on this point. The resulting velocity is used within Heun's method of integration with a truncation error of the order $\sim \left(\frac{1}{N_{steps}}\right)^2$.

In our code, we typically use $N_{steps} = 3 \cdot 10^6$, $N = 60$ and wait around 20 periods to obtain a periodic solution in the long-time limit.

Further, for the higher order terms in the last Part of this Thesis we used the following finite difference formulas. For the term $\hat{\boldsymbol{z}} \times \tilde{\boldsymbol{u}}^{(3)}$ we use

$$\Delta\tilde{z} \sum_{n=1}^{n=N-2} \frac{1}{\Delta\tilde{z}} \left(\frac{\tilde{u}^y_{n+2} - 2\tilde{u}^y_{n+1} + \tilde{u}^y_n}{\Delta\tilde{z}^2}\right) \left(\frac{\tilde{u}^x_{n+2} - \tilde{u}^x_n}{2\Delta\tilde{z}}\right) - \frac{1}{\Delta\tilde{z}} \left(\frac{\tilde{u}^x_{n+2} - 2\tilde{u}^x_{n+1} + \tilde{u}^x_n}{\Delta\tilde{z}}\right) \left(\frac{\tilde{u}^y_{n+2} - \tilde{u}^y_n}{2\Delta\tilde{z}^2}\right).$$

(B.4)

And for the term $\tilde{\boldsymbol{u}}^{(4)}$ we use

$$\Delta\tilde{z} \sum_{i=x,y} \sum_{n=1}^{n=N-1} \left(\frac{\tilde{u}^i_{n+2} - 2\tilde{u}^i_{n+1} + \tilde{u}^i_n}{\Delta\tilde{z}}\right)^2. \tag{B.5}$$

On the Fig.71, we show the convergence of the step $\Delta\tilde{u}$ as function of number of time steps N_{steps}.

C | Solution with damping

Similarly to Sec.6.2, the Thiele equation for the bulk can be written in unscaled coordinates as

$$\begin{cases} \mathcal{G}\frac{\partial u_y(z,t)}{\partial t} + \alpha\mathcal{D}\frac{\partial u_x(z,t)}{\partial t} & = \varepsilon_0 \frac{\partial^2 u_x(z,t)}{\partial z^2} \\ -\mathcal{G}\frac{\partial u_x(z,t)}{\partial t} + \alpha\mathcal{D}\frac{\partial u_y(z,t)}{\partial t} & = \varepsilon_0 \frac{\partial^2 u_y(z,t)}{\partial z^2}\,. \end{cases} \tag{C.1}$$

From the first equation we find $\frac{\partial u_y(z,t)}{\partial t}$ and substitute it in the second equation:

$$\begin{cases} \frac{\partial u_y(z,t)}{\partial t} = \frac{\varepsilon_0}{\mathcal{G}}\frac{\partial^2 u_x(z,t)}{\partial z^2} - \frac{\alpha\mathcal{D}}{\mathcal{G}}\frac{\partial u_x(z,t)}{\partial t} \\ -\mathcal{G}\frac{\partial u_x(z,t)}{\partial t} + \frac{\varepsilon_0\alpha\mathcal{D}}{\mathcal{G}}\frac{\partial^2 u_x(z,t)}{\partial z^2} - \frac{\alpha\mathcal{D}^2}{\mathcal{G}}\frac{\partial u_x(z,t)}{\partial t} = \varepsilon_0\frac{\partial^2 u_y(z,t)}{\partial z^2}\,. \end{cases} \tag{C.2}$$

Further, we partially differentiate the first equation twice with respect to z and partially differentiate the second equation with respect to t once. We obtain

$$-\mathcal{G}\frac{\partial^2 u_x(z,t)}{\partial t^2} + \frac{\varepsilon_0\alpha\mathcal{D}}{\mathcal{G}}\frac{\partial}{\partial t}\frac{\partial^2 u_x(z,t)}{\partial z^2} - \frac{\alpha\mathcal{D}^2}{\mathcal{G}}\frac{\partial^2 u_x(z,t)}{\partial t^2} = \varepsilon_0\frac{\partial}{\partial t}\frac{\partial^2 u_y(z,t)}{\partial z^2}\,. \tag{C.3}$$

Now we use from before

$$\frac{\partial^4 u_x(z,t)}{\partial z^4} - \frac{2\alpha\mathcal{D}}{\varepsilon_0}\frac{\partial}{\partial t}\frac{\partial^2 u_x(z,t)}{\partial z^2} + \frac{\mathcal{G}^2 + \alpha\mathcal{D}^2}{\varepsilon_0^2}\frac{\partial^2 u_x(z,t)}{\partial t^2} = 0\,. \tag{C.4}$$

We find a solution $\left(c = \frac{\varepsilon_0}{\mathcal{G}}, a = \frac{\alpha\mathcal{D}}{\mathcal{G}}, \tilde{a} = \sqrt{1-a^2}, k = \frac{\sqrt{no\tilde{a}}}{\sqrt{c}}\right)$:

$$u_x(z,t) = \sum_{n=1}^{\infty} \frac{\sqrt{c}}{2\sqrt{no\tilde{a}^3}} \Bigg(\cos(not)\left(\sin(kz)\left(\tilde{a}c_{1,n} - ac_{2,n} - c_{4,n}\right) + \sinh(kz)\left(\tilde{a}c_{1,n} + ac_{2,n} + c_{4,n}\right)\right) + \\ \sin(not)\left(\left(ac_{1,n} + \tilde{a}c_{2,n} + c_{3,n}\right)\sin(kz) - \left(ac_{1,n} - \tilde{a}c_{2,n} + c_{3,n}\right)\sinh(kz)\right) \Bigg),$$

$$u_y(z,t) = \sum_{n=1}^{\infty} \frac{\sqrt{c}}{2\sqrt{no\tilde{a}^3}} \Bigg(\cos(not)\left(\left(c_{2,n} + \tilde{a}c_{3,n} + ac_{4,n}\right)\sin(kz) - \left(c_{2,n} - \tilde{a}c_{3,n} + ac_{4,n}\right)\sinh(kz)\right) + \\ \sin(not)\left(-\left(c_{1,n} + ac_{3,n} - \tilde{a}c_{4,n}\right)\sin(kz) + \left(c_{1,n} + ac_{3,n} + \tilde{a}c_{4,n}\right)\sinh(kz)\right) \Bigg).$$

Unfortunately, we haven't been able to determine all constants from boundary conditions.

D | Nonlinear terms

Let us consider the term

$$\int \frac{\left(\boldsymbol{B}\frac{\partial \boldsymbol{u}}{\partial \lambda}\right)^2}{\sqrt{\left(\frac{\partial \boldsymbol{u}}{\partial \lambda}\right)^2}}\, d\lambda \approx \int \left(B_x(t)u'_x + B_z\right)^2 \left(1 - \frac{1}{2}\left(u'^2_x + u'^2_y\right)\right)\, dz\,. \tag{D.1}$$

For parametrisation chosen in Eq.8.6 this invariant produces the terms of the lowest order, which were derived in Sec.5.2. However, in higher order expansion one obtains other nonlinear terms

$$B_z^2 \int 1 + \frac{B_x}{B_z}u'_x + \left(\frac{B_x}{B_z}u'_x\right)^2 - \frac{1}{2}(u'^2_x + u'^2_y) - \frac{1}{2}(u'^2_x + u'^2_y)\frac{B_x}{B_z}u'_x - \frac{1}{2}(u'^2_x + u'^2_y)\left(\frac{B_x}{B_z}u'_x\right)^2 dz\,. \tag{D.2}$$

Similarly, another important invariant is given by

$$\int \frac{\boldsymbol{B}\left(\frac{\partial \boldsymbol{u}}{\partial \lambda} \times \frac{\partial^2 \boldsymbol{u}}{\partial \lambda^2}\right)}{\sqrt{\left(\frac{\partial \boldsymbol{u}}{\partial \lambda}\right)^2}} d\lambda\,. \tag{D.3}$$

For this term we obtain

$$\int \frac{-B_x u''_y + B_y u''_x + B_z(u'_x u''_y - u'_y u''_x)}{\sqrt{(u'_x)^2 + (u'_y)^2 + 1}} dz \approx$$

$$\int \left(-B_x u''_y + B_y u''_x + B_z(u'_x u''_y - u'_y u''_x)\right)\left(1 - \frac{1}{2}(u'^2_x + u'^2_y)\right) dz \tag{D.4}$$

$$B_z \int (u'_x u''_y - u'_y u''_x) - \frac{1}{2}(u'^2_x + u'^2_y)(u'_x u''_y - u'_y u''_x) - \frac{B_x}{B_z}u''_y + \frac{1}{2}\frac{B_x}{B_z}(u'^2_x + u'^2_y)u''_y\, dz\,. \tag{D.5}$$

In the following table, we present all nonlinear terms (without the prefactors) which can be generated using such expansions of relevant invariants, preseneted in Section 8.3.

Term	Bulk	$\delta(z-\frac{L}{2})-\delta(z+\frac{L}{2})$	$\partial_z\delta(z-\frac{L}{2})-\partial_z\delta(z+\frac{L}{2})$
u'_x	-	$-u_x$	-
u''_y	-	$-u'_y$	-
$\lvert\boldsymbol{u}'\rvert^2$	$2\boldsymbol{u}''$	$-2\boldsymbol{u}'$	-
$[\boldsymbol{u}'\times\boldsymbol{u}'']_z$	$2\hat{\boldsymbol{z}}\times\boldsymbol{u}'''$	$-2\hat{\boldsymbol{z}}\times\boldsymbol{u}''$	$\hat{\boldsymbol{z}}\times\boldsymbol{u}'$
$\lvert\boldsymbol{u}''\rvert^2$	$-2\boldsymbol{u}''''$	$2\boldsymbol{u}'''$	$-2\boldsymbol{u}''$
$u'_x\lvert\boldsymbol{u}'\rvert^2$	$(3u_x'^2+u_y'^2)'\hat{\boldsymbol{x}}+2(u'_xu'_y)'\hat{\boldsymbol{y}}$	$-(3u_x'^2+u_y'^2)\hat{\boldsymbol{x}}-2u'_xu'_y\hat{\boldsymbol{y}}$	-
$u''_y\lvert\boldsymbol{u}'\rvert^2$	$2(u'_x\hat{\boldsymbol{z}}\times\boldsymbol{u}'')'$	$-2(u'_x\hat{\boldsymbol{z}}\times\boldsymbol{u}'')$	$-(\boldsymbol{u}'^2)\hat{\boldsymbol{y}}$
$u'_x[\boldsymbol{u}'\times\boldsymbol{u}'']_z$	$3(u'_x\hat{\boldsymbol{z}}\times\boldsymbol{u}'')'$	$-3(u'_x\hat{\boldsymbol{z}}\times\boldsymbol{u}'')$	$u'_x\hat{\boldsymbol{z}}\times\boldsymbol{u}'$
$\lvert\boldsymbol{u}'\rvert^4$	$4(\boldsymbol{u}'\lvert\boldsymbol{u}'\rvert^2)'$	$-4(\boldsymbol{u}'\lvert\boldsymbol{u}'\rvert^2)$	-
$\lvert\boldsymbol{u}'\rvert^2[\boldsymbol{u}'\times\boldsymbol{u}'']_z$	$4(\hat{\boldsymbol{z}}\times\boldsymbol{u}''\lvert\boldsymbol{u}'\rvert^2)'$	$-4\hat{\boldsymbol{z}}\times\boldsymbol{u}'\lvert\boldsymbol{u}'\rvert^2$	$\hat{\boldsymbol{z}}\times\boldsymbol{u}'\lvert\boldsymbol{u}'\rvert^2$

In order to find prefectors of these terms (see Sec.8.3, where this prefactors are introduced) we follow Ref. [122]. Obtained prefactors are functionals of $\theta_0(\tilde{\rho})$, the skyrmion profile in a 2D magnet, and $g(\tilde{\rho})$, which controls the magnitude of rotation (see Ref. [122] for further explanation). We obtain

$$
\begin{aligned}
c_0 &= \int_0^\infty \mathrm{d}\tilde{\rho}\ (-2\tilde{\rho}\cos[\theta_0]),\\
c_{11} &= \int_0^\infty \mathrm{d}\tilde{\rho}\ 2\tilde{\rho}\cos[\theta_0](-1+g(\tilde{\rho})),\\
c_{12} &= \int_0^\infty \mathrm{d}\tilde{\rho}\ (-\tilde{\rho}^3\sin[\theta_0]),\\
c_{21} &= \int_0^\infty \mathrm{d}\tilde{\rho}\ \tilde{\rho}g(\tilde{\rho})\cos[\theta_0](-2+g(\tilde{\rho}))\\
c_{22} &= \int_0^\infty \mathrm{d}\tilde{\rho}\ \tilde{\rho}^2\sin[\theta_0](-1+g(\tilde{\rho})),\\
c_{31} &= \int_0^\infty \mathrm{d}\tilde{\rho}\ \tilde{\rho}\cos[\theta_0](-1+g(\tilde{\rho}))g(\tilde{\rho}),\\
c_{32} &= \int_0^\infty \mathrm{d}\tilde{\rho}\ \tilde{\rho}^2\sin[\theta_0],\\
c_{33} &= \int_0^\infty \mathrm{d}\tilde{\rho}\ \frac{1}{2}\tilde{\rho}^2\sin[\theta_0](-2+g(\tilde{\rho}))g(\tilde{\rho}),\\
c_{41} &= \int_0^\infty \mathrm{d}\tilde{\rho}\ \frac{1}{4}\tilde{\rho}\cos[\theta_0]g(\tilde{\rho})\left(-4+4g(\tilde{\rho})-g(\tilde{\rho})^3\right),\\
c_{42} &= \int_0^\infty \mathrm{d}\tilde{\rho}\ \frac{1}{2}\tilde{\rho}^2(2-g[\rho])(1-g(\tilde{\rho}))\sin[\theta_0].
\end{aligned}
$$

E Derivation of forces

Here we provide an example of an calculation of a partial derivative for the term

$$\mathcal{F}_{\epsilon_3} = \epsilon_3 \int_{-\frac{L}{2}}^{\frac{L}{2}} dz \left(\partial_z u_x \partial_z^2 u_y - \partial_z u_y \partial_z^2 u_x\right). \tag{E.1}$$

We obtain:

$$\begin{aligned}
&-\frac{1}{\epsilon_3}\frac{\delta\mathcal{F}_{\epsilon_3}[u_x(z),u_y(z)]}{\delta u_x(z_0)} = \\
&\quad = -\lim_{\varepsilon\to 0}\frac{1}{\epsilon}\left(\int_{-\frac{L}{2}}^{\frac{L}{2}} dz \left(\partial_z(u_x(z)+\epsilon\delta(z-z_0))\partial_z^2 u_y(z) - \partial_z u_y(z)\partial_z^2(u_x(z)+\epsilon\delta(z-z_0))\right) - \frac{1}{\epsilon_3}\mathcal{F}_{\epsilon_3}\right) \\
&\quad = -\lim_{\varepsilon\to 0}\frac{1}{\epsilon}\int_{-\frac{L}{2}}^{\frac{L}{2}} dz\epsilon\partial_z\delta(z-z_0)\partial_z^2 u_y(z) + \lim_{\varepsilon\to 0}\frac{1}{\epsilon}\int_{-\frac{L}{2}}^{\frac{L}{2}} dz\partial_z u_y(z)\epsilon\partial_z^2\delta(z-z_0) \\
&\quad = -\int_{-\frac{L}{2}}^{\frac{L}{2}} dz\partial_z\delta(z-z_0)\partial_z^2 u_y(z) + \int_{-\frac{L}{2}}^{\frac{L}{2}} dz\partial_z u_y(z)\partial_z^2\delta(z-z_0) \\
&\quad = -\partial_z^2 u_y(z)\delta(z-z_0)\Big|_{-\frac{L}{2}}^{\frac{L}{2}} - \left(-\int_{-\frac{L}{2}}^{\frac{L}{2}} dz u_y(z)\delta(z-z_0)\right) + \partial_z u_y(z)\partial_z\delta(z-z_0)\Big|_{-\frac{L}{2}}^{\frac{L}{2}} \\
&\quad - \int_{-\frac{L}{2}}^{\frac{L}{2}} dz\partial_z^2 u_y(z)\partial_z\delta(z-z_0) \\
&\quad = -\partial_z^2 u_y(z)\delta(z-z_0)\Big|_{-\frac{L}{2}}^{\frac{L}{2}} + \partial_z^3 u_y(z_0) \\
&\quad + \partial_z u_y(z)\partial_z\delta(z-z_0)\Big|_{-\frac{L}{2}}^{\frac{L}{2}} - \partial_z^2 u_y(z)\delta(z-z_0)\Big|_{-\frac{L}{2}}^{\frac{L}{2}} - \left(-\int_{-\frac{L}{2}}^{\frac{L}{2}} dz\partial_z^3 u_y(z)\delta(z-z_0)\right) \\
&\quad = -\partial_z^2 u_y(z)\left(\delta(z-\tfrac{L}{2}) - \delta(z+\tfrac{L}{2})\right) + \partial_z^3 u_y(z_0) + \partial_z u_y(z)\left(\partial_z\delta(z-\frac{L}{2}) - \partial_z\delta(z+\frac{L}{2})\right) \\
&\quad - \partial_z^2 u_y(z)\left(\delta(z-\tfrac{L}{2}) - \delta(z+\tfrac{L}{2})\right) + \partial_z^3 u_y(z_0) \\
&\quad = \partial_z u_y(z)\left(\partial_z\delta(z-\tfrac{L}{2}) - \partial_z\delta(z+\tfrac{L}{2})\right) - 2\partial_z^2 u_y(z)\left(\delta(z-\tfrac{L}{2}) - \delta(z+\tfrac{L}{2})\right) + 2\partial_z^3 u_y(z_0).
\end{aligned}$$

For the functional derivative with respect to u_y we obtain:

$$\begin{aligned}
&-\frac{1}{\epsilon_3}\frac{\delta\mathcal{F}_{\epsilon_3}[u_x(z),u_y(z)]}{\delta u_y(z_0)} = \\
&\quad = -\partial_z u_x(z)(\partial_z\delta(z-\tfrac{L}{2}) - \partial_z\delta(z+\tfrac{L}{2})) + 2\partial_z^2 u_x(z)(\delta(z-\tfrac{L}{2}) - \delta(z+\tfrac{L}{2})) - 2\partial_z^3 u_x(z_0).
\end{aligned}$$

Therefore, the elastic force can be written as

$$\begin{aligned}\boldsymbol{F}^{el}_{\mathcal{F}_{\epsilon_3}} &= 2\epsilon_3\hat{\boldsymbol{z}}\times\partial_z^3\boldsymbol{u} + \epsilon_3[\partial_z\boldsymbol{u}(\partial_z\delta(z-\tfrac{L}{2})-\partial_z\delta(z+\tfrac{L}{2}))]\times\hat{\boldsymbol{z}} \\ &\quad +\epsilon_3\hat{\boldsymbol{z}}\times[2\partial_z^2\boldsymbol{u}(\delta(z-\tfrac{L}{2})-\delta(z+\tfrac{L}{2}))].\end{aligned}$$

For the term

$$\mathcal{F}_{\epsilon_{31}} = \epsilon_{31}\int_{-\frac{L}{2}}^{\frac{L}{2}} dz\,\big(\partial_z u_x((\partial_z u_x)^2+(\partial_z u_y)^2)\big) \tag{E.2}$$

we obtain

$$\begin{aligned}&-\frac{1}{\epsilon_{31}}\frac{\delta\mathcal{F}_{\epsilon_3}[u_x(z),u_y(z)]}{\delta u_x(z_0)} = \\ &\qquad = -(\delta(z-\tfrac{L}{2})-\delta(z+\tfrac{L}{2}))(3(\partial_z u_x)^2+(\partial_z u_y)^2)+2(3\partial_z u_x\partial_z^2 u_x+\partial_z u_y\partial_z^2 u_y)\Big|_{z=z_0}\end{aligned}$$

for x direction and

$$\begin{aligned}&-\frac{1}{\epsilon_{31}}\frac{\delta\mathcal{F}_{\epsilon_3}[u_x(z),u_y(z)]}{\delta u_y(z_0)} = \\ &\qquad = -2(\delta(z-\tfrac{L}{2})-\delta(z+\tfrac{L}{2}))(\partial_z u_x\partial_z u_y)+2(\partial_z u_y\partial_z^2 u_x+\partial_z u_x\partial_z^2 u_y)\Big|_{z=z_0}\end{aligned}$$

in y direction.

Similarly we calculate all elastic forces for other terms.

Acknowledgements

Not everyone's doctoral experience is the same. For me it happened to be one of the most challenging periods of my life, both personally and professionally. The beginning of my graduate studies coincided with the COVID pandemic and continued with the invasion of my home country, a terrible crime against humanity and the deadliest conflict in Europe since World War II. Coming to the end of this long journey, I know that it's only because of the continuous support of the people around me, that I managed to succeed.

Firstly, I deeply thank Prof. Dr. Achim Rosch for providing me with the opportunity to conduct research in his group, already at an early stage of my scientific career. His passion for science was something I could always rely on while facing the hardest scientific problems – part of every PhD thesis. I thank him for his patience, which cannot be overestimated, and sharing his extensive knowledge and wisdom with me over these years.

I am grateful to the members of my Thesis Advisory Committee (Prof. Dr. Simon Trebst and Prof. Dr. Corinna Kollath) for their valuable input. I thank Prof. Dr. Simon Trebst for taking time to read and evaluate my thesis and Prof. Dr. Joachim Hemberger for taking the role of Chairman of my Examination Board.

Furthermore, I have had the great pleasure working with Prof. Dr. Christian Pfleider, Dr. Andreas Bauer and Dr. Denis Mettus from TUM. As a participant in the MINT mentorship program of the University of Cologne, I benefited a lot from discussions and workshops in the context of this program. I deeply thank Prof. Dr. Karin Everschor-Sitte for agreeing to be my mentor, for sharing her experience and supporting me during the initial stages of this work. Moreover, my heartful gratitude goes to PD Dr. Michael Buchhold, my mentor and friend, who has contributed immensely to me growing up as a scientist and a person. Thank you for teaching me the art of small steps.

I am deeply indebted to Mariela Boevska, Andreas Sindermann, Konstantinia Schäfer and Ute Graffenberger for keeping the THP together and for providing quick help if needed. In particular, my deep thanks to Mariela for helping my parents to find housing during the first days of war.

Many mistakes would have been left unseen, would it have not been for Nick, Marcel, Robin, Tom, Dennis, Sagar and Johannes proofreading this Thesis. Furthermore, I had a great pleasure co-supervising the theses of Hannah Duerschmidt, Leon-Sascha Gernert and Carlos Ramos Marimón. As much as I hope this experience was enriching for you, I can say that it was so for me. Aprem, Dennis, Reza and Adrian: sharing an office with you was a blast!

I am very grateful to many people that I am happy to call friends, who have provided me with practical advice and kind words. Among those, there are several people who have played a decisive role in shaping my years. I deeply thank Marcel and Nina for their support, constructive advice and that they never stopped believing in me. To the members of the "Wandergruppe": Nick, Marcel, Dennis, Thomas and Valentin. Thank you for your hope and care during the COVID pandemic. I have many fond memories of our time together. I thank Tom and Tobias for great discussions and many fun moments. Robin and Katja, thank you for being always there for me. I am truly lucky to have you as my friends!

I am so grateful for Erik, being the amazing human he is, for his constant and unwavering support.

I would not be the person I am today without my parents Vasyl and Iryna, together with my sister Yulia. It is your absolute and unconditional love, encouragement and unwavering belief in my abilities throughout my life that made my success possible. I appreciate and value every sacrifice you have made to provide me with the education I have. Thank you for being wonderful role models and for nurturing the curious and explorative instincts in me. You are my foundation and my wings.

To my partner, soulmate, best friend, proofreader, biggest supporter and sounding board. Nick, how can I ever express how much your love and tremendous support during this journey means to me? My every attempt to do so will only make it appear smaller than what it really is. Thank you for keeping me sane and steady over the last years, for going with me through the darkest of times, for celebrating me so that I may never give up. It is your bright optimism that enlightens my soul and puts everything into perspective.

Erklärung zur Dissertation

Hiermit versichere ich an Eides statt, dass ich die vorliegende Dissertation selbstständig und ohne die Benutzung anderer als der angegebenen Hilfsmittel und Literatur angefertigt habe. Alle Stellen, die wörtlich oder sinngemäß aus veröffentlichten und nicht veröffentlichten Werken dem Wortlaut oder dem Sinn nach entnommen wurden, sind als solche kenntlich gemacht. Ich versichere an Eides statt, dass diese Dissertation noch keiner anderen Fakultät oder Universität zur Prüfung vorgelegen hat; dass sie - abgesehen von unten angegebenen Teilpublikationen und eingebundenen Artikeln und Manuskripten - noch nicht veröffentlicht worden ist sowie, dass ich eine Veröffentlichung der Dissertation vor Abschluss der Promotion nicht ohne Genehmigung des Promotionsausschusses vornehmen werde. Die Bestimmungen dieser Ordnung sind mir bekannt. Darüber hinaus erkläre ich hiermit, dass ich die Ordnung zur Sicherung guter wissenschaftlicher Praxis und zum Umgang mit wissenschaftlichem Fehlverhalten der Universität zu Köln gelesen und sie bei der Durchführung der Dissertation zugrundeliegenden Arbeiten und der schriftlich verfassten Dissertation beachtet habe und verpflichte mich hiermit, die dort genannten Vorgaben bei allen wissenschaftlichen Tätigkeiten zu beachten und umzusetzen. Ich versichere, dass die eingereichte elektronische Fassung der eingereichten Druckfassung vollständig entspricht.

Teilpublikationen: –

07.10.2024, Alla Bezvershenko